Imperial College London

Department of Chemistry

Transient spectroscopic studies of disordered semiconductors for solar-driven fuel synthesis

by

Michael Sachs

Supervisor:

James R. Durrant

A thesis submitted in partial fulfilment of the requirements for the degree Doctor of Philosophy

September 2019

The present work was carried out in the period from October 2015 to September 2019 at the Department of Chemistry at Imperial College London under the supervision of by Prof. James Durrant.

Except when specific reference is made, the material presented in this thesis is the result of my own work. Where results from collaborative experiments have been used it is clearly stated. This manuscript does not exceed 100 000 words in length.

September 2019

Copyright Declaration

Abstract

Transient spectroscopic studies of disordered semiconductors for solar-driven fuel synthesis

by Michael Sachs

In this thesis, time-resolved spectroscopic techniques are used to link the activity of materials for solar-driven fuel generation with their excited state dynamics.

Chapter 1 provides an introduction to the wider scope of this work, discussing global warming and the opportunities of solar energy in its mitigation, leading on to artificial photosynthesis as a means of storing solar energy at large scale.

Chapter 2 covers the fundamentals of semiconducting photocatalysts and their photophysics before discussing the properties of metal oxide and polymer photocatalysts in particular. The aims and objectives of this thesis are presented.

Chapter 3 describes the spectroscopic techniques used to characterise the photocatalyst materials in this thesis and elaborates on the experimental challenges which arise from applying these techniques to the materials studied herein.

Chapter 4, the first results chapter, investigates a series of conjugated polymers as photocatalysts for hydrogen evolution. These polymers have sulfone groups embedded into their backbone and represent some of the most active materials discovered in the class of conjugated polymers so far. Photogenerated reaction intermediates are monitored on timescales of femtoseconds to seconds after excitation, and the yield of long-lived electrons is found to qualitatively correlate with the photocatalytic activity in this polymer series.

Photocatalysts prepared via palladium-catalysed coupling reactions typically contain considerable amounts of palladium impurities, which have been shown to act as co-catalysts for hydrogen evolution in F8BT nanoparticles. Chapter 5 studies the effect of these palladium impurities in such F8BT nanoparticles on the excited state of the polymer, and demonstrates that the palladium centres within these particles quench photogenerated excitons about twice as fast as the electron donor diethylamine in the solution phase. A comparison to one of the sulfone polymers characterised in the previous chapter is made under charge accumulation conditions.

Chapter 6 switches the focus to metal oxides and investigates the photophysical differences between near-stoichiometric and highly oxygen-deficient oxides using WO_3 as a model material. Highly oxygen-deficient WO_3 exhibits a strong blue colouration due to a large density of states within the bandgap, which is found to also give rise to rapid trapping of photogenerated holes. This rapid trapping process prolongs the lifetime of photogenerated charges by several orders of magnitude, but also leads to a severe reduction in oxidative driving force, thus compromising the efficiency of demanding oxidation reactions such as water oxidation.

In Chapter 7, a series of 11 different metal oxides is investigated in order to test whether common activity-related photophysical characteristics arise from similarities in their electronic configurations. It is found that metal oxides with empty (d^0) or closed d-shells (d^{10}) exhibit delocalised electrons with generally longer lifetimes compared to oxides with open d-shells. This stark lifetime difference is due to a rapid sub-picosecond localisation process in the latter materials, which is attributed to the formation of small polarons.

Finally, Chapter 8 presents the overall conclusions of this thesis and discusses the different chapters in context to each other. Directions for future work are suggested.

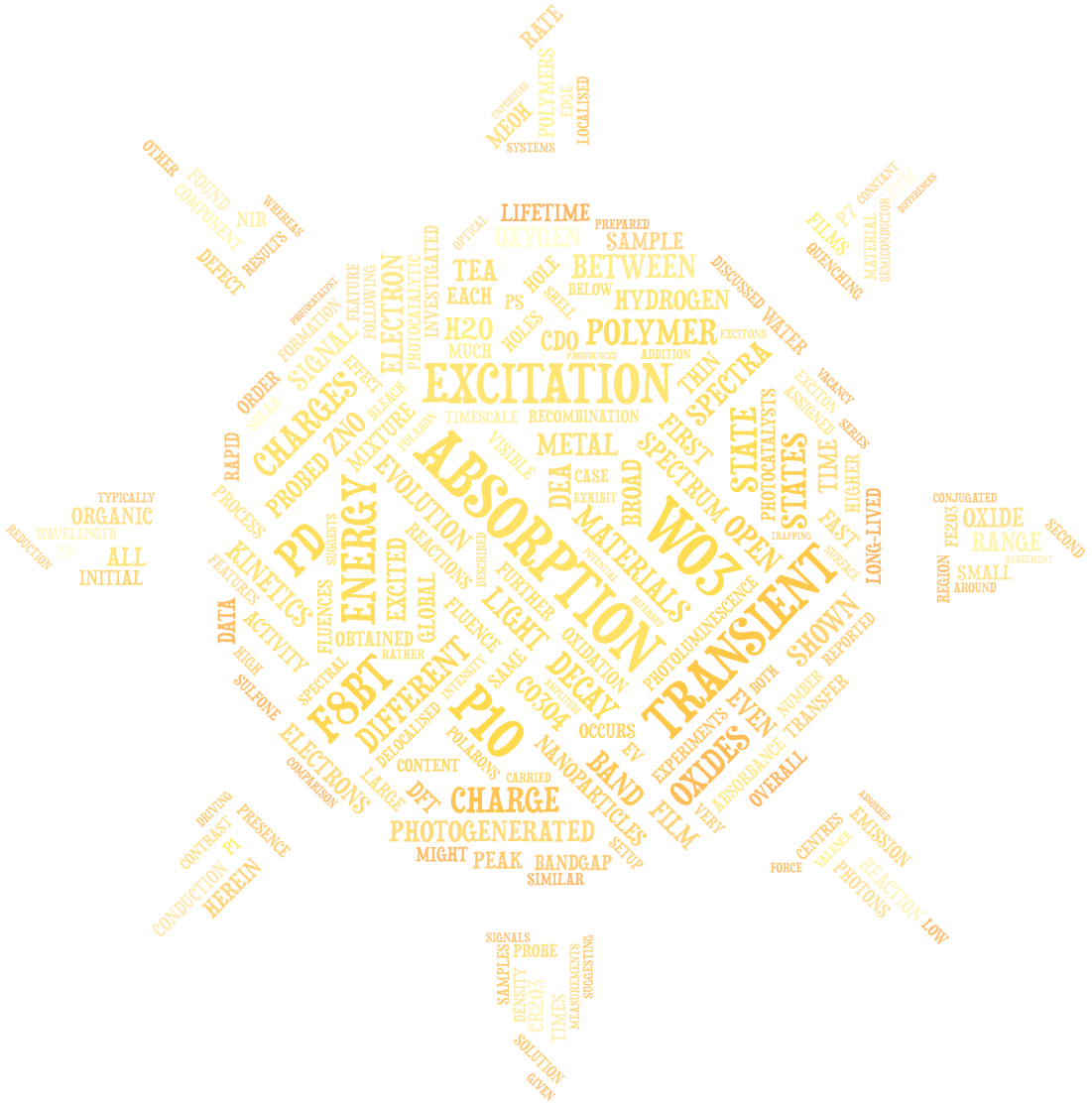

Wordcloud for this thesis.

Acknowledgements

Firstly, I would like to thank my supervisor, James Durrant, for taking me on as an Erasmus student and mentoring me until this point. Thank you for giving me the freedom to pursue my own ideas and approaches while at the same time providing a sense of direction and guidance when drifting off too far. And most importantly, thank you for fostering the supportive group environment which made this PhD journey such a great experience.

Thank you to the European Union, without whose Erasmus+ program I would have never gone to study in the UK in the first place. It can only be hoped that future generations will have similar opportunities.

Thank you to Imperial College for awarding me the President's PhD scholarship that allowed me to carry out the research described in this thesis, provided me with conference funding, and connected me with friends across the cohort.

Thank you to all the collaborators I had the privilege to work with, and without whom the research described in this thesis would not have been possible - special thanks go to the Cooper, Nelson, Kafizas, Walsh, Zwijnenburg, McCulloch, and Tang groups.

A special thank you goes to Li and Pabitra for keeping the group organised and for their help with pretty much anything, as well as for orchestrating our 'big move' to the new Chemistry department in White City. Thank you also to the Chemistry technicians, especially to Stefanos and Richard, who always made time to help me sort out equipment problems and lab issues.

Thank you to my London family for all your invaluable support over the years, particularly Camilo, Ernest, Laia, Lorenzo, Sacha, Hyojung, Shababa, and René.

Thank you to all past and present Durrantites - your friendship throughout the PhD really is what made all the difference to me. I will keep great memories of our h-bar visits, bandgap trips, scientific discussions, cake clubs, squash clubs, gin clubs, and the various other clubs founded over the years. Thank you to Yu-Han, Ludmilla, Ben, Li, Sam, Weidong, Carlota, Anna, Jim, Jiaying, Lin, Yifan, Camilo, Ernest, Laia, Hyojung, Andreas, Sacha, Shababa, Pabitra, Madeleine, Robert, Seb, Wenxing, Steph, Scot, Ching-Hong, Elisa, Yimeng, Stoichko, Carolina, Alex, and everyone I missed when putting together these acknowledgements just before thesis submission.

A particularly big thank you goes to Anne for keeping me motivated and for her unconditional support from both Cambridge and Berlin, especially during the long days of thesis writing.

And finally, thank you to my parents and family, whose support and encouragement I could always rely on regardless of physical distance.

Contents

List of Publications

1. Wang, Y., Vogel, A., **Sachs, M.**, Sprick, R. S., Wilbraham, L., Moniz, S. J. A., Godin, R., Zwijnenburg, M. A., Durrant, J. R., Cooper, A. I. & Tang, J. Current understanding and challenges of solar-driven hydrogen generation using polymeric photocatalysts. *Nat. Energy* **4**, 746–760 (2019).

2. Corby, S., Pastor, E., Dong, Y., Zheng, X., Francàs, L., **Sachs, M.**, Selim, S., Kafizas, A., Bakulin, A. A. & Durrant, J. R. Charge Separation, Band-Bending, and Recombination in WO_3 Photoanodes. *J. Phys. Chem. Lett.* **10**, 5395–5401 (2019).

3. Jiamprasertboon, A., Kafizas, A., **Sachs, M.**, Ling, M., Alotaibi, A. M., Lu, Y., Siritanon, T., Parkin, I. P. & Carmalt, C. J. Heterojunction α-Fe_2O_3/ZnO Films with Enhanced Photocatalytic Properties Grown by Aerosol-Assisted Chemical Vapour Deposition. *Chem. – A Eur. J.* **25**, 11337–11345 (2019).

4. Shankar, R., **Sachs, M.**, Francàs, L., Lubert-Perquel, D., Kerherve, G., Regoutz, A. & Petit, C. Porous boron nitride for combined CO_2 capture and photoreduction. *J. Mater. Chem. A* **44**, 1–26 (2019).

5. Moia, D., Giovannitti, A., Szumska, A. A., Maria, I. P., Rezasoltani, E., **Sachs, M.**, Schnurr, M., Barnes, P. R. F., McCulloch, I. & Nelson, J. Design and evaluation of conjugated polymers with polar side chains as electrode materials for electrochemical energy storage in aqueous electrolytes. *Energy Environ. Sci.* **12**, 1349–1357 (2019).

6. **Sachs, M.**, Park, J.-S., Pastor, E., Kafizas, A., Wilson, A. A., Francàs, L., Gul, S., Ling, M., Blackman, C., Yano, J., Walsh, A. & Durrant, J. R. Effect of oxygen deficiency on the excited state kinetics of WO_3 and implications for photocatalysis. *Chem. Sci.* **10**, 5667–5677 (2019).

7. **Sachs, M.**, Sprick, R. S., Pearce, D., Hillman, S. A. J., Monti, A., Guilbert, A. A. Y., Brownbill, N. J., Dimitrov, S., Shi, X., Blanc, F., Zwijnenburg, M. A., Nelson, J., Durrant, J. R. & Cooper, A. I. Understanding structure-activity relationships in linear polymer photocatalysts for hydrogen evolution. *Nat. Commun.* **9**, 4968 (2018).

8. Corby, S., Francàs, L., Selim, S., **Sachs, M.**, Blackman, C., Kafizas, A. & Durrant, J. R. Water Oxidation and Electron Extraction Kinetics in Nanostructured Tungsten Trioxide Photoanodes. *J. Am. Chem. Soc.* **140**, 16168–16177 (2018).

9. Kosco, J., **Sachs, M.**, Godin, R., Kirkus, M., Francas, L., Bidwell, M., Qureshi, M., Anjum, D., Durrant, J. R. & McCulloch, I. The Effect of Residual Palladium Catalyst Contamination on the Photocatalytic Hydrogen Evolution Activity of Conjugated Polymers. *Adv. Energy Mater.* **8**, 1802181 (2018).

10. **Sachs, M.**, Pastor, E., Kafizas, A. & Durrant, J. R. Evaluation of Surface State Mediated Charge Recombination in Anatase and Rutile TiO_2. *J. Phys. Chem. Lett.* **7**, 3742–3746 (2016).

11. Sprick, R. S., Bonillo, B., **Sachs, M.**, Clowes, R., Durrant, J. R., Adams, D. J. & Cooper, A. I. Extended conjugated microporous polymers for photocatalytic hydrogen evolution from water. *Chem. Commun.* **52**, 10008–10011 (2016).

12. Selim, S., Pastor, E., García-Tecedor, M., Morris, M. R.,1 Francàs, L., **Sachs, M.**, Moss, B., Corby, S., Mesa, C. A., Gimenez, S., Kafizas, A., Bakulin, A. A & Durrant, J. R. Impact of oxygen vacancy occupancy on charge carrier dynamics in $BiVO_4$ photoanodes. *Under revision.*

13. Kosco, J., Bidwell, M., Cha, H., Martin, T., Howells, C., **Sachs, M.**, Anjum, D., Gonzalez Lopez, S., Zou, L., Wadsworth, A., Zhang, W., Zhang, L., Sougrat, R., Laquai, F., DeLongchamp, D., Durrant, J. R. & McCulloch, I. Record photocatalytic hydrogen evolution from organic semiconductor heterojunction nanoparticles. *Submitted.*

14. **Sachs, M.**, Cha, H., Kosco, J., Francàs, L., Corby, S., Wilson, A. A., Sprick, R. S., Godin, R., Fahey-Williams, A., Cooper, A. I., McCulloch, I. & Durrant, J. R. The effect of residual palladium on exciton separation and charge accumulation in conjugated polymer photocatalysts. *In preparation.*

15. **Sachs, M.**, Pastor, E., Park, J.-S., Walsh, A. & Durrant, J. R. Effect of excitation energy on charge localisation in Cr_2O_3. *In preparation.*

16. **Sachs, M.**, Pastor, E., Park, J.-S., Kafizas, A., Selim, S., Corby, S., Walsh, A. & Durrant, J. R. Localisation of photogenerated charges in metal oxides. *In preparation.*

17. Windle, C. D., Cockcroft, J. K., Wieczorek, A., Cha, H., **Sachs, M.**, Bozal-Ginesta, C., Durrant, J. R. & Tang, J. Covalent functionalisation of carbon nitrides for robust, efficient and well-defined photocatalysts. *In preparation.*

18. Aitchison, C. M., Sprick, R. S., **Sachs, M.**, Little, M. A., Kane, C. M., Wilbraham, L., Brownbill, N. J., Blanc, F., Zwijnenburg, M. A., Durrant, J. R. & Cooper A. I. Investigating structure-activity relationships in well-defined oligomer photocatalysts for hydrogen production from water. *In preparation.*

19. Hillman, S. A. J., Sprick, R. S., Shi, X., **Sachs, M.**, Pearce, D., Woods, D. J., Guilbert, A. A. Y., Cooper, A. I., Durrant, J. R. & Nelson, J. Mechanistic limitations of linear conjugated polymer photocatalysts for hydrogen evolution from water and the deposition of thin films as a microstructural solution. *In preparation.*

20. Pastor, E., **Sachs, M.**, Dyson, M., Dimitrov, S., Luo, J., Kim, J., Kafizas, A., Francàs, L., Tilley, D., Mayer, M., Gratzel, M., Stavrinou, P. N. & Durrant, J. R. Photoinduced refractive index changes in inorganic and hybrid thin films for energy conversion. *In preparation.*

List of Figures

List of Tables

Abbreviations

A	**A**bsorbance
CB	**C**onduction **B**and
DEA	**D**i**e**thyl**a**mine
EQE	**E**xternal **Q**antum **E**fficiency
EXAFS	**E**xtended **X**-ray **A**bsorption **F**ine **S**tructure
FTO	**F**luorine-doped **T**in **O**xide
GA	**G**lobal **A**nalysis
HOMO	**H**ighest **O**ccupied **M**olecular **O**rbital
ICP-OES	**I**nductively **C**oupled **P**lasma **O**ptical **E**mission **S**pectrometry
IPCE	**I**ncident **P**hoton - to - **C**urrent Conversion **E**fficiency
IQE	**I**nternal **Q**antum **E**fficiency
IRF	**I**nstrument **R**esponse **F**unction
LED	**L**ight-**e**mitting **D**iode
LMCT	**L**igand-to-**M**etal **C**harge **T**ransfer
LUMO	**L**owest **U**noccupied **M**olecular **O**rbital
MMCT	**M**etal-to-**M**etal **C**harge **T**ransfer
NIR	**N**ear-**I**nfra**r**ed
OPV	**O**rganic **p**hoto**v**oltaics
PIAS	**P**hoto**i**nduced **A**bsorption **S**pectroscopy
PV	**P**hoto**v**oltaic
SCLJ	**S**emi**c**onductor-**l**iquid **j**unction
SEC	**S**pectro**e**lectro**c**hemistry
STH	**S**olar-**t**o-**h**ydrogen
TAS	**T**ransient **A**bsorption **S**pectroscopy
TCSPC	**T**ime-**C**orrelated **S**ingle **P**hoton **C**ounting

TEA	**T**ri**e**thyl**a**mine
UV	**U**ltra-**V**iolet
VB	**V**alence **B**and
XANES	**X**-ray **A**bsorption **N**ear **E**dge **S**tructure
XPS	**X**-ray **P**hotoelectron **S**pectroscopy

To my parents

Chapter 1

Introduction

1.1 Global warming

In 2018, the global average atmospheric CO_2 concentration reached a new record high of 407.4 ppm, as reported by the American Meteorological Society [1]. In fact, the global average CO_2 concentration has increased every year since direct measurements were started by Charles David Keeling in 1958, exceeding 400 ppm for the first time in 2013 [2]. This unprecedentedly high CO_2 concentration and constant increase are alarming, especially given that data from Antarctic ice cores demonstrate that global CO_2 levels had never exceeded 300 ppm in the past 800 000 years until the beginning of industrialisation [3, 4]. In light of the overwhelming amount of evidence, the scientific community widely acknowledges that this rise in CO_2 levels is caused by human activities and has severe implications for the global climate.

CO_2 acts as a greenhouse gas. At current concentrations, it leads to global warming with the potential to cause heatwaves, extreme storms, draughts, floods, Arctic ice loss, and rising global sea levels [5]. These effects constitute severe threats, with possible consequences being food shortages, flooding of coastal cities, and the extinction of a variety of species. In addition, CO_2 has a particularly long lifetime in the atmosphere, and the rate of its current accumulation is thus likely have an impact on the global climate for the next 500-2000 years or longer [6].

The gravity of the situation has given rise to coordinated efforts on an international level. At the end of 2015, the Paris agreement within the United Nations Framework Convention on Climate Change (UNFCCC) was finalised, where the target was set to keep the global temperature rise 'well below' 2 °C above pre-industrial levels and to pursue measures that would limit the

temperature increase to 1.5 °C. The agreement is currently ratified by 185 state parties [7]. Although it was clear that drastic measures would be required to meet these targets, the world is at present not on track to meet them: the 1.5 °C goal now seems almost impossible to achieve, 2 °C appears difficult, and the world is on a course towards 3 °C warming above pre-industrial times [8, 9].

Due to this lack of satisfactory progress, increasing momentum is currently building in the public domain. Sparked by the school strike for climate movement, global climate change protests in late September this year have drawn an estimated 6 million protesters worldwide [10]. Given the growing energy demand discussed in the next section, it can only be hoped that such protests will convince politicians to take more drastic measures in order to get back on track.

1.2 Renewable energy

In 2018, the global energy consumption showed the fastest growth since 2010, and global carbon emissions related to energy use grew at the fastest rate in seven years [11]. Furthermore, the U.S. Energy Information Administration (EIA) projects an almost 50% increase in world energy usage between 2018 and 2050, primarily driven by strong economic growth in Asia [12]. Given the aforementione urgent need to reduce global emissions, it is clear that a much greater focus on renewable energy sources will be necessary in order to mitigate the consequences of climate change.

The global investment in renewable energy sources was USD 304.9 billion in 2018, in fact far exceeding investments in fossil fuels and nuclear power. The vast majority of this investment was in wind and solar photovoltaics (PV), and the resulting new capacities met almost a quarter of the global growth in energy demand [13]. Figure 1.1 illustrates the share of renewables in the total final energy consumption of 2018, subdivided into three commonly used sectors: heating and cooling, transport, and power (i.e. electricity). Note that the total final energy consumption captures only energy used in its final form and thus does not take into account energy used during refinement and delivery of the final energy carrier (e.g. the refinement of oil and delivery of petrol to its final destination).

The power sector, where renewables now cover 26% of the world's electricity generation, has clearly led the way in these latest capacity gains but it should be kept in mind that power only accounts for 17% of the total energy consumption [13]. This capacity increase in the power sector

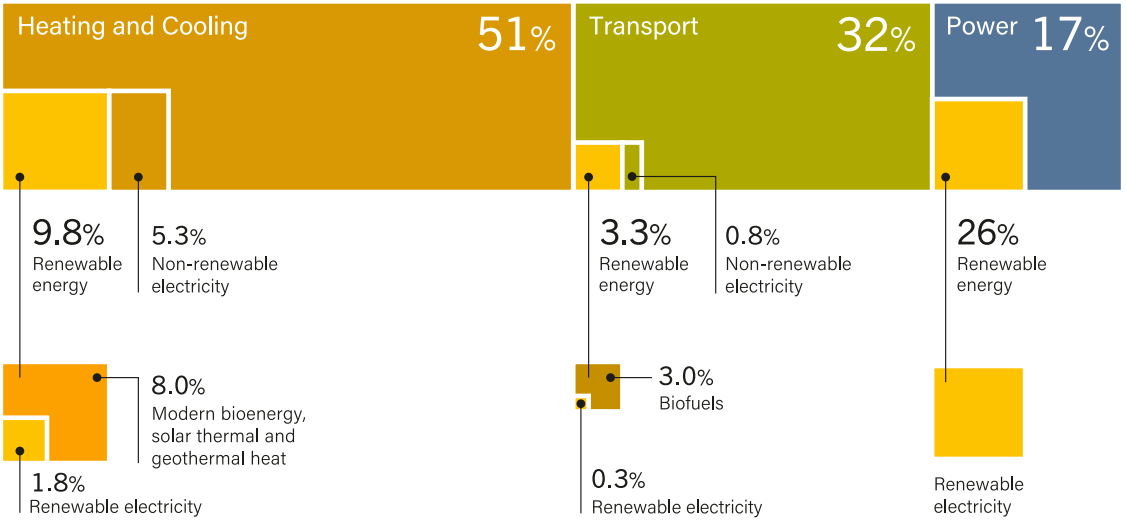

Figure 1.1: Contribution of renewable energy sources to the total final global energy consumption, subdivided by sector. Reproduced from reference [8].

largely arises from improved cost-competition of renewable power compared to conventional fossil fuel-based power plants. In contrast, heating and cooling makes up over half of the global energy consumption, and the fraction of direct renewables (e.g. modern bioenergy, geothermal and solar thermal heat) and renewable electricity in this sector is only about 10%. In the transport sector, three quarters of which were accounted for by road transport in 2016 [13], biofuels made up almost the entire renewable energy share, which only totalled 3.3%. Overall, these statistics show that progress in the dissemination of renewable energy technologies is largely concentrated in the power sector. Heating and cooling as well as transport, making up over 80% of the total energy demand, are lagging behind [13], which can at least partially be attributed to a lack of widely available renewable fuels.

Although some of these numbers may seem encouraging, Figure 1.2 shows that the share of fossil fuels in the total energy consumption was still close to 80% in 2017, with another 7.5% accounted for by traditional biomass. The share of modern renewable energy sources was 10.6%, with the greatest contributor being renewable thermal energy (4.2%), followed by hydropower (3.6%), wind power (1.2%), solar PV (0.8%), and transport biofuels (1.0%) [13]. This low proportion of renewables demonstrates that significant efforts will be required in order to increase their share and meet the outlined emission targets.

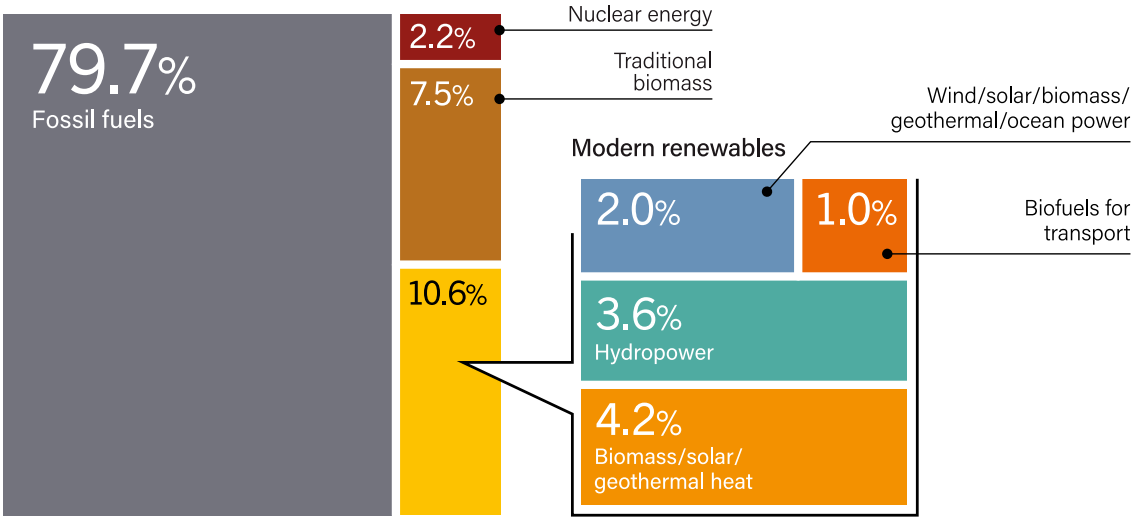

Figure 1.2: Estimated renewable share in total final energy consumption in 2017. Reproduced here from reference [8].

1.3 Solar energy

The fact that solar PV accounts for only ∼8% of the total renewable energy mix seems surprising, given that solar energy is the largest renewable energy source available. The energy of solar irradiation impinging on the surface of the Earth amounts to 100 000 TWy, which means that only one hour of global solar irradiation supplies enough energy to cover humanity's energy demand for an entire year [14, 15]. The wide availability of solar energy as a resource holds the potential to alleviate some of the geopolitical concerns related to our current reliance on fossil fuels, and makes it a well-suited energy source for off-grid power generation in areas without well-developed infrastructure [15]. For instance, an estimated 2% of the population in Asia and 5% of the population in Africa currently have access to electricity generated by off-grid solar PV systems [8]. Given these preconditions, it seems hard not to acknowledge that solar energy will have to be a key driver behind an increasing penetration of renewable energy sources into the overall energy mix.

Indeed, the potential of solar energy is increasingly recognised, and solar PV is now the fastest-growing source of renewable electricity [8]. Solar cells have been commercial since the 1970s, and the increasingly widespread adoption of this technology was largely driven by striking reductions in the cost of silicon solar cell modules over the years, amounting to a price drop of 97% between 1980 and 2012 [16]. In early years, improvements in module efficiencies were essential to reduce module prices, whereas scale economies related to ever-larger production volumes were the dominant driver behind cost reductions since around the turn of the millennium. In

addition, policies to stimulate market growth have been instrumental in the promotion of silicon PVs [16]. Figure 1.3 shows the global peak capacity of solar PV installations, reaching a total of 505 GW in 2018, as well as the newly added capacity for each year between 2008 and 2018. It is clear that the growth in solar PV peak capacity increased more and more in each subsequent year until stagnation occurred in 2018 for the first time in the shown time period. The latest stagnation can be ascribed to policy changes in China such as subsidy cuts, the leading country for PV investments in recent years [8].

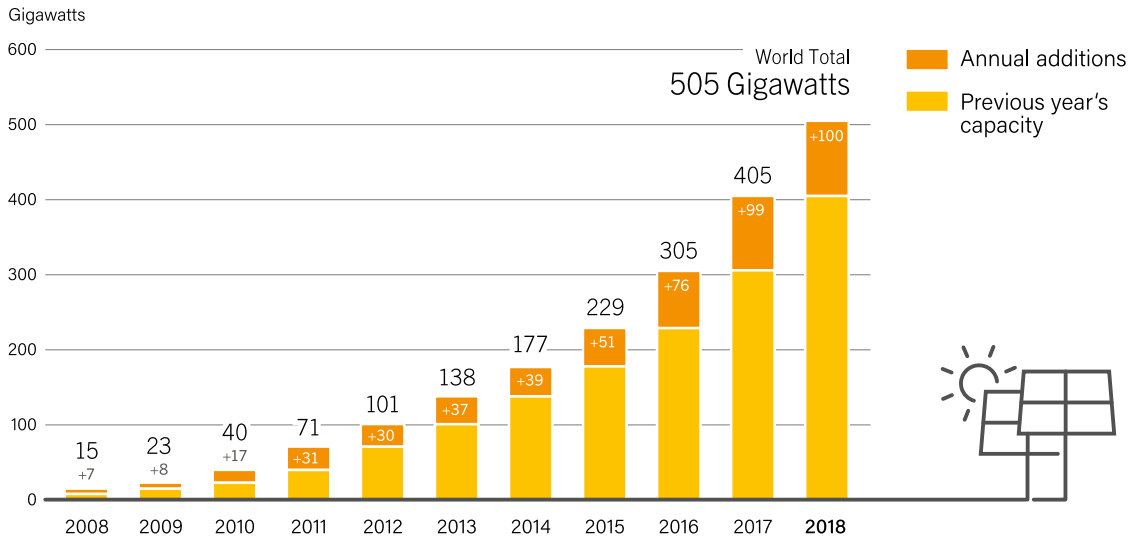

Figure 1.3: Global peak capacity of solar PV installations and annual additions between 2008 and 2018, adapted from reference [8]. Data are provided in direct current (prior to alternating current conversion).

While the outlined developments have caused silicon to become the most dominant PV technology by far, other technologies have been developed and are currently in various stages of deployment. However, it will be difficult for emerging PV technologies to compete with silicon solar cells purely on a cost basis, since the latter have already entered high-volume production. Therefore, niche applications for which silicon does not perform well currently appear most promising for such emerging technologies. For instance, organic photovoltaics (OPVs) [17], which are made from blends of polymers or polymers and small molecules, are lightweight and can be fabricated by simply printing the active layer onto a substrate. Flexible substrates can be used in the printing process, thus demonstrating potential for wearable technologies. Lab-scale devices with efficiencies of up to 14.3% have been reported using ternary blends [18] and up to 17.3% have been achieved using tandem OPV devices [19]. Impressive improvements in efficiency have been achieved in the class of lead-based perovskite solar cells, which are solution processable like OPVs and have reached an efficiency of 25.2% after a comparably short time

of active research [20]. Another promising application are combined silicon-perovskite devices, currently demonstrating efficiencies of up to 28% [21]. While these new technologies still suffer from stability limitations [22, 23], a significant advantage over silicon-based solar cells is their much lower energy payback time, i.e. the time after which they have produced the energy invested into their fabrication. The energy payback time is typically a few years for silicon solar cells [24] but can be as short as a few months for OPVs and perovskites [25].

Despite these advances in commercial deployment and research, the ultimate limitation of solar energy lies in its intermittency. This intermittency induces a timing imbalance between peak supply and peak demand for solar electricity [26], where most electricity is produced around midday although it is predominantly needed in the mornings and evenings. In addition to variations in solar irradiation intensity over the course of a day, weather-related fluctuations and seasonal variations lead to a considerable uncertainty surrounding sunlight as an energy source [27]. Therefore, in order for solar energy to reach high penetration into the overall energy mix, robust ways of storing it must be developed. In particular, solar energy storage solutions will be required to address the current shortcomings in the transport sector outlined in Section 1.2.

1.4 Artificial photosynthesis

Inspiration for ways to store solar energy can be found in nature, where solar energy is stored in the form of carbohydrates in the process of natural photosynthesis. This photosynthetic process is estimated to store 100 TWy of energy averaged over the period of one year, primarily in the form of wood and fibres, and is also responsible for a similar amount of photosynthetic activity in the oceans where the produced carbohydrates are rapidly fed back into the food chain [14].

Natural photosynthesis employs two light-absorbing photosystems, PSI and PSII, which were named in the order of their discovery rather than after their position in the reaction sequence. The natural photosynthetic process is initiated by the absorption of a photon via antenna systems containing chlorophyll and other pigments, which funnel the photon's energy to the PSII reaction centre. This reaction centre is where charges are separated via the generation of a radical pair state, which subsequently passes its reducing equivalent onto an electron transport chain. Through this electron transport chain, the reducing equivalent reaches PSI where it can be excited again by a second photon. This second excitation generates an electron with a sufficiently reductive potential to drive the fixation of CO_2, for instance into glucose. The oxidising

equivalents at the PSII centre then drive the water oxidation reaction via a manganese cluster, thus restoring the original state of the PSII centre. Overall, this sequence implies that each reaction centre must absorb four photons in order for one molecule of oxygen to be produced [14, 28, 29]. Importantly, in the absence of light, the photosynthetic organism can convert the produced hydrocarbons (e.g. glucose) back into usable energy in a process called respiration as illustrated in Figure 1.4. This respiration process corresponds to the reverse of the photosynthetic reaction and thus effectively releases solar energy stored in the form of chemical bonds [14].

While many of the individual charge transfer steps in this reaction sequence are remarkably efficient, photosynthetic organisms have to invest significant of amounts energy into maintaining their metabolism, organisation, and into their own reproduction. The energy cost associated with these processes lowers the energy yield in the form of biomass to below one percent, which means that the overall amount of energy stored in a form that mankind may consume is very low [14]. This is perhaps hardly surprising - after all, photosynthetic organisms evolved to survive in their respective environments rather than to provide biomass in high yields for humans [27].

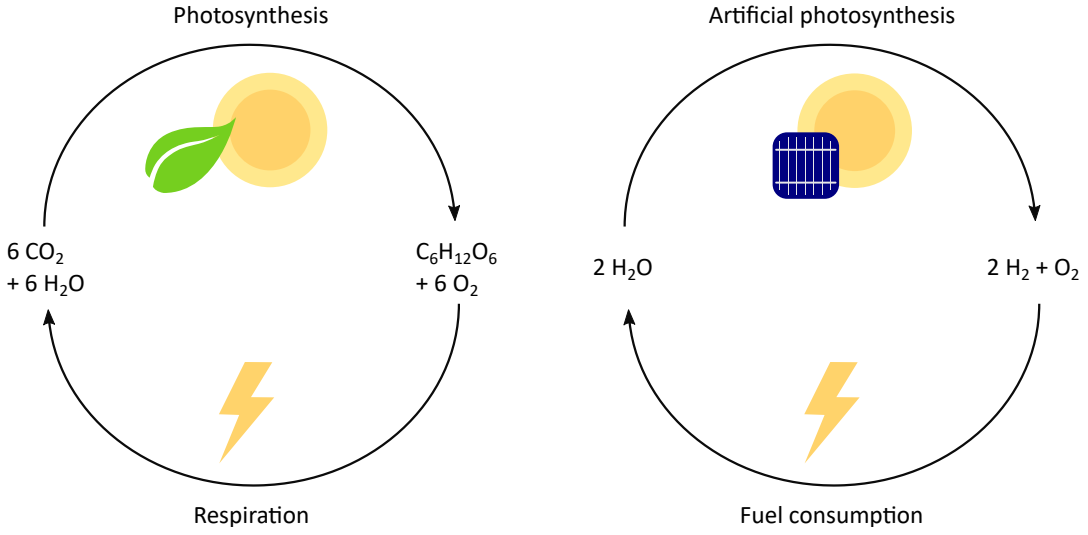

Figure 1.4: Schematic comparison of natural photosynthesis (left) and artificial photosynthesis (right).

Natural photosynthesis can serve as a blueprint for artificial photosynthetic systems which, unlike naturally occurring systems, may be specifically targeted towards the production of useful energy carriers in high yields. Conceptually, this means that a light-induced charge separation process must be coupled to reactions that produce chemical fuels. With natural photosynthesis in mind, such an artificial system would have to comprise a light absorbing unit, a reaction centre for

charge separation, and a catalyst to mediate the fuel-forming reactions [28]. In this thesis, so-called photocatalysts, which aim to fulfil several if not all of these tasks, will be investigated. The materials used to construct such artificial systems should be earth abundant and inexpensive in order to allow development on the large scale on which those materials will be required.

Which synthetic fuels should be targeted by such artificial photosynthetic systems is a matter of ongoing debate. Hydrogen is an attractive candidate since it is energy dense and can be produced via water splitting in a carbon-free energy cycle, as illustrated in Figure 1.4. Therefore, hydrogen will be the target fuel for the photocatalyst materials studied in this thesis. Alternatives to hydrogen are carbon-based fuels, produced via direct reduction of CO_2. Liquid carbon-based fuels have the advantage of being easier to handle than gaseous hydrogen, but the resulting energy cycle is carbon-neutral rather than carbon-free and the required CO_2 reduction reactions are kinetically even more demanding than water splitting.

1.5 References

1. American Meteorological Society. State of the climate in 2018 (2019).
2. Showstack, R. Carbon dioxide tops 400 ppm at Mauna Loa, Hawaii. *Eos, Transactions American Geophysical Union* **94,** 192–192 (2013).
3. Higgins, J. A. *et al.* Atmospheric composition 1 million years ago from blue ice in the Allan Hills, Antarctica. *Proceedings of the National Academy of Sciences of the United States of America* **112,** 6887–6891 (2015).
4. Lüthi, D. *et al.* High-resolution carbon dioxide concentration record 650,000–800,000 years before present. *Nature* **453,** 379–382 (2008).
5. U.S. Global Change Research Program. *Climate Science Special Report. Fourth National Climate Assessment (NCA4), Volume I* tech. rep. (2017).
6. Lewis, N. S. & Nocera, D. G. Powering the planet: chemical challenges in solar energy utilization. *Proceedings of the National Academy of Sciences of the United States of America* **103,** 15729–15735 (2006).
7. United Nations Framework Convention on Climate Change. *What is the Paris Agreement?* (2019).
8. REN21. *Renewables 2019 Global Status Report* (REN21 Secretariat, Paris, 2019).
9. Tollefson, J. *The hard truths of climate change - by the numbers* 2019. (2019).

10. The Guardian. *Climate crisis: 6 million people join latest wave of global protests* (2019).

11. p.l.c., B. *BP Statistical Review of World Energy* tech. rep. (2019).

12. U.S. Energy Information Administration. *International Energy Outlook 2019* tech. rep. (2019).

13. International Energy Agency. *Global Energy & CO2 Status Report* tech. rep. (2018).

14. Barber, J. & Tran, P. D. From natural to artificial photosynthesis. *Journal of The Royal Society Interface* **10,** 20120984 (2013).

15. Schiermeier, Q., Tollefson, J., Scully, T., Witze, A. & Morton, O. Energy alternatives: Electricity without carbon. *Nature* **454,** 816–823 (2008).

16. Kavlak, G., McNerney, J. & Trancik, J. E. Evaluating the causes of cost reduction in photovoltaic modules. *Energy Policy* **123,** 700–710 (2018).

17. Clarke, T. M. & Durrant, J. R. Charge Photogeneration in Organic Solar Cells. *Chemical Reviews* **110,** 6736–6767 (2010).

18. Ma, L. *et al.* A ternary organic solar cell with 300 nm thick active layer shows over 14% efficiency. *Science China Chemistry,* 1–7 (2019).

19. Meng, L. *et al.* Organic and solution-processed tandem solar cells with 17.3% efficiency. *Science* **361,** 1094–1098 (2018).

20. NREL. *Best Research-Cell Efficiency Chart* 2019. (2019).

21. Oxford PV. *Oxford PV perovskite solar cell achieves 28% efficiency* 2018. (2019).

22. Cheng, P. & Zhan, X. Stability of organic solar cells: challenges and strategies. *Chemical Society Reviews* **45,** 2544–2582 (2016).

23. Li, F. & Liu, M. Recent efficient strategies for improving the moisture stability of perovskite solar cells. *Journal of Materials Chemistry A* **5,** 15447–15459 (2017).

24. Bhandari, K. P., Collier, J. M., Ellingson, R. J. & Apul, D. S. Energy payback time (EPBT) and energy return on energy invested (EROI) of solar photovoltaic systems: A systematic review and meta-analysis. *Renewable and Sustainable Energy Reviews* **47,** 133–141 (2015).

25. Gong, J., Darling, S. B. & You, F. Perovskite photovoltaics: life-cycle assessment of energy and environmental impacts. *Energy & Environmental Science* **8,** 1953–1968 (2015).

26. U.S. Energy Information Administration. *California wholesale electricity prices are higher at the beginning and end of the day* 2017. (2019).

27. Gust, D., Moore, T. A. & Moore, A. L. Solar Fuels via Artificial Photosynthesis. *Accounts of Chemical Research* **42,** 1890–1898 (2009).

28. McConnell, I., Li, G. & Brudvig, G. W. Energy Conversion in Natural and Artificial Photosynthesis. *Chemistry & Biology* **17,** 434–447 (2010).

29. Tachibana, Y., Vayssieres, L. & Durrant, J. R. Artificial photosynthesis for solar water-splitting. *Nature Photonics* **6,** 511–518 (2012).

Chapter 2

Disordered semiconductors as photocatalysts

The key component in a device that produces chemical fuels using sunlight as an energy input is a photocatalyst, i.e. the material that absorbs light, generates charges, and uses these charges to drive desired chemical reactions. Traditionally, most photocatalysts have been inorganic materials such as transition metal oxides, sulfides, or nitrides. While these inorganic materials continue to dominate the field of sunlight-driven fuel generation, there has also been a rapidly increasing interest in organic photocatalysts such as polymers in the last 10 years. This chapter starts with an overview of the semiconducting properties of these materials, discusses which processes are triggered when they are illuminated, and describes how their activity is evaluated. Metal oxides and organic polymers are then discussed in more detail towards the end of the chapter, as they will be the photocatalyst materials of choice in the studies presented in this work. Finally, the objectives of this thesis are summarised.

2.1 Semiconductors as photocatalysts

2.1.1 Electronic structure

When two atoms with orbital energies that are suitable for the formation a stable chemical bond approach each other, their electrons experience a change in both potential energy and kinetic energy because they redistribute in response to the changing nuclear configuration. When the two nuclei reach their equilibrium distance, the total energy of the system is minimised as a proportion of their electron density is transferred into the region between the nuclei, thus forming a chemical bond. This leads to the formation of occupied and unoccupied molecular orbitals. As illustrated in Figure 2.1, the formation of a cluster or molecule through a continued addition of atoms steadily increases the number of electronic states and their spread in energy. The large number of atoms in a bulk solid causes gaps between these individual energy levels to become so small that the density of states can effectively be considered continuous, and such continuous ranges of energetic levels are then referred to as bands [1]. Since this energetic overlap is due to a relative uniformity of bonding environments throughout the material, energetic states at very different energies can be created if drastic changes in the local bonding environment occur. This is the case for defect sites, which are typically present in considerable numbers in the disordered materials studied herein.

The occupation of such bands with electrons defines the electronic nature of the bulk solid: a metal is characterised by a partially occupied highest energy band, whereas insulators and semiconductors exhibit a fully occupied highest energy band (valence band) with an energy gap to the next higher, unoccupied band (conduction band). The energy gap between the highest valence band energy level and the lowest conduction band energy level is referred to as bandgap [2]. Materials with an intermediate size bandgap are considered semiconductors, and will be the materials studied in this thesis. In contrast, materials with a large band gap are referred to as insulators.

The movement of an electron between different states requires an unoccupied energy level to move into. Therefore, charge transport requires a partially occupied highest energy band. As this is the case for metals by definition, they typically have very high electronic conductivities. For an intrinsic semiconductor, i.e. a pristine semiconductor without impurities, this means that electrons need to be transferred from the valence band to the conduction band in order to move through the material. This transfer across the bandgap can be achieved though the absorption

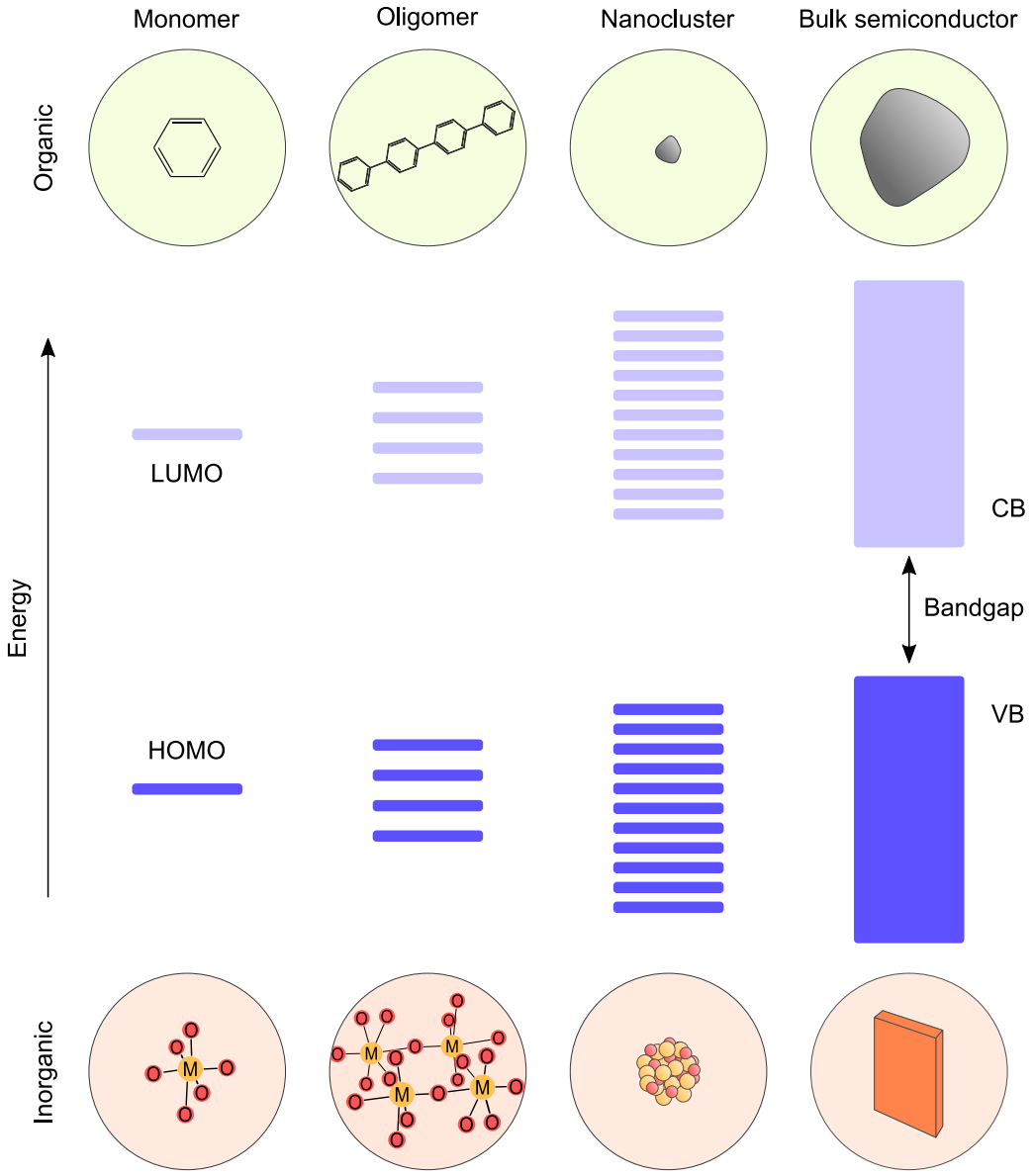

Figure 2.1: Schematic illustration of the increase in the number of occupied and unoccupied states when more and more monomers are fused together, resulting in a steady decrease in the HOMO-LUMO energy gap until a bulk semiconductor with a continuous valence band (VB) and conduction band (CB) is obtained.

of photons or phonons, which give rise to optically and thermally excited states, respectively. The probability of an electronic state with energy E being occupied is given by the Fermi-Dirac distribution *f(E)* [2]:

$$f(E) = \frac{1}{\exp((E - E_F)/k_B T)} \tag{2.1}$$

where k_B is the Boltzmann constant, T is the temperature, and E_F is the Fermi energy, i.e. the energy at which $f(E) = 0.5$ at any temperature. Since the Fermi energy is an energy level, states at this energy do not necessarily have to exist. With increasing temperature, the probability of

finding electrons with higher energy increases, which means that states at higher energy become more thermally accessible by electrons. If a material has a large bandgap, electronic states only exist far from the Fermi energy and the conductivity thus remains close to zero at room temperature. In this way, the distinction between semiconductors and insulators is based on the size of their bandgap [2] as introduced above.

The number of thermally excited electrons can be dramatically increased though doping, which means that additional energy levels close to the valence or conduction band are introduced by slightly altering the composition of the semiconductor [2]. If these newly introduced states are sufficiently close to the valence band, they make the material a p-type semiconductor in which electrons may be thermally excited from the valence band into these states. Analogously, an n-type semiconductor is created if the newly introduced states are close to the conduction band so that electrons from these states may be thermally excited to the conduction band. Doping can be done intentionally, e.g. by introducing heteroatoms into the semiconductor lattice, as is the case for the conventional silicon semiconductors used in photovoltaic cells or transistors. In contrast, doping can also occur unintentionally, e.g. through the formation of defects in the semiconductor lattice. Such a defect-induced doping is the dominant source of room temperature conductivity for many of the disordered semiconductors studied in this thesis.

2.1.2 Energetic requirements for solar water splitting

This section discusses the requirements photons need to fulfil to drive the photocatalytic reactions of interest in this thesis, i.e. proton reduction and water oxidation:

$$2H^+ + 2e^- \rightarrow H_2 \tag{2.2}$$

$$2H_2O + 4h^+ \rightarrow 4H^+ + O_2 \tag{2.3}$$

Overall water splitting combines both of these half reactions:

$$2H_2O \rightarrow 2H_2 + O_2 \tag{2.4}$$

When a photon is irradiated with an energy that corresponds to the energy difference between an occupied and an unoccupied state of a material, this photon can be absorbed and thus promote an electron from the occupied to the unoccupied state. For a semiconductor, this absorption

process normally promotes an electron from the valence band to the conduction band, thus generating an excited state which is characterised by a hole in the valence band and an electron in the conduction band. Instead of the single Fermi level that characterises a material in thermal equilibrium in the dark, two local equilibria are established for electrons and holes, with their respective chemical potentials being referred to as quasi Fermi levels. The potential difference between these two quasi Fermi levels defines the photovoltage that the semiconductor generates and hence the driving force available to perform oxidation and reduction reactions [3].

As illustrated in Figure 2.2, in the case of water splitting at pH = 0, the electron must have an energy negative of 0 V vs. RHE and the hole must have an energy positive of 1.23 V vs. RHE. This means that the minimum photon energy required to drive photocatalytic water splitting is 1.23 V, however, due to additional overpotentials, 1.8 V is often considered a more realistic minimum photovoltage [4]. This photovoltage can in principle be supplied by a single semiconductor with a sufficiently large bandgap and suitably positioned valence and conduction band edges, which need to straddle the water oxidation and proton reduction potentials. Due to these stringent requirements, single materials capable of overall water splitting typically exhibit large bandgaps and thus only absorb a small proportion of incident sunlight. Alternatively, the required photovoltage can also be generated using a combination of two light absorbers in tandem. Such a tandem system relaxes some of these requirements as the conduction band of only one of the materials needs to provide sufficient driving force for proton reduction while the other material provides the driving force for water oxidation. Therefore, a tandem device can combine semiconductors with different bandgaps to achieve complementary light absorption and thus harvest photons over a larger part of the solar spectrum.

2.1.3 Light-induced processes

Figure 2.3 illustrates the sequence of steps in a photocatalytic reaction: (i) light absorption, (ii) charge separation, (iii) charge transport to the electrolyte interface, and (iv) charge transfer to the desired substrate [5–7]. Since the yield of any of these steps is of fundamental importance for the efficiency of a photocatalytic reaction, these processes will be discussed in detail in the following.

(i) *Absorption.* When a semiconductor photocatalyst absorbs a photon, an electron-hole pair is generated. The total number of photogenerated electron-hole pairs depends on the

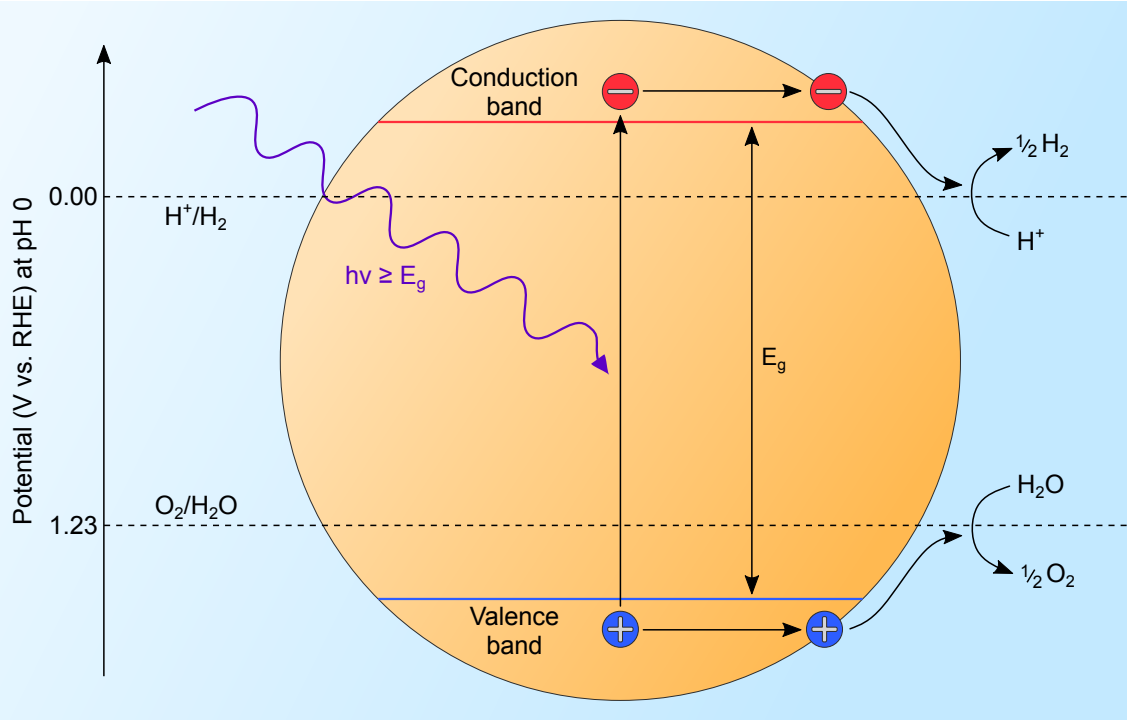

Figure 2.2: Schematic illustration energy requirements for photocatalytic water splitting. In the case of a single light absorber as shown here, valence and conduction band edge (drawn as blue and red lines, respectively) define the size of the bandgap E_g which needs to straddle the water oxidation and proton reduction potentials to provide a sufficiently high driving force for the reaction.

number of absorbed photons which is limited by the number of photons in the solar spectrum with an energy equal to or larger than the bandgap of the photocatalyst. However, even if a photon has an appropriate energy, it is not necessarily absorbed by a sufficiently thin semiconductor. How strongly a semiconductor absorbs light of a given wavelength is defined by its attenuation coefficient (also referred to as extinction coefficient, see Section 3.1) at that wavelength. Ultimately, the number of photogenerated electron-hole pairs constitutes the upper limit for how many reduction and oxidation events a semiconductor can perform upon light irradiation.

(ii) *Charge separation.* Once an electron-hole pair, commonly known as an exciton, is generated, it needs to be separated into individual charges. How easily spontaneous charge separation can occur depends on how efficiently the field between electron and hole is screened by the medium that separates them, i.e. the semiconducting material itself, and can be quantified using its dielectric constant. The larger the dielectric constant of a material, the more efficiently it shields electric fields, and the more likely spontaneous separation of photogenerated electron-hole pairs becomes. Many inorganic semiconductors have large dielectric constants and thus generate separated charges upon photoexcitation,

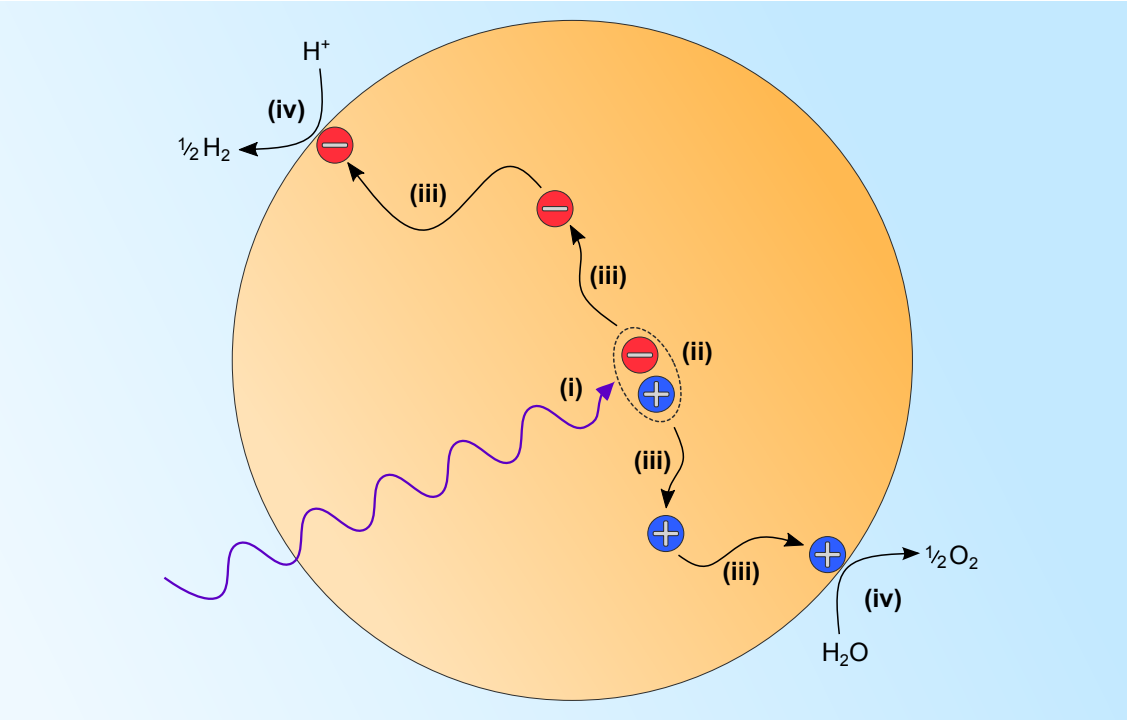

Figure 2.3: Schematic illustration of the steps of a photocatalytic reaction: (i) light absorption, (ii) charge separation, (iii) charge transport to the electrolyte interface, and (iv) reaction in the form of water oxidation and proton reduction.

whereas organic semiconductors usually have small dielectric constants and can therefore only generate bound charges (excitons). In the case of bound charges, a junction with another material is required for charge separation: this material can be another semiconductor (organic [8] or inorganic [9]), a small molecule [10, 11], a metal [12, 13], or a chemical electron donor/acceptor [14]. Differences in ionisation potential and/or electron affinity between the light absorber and the second material provide a driving force for charge transfer across the junction and thus enable charge separation.

(iii) *Charge transport.* If charge separation occurs within the bulk of a semiconductor, the generated charges must then be transported to the semiconductor-electrolyte interface in order to perform a reduction/oxidation via charge transfer to a substrate in the aqueous phase. For a single semiconductor and in the absence of external perturbations, this transport occurs via diffusion, i.e. by random movement along a concentration gradient of charges. For inorganic semiconductors, a depletion layer is formed at the liquid interface (see Section 2.4) within which an electric field drives the migration of charges either towards or away from the electrolyte.

(iv) *Reaction.* Once an electron/hole reaches the semiconductor-liquid interface, it can be transferred to a substrate of suitable reduction/oxidation potential in solution. As detailed

for the case of the water splitting reaction in Subsection 2.1.2, an electron must have an energy more negative than the reduction potential of the substrate to be able reduce it, whereas for an oxidation a hole must have an energy more positive than the substrate's oxidation potential. A higher energy input than thermodynamically necessary is typically required due to overpotentials. Such overpotentials arise from kinetic limitations and depend on the exact reaction mechanism. For instance, in the case of multi-electron reactions, the accumulation of several charge carriers might be required before charge transfer occurs [15].

2.1.4 Loss pathways

The successful completion of these four photocatalytic steps upon light irradiation results in the conversion of solar energy into chemical energy. However, real photocatalytic systems exhibit efficiencies less than unity as not all incident or even absorbed photons eventually drive the formation of the desired product. Such inefficiencies are due to loss processes in the material, which can occur in any of the steps of the outlined reaction sequence. These losses are mostly due to recombination, i.e. the annihilation of a photogenerated electron and hole, which converts an excited state back to the ground state. The dominant loss pathway for essentially all photocatalysts is rapid charge recombination between picoseconds and nanoseconds after light absorption. The resulting short charge carrier lifetimes lead to a severe mismatch with the timescales of photocatalytic target reactions such as water oxidation and proton reduction, which typically occur on the millisecond to second timescale. As a result, the lifetimes of photogenerated charge carriers are therefore a key limitation for the activity of photocatalysts chemical, and scavengers or applied electrical bias are usually used to reduce this fast recombination [16].

(i) *Absorption.* Irradiated photons do not result in the generation of an excited state if they are not absorbed. This can occur if the electronic structure of the light absorber is such that the energy of the irradiated photon does not match the energy difference between an occupied and an unoccupied state. More generally, photon absorption can fail if the combination of light absorber thickness and its attenuation coefficient at the irradiation wavelength does not allow for quantitative absorption, which can be the case even if there are suitably positioned occupied and unoccupied energy levels.

(ii) *Charge separation.* If a photogenerated electron-hole pair does not separate within its lifetime, it will undergo recombination. Recombination of excitonic charges is often radiative and thus occurs via the re-emission of a photon.

(iii) *Charge transport.* Before an electron or hole reaches the semiconductor - electrolyte interface and reacts, it may encounter a charge carrier of opposite sign and recombine with it. Charge recombination can occur radiatively, i.e. via the emission of a photon as indicated in (ii), or non-radiatively, where the excitation energy is ultimately dissipated as heat. For separated charges, two types of recombination can be distinguished: Geminate recombination describes the recombination of two charge carriers which originated from the same electron-hole pair, whereas non-geminate recombination is the recombination of charges generated from two different electron-hole pairs. These recombination mechanisms are particularly critical because charge transport in many photocatalyst materials occurs predominantly via diffusion. Diffusion takes place in random steps and thus does not allow for directional charge extraction, which increases the likelihood of charges meeting each other before they can react at a liquid interface. As mentioned above, fast charge recombination between pico- and nanoseconds after their generation is considered the primary limiting factor for the photocatalytic activity of typical semiconductors [16].

(iv) *Reaction.* Even a charge carrier that reaches the semiconductor-liquid interface might eventually not react. This may occur due to a lack of driving force (including overpotentials) for the reduction/oxidation of the desired substrate, or other factors, such as the depletion of substrates close to the surface of the photocatalyst.

2.2 Performance evaluation

This section discusses the figures of merit that quantify how many charges ultimately complete the photocatalytic reaction sequence and react. The activity for overall solar water splitting is evaluated by determining the solar-to-hydrogen (STH) conversion efficiency, which is the ratio between a system's energy input in the form of light and energy output in the form of hydrogen [17]:

$$\text{STH}\ (\%) = \frac{\text{Energy of produced } H_2}{\text{Energy of incident photons}} \times 100 \tag{2.5}$$

The energy of produced hydrogen is taken as the change in Gibbs free energy for the overall water splitting reaction (Equation 2.4), corresponding to $\Delta G^0 = 237\,\text{kJ}$ per mol H_2 [5, 18]. Note

that the STH efficiency quantifies the efficiency of an overall water splitting device, analogously to the power conversion efficiency of a photovoltaic cell [5]. Therefore, STH does not apply to the hydrogen evolution half-reaction alone. With a fixed solar spectrum, the maximum theoretical STH efficiency of a semiconductor is defined only by its bandgap [19].

For individual half-reactions, quantum efficiencies are the preferred performance metric [20]. Quantum efficiencies are measured by quantifying the amount of product formed when using a monochromatic light source, and are determined by calculating the ratio of reacted charges to incident or absorbed photons. When the number of incident photons is used, an external quantum efficiency (EQE) is obtained:

$$\text{EQE, IPCE (\%)} = \frac{\text{Number of reacted electrons/holes}}{\text{Number of incident photons}} \times 100 \tag{2.6}$$

Although the EQE is often referred to as 'apparent quantum yield' in the photocatalysis literature, the EQE terminology is adopted herein for consistency with the photovoltaics community. For a photoelectrode, the number of reacted electrons can also be determined by measuring a photocurrent instead of the amount of formed product as indicated in the previous section, which is then referred to as incident photon-to-current conversion efficiency (IPCE). However, care must be taken to make sure that no side reactions occur, as these would contribute to the observed photocurrent without driving the formation of the desired product. Since photocurrent measurements are considerably less time consuming than actual product quantifications, IPCE is the metric typically reported for metal oxide photoelectrodes such as the ones used in Chapter 6 and Chapter 7. For suspension systems such as the polymer photocatalysts studied in Chapter 4 and Chapter 5, EQEs need to be used since photocurrent measurements are not possible. Analogously, using the number of absorbed photons results in an internal quantum efficiency (IQE) or an absorbed photon-to-current conversion efficiency (APCE):

$$\text{IQE, APCE (\%)} = \frac{\text{Number of reacted electrons/holes}}{\text{Number of absorbed photons}} \times 100 \tag{2.7}$$

EQE and IQE (or IPCE and APCE) are equal if all incident photons are absorbed. However, since a certain number of photons is typically transmitted or scattered, the EQE of a photocatalyst is smaller than its IQE in practice. EQE and IQE are diagnostic efficiencies (i.e. not device efficiencies such as STH) and are defined with respect to one particular target reaction, e.g. proton reduction or water oxidation.

Although quantum efficiencies provide the possibility to characterise a photocatalyst using well-defined illumination conditions, in many cases only hydrogen/oxygen evolution yields using non-standardised white light sources are reported. Therefore, differences in reaction setups complicate the comparability of results between different laboratories significantly [21]. This lack of standardisation in the field of photocatalysis is perhaps due to the large variety of products which can be accessed via photocatalytic reactions, as well as the different types of reaction setups through which they can be produced. In photovoltaics, for example, the desired 'product' is always a current flow and the photoactive material is always fabricated into a film. This relative uniformity has lead to well-established standard conditions: a radiant flux of $1000\,\mathrm{W\,m^{-2}}$ with an AM 1.5 solar spectrum at a temperature of 25 °C. In photocatalysis, however, a variety of light sources with different emission spectra and intensities are used and temperature control is not common. Furthermore, additional variables such as photocatalyst concentration, reactor pressure, and salt additives in the aqueous phase affect both reaction rates and quantum efficiencies [21].

2.3 Heterogeneous photocatalysts

There are generally two types of catalysts: homogenous and heterogeneous ones. In homogeneous systems, the catalyst is found in the same phase as the reactant, as is, for instance, the case when a molecular water oxidation catalyst is dissolved in water. In heterogeneous systems, in contrast, the catalyst resides in a different phase than the reactant, which is for example the case for a solid semiconductor immersed in an aqueous electrolyte. As outlined in the previous section, such heterogeneous systems have interfaces where the desired reactions occur, and these interfaces are thus critical for their operation. Since all photocatalysts studied in this thesis are heterogeneous, this section provides an overview of possible architectures of heterogeneous photocatalysts in photocatalytic setups.

2.3.1 Particle suspensions

In suspension systems, photocatalyst particles are dispersed in an aqueous phase. Thanks to the simplicity of this reaction setup and the fact that suspensions are highly scalable, suspension systems are very attractive for large-scale commercial applications. It has been predicted that such suspension systems could be operated at \$1.60 - \$3.20 per kg hydrogen, which compares

well with the target range of \$2.00 – \$4.00 per kg hydrogen set by the United States Department of Energy [22]. Suspension systems thus represent the most economic potential implementation of solar-driven fuel production.

A large number of inorganic materials has been found to be active for photocatalytic water splitting UV irradiation [5, 23, 24]. Interestingly, the vast majority of these materials appear to incorporate metal cations with either d^0 or d^{10} configurations, which will be further explored in Chapter 7. For example, Zn-doped Ga_2O_3 was found to drive water oxidation with an EQE of 71% at 254 nm [25], and an EQE of 30% at 360 nm has been observed for Al-doped $SrTiO_3$ [26]. Achieving similarly high efficiencies with visible light has proven considerably more difficult and is an ongoing challenge. $(Zn_{0.12}Ga_{0.88})(N_{0.88}O_{0.12})$ is an example for a material with notable visible light activity, reaching an EQE of 5.9% at 420 - 440 nm [27]. More recently, organic photocatalysts have started to attract more and more attention, particularly targeting the issue of visible light absorption. For instance, a composite of carbon nitrides (further discussed in Section 2.5) and carbon nanodots has been reported with an EQE for water splitting of 16% at (420 ± 20) nm and 6% at (580 ± 15) nm [8].

The primary challenge of suspension systems for overall water splitting is that both hydrogen and oxygen are evolved in one place and thus form a product mixture, which means that the resulting gas mixture needs to be separated after the photocatalytic reaction. In addition, product mixing enables back reactions through reduction of oxygen or oxidation of hydrogen, which reduces the overall efficiency of the system. These problems can be circumvented by using separate hydrogen and oxygen evolution photocatalysts in separate reaction vessels, however, at the cost of increased complexity [22].

2.3.2 Particle films

Alternatively, instead of suspending photocatalyst particles in an aqueous medium, they can be deposited on a substrate such as glass or metal to produce nanoparticle films. Particle films are herein distinguished from photoelectrodes (next subsection) in that they operate without any applied external bias, and are thus essentially an immobilised version of the suspension systems described in Subsection 2.3.1. Solar water splitting setups employing this particle film configuration have achieved solar-to-hydrogen efficiencies of over 1% [28, 29], in this case using a tandem of doped $SrTiO_3$ and $BiVO_4$ semiconductors. This makes them the highest performing demonstration of photocatalytic overall water splitting reported so far, albeit without product

separation. Such particle films can be fabricated at relatively large scale using screen printing techniques [29], which maintains some of the scope for scalability.

2.3.3 Photoelectrodes

Besides photocatalytic systems which only use sunlight as an energy input, there are photoelectrocatalytic systems which drive a desired reaction using both sunlight and an applied electrical bias. These photoelectrocatalytic systems represent a mixture between purely photocatalytic and purely electrocatalytic setups, where sunlight is used to lower the required electrical bias. To prepare a photoelectrode, a film of the photocatalyst material is deposited on a conductive substrate such as glass coated with a layer of fluorine-doped tin oxide (FTO) or on a metal substrate. A major advantage of such photoelectrodes is that photocurrents can be measured under operating conditions and can be used as a proxy for the rate of reaction at the surface of the photoelectrode as outlined in Section 2.2. Whilst quantifying activity using photocurrents is straightforward and convenient, it assumes that the desired product is formed exclusively, which might not be the case if by-products are formed via alternative reaction pathways. The vast majority of photoelectrode materials are inorganic, and examples for metal oxides will thus be discussed in Section 2.4. In addition, alternatives based on organic light absorbers are currently being explored. Such organic photoelectrodes are typically based on a bulk heterojunction like that of an organic photovoltaic cell, which is covered by an inorganic layer to protect it from electrolyte corrosion [30]. Due to the strong light absorption of organic semiconductors, high current densities of several $\mathrm{mA\,cm^{-2}}$ have been obtained even with relatively early systems [31].

2.4 Metal oxide photocatalysts

Owing to advantages such as low cost, natural abundance, and relative stability, semiconducting transition metal oxides are the most commonly used photocatalyst materials for solar water splitting. They are composed of metal atoms which, depending on the crystal structure of the material, are surrounded by oxygen atoms in a particular geometric arrangement (e.g. octahedral or tetrahedral). This arrangement essentially defines the electronic structure of the oxide and can lend it a semiconducting nature. The resulting electronic structure at energies in the bandgap region is thus dominated by states originating from metal-like and oxygen-like orbitals, and their relative contributions to valence and conduction band vary from metal oxide to metal oxide. The

energetic positions of these constituent orbitals are illustrated in Figure 2.4 for a selection of different semiconducting metal oxides relative to the redox potentials for proton reduction and water oxidation.

These electronic structures represent those of a perfect crystal of the respective metal oxide. However, metal oxides are typically prone to the formation of lattice defects, which is partially linked to the low cost preparation procedures that make them attractive as materials for solar energy conversion. The formation of defects alters the ideal electronic structures shown in Figure 2.4 and introduces defect states which may, for instance, fall within the bandgap of the metal oxide [32]. In addition, a metal oxide becomes doped when such defects are formed, which is often the primary source of its conductivity in the absence of additional extrinsic doping [33]. For instance, the formation of oxygen vacancies typically gives rise to n-type metal oxides, whereas cation vacancies render them p-type [34]. Metal oxides are most commonly used as films in photoelectrochemical setups, where n-type oxides are used as photoanodes and p-type oxides are used as photocathodes.

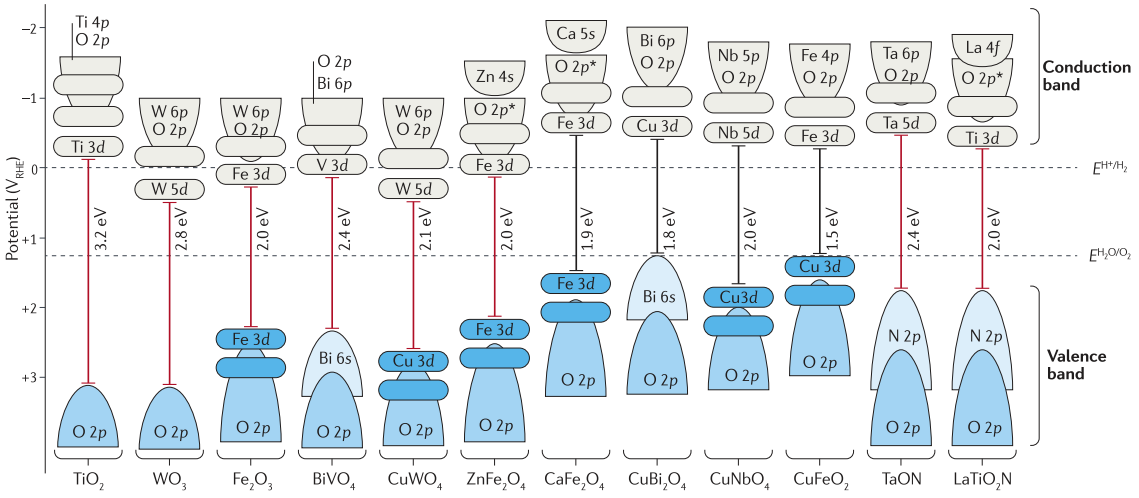

Figure 2.4: Illustration of the energetic positions of the valence and conduction band edges of selected metal oxides/oxynitrides, here represented by their constituent atomic orbitals, relative to the redox potentials for proton reduction and water oxidation. Reproduced from reference [35] with permission.

When such a metal oxide film is immersed in electrolyte, a semiconductor-liquid junction (SCLJ) is formed [3]. During the formation of the SCLJ, an electron flow between semiconductor and electrolyte takes place until the electrochemical potential of the semiconductor (as quantified by its Fermi level) has equilibrated with the electrochemical potential of the electrolyte (as quantified by its redox potential). Since the electrolyte constitutes a much greater charge reservoir than the semiconductor, the redox potential of the electrolyte remains essentially unchanged during

this equilibration process. Instead, the Fermi level of the semiconductor shifts to match the redox potential of the electrolyte, which induces band bending at the semiconductor surface. For an n-type semiconductor, where the Fermi level lies close to the conduction band, this means that the Fermi level is lowered during the equilibration process. This causes bands to bend upwards at the surface, and photogenerated holes (minority charge carriers in an n-type semiconductor) are thus driven to the surface to make the n-type semiconductor function as a photoanode. In a p-type semiconductor, where the Fermi level lies close to the valence band, the Fermi level is raised during equilibration and bands bend downward at the surface. This downward band bending drives photogenerated electrons (minority charge carriers in a p-type semiconductor) to the surface and makes the semiconductor function as a photocathode. Redox couples of interest are the O_2/H_2O couple for a photoanode and the H^+/H_2 couple for a photocathode. The part of the interfacial region within the semiconductor which becomes depleted of minority carriers is referred to as space charge layer. The electric field within the space charge layer is essential for an efficient spatial separation of photogenerated charges and for their accumulation at the surface of the semiconductor. The width of the space charge layer can be modulated by applying an electrical bias to the metal oxide photoelectrode. In fact, an electrical bias is required for all metal oxide photoelectrodes in addition to illumination for the generation of appreciable water oxidation or proton reduction photocurrents.

As laid out in the previous section, the overall efficiency of a solar-driven water splitting device is ultimately limited by how many of the photons in the solar spectrum it can use to drive this process, and thus relates to the bandgap of the used semiconductor. A large variety of different metal oxides has been used for at least one of the two water splitting half reactions [19, 35], and over time these materials have approached their upper efficiency limits to varying degrees. For instance, large research effort has been devoted to Fe_2O_3, particularly because of its relatively small bandgap of 2.1 eV and its chemical stability. Using such a Fe_2O_3 photoanode, photocurrents for water oxidation up to $4.32\,mA\,cm^{-2}$ at 1.23 V vs. RHE have been reported [36]. However, even this record efficiency still only corresponds to about one third of the theoretical maximum of $12.9\,mA\,cm^{-2}$ for Fe_2O_3 [19], and most other reported Fe_2O_3 systems yield considerably lower photocurrents despite decades of research on this material. In contrast, some of the most efficient photoanodes are based on $BiVO_4/WO_3$ heterojunctions, which can reach IPCEs exceeding 90% over most of their optically active spectral range [37, 38]. This impressive performance can give rise to photocurrents as high as $6.72\,mA\,cm^{-2}$ at 1.23 V vs. RHE [38], which approaches the theoretical maximum of $7.4\,mA\,cm^{-2}$ for $BiVO_4$ [19]. Again, the larger

bandgap of $BiVO_4$ prevents even higher photocurrents.

In order to identify promising metal oxide photocatalysts, for example among the large number of possible ternary and quaternary combinations, an understanding of what dictates their activity on a fundamental level is indispensable. However, although activity gaps like the one between Fe_2O_3 and $BiVO_4$ suggest that there may be oxides which are inherently more active than others, it is still unknown how the variations in orbital composition between different oxides (Figure 2.4) affect the behaviour of photogenerated charge carriers and ultimately their reactivity. For instance, it is understood that most of the charge carriers in these materials are lost as early as picoseconds to nanoseconds after light absorption [39]. Therefore, if critical features of materials where this fast loss process is less pronounced could be identified, a targeted search for new materials could be conducted in the large structural space of multinary oxides. In addition, limited visible light absorption limits the efficiency of otherwise efficient materials such as the described $BiVO_4/WO_3$ heterojunction electrodes. The results presented in this thesis aim to contribute to a better understanding of fast loss processes and of possible strategies to enhance visible light absorption, as will be outlined in Section 2.6.

2.5 Polymer photocatalysts

Inorganic materials such as metal oxides are most widely used as photocatalyst materials, however, their often large bandgaps limit their photocatalytic efficiencies. While efficient visible light absorption has been identified as the main challenge on the way to increased photocatalytic efficiencies of inorganic systems [23], conduction and valence band positions of inorganic materials remain notoriously difficult to tune. As a result, organic polymers are currently becoming more and more popular for application as photocatalysts. Organic polymers typically exhibit strong light absorption due to their high absorption cross sections [40] and their electronic properties can easily be tuned by selecting suitable monomers as starting materials. For instance, the energetic positions of their HOMO and LUMO levels can be tuned such that their light absorption is varied over large parts of the visible range [41, 42].

Figure 2.5 gives some examples of typical classes of polymer photocatalysts. Carbon nitrides [43–45] are the most commonly used organic photocatalysts and consist of triazine or heptazine building blocks. They are typically prepared at high temperatures, for instance via molten salt

routes, which only offers limited synthetic control and can be expected to lead to relatively defect-rich products. It should therefore be kept in mind that the molecular structure of real synthesised carbon nitrides is likely far from the idealised structure shown here [21]. Like carbon nitrides, covalent triazine frameworks [46–48] are based on triazine units but can be synthesised at lower temperatures, thus allowing a larger degree of synthetic control. Covalent organic frameworks [49–51], can produce 3D networks with long-range order and defined pore sizes. Conjugated microporous polymers [52–54] form structures with high surface areas, which can be beneficial for catalytic reactions, and can maintain conjugation across their network. However, the polymer photocatalysts studied in this thesis belong to the class of linear conjugated polymers [54–56] which have shown promising activities despite typically lower surface areas, and are likely the most versatile structural platform due to the large number of usable monomers.

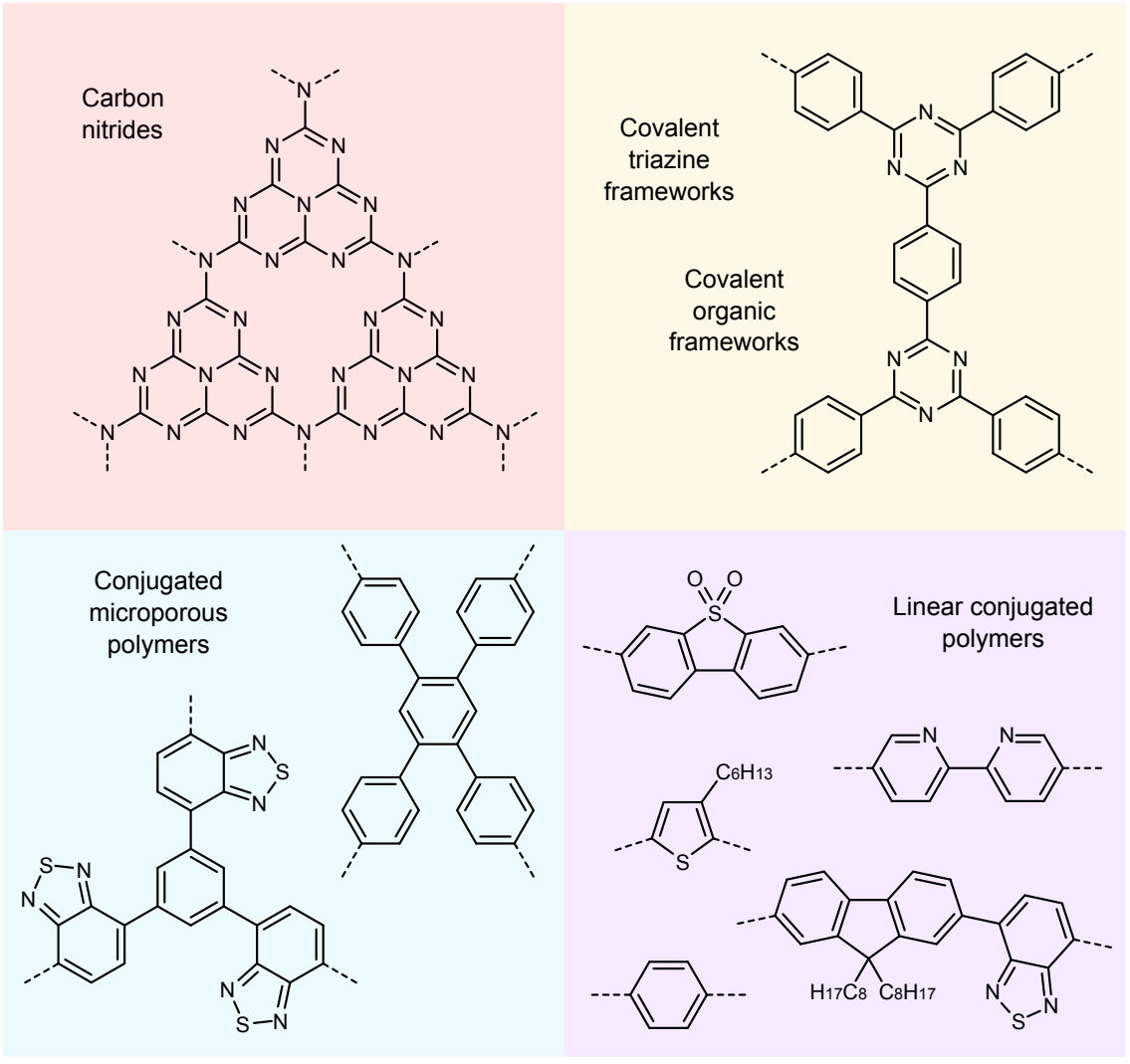

Figure 2.5: Exemplary representation of different classes of polymer photocatalysts: carbon nitrides (here shown with their idealised structure), covalent triazine frameworks, covalent organic frameworks, conjugated microporous polymers, and linear conjugated polymers. The dashed lines indicate bonds to the next building block.

Organic photocatalysts for hydrogen evolution have started to receive renewed interest after carbon nitrides have been adopted for this application in 2009 [43]. Since this initial report, photocatalytic activities of carbon nitrides have improved significantly and reach EQEs of up to 60% [44] in the best performing systems. Conjugated polymers have been used as hydrogen evolving photocatalysts even more recently but already show EQEs exceeding 20% [57]. In contrast to carbon nitrides, which are limited to triazine and heptazine building blocks, conjugated polymers can be made from a large variety of different monomers and thus provide a large structure space in the search for more efficient photocatalysts. To navigate this large structure space, high-throughput experimental and computational studies are becoming increasingly attractive to explore many different possible candidates in a comparably short amount of time [58, 59].

Since polymer photocatalysts are a relatively new class of materials, demonstrations of overall water splitting are still very scarce. Most studies focus on the hydrogen evolution reaction by employing a sacrificial electron donor which becomes oxidised and serves as an electron source instead of water. Such an electron donor is generally expected to be essential for charge separation of photogenerated excitons in these organic materials, as their low dielectric constant makes spontaneous charge separation unlikely [43]. In a photocatalytic system, the electron donor enables charge separation across the polymer-electrolyte interface due to a difference in ionisation potential/electron affinity, similar to the donor-acceptor junction in an organic solar cell. While the use of sacrificial electron donors is generally undesired, this route can be commercially viable if the oxidised electron donor is itself more valuable than the original substrate. In this way, two valuable products can generated simultaneously: hydrogen and an oxidised organic substrate. At the same time, overall water splitting remains a goal for solar hydrogen production on a global scale.

However, precisely because polymer photocatalysts are a rather new field of research, there is currently only a limited understanding of how these materials function on a more fundamental level. While some parallels can be drawn to the field of organic photovoltaics as exemplified by the comparison of a polymer-electrolyte interface to the donor-acceptor junction in an organic solar cell made above, little is known about the behaviour of such organic materials when they are immersed in an aqueous medium. As a result, it is unclear which parameters need to be tuned to obtain efficient polymer photocatalysts. In addition, it is also unclear where the catalytically active sites in such all-organic photocatalysts lie and what they look like, which effectively prevents the controlled tuning of catalytic properties. The studies reported in this

thesis aim to contribute to a better understand of these materials as detailed in the following section.

2.6 Aims and objectives

The development of more efficient photocatalysts for solar-driven water splitting is currently hampered by an incomplete understanding of the factors that dictate their activity on a fundamental level. In the relatively new class of polymer photocatalysts, little is known about the effect of the aqueous environment on fundamental photophysical processes such as charge generation in these organic materials. In addition, it has so far remained elusive how catalytically active sites in such all-organic materials could look like. Perhaps surprisingly, even for the much more established class of metal oxide photocatalysts a more detailed understanding of how the complex electronic structure of these materials affects the nature of their photogenerated charges, and ultimately the ability of these charges to drive desired reactions, is still missing.

In Chapter 4, a series of linear conjugated polymers with striking differences in hydrogen evolution activity is studied spectroscopically. Differences in charge yield are correlated with the observed activity trends and the varying affinity of the studied polymers for an aqueous solvent environment.

Many polymer photocatalysts contain metal impurities as residues from the metal-catalysed coupling reactions with which they are synthesised. In Chapter 5, the linear conjugated polymer F8BT is used to show how such metal impurities can act as co-catalysts for the hydrogen evolution reaction. A particular focus lies on the effect of palladium impurities on the excited state of the polymer and the localisation of photogenerated charges.

In Chapter 6, the metal oxide WO_3 is used as a model system to investigate how different oxygen vacancy densities affect the behaviour of photogenerated charges in these materials, and to evaluate how practicable the deliberate introduction of such oxygen vacancy defects is in attempts to enhance their visible light absorption.

In Chapter 7, the photophysical behaviour within a large series of different transition metal oxides is compared with respect to the orbital composition in the bandgap region of these materials, and the impact of different types of optical transitions on characteristics such as the lifetime of photogenerated charges is investigated.

2.7 References

1. Kittel, C. *Introduction to Solid State Physics* (Wiley, 1996).
2. Atkins, P. W. & de Paula, J. *Physical Chemistry* 10th ed. (2014).
3. Walter, M. G. *et al.* Solar Water Splitting Cells. *Chemical Reviews* **110,** 6446–6473 (2010).
4. Prévot, M. S. & Sivula, K. Photoelectrochemical Tandem Cells for Solar Water Splitting. *The Journal of Physical Chemistry C* **117,** 17879–17893 (2013).
5. Kudo, A. & Miseki, Y. Heterogeneous photocatalyst materials for water splitting. *Chem. Soc. Rev.* **38,** 253–278 (2009).
6. Zhu, S. & Wang, D. Photocatalysis: Basic Principles, Diverse Forms of Implementations and Emerging Scientific Opportunities. *Advanced Energy Materials* **7,** 1700841 (2017).
7. Kong, D. *et al.* Recent advances in visible light-driven water oxidation and reduction in suspension systems. *Materials Today* **21,** 897–924 (2018).
8. Liu, J. *et al.* Metal-free efficient photocatalyst for stable visible water splitting via a two-electron pathway. *Science* **347,** 970–974 (2015).
9. Kailasam, K. *et al.* Mesoporous Carbon Nitride-Tungsten Oxide Composites for Enhanced Photocatalytic Hydrogen Evolution. *ChemSusChem* **8,** 1404–1410 (2015).
10. Holliday, S. *et al.* High-efficiency and air-stable P3HT-based polymer solar cells with a new non-fullerene acceptor. *Nature Communications* **7,** 11585 (2016).
11. Hwang, I.-w., Moses, D. & Heeger, A. J. Photoinduced Carrier Generation in P3HT/PCBM Bulk Heterojunction Materials. *The Journal of Physical Chemistry C* **112,** 4350–4354 (2008).
12. Wu, K., Zhu, H., Liu, Z., Rodríguez-Córdoba, W. & Lian, T. Ultrafast Charge Separation and Long-Lived Charge Separated State in Photocatalytic CdS–Pt Nanorod Heterostructures. *Journal of the American Chemical Society* **134,** 10337–10340 (2012).
13. Wu, K., Zhu, H. & Lian, T. Ultrafast Exciton Dynamics and Light-Driven H 2 Evolution in Colloidal Semiconductor Nanorods and Pt-Tipped Nanorods. *Accounts of Chemical Research* **48,** 851–859 (2015).
14. Pellegrin, Y. & Odobel, F. Sacrificial electron donor reagents for solar fuel production. *Comptes Rendus Chimie* **20,** 283–295 (2017).
15. Le Formal, F. *et al.* Rate Law Analysis of Water Oxidation on a Hematite Surface. *Journal of the American Chemical Society* **137,** 6629–6637 (2015).

16. Cowan, A. J. & Durrant, J. R. Long-lived charge separated states in nanostructured semiconductor photoelectrodes for the production of solar fuels. *Chem. Soc. Rev.* **42,** 2281–2293 (2013).

17. Hisatomi, T., Kubota, J. & Domen, K. Recent advances in semiconductors for photocatalytic and photoelectrochemical water splitting. *Chem. Soc. Rev.* **43,** 7520–7535 (2014).

18. Hisatomi, T. & Domen, K. Reaction systems for solar hydrogen production via water splitting with particulate semiconductor photocatalysts. *Nature Catalysis* **2,** 387–399 (2019).

19. Li, J. & Wu, N. Semiconductor-based photocatalysts and photoelectrochemical cells for solar fuel generation: a review. *Catalysis Science & Technology* **5,** 1360–1384 (2015).

20. Kisch, H. & Bahnemann, D. Best Practice in Photocatalysis: Comparing Rates or Apparent Quantum Yields? *The Journal of Physical Chemistry Letters* **6,** 1907–1910 (2015).

21. Wang, Y. *et al.* Current understanding and challenges of solar-driven hydrogen generation using polymeric photocatalysts. *Nature Energy* **4,** 746–760 (2019).

22. Pinaud, B. A. *et al.* Technical and economic feasibility of centralized facilities for solar hydrogen production via photocatalysis and photoelectrochemistry. *Energy & Environmental Science* **6,** 1983 (2013).

23. Chen, S., Takata, T. & Domen, K. Particulate photocatalysts for overall water splitting. *Nature Reviews Materials* **2,** 17050 (2017).

24. Inoue, Y. Photocatalytic water splitting by RuO2-loaded metal oxides and nitrides with d0- and d10 -related electronic configurations. *Energy & Environmental Science* **2,** 364 (2009).

25. Sakata, Y., Hayashi, T., Yasunaga, R., Yanaga, N. & Imamura, H. Remarkably high apparent quantum yield of the overall photocatalytic H 2 O splitting achieved by utilizing Zn ion added Ga 2 O 3 prepared using dilute CaCl 2 solution. *Chemical Communications* **51,** 12935–12938 (2015).

26. Ham, Y. *et al.* Flux-mediated doping of SrTiO 3 photocatalysts for efficient overall water splitting. *Journal of Materials Chemistry A* **4,** 3027–3033 (2016).

27. Maeda, K., Teramura, K. & Domen, K. Effect of post-calcination on photocatalytic activity of (Ga1-xZnx)(N1-xOx) solid solution for overall water splitting under visible light. *Journal of Catalysis* **254,** 198–204 (2008).

28. Wang, Q. *et al.* Scalable water splitting on particulate photocatalyst sheets with a solar-to-hydrogen energy conversion efficiency exceeding 1%. *Nature Materials* **15,** 611–615 (2016).

29. Wang, Q. *et al.* Particulate Photocatalyst Sheets Based on Carbon Conductor Layer for Efficient Z-Scheme Pure-Water Splitting at Ambient Pressure. *Journal of the American Chemical Society* **139,** 1675–1683 (2017).

30. Steier, L. & Holliday, S. A bright outlook on organic photoelectrochemical cells for water splitting. *Journal of Materials Chemistry A* **6,** 21809–21826 (2018).

31. Francàs, L. *et al.* Rational design of a neutral pH functional and stable organic photocathode. *Chemical Communications* **54,** 5732–5735 (2018).

32. Heller, A. Conversion of sunlight into electrical power and photoassisted electrolysis of water in photoelectrochemical cells. *Accounts of Chemical Research* **14,** 154–162 (1981).

33. Cox, P. A. *Transition Metal Oxides: An Introduction to Their Electronic Structure and Properties* (Clarendon Press, 2010).

34. Greiner, M. T. & Lu, Z.-H. Thin-film metal oxides in organic semiconductor devices: their electronic structures, work functions and interfaces. *NPG Asia Materials* **5,** e55 (2013).

35. Sivula, K. & van de Krol, R. Semiconducting materials for photoelectrochemical energy conversion. *Nature Reviews Materials* **1,** 15010 (2016).

36. Kim, J. Y. *et al.* Single-crystalline, wormlike hematite photoanodes for efficient solar water splitting. *Scientific Reports* **3,** 2681 (2013).

37. Shi, X. *et al.* Efficient photoelectrochemical hydrogen production from bismuth vanadate-decorated tungsten trioxide helix nanostructures. *Nature Communications* **5,** 4775 (2014).

38. Pihosh, Y. *et al.* Photocatalytic generation of hydrogen by core-shell WO3/BiVO4 nanorods with ultimate water splitting efficiency. *Scientific Reports* **5,** 11141 (2015).

39. Yuan, Y.-P., Ruan, L.-W., Barber, J., Joachim Loo, S. C. & Xue, C. Hetero-nanostructured suspended photocatalysts for solar-to-fuel conversion. *Energy Environ. Sci.* **7,** 3934–3951 (2014).

40. Vyas, V. S., Lau, V. W.-h. & Lotsch, B. V. Soft Photocatalysis: Organic Polymers for Solar Fuel Production. *Chemistry of Materials* **28,** 5191–5204 (2016).

41. Sprick, R. S. *et al.* Tunable Organic Photocatalysts for Visible-Light-Driven Hydrogen Evolution. *Journal of the American Chemical Society* **137,** 3265–3270 (2015).

42. Sprick, R. S. *et al.* Maximising the hydrogen evolution activity in organic photocatalysts by co-polymerisation. *Journal of Materials Chemistry A* **6,** 11994–12003 (2018).

43. Wang, X. *et al.* A metal-free polymeric photocatalyst for hydrogen production from water under visible light. *Nature Materials* **8,** 76–80 (2009).

44. Zhang, G. *et al.* Ionothermal Synthesis of Triazine-Heptazine-Based Copolymers with Apparent Quantum Yields of 60 % at 420 nm for Solar Hydrogen Production from "Sea Water". *Angewandte Chemie International Edition* **57,** 9372–9376 (2018).

45. Ye, S., Wang, R., Wu, M.-Z. & Yuan, Y.-P. A review on g-C3N4 for photocatalytic water splitting and CO2 reduction. *Applied Surface Science* **358,** 15–27 (2015).

46. Schwinghammer, K., Hug, S., Mesch, M. B., Senker, J. & Lotsch, B. V. Phenyl-triazine oligomers for light-driven hydrogen evolution. *Energy & Environmental Science* **8,** 3345–3353 (2015).

47. Meier, C. B. *et al.* Structure-property relationships for covalent triazine-based frameworks: The effect of spacer length on photocatalytic hydrogen evolution from water. *Polymer* **126,** 283–290 (2017).

48. Kuecken, S. *et al.* Fast tuning of covalent triazine frameworks for photocatalytic hydrogen evolution. *Chemical Communications* **53,** 5854–5857 (2017).

49. Wang, X. *et al.* Sulfone-containing covalent organic frameworks for photocatalytic hydrogen evolution from water. *Nature Chemistry* **10,** 1180–1189 (2018).

50. Stegbauer, L., Schwinghammer, K. & Lotsch, B. V. A hydrazone-based covalent organic framework for photocatalytic hydrogen production. *Chem. Sci.* **5,** 2789–2793 (2014).

51. Pachfule, P. *et al.* Diacetylene Functionalized Covalent Organic Framework (COF) for Photocatalytic Hydrogen Generation. *Journal of the American Chemical Society* **140,** 1423–1427 (2018).

52. Jiang, J.-X. *et al.* Conjugated Microporous Poly(aryleneethynylene) Networks. *Angewandte Chemie International Edition* **46,** 8574–8578 (2007).

53. Sprick, R. S. *et al.* Extended conjugated microporous polymers for photocatalytic hydrogen evolution from water. *Chemical Communications* **52,** 10008–10011 (2016).

54. Yang, C. *et al.* Molecular Engineering of Conjugated Polybenzothiadiazoles for Enhanced Hydrogen Production by Photosynthesis. *Angewandte Chemie International Edition* **55,** 9202–9206 (2016).

55. Sprick, R. S. *et al.* Visible-Light-Driven Hydrogen Evolution Using Planarized Conjugated Polymer Photocatalysts. *Angewandte Chemie International Edition* **55,** 1792–1796 (2016).

56. Pati, P. B. *et al.* An experimental and theoretical study of an efficient polymer nanophotocatalyst for hydrogen evolution. *Energy Environ. Sci.* **10,** 1372–1376 (2017).

57. Aitchison, C. M., Sprick, R. S. & Cooper, A. I. Emulsion polymerization derived organic photocatalysts for improved light-driven hydrogen evolution. *Journal of Materials Chemistry A,* 37–39 (2019).

58. Bai, Y. *et al.* Accelerated Discovery of Organic Polymer Photocatalysts for Hydrogen Evolution from Water through the Integration of Experiment and Theory. *Journal of the American Chemical Society* **141,** 9063–9071 (2019).

59. Meier, C. B. *et al.* Structurally Diverse Covalent Triazine-based Framework Materials for Photocatalytic Hydrogen Evolution from Water (2019).

Chapter 3

Experimental methods

This chapter describes the experimental techniques and characterisation methods which are used to investigate the photocatalytic systems described in the chapters of this thesis, and ends with an evaluation of the general and specific challenges that arise when these techniques are used to study disordered samples such as the ones used herein. The protocols for synthesis and preparation of the studied materials are detailed individually in each results chapter.

3.1 Steady-state absorption spectroscopy

Steady-state absorption spectroscopy is an essential tool for the materials studied in this thesis and is used to quantify how much light a sample absorbs at a defined wavelength, e.g. to determine suitable excitation wavelengths for a transient experiment. As illustrated in Figure 3.1, a photon impinging onto a material can be (i) absorbed, (ii) reflected, (iii) scattered, or (iv) transmitted when none of the former processes occurs. The relative amount of transmitted light is referred to as transmittance T and is defined as

$$T = \frac{I_T}{I_0} \tag{3.1}$$

where I_T is the amount of transmitted light and I_0 is the amount of incident light [1]. Analogously, the absorptance a, reflectance R, and scatter S are defined as

$$a = \frac{I_A}{I_0} \tag{3.2}$$

$$R = \frac{I_R}{I_0} \tag{3.3}$$

$$S = \frac{I_S}{I_0} \tag{3.4}$$

with I_A, I_R, and I_S being the amount of absorbed, reflected, and scattered light, respectively. Because every incident photon has to undergo one of these four processes when passing through the sample, the contributions from a, T, R, and S must sum to unity [2]:

$$a + T + R + S = 1 \tag{3.5}$$

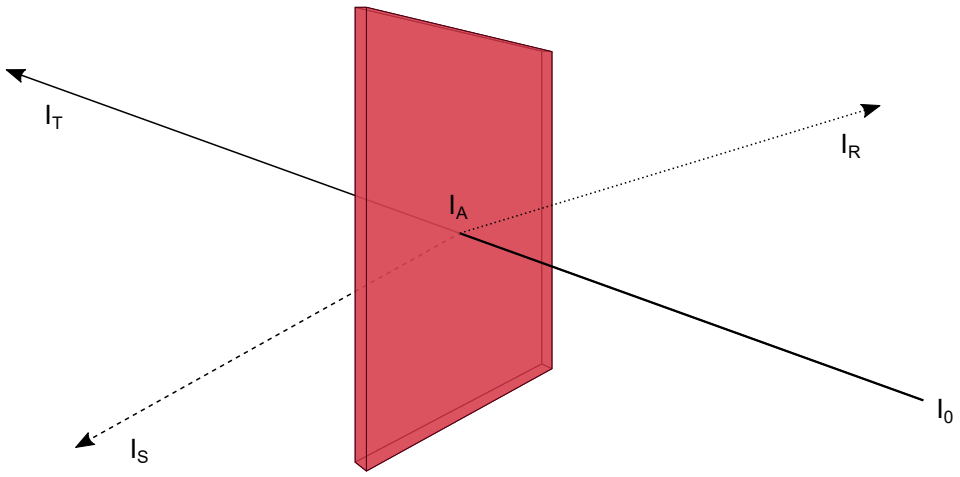

Figure 3.1: Exemplary representation of how the amount of incident light I_0 is distributed into absorbed light I_A, transmitted light I_T, reflected light I_R, and scattered light I_S upon interaction with a sample.

Since a is typically determined in a transmission experiment, contributions from R and S complicate its measurement. Reflection can occur in a specular or in a diffuse manner, which dominate for mirror-like and rough surfaces, respectively. R can be measured by collecting reflected photons with an integrating sphere and can thus be accounted for in Equation 3.5. Scatter is relevant for disordered materials such as the ones studied in the following chapters, which are typically not perfectly transparent and thus scatter a certain amount of light. S is, however, much harder to take into account as it involves spectral fitting using models that require certain assumptions about the properties of the sample [2].

In many cases, for instance when calculating the transient absorption signals reported herein, T is transformed onto a logarithmic scale which yields a quantity referred to as absorbance A:

$$A = -lg(T) \tag{3.6}$$

where lg indicates the decadic logarithm. This means that A is a logarithmic measure, in contrast to a which lies on a linear scale from 0 to 1 (for no absorption and quantitative absorption, respectively). The value of A depends on the density of light absorbing centres, and for molecules in solution it relates to their concentration as

$$A = \epsilon c l \tag{3.7}$$

with ϵ being the molar attenuation coefficient, c the concentration, and l the optical path length. ϵ quantifies how strongly a light absorber absorbs light at a wavelength of interest independently of the number of light absorbers present, and thus enables comparison of different absorbers under different conditions.

The experiments described in this thesis were conducted using a Shimadzu UV-2600 spectrophotometer, which was equipped with a two-detector integrating sphere module (Shimadzu ISR-2600Plus), or using an Agilent Cary 60 spectrophotometer.

3.2 Steady-state photoluminescence spectroscopy

Steady-state photoluminescence spectroscopy directly probes photons which are emitted by a sample as a result of radiative recombination. While photoluminescence spectroscopy is therefore limited to the investigation of radiative transitions, it offers much higher sensitivity than absorption spectroscopy - even the detection of single photons is possible. Photoluminescence measurements are routinely used to study organic materials, which often exhibit pronounced radiative transitions, such as the polymers used as photocatalysts in Chapter 4 and Chapter 5. Steady-state photoluminescence spectroscopy experiments can be conducted in two modes:

(i) Emission mode. The excitation wavelength is fixed and the emission wavelength is scanned using a monochromator after the sample. This measurement yields the spectral distribution of emitted photons when the sample is excited at the fixed excitation wavelength, referred to as photoluminescence emission spectrum.

(ii) Excitation mode. The emission wavelength is fixed and the excitation wavelength is scanned using a monochromator in front of the sample. Photoluminescence will only be observed when the sample absorbs at the excitation wavelength, and this experiment can therefore be regarded as a photoluminescence-detected absorption measurement. The obtained spectrum is a photoluminescence excitation spectrum which in many cases closely resembles the absorption spectrum.

Photoluminescence experiments in this thesis were carried out using a Horiba Fluorolog-3 modular spectrofluorometer.

3.3 Transient absorption spectroscopy

3.3.1 Background

Transient absorption spectroscopy (TAS) is used to monitor the temporal evolution of photogenerated reaction intermediates, so-called transients, based on their optical absorption signature. TAS was pioneered in the form of flash photolysis by Ronald George Wreyford Norrish and George Porter, who were subsequently awarded the 1967 Nobel Prize in Chemistry together with Manfred Eigen "for their studies of extremely fast chemical reactions, effected by disturbing the equilibrium by means of very short pulses of energy" [3].

TAS is the primary spectroscopic tool used in this thesis, and the variety of studied materials over the different chapters provides a good example of how versatile it is as a technique. As shown in Figure 3.2, TAS is a pump-probe technique which uses a pump pulse to bring the studied system into an excited state and then interrogates the temporal evolution of this excited state using a second, much weaker, probe pulse. The time difference between the pump and probe pulses therefore defines how long after the photoexcitation event the system is probed, and different steps in a photoinduced reaction sequence can thus be observed when varying the time delay between these two pulses.

By selectively blocking every other pump pulse, the probe pulses alternately record the absorption of the studied system in the excited state and in the ground state. The transient absorption is then calculated as the absorbance difference ΔA between the excited state absorbance A_{ES}

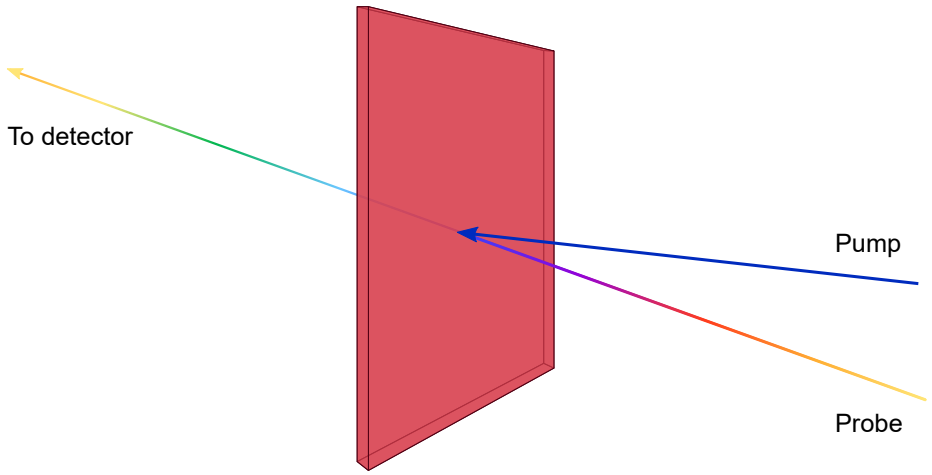

Figure 3.2: Geometric arrangement at the sample position during a transient absorption measurement in transmission mode. Pump and probe are overlapped on the sample to generate and probe excited states, respectively. The probe can be a wavelength continuum or a monochromated single-wavelength pulse.

and ground state absorbance A_{GS} according to

$$\Delta A(\lambda, t) = A_{ES}(\lambda, t) - A_{GS}(\lambda, t) \tag{3.8}$$

This means that a positive ΔA will be observed when $A_{ES} > A_{GS}$, whereas a negative ΔA is found in the (perhaps somewhat counter-intuitive) case of $A_{ES} < A_{GS}$. In general, there are one positive and two negative possible contributions to the ΔA signal [4], which are described in the following.

(i) Excited state absorption ($\Delta A > 0$). When a generated transient species absorbs light at the probe wavelength, this leads to an increased absorption in the excited state and thus produces a positive ΔA signal. For instance, photogenerated excitons or separated charges are can directly be monitored via their excited state absorption. During this absorption process, the probe light effectively excites the already excited state to produce a secondary excited state of even higher energy. Therefore, care should be taken to make sure that this higher lying excited state does not contribute to the observed dynamics to a significant extent, for instance by keeping the intensity of the probe beam low compared to the pump beam.

(ii) Ground state bleach ($\Delta A < 0$). Typically the absorption signature of an excited state is very different from that of its corresponding ground state. This means that once a ground state is converted into an excited state, its original ground state absorption (i.e.

the absorption observed in a UV-vis experiment) may no longer exist. In a spectral region where the ground state absorbs, this loss in absorption then leads to a lower absorption in the excited state, and thus gives rise to a negative ΔA signal which is referred to as a ground state bleach. A ground state bleach can therefore only be observed at probe energies larger than the bandgap of a photocatalyst.

(iii) Stimulated emission ($\Delta A < 0$). The photoluminescence setup described in Section 3.2 detects spontaneous emission where an excited state spontaneously relaxes back to the ground state with the energy difference between the two states being emitted in the form of a photon. It is also possible to induce this excited state to ground state conversion by irradiating a photon that matches the energy difference between these two states, referred to as stimulated emission. The emitted photon has the same energy as the incident one and is emitted in the exact same direction. Therefore, if the probe wavelength corresponds to an energy which is suitable to induce stimulated emission, this process increases the number of photons impinging on the detector and makes the sample seem to absorb less than it actually does. In this way, a negative ΔA signal is observed.

Equation 3.8 shows that ΔA is a function of both probe wavelength λ and pump-probe delay time t. Changing the probe wavelength for a fixed time delay yields a transient spectrum, i.e. the spectrum of the transient species present at that delay time. If several different species are present at the selected delay time, the sum of their transient spectra will be observed. Similarly, it is possible to vary the time delay while monitoring the absorbance at a fixed probe wavelength, which produces a kinetic trace that describes the temporal evolution of all transient species absorbing at the chosen probe wavelength. Typically, transient spectra are used to identify which photogenerated species is probed, and its temporal evolution is then monitored via a kinetic trace at a wavelength where this species absorbs strongly. When the transient absorption of individual species overlaps both spectrally and temporally, these species can be separated using more advanced global analysis techniques [5] which, however, require a kinetic or spectral model as an input.

TAS allows to study photoinduced reactions on a wide range of time scales. For the experiments in this thesis two different setups were used: An ultrafast transient absorption setup which probes on a timescale of fs - ns after excitation, and a microsecond setup which probes µs - s times after excitation. Both setups have different operating principles and components, which

are described in the following two subsections. Experimental challenges arising from differences between the two different transient absorption setups are discussed in Section 3.6.

3.3.2 fs - ns timescale

As illustrated in Figure 3.3, the ultrafast transient absorption setup uses a regeneratively amplified Ti:sapphire laser (Solstice, Spectra-Physics), which produces 800 nm laser pulses with a width of 92 fs at 1 kHz repetition rate. The transient absorption setup described in the following is commercially available (Helios, Ultrafast Systems). After the Solstice amplifier, each pulse is divided into what will become pump and probe pulse using a semitransparent mirror. The pump pulse is directed through an optical parametric amplifier (TOPAS Prime, Light Conversion) and a frequency mixer (NirUVis, Light Conversion), which allows for tuning of the excitation wavelength from ∼290 nm up to the NIR region. The probe pulse is directed through a delay stage which delays it by an adjustable time period with respect to its corresponding pump pulse, thus defining the time at which the sample is probed. The maximum delay is ultimately defined by the total length of the delay stage, and in this case corresponds to ∼6 ns. After the delay stage, the (at this point still 800 nm) probe pulse is focussed into a sapphire crystal, which transforms the monochromatic beam into a white light continuum via self-phase modulation. The resulting continuum allows to probe an entire wavelength range at once. Depending on the thickness of the inserted sapphire crystal, either a visible probe continuum (450 - 800 nm) or an NIR probe continuum (850 - 1400 nm) can be generated as shown below. The generated continuum pulses are then again divided using a semitransparent mirror, where one of them probes through the sample and the other one serves as a reference to account for fluctuations and improve the signal-to-noise ratio. Each of the two continuum pulses is eventually focussed into a separate multichannel spectrometer (Si or InGaAs sensors) via optical fibres. The continuum pulse that probes through the sample is then spatially overlapped with the pump pulse on the sample. The measurement of A_{ES} and A_{GS} for the calculation of ΔA is achieved by blocking every other pump pulse with an optical chopper rotating at 500 Hz. Pulse energies were measured using an energy meter (VEGA P/N 7Z01560, OPHIR Photonics) equipped with a 500 µm diameter aperture, roughly corresponding to the diameter of the probe beam. The pump beam was slightly larger than 500 µm at the sample position.

Due to the required changes in sapphire crystal and detectors when switching between visible and NIR detection, the same measurement with identical excitation conditions has to be performed

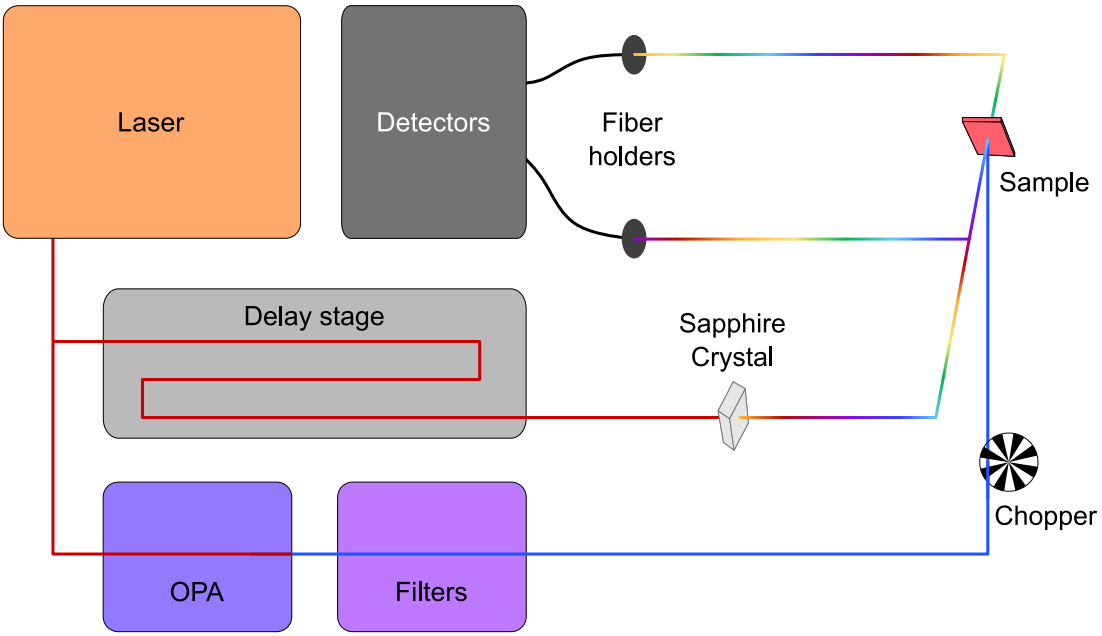

Figure 3.3: Schematic illustration of the fs - ns TAS setup components. The red line represents the 800 nm laser output, the blue line represents the tuned pump beam wavelength, and the rainbow-coloured line represents the white light continuum.

twice to obtain a full visible - NIR probe spectrum. The visible and NIR probe continua are shown in Figure 3.4. Note that their spectral distribution leads to a gap around the laser fundamental at 800 nm.

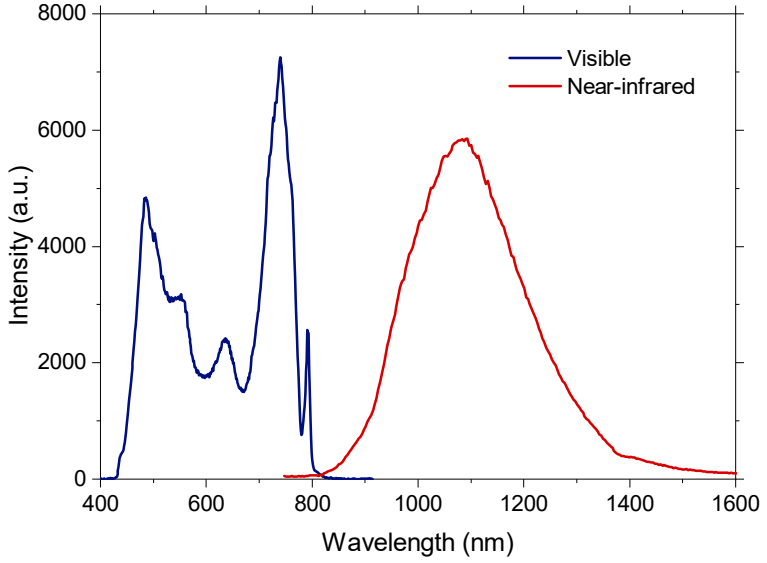

Figure 3.4: Spectra of the visible and near-infrared probe continua used in the fs - ns transient absorption setup.

3.3.3 µs - s timescale

Transient absorption experiments on the µs - s timescale were performed using a home-built setup. Since these probe times are much longer than those of the ultrafast setup, it is possible to time pump and probe electronically rather than via an optical delay. In this setup, the probe is a continuous and monochromated beam, which monitors pump pulse induced absorption differences at one selected wavelength at a time. This means that transient spectra need to be built up by probing different wavelengths sequentially. However, this configuration offers greater sensitivity than the multichannel spectrometers used in the ultrafast setup, thus enabling the detection of even smaller transient signals.

The µs - s TAS setup uses a Nd:YAG laser (OPOTEK Opolette 355 II, 4–7 ns pulse width), which generates UV excitation pulses (355 nm, fixed) via a third harmonic output port as well visible/NIR pulses (410 - 2200 nm, tuneable) via an optical parametric oscillator. The selected pump pulses are then directed to the sample via a liquid light guide, and are overlapped with the probe beam at the position of the sample. The probe beam originates from a 100 W quartz halogen lamp driven by a stabilised power supply (Bantham IL1) which is sequentially directed through a first monochromator, the sample, and then a second monochromator before it impinges onto a Si photodiode detector (Hamamatsu S3071). Additional appropriate long pass filters are positioned between sample and detector to attenuate scattered laser light. Data acquisitions are triggered by scattered laser light using a photodiode (Thorlabs DET210) positioned close to the laser output. A home-built LabVIEW-based software package acquires data on two different time scales simultaneously: the µs - ms signal is sampled using an oscilloscope (Tektronix DPO 2012B) after amplification (Costronics 1999 amplifier), whereas the ms - s signal is sampled without amplification using a DAQ card (National Instruments USB-6211 or USB-6361). Excitation fluences were measured using a pyroelectric energy sensor (Ophir Photonics PE9).

3.4 Photoinduced Absorption Spectroscopy

Photoinduced Absorption Spectroscopy (PIAS) is similar to the transient absorption techniques described above, but instead of short laser pulses (fs or ns pulse width) uses LED light pulses with a duration of several seconds as an excitation source. While TAS is employed to probe a sample under transient conditions, PIAS is therefore used to study a photocatalyst under quasi-steady state conditions where photogenerated reaction intermediates accumulate during

the much longer irradiation periods. This accumulation regime may provide insights into the nature of the active species and the mechanism according to which it ultimately reacts [6].

PIAS experiments were performed on the µs - s TAS setup with the following modifications: The laser is replaced by a high power LED (Cree XLamp XP-E 465 nm), which is driven by a high precision DC power supply (TTi QL564P). Again, a liquid light guide is used to direct the LED output to the sample. Light pulses are generated via a MOSFET transistor (STMicroelectronics STF8NM50N), where the gate is modulated by the DAQ card (National Instruments USB-6361). The DAQ card initiates a light pulse by switching the gate using a voltage signal, which simultaneously serves as a trigger to start the data acquisition. In this case, all data is sampled without prior amplification using the DAQ card. Excitation fluences were measured with a silicon photodiode power sensor (Thorlabs S120UV) in conjunction with a digital power meter (Thorlabs PM100).

3.5 Time-Correlated Single Photon Counting

Time-Correlated Single Photon Counting (TCSPC) is one of the most commonly used techniques for time-resolved photoluminescence measurements, again especially used for the organic semiconductors studied in this thesis, and can achieve time resolutions down to the picosecond timescale [1, 7]. TCSPC uses a pulsed excitation source such as a laser or a fast LED to excite the sample under study, and then probes its photoluminescence decay as a function of time at a defined wavelength. The collection of time-resolved emission spectra is possible by probing different wavelengths sequentially. It is important to note that TCSPC does not sample the entire photoluminescence decay within a single excitation event. As the name may suggest, the key operation principle of this technique is to record no more than one photon per excitation pulse. To build up the decay trace, the time delay between excitation and single photon detection is determined for a large number of successive excitation pulses, and by sorting detection times into defined time ranges the photoluminescence decay is obtained in the form of a histogram. Once a photon is detected, data acquisition is stopped until the next excitation pulse. If a second photon were to impinge on the detector after the acquisition has already been stopped it would not be detected, which would lead to an over-representation of early time photons in the histogram. This effect is referred to as 'pile up', and it is therefore essential to ensure that no more than one photon impinges on the detector following a single excitation pulse. To maintain single photon statistics at the detector, the detection rate is typically chosen to be less than 2%

of the excitation rate, although this means that in the majority of excitation events no photon is detected at all. Such a low detection rate can be achieved by using a sample of sufficiently low absorbance and/or inserting additional neutral density filters between sample and detector.

In a traditional TCSPC setup, the detector signal is fed into a constant fraction discriminator (CFD) which essentially determines at which time the leading edge of the detector pulse reaches a defined constant fraction of its final amplitude. Because signals received from the detector vary in amplitude, the use of a constant fraction is preferable over other metrics such as the time at which the pulse maximum occurs. The time obtained from the CFD is then compared to the reference signal supplied by the excitation source using a Time to Amplitude Converter (TAC). The TAC generates a linear voltage ramp which starts with the first signal and stops with the second one, and the final voltage is proportional to the time difference between the two input signals. An Analog to Digital Converter (ADC) then converts the TAC voltage to a digital timing value, which is fed into the histogrammer to increment the time channel which it falls into by one. [7]

The time resolution of a TCSPC setup is primarily determined by the combination of detector and excitation source [7]. The limiting factor is usually the timing accuracy of the detector (rather than its pulse response), which is a result of the timing uncertainty upon conversion of the photon to an electrical signal. In this way, the timing accuracy of the detector determines how reliable the detection time is with respect to the reference start signal. Excitation sources in modern TCSPC setups provide a relatively precise electrical timing reference for the start signal. The excitation pulse width may also limit time resolution depending on how it compares to the timing accuracy of the detector. Each element introduces a component instrument response, the combination of which then determines the total instrument response function (IRF) of the setup. For any TCSPC experiment, the IRF should be measured experimentally, for instance by inserting a scattering medium of the same geometry as the fluorescent sample and probing its decay at the excitation wavelength. The IRF can then be taken into account when fitting a measured florescence decay via iterative reconvolution, meaning that the model function is convoluted with the measured IRF during the fitting procedure.

The TCSPC experiments described in this thesis were carried out using a commercial TCSPC setup (Horiba DeltaFlex) equipped with a pulsed LED excitation source (Horiba NanoLED series) and a fast rise-time photomultiplier detector (Horiba PPD-650). The IRF was measured

at the wavelength of the excitation source. During all other measurements, a suitable long pass filter was inserted between sample and detector to block off scattered excitation light.

3.6 Experimental conditions and challenges

One of the primary experimental limitations of the studies presented herein is that later nanosecond delay times are not accessible with the available setups. The comparison of absolute signal amplitudes between the fs - ns and the µs - s transient absorption setups often proves difficult, even if the used fluence is controlled as accurately as possible. The observed discrepancies can, for instance, be assigned to different beam geometries, since pump and probe beam on the fs - ns setup exhibit diameters on the order of ∼500 µm whereas the probe beam diameter on the µs - s setup is rather on the order of a centimetre. In addition, the repetition rate of excitation pulses is 500 Hz for the fs - ns setup, but experiments on the µs - s timescale typically employ repetition rates between 0.5 - 5 Hz, depending on the upper time limit of the experiment. Therefore, the excitation power is considerably higher for the fs - ns setup, although pulse energies tend to be higher on the µs - s setup. Higher repetition rates also make charge accumulation more likely, which can perturb the observed kinetics if very long-lived transient species are generated. Especially for the polymer photocatalysts studied herein, such accumulation effects need to be mitigated by stirring the suspensions during the experiment when using the fs - ns setup. Similarly, since the probe beam used in the µs - s setup is continuously irradiating the sample, its overall power is also rather high and care should thus be taken when probing a spectral region in which the investigated sample absorbs. It should be noted that heating effects resulting from high excitation powers have been claimed to affect the observed transient signals [8, 9], however, in the context of results presented herein such observations can be interpreted to rather result from common underlying mechanisms such as the depopulation of sub-bandgap states through thermal excitation and through trapping of photogenerated charges. Therefore, none of the features in the datasets presented herein is ascribed directly to such heating effects.

The excitation fluences used herein are on the order of microjoules per cm^2 under normal conditions, and reach up to a few millijoules per cm^2 in fluence studies. It should be noted that these fluences are relatively low compared to those frequently used in the literature, which often are on the order of several millijoules per cm^2 even outside of fluence studies, at least for inorganic photocatalysts. As a result, the excitation intensities used herein are typically closer to catalytic one-sun illumination conditions than in other studies. Fluences used for TCSPC experiments

were much lower due to the higher sensitivity of photoluminescence measurements, which makes higher-order carrier effects less likely than in transient absorption experiments.

Complications of spectroscopic measurements can arise from to the disordered nature of the materials studied herein. All of the transient absorption measurements reported herein were carried out in transmission mode, which technically requires highly transmissive samples. In reality, however, at least some degree of scattering occurs for each of the investigated samples. Samples were prepared such that scattering was reduced as far as possible, for instance via choosing an appropriate dilution level for suspensions which yields a good compromise between reducing scattering effects and ensuring that a sufficiently high number of photons is absorbed. For thin film samples prepared via spin coating, spin coating conditions were optimised to reduce scattering of the resulting films as far as possible.

All experiments described in this thesis were carried out at room temperature. The kinetics observed in time-resolved measurements may be affected by the presence of atmospheric oxygen which can easily become reduced by photogenerated electrons. Therefore, all time-resolved experiments were carried out under inert conditions, i.e. in an argon or nitrogen saturated atmosphere.

In between experiments, samples were stored in air. The used metal oxide films showed good stability over time with no obvious changes in their optical properties, even under the rather intense laser radiation. These films were thus used for multiple experiments and all experiments for one material were carried out using the same film for consistency. The polymer suspension samples were prepared from stock suspensions for each individual measurement and, although these suspension samples did exhibit good stability over the course of an experiment, they were not reused. The details of how stock suspensions and suspension samples for spectroscopy were prepared are described in the individual chapters.

3.7 References

1. Tkachenko, N. V. *Optical Spectroscopy: Methods and Instrumentations* (Elsevier Science, 2006).
2. Stenzel, O. *The Physics of Thin Film Optical Spectra - An Introduction* 285 (2005).
3. NobelPrize.org. *The Nobel Prize in Chemistry 1967* 2019. (2019).

4. Berera, R., van Grondelle, R. & Kennis, J. T. M. Ultrafast transient absorption spectroscopy: principles and application to photosynthetic systems. *Photosynthesis Research* **101,** 105–118 (2009).

5. Van Stokkum, I. H., Larsen, D. S. & van Grondelle, R. Global and target analysis of time-resolved spectra. *Biochimica et Biophysica Acta (BBA) - Bioenergetics* **1657,** 82–104 (2004).

6. Francàs, L., Mesa, C. A., Pastor, E., Le Formal, F. & Durrant, J. R. in *RSC Energy and Environment Series* 20, 128–162 (2018).

7. Wahl, M. *Time-Correlated Single Photon Counting* tech. rep. (PicoQuant GmbH, Berlin, 2014), 1–14.

8. Hayes, D. *et al.* Electronic and nuclear contributions to time-resolved optical and X-ray absorption spectra of hematite and insights into photoelectrochemical performance. *Energy Environ. Sci.* **9,** 3754–3769 (2016).

9. Cooper, J. K. *et al.* Physical Origins of the Transient Absorption Spectra and Dynamics in Thin-Film Semiconductors: The Case of BiVO 4. *The Journal of Physical Chemistry C* **122,** 20642–20652 (2018).

Chapter 4

Hydrogen evolution activity of amphiphilic conjugated polymers

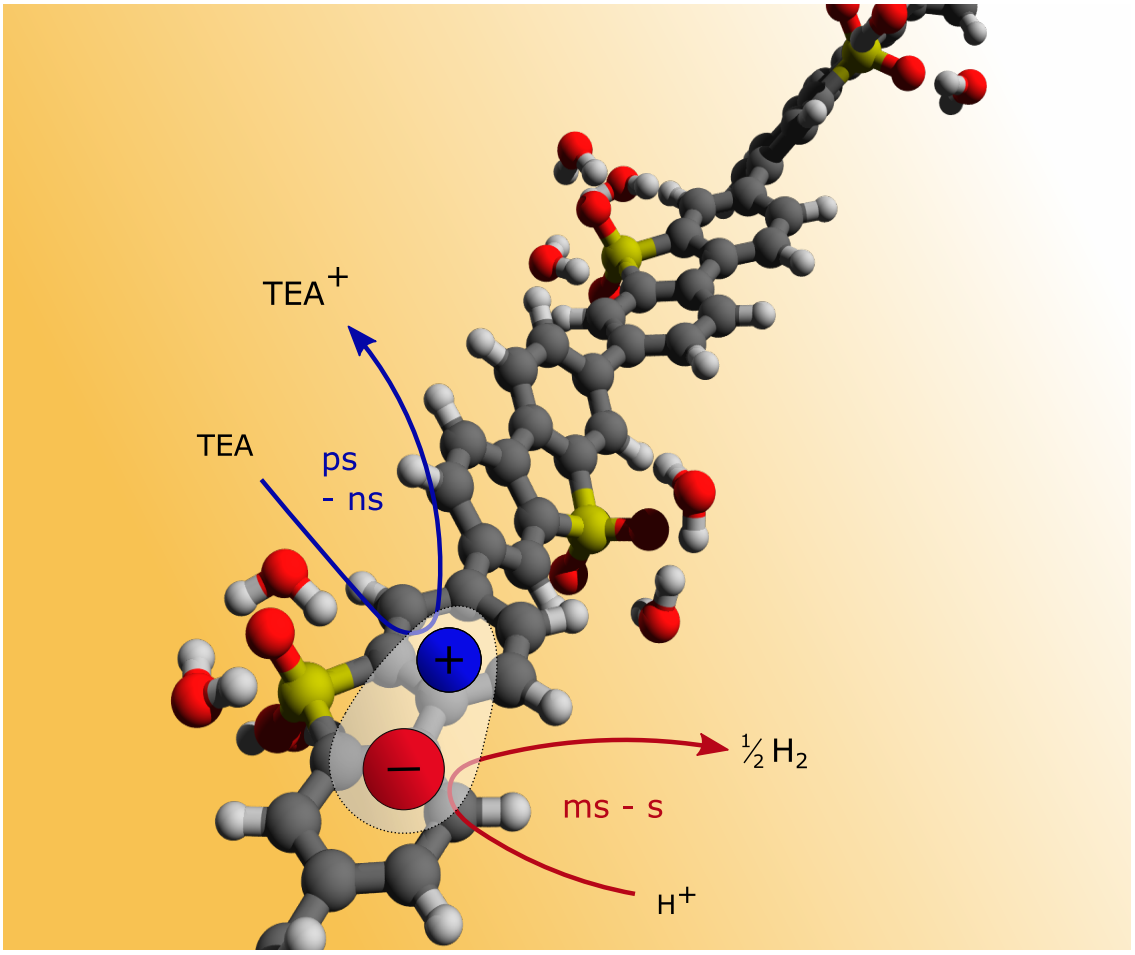

Figure 4.1: Graphical abstract for Chapter 4.

This chapter spectroscopically investigates the hydrogen evolution activity of a series of conjugated polymers with external quantum efficiencies ranging from 0.4 to 11.6%, where polymers with sulfone groups in their backbone constitute the upper end of this range, exhibiting some of the highest hydrogen evolution activities reported to date. Photogenerated reaction intermediates are tracked on timescales ranging from femtoseconds to seconds after light absorption and the yield of photogenerated long-lived electron polarons is correlated with the hydrogen evolution activity of the respective polymer. The generation of this active species, or at least its precursor, occurs on the early picosecond timescale in the most active polymers, suggesting strong interaction with the solvent environment. This strong interaction is further supported by DFT calculations and molecular dynamics simulations, which demonstrate that the polar sulfone groups attract water and alter charge transfer driving forces via the polarity of the solvent environment. This interplay between the hydrophilicity of the polymer chain, charge yield, and reaction driving force provides directions for the design of more efficient organic photocatalysts for hydrogen evolution.

The results presented in this chapter are in part included in this publication:

> Michael Sachs, Reiner Sebastian Sprick, Drew Pearce, Sam A.J. Hillman, Adriano Monti, Anne A.Y. Guilbert, Nick J. Brownbill, Stoichko Dimitrov, Xingyuan Shi, Frédéric Blanc, Martijn A. Zwijnenburg, Jenny Nelson, James R. Durrant & Andrew I. Cooper. Understanding structure-activity relationships in linear polymer photocatalysts for hydrogen evolution. *Nature Communications* **9**, 4968 (2018).

The following results shown in this chapter have been contributed by collaborators:
Sebastian Sprick synthesised the photocatalysts, carried out the activity experiments, and performed the contact angle and surface area measurements. Drew Pearce, Anne Guilbert, Adriano Monti, and Martijn Zwijnenburg performed the DFT and MD calculations. Sam Hillman and Anne Guilbert performed the particle size measurements. Xingyuan Shi acquired the shown steady-state absorbance and photoluminescence spectra.

4.1 Introduction

Organic photocatalysts are an area of rapidly growing interest owing to advantages such as their facile synthetic tuneability, as has been introduced in Section 2.5. This growth is especially visible in the field of solar-driven hydrogen production and has resulted in the fast development

of many new materials. However, the rate at which new organic photocatalysts are developed has now far outpaced our understanding of how they function on a more fundamental level. Most studies try to establish links to the molecular structure of the photocatalyst or to properties such as thermodynamic driving force for the hydrogen evolution reaction, however, not much is known about the photophysics and surface processes of polymer particles when suspended in an aqueous medium. As a result, materials development is currently primarily based on trial and error, which makes an exploration of the large variety of different possible polymer structures difficult. This study provides an attempt at identifying which factors are most important for the development of new polymer photocatalysts in order to guide the design of new materials.

To this end, some of the most active polymer photocatalysts discovered to date are investigated in this chapter: conjugated linear polymers which incorporate dibenzo[*b,d*]thiophene sulfone units and thus have sulfone groups embedded in their backbone. In 2016, the first report of this class of polymers for photocatalytic hydrogen evolution demonstrated a record EQE of 7.2% at 420 nm (later corrected from 2.3%) in the presence of triethylamine as a sacrificial electron donor [1]. This EQE has since been improved to 11.6% for a dibenzo[*b,d*]thiophene sulfone homopolymer (as reported in this chapter and in reference [2]), and most recently to 20.4% using the same polymer prepared via a mini-emulsion procedure that produces smaller polymer particles [3]. The success of this sulfone-containing building block has inspired the development of other linear conjugated polymers [4, 5] but also donor-acceptor polymers [6, 7], conjugated microporous polymers [8–11], and covalent organic frameworks [12]. In addition, multi-component systems such as polymer-polymer composites [13] and organic-inorganic composites [14] have been reported.

In this chapter, the three conjugated polymers shown in Figure 4.2 are investigated, spanning an EQE range from 0.4% to 11.6% at 420 nm. This set of conjugated polymers comprises poly(*p*-phenylene) P1, a phenylene-dibenzo[*b,d*]thiophene sulfone P7, and the dibenzo[*b,d*]thiophene sulfone homopolymer P10. The wide range of photocatalytic activities in this polymer series makes these materials highly interesting for a spectroscopic investigation of their performance. Using transient absorption experiments higher charge yields are found for the more active polymers, owing to a surprisingly fast generation of the active species (or at least its precursor) with a half-rise time of only 1.6 ps for P10 and 3.8 ps for P7. These different charge yields are supported by electronic structure calculations and molecular dynamics simulations, which illustrate the importance of the polar sulfone group in the polymer backbone of P7 and P10.

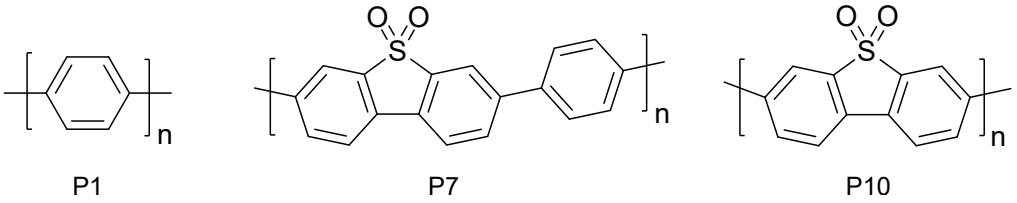

Figure 4.2: Molecular structures of the investigated polymer photocatalysts P1, P7, and P10.

4.2 Results

4.2.1 Photocatalytic activity and optical properties

While the focus of this chapter lies on the spectroscopic characterisation of this polymer series, activity measurements and particle characterisation are required to put the spectroscopic results into context. Therefore, these experiments are discussed first herein. Hydrogen evolution experiments for the three polymers investigated in this chapter were carried out by Sebastian Sprick in a solvent mixture consisting of equal volumes of H_2O, methanol (MeOH), and triethylamine (TEA), hereafter also referred to as reaction mixture. TEA acts as a sacrificial electron donor and MeOH serves as a co-solvent to enhance the miscibility of H_2O and TEA. The hydrogen evolution activity of P1, P7, and P10 in the reaction mixture is shown in Figure 4.3 over a period of 44 d using >420 nm illumination. P7 reaches an about 23-fold higher hydrogen evolution rate (HER) than P1, and the HER of the most active polymer P10 is again more than twice as high as that of P7.

2.7 mmol of H_2 were evolved over the course of this run for P10, which exceeds the amount of hydrogen present in the polymer sample and thus proves that the evolved H_2 does not originate from degradation of the polymer. In addition, hydrogen evolution experiments using a mixture of of the hydrogen-free scavengers Na_2S and Na_2SO_3 showed a HER of 19.8 µmol h^{-1} for P10 (Figure A.1), thus demonstrating that the produced H_2 is also not due to decomposition of TEA. Taken together, these experiments demonstrate that the evolved H_2 indeed comes from H_2O. All three polymers were synthesized via Pd(0)-catalysed Suzuki–Miyaura polycondensation reactions, and significant amounts of residual palladium were found in the resulting polymer particles after purification (0.33 wt.% for P1, 0.38 wt.% for P7, 0.40 wt.% for P10). Such residual metal impurities have been suggested to partake in the catalytic reaction as will be discussed in detail in Chapter 5. For the purposes of the current chapter, the palladium content can be considered

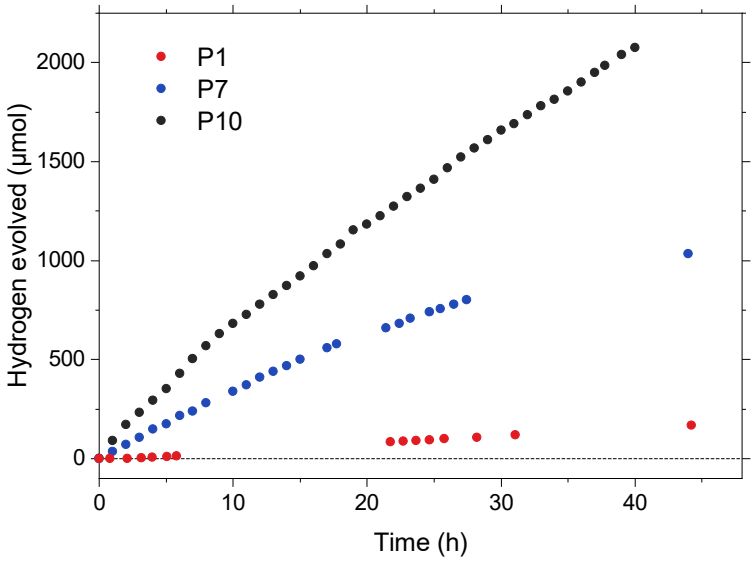

Figure 4.3: Photocatalytic hydrogen evolution of P1, P7, and P10 under visible light (>420 nm) illumination using 25 mg of photocatalyst in 22.5 ml of a mixture consisting of equal volumes of H_2O, MeOH, and TEA.

high for all three polymers and is therefore unlikely to lead to large activity differences between them.

To elucidate the reasons for this striking difference in hydrogen evolution activity, the steady state optical properties of these polymers are investigated first. The UV-vis spectra in Figure 4.4 acquired by Xingyuan Shi show a steadily red-shifting absorption onset in the P1-P7-P10 series (Table 4.1), along with a corresponding red-shift of their photoluminescence emission maxima. Although this enhanced light absorption in the visible range likely contributes to the higher activity of P7 and P10, the increasing H_2 evolution activity is also reflected in the external quantum efficiencies (EQEs) estimated at 420 nm by Sebastian Sprick as shown in Table 4.1. Since the absorption difference at this wavelength alone (0.90 for P10 vs. 0.51 for P1) cannot account for the difference in EQE (11.6% for P10 vs. 0.4% for P1), it can be concluded that absorption differences are not the primary reason for the observed activity trend.

The BET surface areas, determined by Sebastian Sprick via N_2 sorption experiments, were $29\,m^2\,g^{-1}$ for P1, $69\,m^2\,g^{-1}$ for P7, and $56\,m^2\,g^{-1}$ for P10. These surface areas are about an order of magnitude smaller than, for example, surface areas of conjugated microporous polymers [15] and can thus be considered to be rather low. Particle size measurements via dynamic light scattering (DLS), carried out by Sam Hillman and Anne Guilbert, show that all polymers fall into the hundreds of nanometers to micrometer range when dispersed in H_2O (534 ± 47 nm for P1; 913 ± 76 nm for P7; 647 ± 11 nm for P10). In H_2O/MeOH/TEA, in contrast, P1 particles

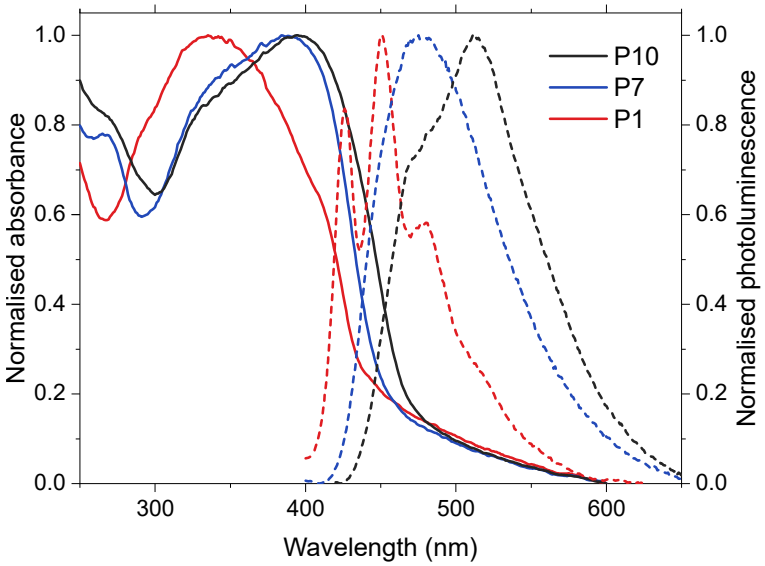

Figure 4.4: UV-vis absorbance spectra (full lines) and photoluminescence emission spectra acquired at 360 nm excitation (dashed lines) of aqueous suspensions of P1, P7, and P10.

are smaller, but P7 and P10 particles are larger (431 ± 39 nm for P1; 2199 ± 103 nm for P7; 1507 ± 314 nm for P10). This implies that P1 particles agglomerate more in H_2O whereas P7 and P10 particles agglomerate less under these conditions, which can be rationalised via their hydrophilicity as discussed in Subsection 4.2.5 below.

Table 4.1: Comparison of absorption onset, surface hydrophilicity, and hydrogen evolution activity for P1, P7, and P10. The optical gap was determined from the absorption onset; the contact angle was measured on the surface of pressed polymer pellets; the hydrogen evolution rate was measured using 25 mg polymer suspended in a 22.5 ml solvent mixture consisting of equal volumes of water, methanol, and triethylamine; the external quantum efficiency (EQE) was determined using a 420 nm LED.

Polymer	Optical gap (eV)	Contact angle vs. H_2O (°)	HER >420 nm H_2O/MeOH/TEA (µmol h^{-1})	EQE at 420 nm (%)
P1	2.76	88 ± 2.9	1.6 ± 0.1	0.4 ± 0.1
P7	2.73	67 ± 1.7	37.3 ± 0.8	7.2 ± 0.3
P10	2.62	59 ± 0.8	81.5 ± 4.1	11.6 ± 0.5

4.2.2 Lifetimes and yields of early transients

To investigate this activity difference on a more fundamental level, transient absorption spectroscopy (TAS) was used to study photogenerated reaction intermediates for all three polymers. Figure 4.5 shows transient absorption spectra probed from 0.5 ps - 6.0 ns after photoexcitation at 355 nm, both in the reaction mixture H_2O/MeOH/TEA and in H_2O only. The same initial

spectral shape is found for all polymers in both environments, and consists of a broad bleach around 450 - 700 nm and the onset of an excited state absorption above 700 nm. The broad bleach spectrally coincides with the photoluminescence of these polymers (Figure 4.4) and is thus assigned primarily to stimulated emission from polymer excitons. The excited state absorption peaks in the 800 - 850 nm range and then tails off when progressing further into the near-infrared (NIR) range (Figure A.2), in good agreement with spectral signatures of singlet excitons in fluorene-based polymer films [16–18] which share the fluorene-like backbone of P7 and P10. This excited state absorption is therefore assigned to photogenerated polymer excitons, meaning that both the ground state bleach and the excited state absorption are related to excitons. This assignment is further corroborated by an inspection of the decay kinetics in both spectral regions as a function of excitation density, where both signals exhibit the same intensity dependence (Figure A.3): The decay over the first 3 ps is dominated by a strongly intensity dependent decay component, whereas the decay above 3 ps is much less intensity dependent. The strongly intensity dependent component at early times is commonly observed in polymer films when excitation densities are high enough for photogenerated excitons to interact with each other [18–20], and is thus assigned to exciton-exciton annihilation. It is worth noting that the kinetics were not mono-exponential even at the lowest used fluence of 5 µJ cm^{-2}, suggesting that the fluences required to obtain resolvable signals from such suspension systems are higher than the exciton-exciton annihilation threshold, at least for the transient absorption setup used herein, or that these samples are characterised by a considerable degree of disorder.

The exciton absorption band above 700 nm can be used to probe the lifetime of photogenerated excitons, as shown in Figure 4.6a for all three polymers in H_2O and in H_2O/MeOH/TEA. The exciton decay kinetics observed via TAS show no significant differences between P1 and P7 in H_2O and also do not appear to be affected by the presence of TEA for those two polymers in H_2O/MeOH/TEA. In contrast, the decay for P10 in H_2O is significantly faster (half-lifetime of 2.8 ps as compared to 11.5 ps for P1/P7), but is also unaffected by the presence of TEA until 10 ps, after which it deviates as it evolves into a bleach. Although the reason for this bleaching behaviour is at present unclear, it is evident that the early time signals are unaffected by TEA for all three polymers. This TEA independence is somewhat surprising as one might expect an effect of TEA on the exciton dynamics in materials which separate a sufficient number of excitons to achieve hydrogen evolution EQEs of 11.6% and 7.2%, respectively. To confirm these results, photoluminescence lifetime measurements were carried out via Time-Correlated Single Photon Counting (TCSPC) in order to probe exciton populations based on the photons they emit during

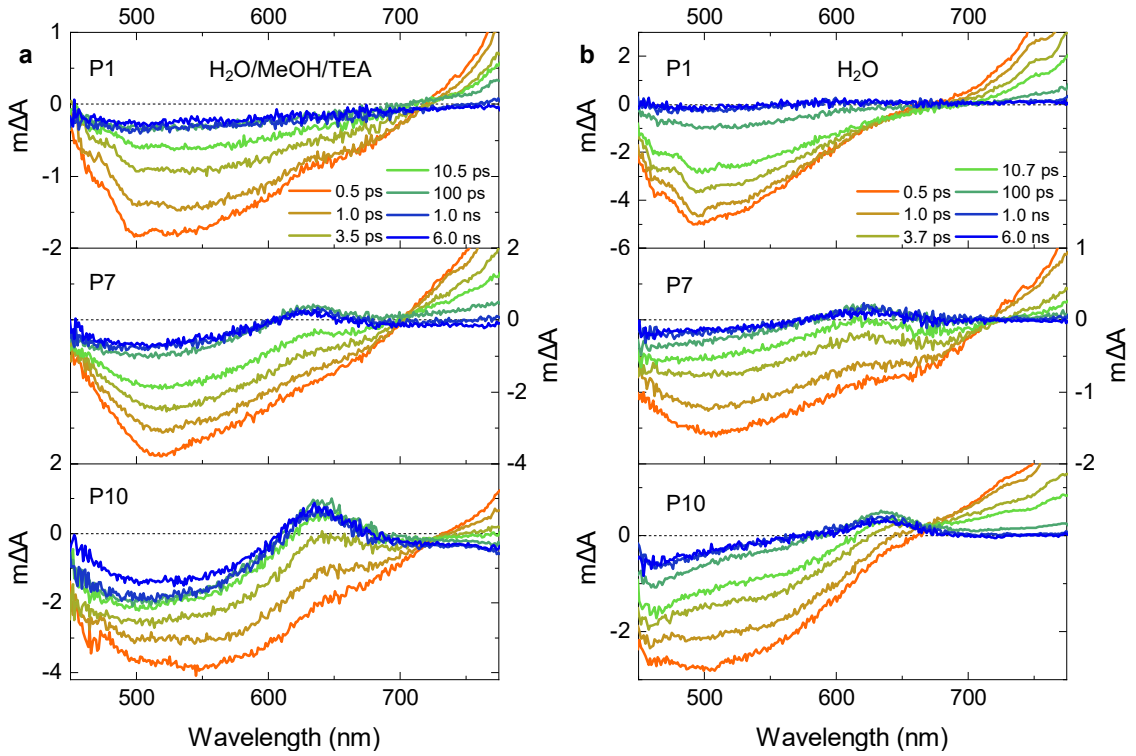

Figure 4.5: Transient absorption spectra of photogenerated reaction intermediates, probed from 0.5 ps to 6.0 ns for P1, P7, and P10 (top to bottom) in (**a**) a mixture consisting of equal volumes of H_2O, MeOH, and TEA, and (**b**) H_2O only. In all cases, an excitation wavelength of 355 nm and a fluence of 0.08 mJ cm^{-2} were used.

recombination. In a TCSPC setup, the higher sensitivity of photoluminescence measurements allows for much lower excitation densities, in this case with an LED as excitation source. Even at these low fluences, decay kinetics were not mono-exponential, which indicates that there are other factors that lead to lifetime variations within one sample of polymer particles such as the disorder of the material. A sum of three exponentials was used to fit and compare decay kinetics between the different polymers, probed for a total of three different emission wavelengths (455 nm, 480 nm, and 600 nm) as illustrated in Figure 4.6b-d. Such multi-exponential fits should be treated with caution because the kinetic model they impose is almost certainly unphysical (at least for the system under study here), but they can nevertheless be useful for a relative comparison of the decay rates in related systems. The fastest time constant τ_1 is shorter for P10 compared to P1 at all probe wavelengths, with that of P7 falling in between the two. The addition of TEA leads to a small but likely not significant decrease in τ_1. In addition, lifetimes generally appear to become longer when longer probe wavelengths are used, which could suggest that a certain degree of energy transfer takes place from shorter to longer polymer chains (i.e. larger to smaller bandgap oligomers). Overall, there appears to be little evidence of exciton lifetime quenching through addition of TEA, suggesting that most photogenerated

excitons recombine without charge transfer, even in the best-performing P10 system. These experiments also indicate that the higher activity of P7 and P10 is not related to intrinsically longer exciton lifetimes.

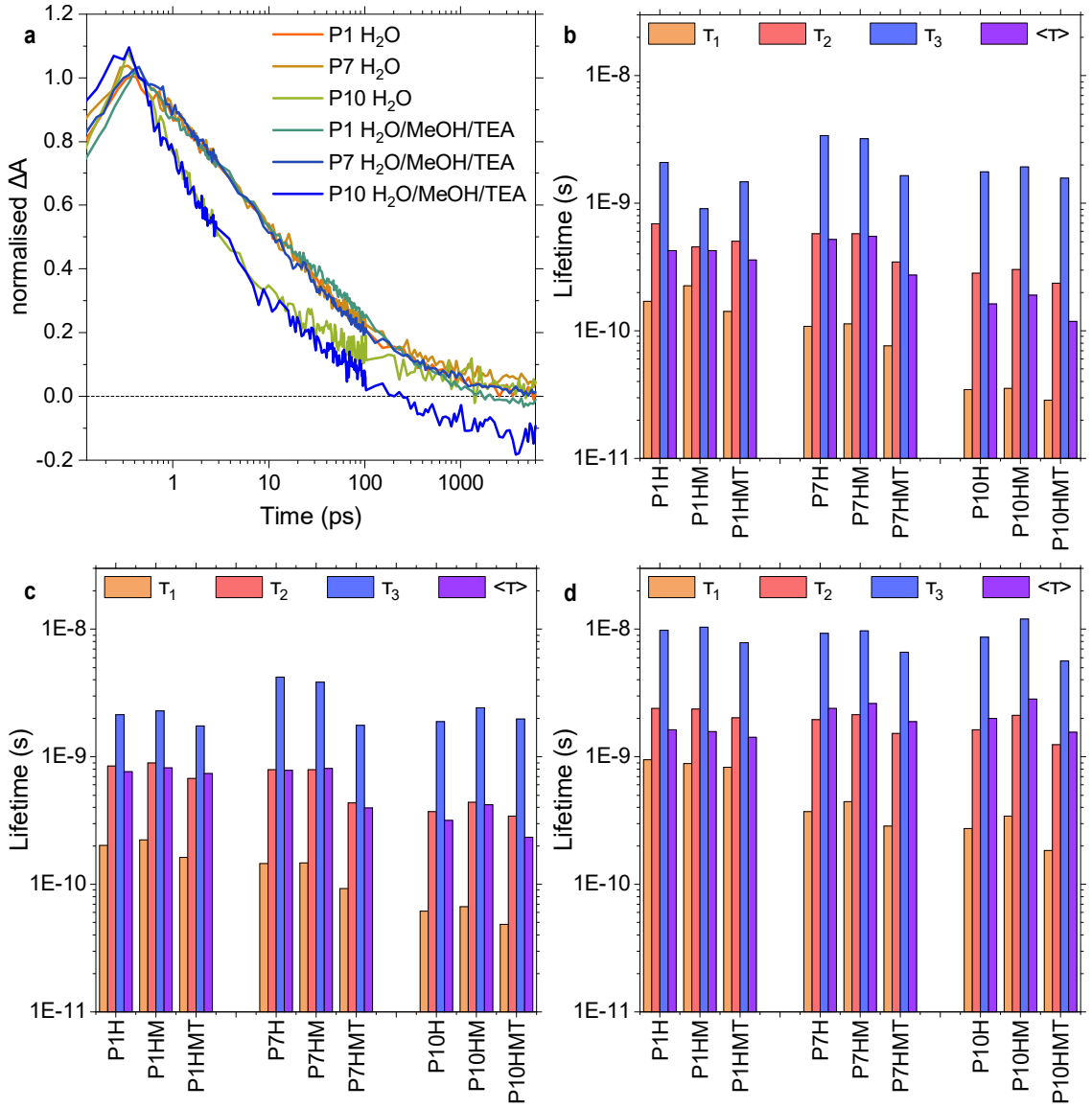

Figure 4.6: Exciton lifetime comparison for P1, P7, and P10 in suspended in H_2O and in a 1:1:1 H_2O/MeOH/TEA mixture. (**a**) Probed via the exciton transient absorption feature at 1000 nm following 355 nm excitation. Transient kinetics were normalised at 0.5 ps for better comparability. (**b** - **d**) Photoluminescence lifetimes determined from Time-Correlated Single Photon Counting experiments using an excitation wavelength of 404 nm and probe wavelengths of (**a**) 455 nm, (**b**) 480 nm, and (**c**) 600 nm. The time constants τ_1, τ_2, and τ_3 were obtained from a triple exponential fits $\sum_{i=1}^{3}(A + B_i exp(-t/\tau_i))$, and $<\tau>$is the weighted average lifetime calculated as $\sum_{i=1}^{3}(B_i\tau_i)$. All polymers were studied in H_2O (H), a 1:1 MeOH/TEA mixture (HM), and (**d**) a 1:1:1 H_2O/MeOH/TEA mixture (HMT).

While the excitonic early-time signal is present for all polymers both in H_2O and in the reaction mixture in the transient data shown in Figure 4.5, pronounced differences can be observed at

later times: In the reaction mixture (Figure 4.5a), the P1 exciton signal simply decays over time with no signifiant spectral evolution. In contrast, a new peak around 630 nm appears over time in the case of P7, suggesting the generation of a long-lived species. This 630 nm peak is even more pronounced for P10, which demonstrates that its amplitude in H_2O/MeOH/TEA qualitatively correlates with the activity of the respective polymer. Since this 630 nm signal overlaps with the broad bleach, it is desirable to separate it from its exciton background. Although global analysis routines did not yield reliable fits due to the non-exponential character of the exciton decay, it was possible to simply mathematically subtract the exciton background. This subtraction is based on the assumption that the 630 nm species is absent at very early times (<0.5 ps), which appears to be a reasonable approximation judging by the transient spectra at those times. As shown in Figure 4.7, the isolated 630 nm trace rises towards a maximum at ∼100 ps, with half-rise time of only 1.6 ps for P10 and 3.8 ps for P7. The absolute signal amplitude for P10 is considerably higher than that for P7, in at least qualitative agreement with the observed hydrogen evolution activity trend. As will be shown below, a similar feature is observed at µs - s times where it is assigned to photogenerated electrons on the polymer, and it can therefore be concluded that the species responsible for this spectral signature on this faster timescale is at least a precursor for the active species that drives the hydrogen evolution reaction. The fact that no such feature is observed for P1 even in the presence of TEA is in good agreement with this interpretation, given the low hydrogen evolution activity of P1 under illumination.

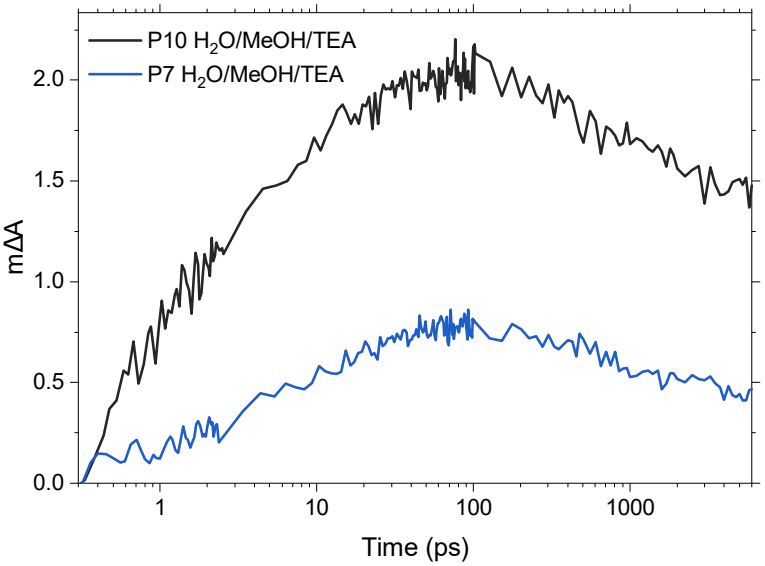

Figure 4.7: Temporal evolution of the 630 nm feature for P7 and P10 in H_2O/MeOH/TEA upon subtraction of the broad bleach background. Data were recorded using an excitation wavelength of 355 nm and a fluence of 0.08 mJ cm^{-2}.

On this fast fs - ns timescale, however, a 630 nm peak is observed for P7 and P10 even in pure

H_2O (Figure 4.5b). Its appearance in pure H_2O suggests that this feature might not be due to a separated charge on this faster timescale, but might rather arise from an exciton with increased charge transfer character, such as a polaron pair where electron and hole are delocalised over adjacent polymer chains. It has been observed that the spectral signatures of such polaron pairs and separated charges can be very similar [21, 22], which might explain the apparently identical spectrum to photogenerated electrons at µs times onwards. While the presence of this feature in pure H_2O does not affect the conclusions for the later time signal, it is interesting to consider at which point the hole transfer to TEA takes place.

Next, the relative amplitude of the 630 nm peak with respect to the amplitude of the broad bleach in the visible range is considered in the different reaction mixture components. Relative amplitudes are compared in this case since changes in the solvent composition affect how well the polymer particles disperse, and absolute amplitude differences are thus affected by the presence of aggregates of different sizes. Figure A.4 shows that the relative amplitude of the 630 nm feature is very similar in pure H_2O and in pure MeOH, but significantly enhanced in MeOH/TEA mixtures and H_2O/MeOH/TEA mixtures. Although measurements in TEA only were not feasible due to strong particle agglomeration, these experiments demonstrate that, even on this fs - ns timescale, the 630 nm amplitude for P10 is mainly modulated by the presence of TEA.

4.2.3 Long-lived transient species

To investigate how these different spectral signatures translate onto the timescale relevant for hydrogen evolution, TAS is used to probe the photogenerated reaction intermediates at µs - s times after excitation. Figure 4.8a shows the transient spectra of the different polymer photocatalysts at 100 µs, which in the case of P7 and P10 in H_2O/MeOH/TEA are dominated by a distinct peak around 600 - 650 nm. The amplitude of this peak for P10 is about five times higher than for P7 and no such feature is observed for P1, which is in at least qualitative agreement with the observed trend in hydrogen evolution activity. It is worth noting that these transient spectra are in overall good agreement with the 6.0 ns transient spectra shown in Figure 4.5, suggesting no significant transformations between these two timescales. In pure H_2O, an increasing amplitude in the series P1-P7-P10 is also observed, but with a different spectral shape. While an aqueous P1 suspension did not yield appreciable signals, the absolute signal amplitudes for P7 and P10 are much lower compared to when TEA is present. In addition, these transient spectra are much broader and exhibit a steadily increasing amplitude towards the NIR. Although the

identity of the species giving rise to this broad absorption is at present unclear, this species does not appear to be active for hydrogen evolution given that little H_2 is evolved in the absence of TEA.

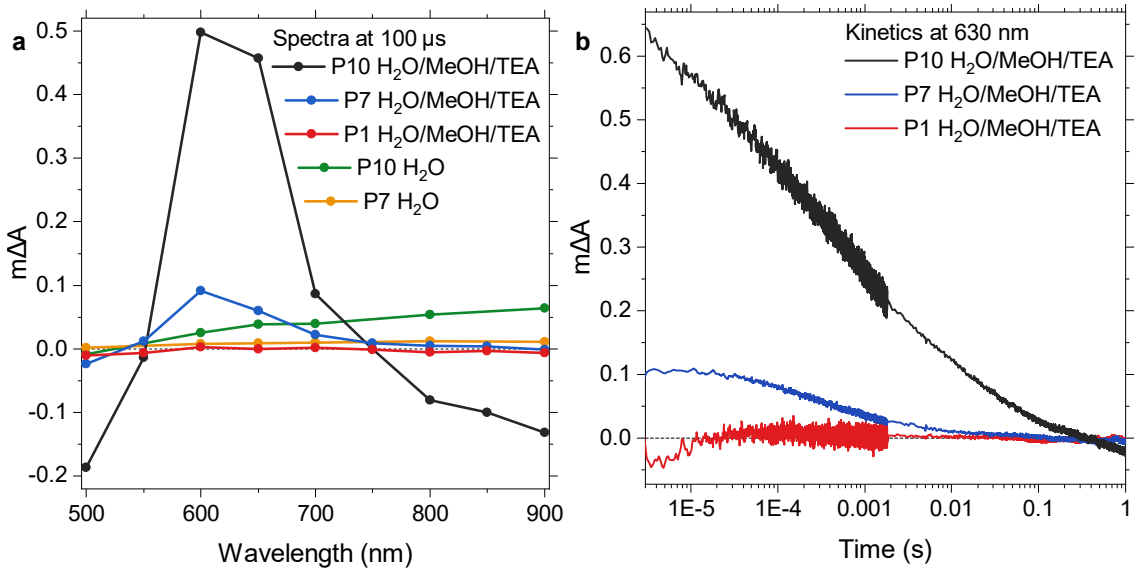

Figure 4.8: Transient absorption experiments on suspensions of P1, P7, and P10 on the µs - s timescale. (**a**) Transient spectra probed at 100 µs in H_2O/MeOH/TEA and H_2O only. The spectrum for P1 in H_2O is omitted here because no appreciable signal was observed. (**b**) Transient kinetics in H_2O/MeOH/TEA, probed at 630 nm to track the decay of the main absorption feature. In all cases, an excitation wavelength of 355 nm and a fluence of 0.32 mJ cm^{-2} were used.

The peak-like shape observed for P7 and P10 in the presence of TEA is consistent with the spectral signatures of charged polymers: In general, two absorption peaks can be expected for a charge carrier on a polymer, one of which is often found in the visible range while the second one appears at lower energies in the NIR [23–25]. Based on this agreement and the evidence laid out in the following, the 630 nm feature is assigned to an electron on the polymer on this µs - s timescale, hereafter referred to as an electron polaron for consistency with the organic photovoltaics literature.

The 630 nm peak is observed only in the presence of TEA on this timescale but not in pure H_2O (Figure 4.8a), which discounts other possible assignments such as triplet states. The addition of electron scavengers to the reaction mixture suggests the presence of reducing intermediates: After addition of methylviologen (MV^{2+}, *N,N*'-dimethyl-4,4'-bipyridinium dichloride), the continuous growth of two new absorption features around 430 nm and 600 nm is found after the repeated 355 nm pulsed laser excitation of a transient absorption measurement (Figure 4.9a), which are known to originate from the reduced $MV^{\bullet+}$ radical cation [26]. When probing the kinetics of this $MV^{\bullet+}$ formation, P1 does not lead to considerably more $MV^{\bullet+}$ generation than occurs

without any photocatalyst via direct electron transfer from TEA. However, in the presence of P7 and P10 significantly more $MV^{\bullet+}$ than this background is formed with electron transfer taking place earlier than 10 µs after illumination based on the mostly constant kinetic amplitude at µs times (Figure 4.9b). When a P10 dispersion in H_2O/MeOH/TEA is purged with O_2, the signal amplitude at 630 nm decreases by a factor of ∼7 (Figure 4.9c), suggesting that the photogenerated electron polarons are scavenged by O_2 before they can react with protons to form H_2. As a result, a reduced hydrogen evolution performance is observed when the photocatalytic mixture is not purged with N_2 to displace environmental O_2 prior to a hydrogen evolution experiment (Figure 4.9d). All these experiments support the assignment of the 630 nm feature in P7 and P10 on this µs - s timescale to reducing intermediates generated upon irradiation in the presence of TEA.

Following this assignment, the µs - s decay kinetics of these 630 nm electron polarons are investigated in more detail. While the kinetics appear to be best approximated as stretched exponentials, the resulting fits are not really satisfactory, especially in the tail of the decay. This suggests that the decay profile is defined by a more complex combination of different factors. Based on the signal amplitudes at 10 µs, the decay-half times for P7 and P10 are 420 µs and 700 µs respectively, which demonstrates that the electron polarons in P10 are considerably more long lived than in P7 and is also illustrated by the normalised decay kinetics in Figure A.5. When varying the excitation fluence, no significant changes in the kinetic profiles are observed for either P7 or P10 (Figure A.6). This invariance with excitation density is consistent with the idea that the monitored electron polarons are essentially the only charge carriers present on this long timescale, since holes have already reacted with TEA much earlier. As a result, the recombination rate of these electron polarons is not enhanced by the higher charge carrier densities present at higher fluences.

4.2.4 Summary of photoinduced reactions

The sequence of photoinduced reactions is summarised in Figure 4.10. Upon photoexcitation, a polymer exciton P* is generated and subsequently undergoes hole transfer to TEA in direct competition with exciton recombination. This first hole transfer step produces a polymer-centred electron polaron P^- and a $TEA^{\bullet+}$ radical cation (pathway a). Hence, the electron polaron yield P^- is determined by the quantum efficiency of the TEA photooxidation. The population of P* is observed as a peak above 700 nm on fs - ns timescales and the P^- population is observed in

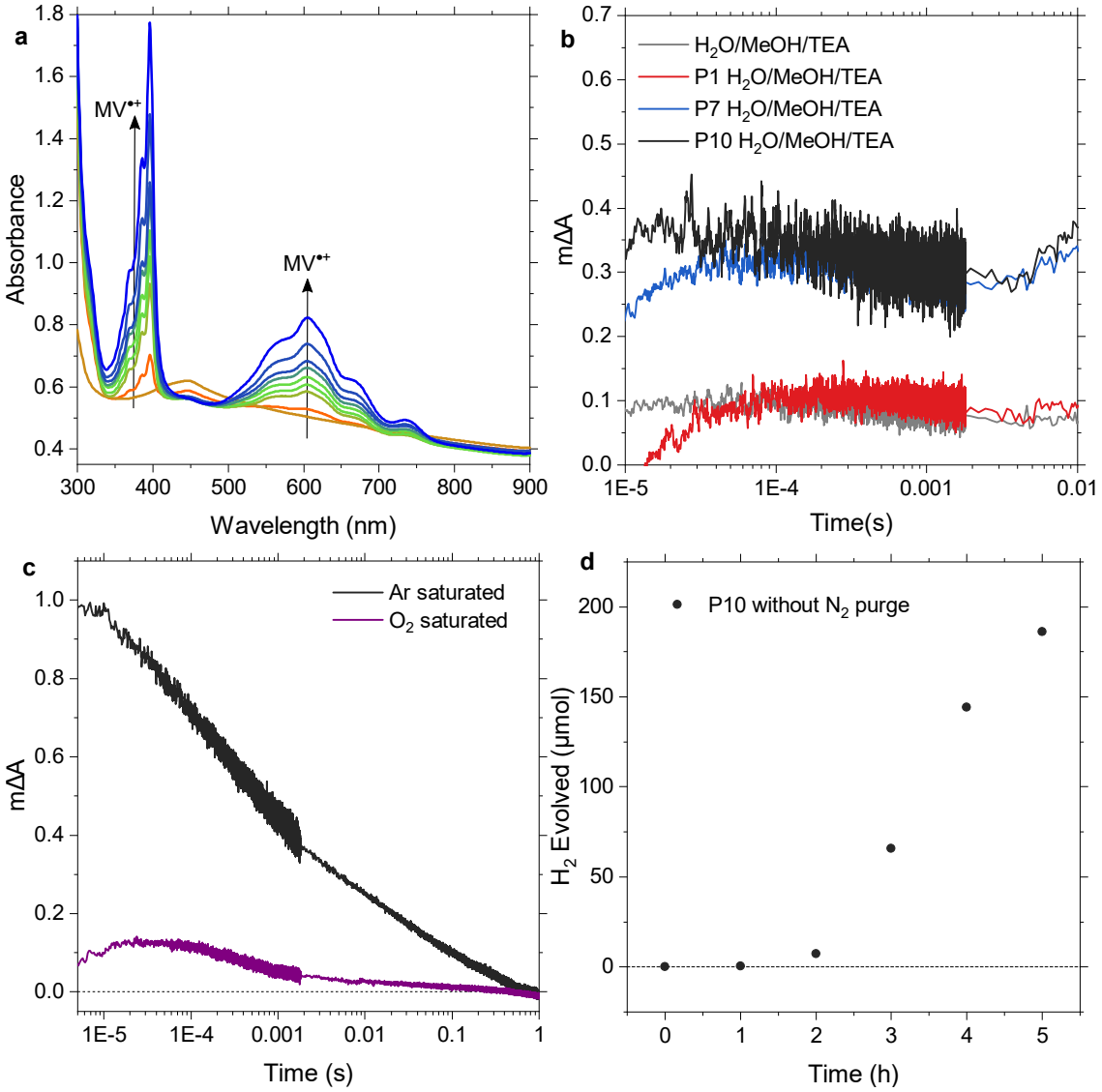

Figure 4.9: Effect of electron scavengers on transient absorption kinetics and hydrogen evolution rate. (**a**) Absorbance spectra following repeated photoexcitation of P10 in a 1:1:1 H_2O/MeOH/TEA mixture in the presence of 15 mmol L^{-1} methyl viologen (*N,N*'-dimethyl-4,4'-bipyridinium dichloride). (**b**) Transient kinetics probed at 600 nm using the same solution composition with suspended P1, P7, and P10. (**c**) Transient kinetics probed at 630 nm using a suspension of P10 in H_2O/MeOH/TEA and a fluence of 1.0 mJ cm^{-2}. The same suspension was first purged with argon (black trace) and then O_2 (purple trace). (**d**) Photocatalytic hydrogen evolution under visible light (>420 nm) illumination using 25 mg of photocatalyst in a 1:1:1 H_2O/MeOH/TEA mixture, without purging the mixture with N_2 prior to the experiment (as opposed to the hydrogen evolution experiments with N_2 purging shown in Figure 4.3).

the form of the 630 nm peak at least from the µs timescale onwards. The generated P^- may then undergo proton reduction to form hydrogen (pathway c), however, this proton reduction reaction is in kinetic competition with the reduction of other electron acceptors in the reaction mixture such as $TEA^{\bullet+}$ (effectively a recombination process, pathway d) or molecular oxygen.

To prevent recombination with P^-, $TEA^{\bullet+}$ can instead be deprotonated by donating a proton to another TEA molecule (pathway b), which makes the hole transfer reaction irreversible.

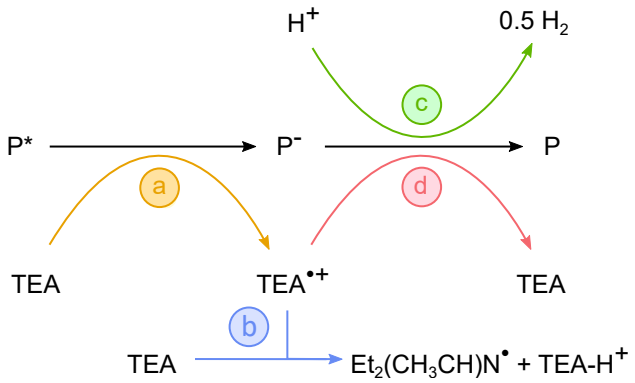

Figure 4.10: Schematic illustration of the sequence of possible photoinduced reactions for a photoexcited polymer P* in water and in the presence of TEA: (**a**) TEA oxidation, (**b**) deprotonation of the $TEA^{\bullet+}$ radical cation, (**c**) proton reduction, and (**d**) re-reduction of the $TEA^{\bullet+}$ radical cation. Proton reduction via the polymer electron polaron P^- is in kinetic competition with the re-reduction of $TEA^{\bullet+}$.

These presented transient data clearly demonstrate that the yield of electron polarons, as observed at µs times onwards in the form of the 630 nm TAS peak, increases in the order of P1-P7-P10 and thus correlates with the hydrogen evolution activity in this polymer series. This difference in charge yield already originates at fs - ps times, although it is not entirely clear whether charges are already fully separated on this early timescale.

4.2.5 Interaction between polymer and water

To further improve the understanding of the reasons behind these different charge yields, density functional theory (DFT) and molecular dynamics (MD) simulations were carried out by Drew Pearce, Anne Guilbert, Adriano Monti, and Martijn Zwijnenburg. Based on the transient data shown above, the sulfone group appears to play a key role in the process of charge generation for the polymers investigated herein: long-lived electron polarons are only observed for the two sulfone polymers P7 and P10, and with a higher yield for the polymer with the higher sulfone density P10, whereas the sulfone-free P1 shows no detectable quantities of such long-lived charges. As measured by Sebastian Sprick and shown in Table 4.1, the contact angles of water droplets on pressed polymer pellets are 88° for P1, 67° for P7, and 59° for P10, suggesting a stronger polymer-water interaction at higher sulfone content. Density functional theory calculations reveal that the dibenzo[*b*,*d*]thiophene sulfone unit in P7 and P10 exhibits a large

static dipole moment of 5.7 D, pointing away from the sulfone group (Figure A.7), whereas the phenylene unit in P1 has no dipole moment.

To investigate the effect of these differences in dipole moment on the interaction with the reaction mixture, MD simulations of fluorene, dibenzo[*b,d*]thiophene sulfone-co-phenylene, and dibenzo[*b,d*]thiophene sulfone were carried out in mixtures of H_2O and TEA. These oligomers represent model systems of P1, P7, and P10, respectively, where fluorene rather than phenylene was chosen to eliminate effects arising from differences in polymer conformation, thus focussing fully on the role of the sulfone group. Figure 4.11 shows MD snapshots of fluorene and dibenzo[*b,d*]thiophene sulfone hexamers in a H_2O/TEA mixture. It is evident that the fluorene oligomer essentially fully surrounds itself with TEA, whereas the dibenzo[*b,d*]thiophene sulfone oligomer resides at the interface between H_2O and TEA domains with its sulfone groups pointing towards the aqueous phase. The radial distribution function between the position of the sulfone group and that of surrounding H_2O molecules demonstrates that a structured water shell is established around the sulfone group, whereas water is absent around the bridging carbon atom in the fluorene oligomer (Figure A.8). The same behaviour is observed when MeOH is added to simulate the full H_2O/MeOH/TEA reaction mixture (Figure A.9). These differences in hydrophilicity also explain why larger particle aggreagates of P1 are found in H_2O, whereas the sizes of P7 and P10 partiles are smaller in H_2O than they are in H_2O/MeOH/TEA.

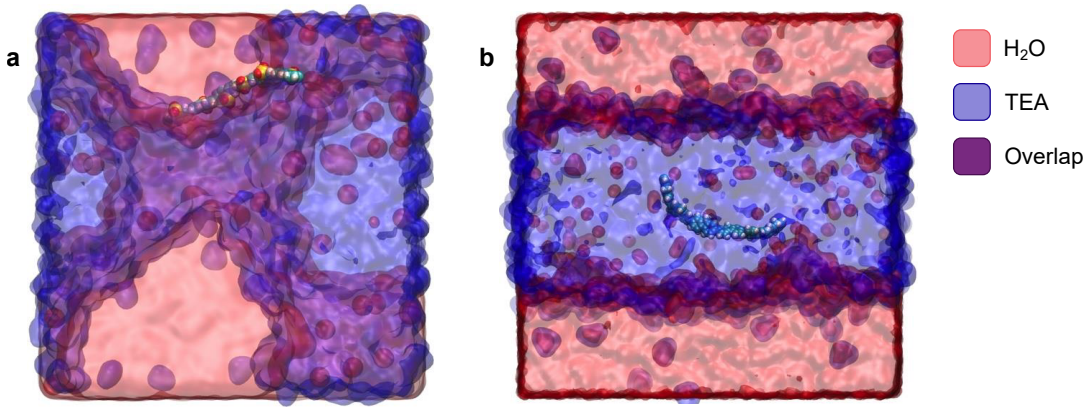

Figure 4.11: Snapshots of atomistic molecular dynamics simulations showing (**a**) the polar P10 polymer and (**b**) the non-polar fluorene polymer, as a model for P1, in a mixed environment of water (red) and TEA (blue). The purple regions are the projections of overlapping water and TEA domains inside the 3-dimensional box. While the non-polar fluorene polymer resides in the TEA phase, the amphiphilic P10 locates itself at the interface between water and TEA domains.

4.2.6 Effect of solvent environment on energetics

Finally, the impact of the preferred solvent environments of these polymers on their driving forces for the reactions outlined in Figure 4.10 are considered in order to further support the presented spectroscopic results. To this end, DFT-based calculations were used in which H_2O and TEA are represented by their relative permittivity (80.1 for H_2O vs 2.38 for TEA). The primary focus of these calculations lies on the first hole transfer step from the polymer exciton to TEA and the deprotonation of the $TEA^{\bullet+}$ radical cation, which makes the TEA oxidation irreversible. The ground state ionisation potential (IP) and excited state electron affinity (EA*), which measure how easily the polymer donates a hole, become steadily more positive in the P1-P7-P10 series in a H_2O environment (Figure 4.12a), suggesting an increasing driving force for hole transfer. Similarly, the ground state electron affinity, representing the tendency of the polymer to donate an electron, become steadily more positive in the P1-P7-P10 series. The IP-EA* and EA-IP* differences are small in H_2O meaning that the excitonic energy levels lie close to those of the polaronic states. Despite the resulting decrease in reductive driving force along this series, a comparison to the H^+/H_2 potential shows that a significant driving force for proton reduction (>0.5 eV) remains in all cases. On the oxidation side, the first hole transfer step is thermodynamically most demanding as it occurs at the most positive potential, but nevertheless is exergonic for all three polymers in H_2O.

When turning to a TEA environment (Figure 4.12b), the difference between excitonic and polaronic energy levels becomes much larger for all polymers, which can be ascribed to the weaker stabilisation of charged intermediates when placed in a environment of lower relative permittivity. This weaker stabilisation also results in a shift of all solution potentials to more positive values, which lowers the driving force for all hole transfer steps. The overall oxidation DEA+ACO/TEA is now endergonic for P1, and, although exergonic for P7 and P10, is likely slowed down by the thermodynamic barrier opposing the first hole transfer step.

The MD simulations in the previous subsection demonstrate that P1 resides in an essentially pure local TEA environment whereas P7 and P10 favour a mixed H_2O/TEA environment, which is likely more similar to that of H_2O simulated herein due to the dominating character of its much higher relative permittivity. Based on the DFT results, this means that the first hole transfer step as well as the overall TEA oxidation is thermodynamically uphill for P1, which helps to rationalise the absence of any spectroscopic feature related to polarons in this material. In contrast, the more H_2O-like environment of P7 and P10 implies a larger driving force for hole

transfer for these polymers. With this larger driving force, the first hole transfer step and the overall TEA oxidation are much more favourable for P7 and P10, resulting in appreciable yields of electron polarons on the timescale relevant for proton reduction.

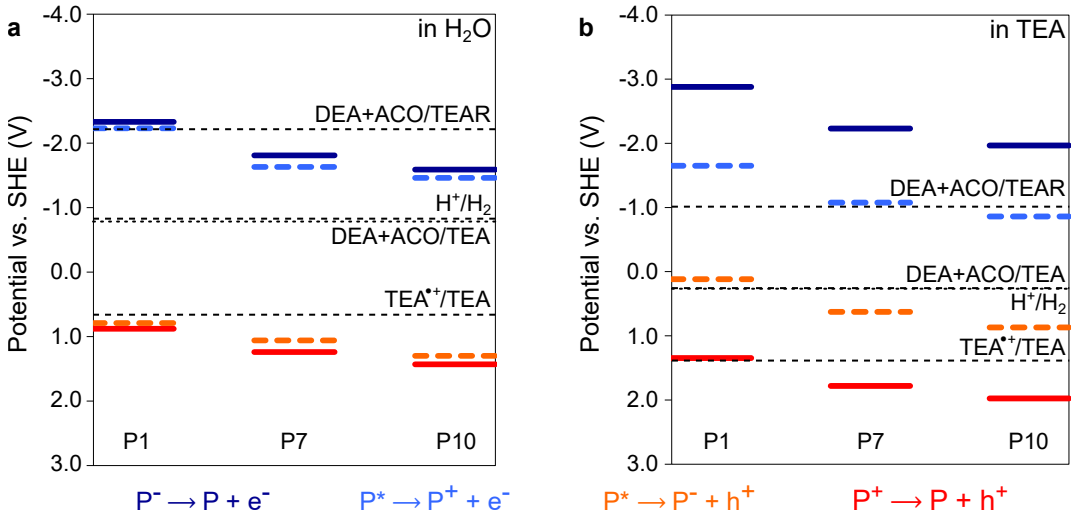

Figure 4.12: DFT energy level calculations for oligomers of P1, P7, and P10 (**a**) in water and (**b**) in TEA. The coloured energy levels correspond to the ground state ionisation potential (IP, red solid line) and electron affinity (EA, blue solid line) for each oligomer, as well as their exciton electron affinity (EA*, orange dashed line) and exciton ionisation potential (IP*, blue dashed line). These oligomer energy levels are shown in comparison to the potentials for proton reduction (H_2/H^+), the first TEA oxidation step ($TEA^{\bullet+}$/TEA), the second oxidation step of the TEA oxidation product TEAR (DEA+ACO/TEAR), and the overall TEA oxidation (DEA+ACO/TEA). TEAR represents the deprotonated TEA radical $Et_2(CH_3CH)N^{\bullet+}$ and ACO stands for acetaldehyde.

4.3 Discussion

The photocatalytic activity of polymer photocatalysts is often dictated by a complex interplay of various factors [27] such as light absorption, reaction driving force, particle morphology, and interfacial interactions, just to name a few. The presented results provide a clear connection between the photocatalytic activity of conjugated polymer particles and their photophysics in the reaction medium. The increasing activity in the P1-P7-P10 series is found to arise from an increasing yield of photogenerated electron polarons in this series, e.g. with a decay-half times for P10 of 700 µs based on the signal amplitudes at 10 µs. The long lifetimes of these electron polarons are consistent with the millisecond to early second timescale reported for proton reduction in other photocatalytic systems [28–30]. Given that no appreciable yields of such polarons are observed for P1, the presence of the sulfone groups in P7 and P10 appears

to be critical for charge generation. This observation is supported by DFT calculations, which demonstrate that the sulfone groups in the dibenzo[*b,d*]thiophene sulfone monomers induce a large static dipole moment, and MD simulations further suggest that these sulfone groups establish a shell of H_2O molecules around them when the polymer is located in the reaction mixture. This enhanced polymer-water interaction is further confirmed by a gradual decrease in H_2O contact angles with increasing sulfone content.

While surface areas as measured by N_2 sorption measurements are low for all three polymers (29 - 69 $m^2\,g^{-1}$), it is worth noting that these experiments measure the surface areas of dry polymer powders. However, the differences in hydrophilicity might lead to a different degrees of swelling in an aqueous environment, which might increase the effectively accessible surface area in the case of the sulfone polymers. Given the relatively large particle sizes in the range of several hundred nanometres up to the micrometer range for all polymers, it seems likely that some interpenetration of water (and with it likely also of the scavenger) must take place in order to achieve charge yields and EQEs as high as the ones observed here, especially given that typical exciton diffusion lengths are on the order of a few to 10 nm in films of conjugated polymers [31–33]. This large disparity between particle size and exciton diffusion length suggests that significant further improvements should be possible via surface engineering and tuning of the particle morphology. Such improvements have recently been demonstrated using P10 particles with smaller size (20.4% EQE) [3] and sulfone polymers with greater intrinsic porosity (13.2% EQE) [34], but these approaches can likely be taken even further or combined to achieve even higher performances.

4.4 Conclusions

The spectroscopic results presented in this chapter shed light onto the pronounced increase in hydrogen evolution activity along the P1-P7-P10 series. While factors such as enhanced light absorption likely contribute to the observed activity trend, the main difference is the incorporation of the polar sulfone groups in the more active polymers P7 and P10. The yield of long-lived photogenerated electrons, which ultimately drive the H_2 evolution reaction, qualitatively increases with the density of sulfone groups in the polymer backbone. Perhaps surprisingly for organic photocatalysts, the generation of at least the precursor species for these long-lived electrons occurs on the early picosecond timescale, with half-rise times of 1.6 ps for P10 and 3.8 ps for

P7. This increase in charge yield is further supported by DFT calculations and MD simulations, which demonstrate the creation of a water shell around the dipolar sulfone groups, and that the polarity of the local environment affects the driving forces for charge transfer. These results highlight the importance of surface engineering to make the dispersed polymer particles more accessible to H_2O, not only in the presence of sacrificial reagents but also for systems that eventually target overall water splitting.

4.5 Materials and methods

Polymer synthesis

P1, P7, and P10 were synthesized through polymerization of the respective dibromoarenes and diboronic acids or diboronic pinacol esters using Pd(0)-catalysed Suzuki-Miyaura polycondensation at 150 °C in N,N-dimethylformamide and in the presence of aqueous K_2CO_3 for 2 days. The detailed synthetic protocols for P1 and P7 are described in reference [1] and for P10 in reference [2].

The palladium content for all samples was determined by Butterworth Laboratories Ltd (Teddington, United Kingdom) via ICP-OES.

Hydrogen evolution experiments

The experimental details for the H_2 evolution experiments can be found in reference [2]. In brief, 25 mg of polymer powder were dispersed in a flask containing 25 ml of a 1:1:1 H_2O/MeOH/TEA mixture. The resulting suspension was ultrasonicated until the polymer powder was fully dispersed and then purged with N_2 for 30 min. This mixture was then illuminated with a 300 W Xe lamp (Newport 6258, Ozone free) under atmospheric pressure and samples were injected manually into a gas chromatograph (Bruker 450-GC).

Sample preparation for spectroscopy

Dispersions of P1, P7, and P10 with a concentration of $1.67\,\mathrm{g\,L^{-1}}$ were prepared in water and ultrasonicated to enhance dispersibility. In general, the dispersion quality improved when the powders were allowed to soak in this stock solution for several days with intermittent daily

sonication, especially that of P1 dispersions. While the soaking time varied from several days up to about one week for the different spectroscopic experiments reported herein, samples used for the same experiments always soaked for the same amount of time.

TAS samples with a concentration of $0.24\,\mathrm{g\,L^{-1}}$ were then prepared from the stock dispersion on the day of the experiment using the given solvent ratios in quartz cuvettes with a path length of 2 mm (Hellma Suprasil quartz 700 µL). Cuvettes were then sealed using rubber septa caps and purged with argon for 20 min, which was found to be a good trade-off between purging for an insufficient time (thus risking that not all O_2 is displaced) and purging fro too long (typically resulting in the accumulation of polymer particles on the cuvette walls close to the neck). Dispersions were stirred continuously during the ultrafast TAS measurements using a magnetic stirrer to prevent settling, as convection does not affect signals on this fast timescale. For measurements in the µs timescale, samples were stirred occasionally using a magnetic stirrer in between different probe wavelength acquisitions.

MD simulations

MD simulations were performed out using the GROMACS 5.1.4 package [35] with force fields based on OPLS-AA [36]. Initial configurations were made using Gromacs and PACKMOL [37]. Further details can be found in reference [2].

DFT calculations

The experimental details for the performed (TD-)DFT calculations can be found in reference [2]. In brief, the energy levels of the oligomers in different solvent environments, the solution redox potentials, and the free energy of the deprotonation step were obtained from (TD-)DFT calculations using the B3LYP density functional [38, 39], the DZP basis-set [40] and the COSMO solvation model [41]. Protons were treated in the form of adducts with TEA (TEA-H^+) and relative permittivity values of 80.1 and 2.38 were used for H_2O and TEA, respectively.

4.6 References

1. Sprick, R. S. *et al.* Visible-Light-Driven Hydrogen Evolution Using Planarized Conjugated Polymer Photocatalysts. *Angewandte Chemie International Edition* **55,** 1792–1796 (2016).

2. Sachs, M. *et al.* Understanding structure-activity relationships in linear polymer photocatalysts for hydrogen evolution. *Nature Communications* **9,** 4968 (2018).

3. Aitchison, C. M., Sprick, R. S. & Cooper, A. I. Emulsion polymerization derived organic photocatalysts for improved light-driven hydrogen evolution. *Journal of Materials Chemistry A,* 37–39 (2019).

4. Dai, C. *et al.* Dibenzothiophene- S , S -Dioxide-Based Conjugated Polymers: Highly Efficient Photocatalyts for Hydrogen Production from Water under Visible Light. *Small* **14,** 1801839 (2018).

5. Vogel, A. *et al.* Photocatalytically active ladder polymers. *Faraday Discussions* **215,** 84–97 (2019).

6. Lan, Z.-a. *et al.* Reducing the Exciton Binding Energy of Donor-Acceptor-Based Conjugated Polymers to Promote Charge-Induced Reactions. *Angewandte Chemie International Edition* **58,** 10236–10240 (2019).

7. Lan, Z.-A., Ren, W., Chen, X., Zhang, Y. & Wang, X. Conjugated donor-acceptor polymer photocatalysts with electron-output "tentacles" for efficient hydrogen evolution. *Applied Catalysis B: Environmental* **245,** 596–603 (2019).

8. Zhao, Y. *et al.* Effect of Linking Pattern of Dibenzothiophene- S , S -dioxide-Containing Conjugated Microporous Polymers on the Photocatalytic Performance. *Macromolecules* **51,** 9502–9508 (2018).

9. Sprick, R. S. *et al.* Nitrogen Containing Linear Poly(phenylene) Derivatives for Photocatalytic Hydrogen Evolution from Water. *Chemistry of Materials* **30,** 5733–5742 (2018).

10. Wang, Z. *et al.* Dibenzothiophene Dioxide Based Conjugated Microporous Polymers for Visible-Light-Driven Hydrogen Production. *ACS Catalysis* **8,** 8590–8596 (2018).

11. Wang, X. *et al.* Hydrophilicity-Controlled Conjugated Microporous Polymers for Enhanced Visible-Light-Driven Photocatalytic H 2 Evolution. *Macromolecular Rapid Communications* **40,** 1800494 (2019).

12. Wang, X. *et al.* Sulfone-containing covalent organic frameworks for photocatalytic hydrogen evolution from water. *Nature Chemistry* **10,** 1180–1189 (2018).

13. Di Maria, F. *et al.* Poly(3-hexylthiophene) Nanoparticles Containing Thiophene- S , S -dioxide: Tuning of Dimensions, Optical and Redox Properties, and Charge Separation under Illumination. *ACS Nano* **11,** 1991–1999 (2017).

14. Dai, C., Gong, X., Zhu, X., Xue, C. & Liu, B. Molecular modulation of fluorene-dibenzothiophene-S , S -dioxide-based conjugated polymers for enhanced photoelectrochemical water oxidation under visible light. *Materials Chemistry Frontiers* **2,** 2021–2025 (2018).

15. Sprick, R. S. *et al.* Extended conjugated microporous polymers for photocatalytic hydrogen evolution from water. *Chemical Communications* **52,** 10008–10011 (2016).

16. Xu, S., Klimov, V. I., Kraabel, B., Wang, H. & McBranch, D. W. Femtosecond transient absorption study of oriented poly(9,9-dioctylfluorene) film: Hot carriers, excitons, and charged polarons. *Physical Review B* **64,** 193201 (2001).

17. Kraabel, B. *et al.* Unified picture of the photoexcitations in phenylene-based conjugated polymers: Universal spectral and dynamical features in subpicosecond transient absorption. *Physical Review B* **61,** 8501–8515 (2000).

18. Stevens, M. A., Silva, C., Russell, D. M. & Friend, R. H. Exciton dissociation mechanisms in the polymeric semiconductors poly(9,9-dioctylfluorene) and poly(9,9-dioctylfluorene-co-benzothiadiazole). *Physical Review B* **63,** 165213 (2001).

19. Lewis, A. *et al.* Singlet exciton diffusion in MEH-PPV films studied by exciton–exciton annihilation. *Organic Electronics* **7,** 452–456 (2006).

20. Guo, J., Ohkita, H., Benten, H. & Ito, S. Near-IR Femtosecond Transient Absorption Spectroscopy of Ultrafast Polaron and Triplet Exciton Formation in Polythiophene Films with Different Regioregularities. *Journal of the American Chemical Society* **131,** 16869–16880 (2009).

21. Frankevich, E. *et al.* Formation of polaron pairs and time-resolved photogeneration of free charge carriers in π-conjugated polymers. *Physical Review B* **62,** 2505–2515. arXiv: `1011.1669` (2000).

22. Müller, J. G., Lemmer, U., Feldmann, J. & Scherf, U. Precursor States for Charge Carrier Generation in Conjugated Polymers Probed by Ultrafast Spectroscopy. *Physical Review Letters* **88,** 147401 (2002).

23. Österbacka, R., An, C. P., Jiang, X. M. & Vardeny, Z. V. Two-Dimensional Electronic Excitations in Self-Assembled Conjugated Polymer Nanocrystals. *Science* **287,** 839–842 (2000).

24. Baniya, S., Vardeny, S. R., Lafalce, E., Peygambarian, N. & Vardeny, Z. V. Amplitude-Mode Spectroscopy of Charge Excitations in PTB7 π-Conjugated Donor-Acceptor Copolymer for Photovoltaic Applications. *Physical Review Applied* **7,** 064031 (2017).

25. Fesser, K., Bishop, A. R. & Campbell, D. K. Optical absorption from polarons in a model of polyacetylene. *Physical Review B* **27,** 4804–4825 (1983).

26. Méndez, E. E., Crespo-Hernández, C., Figueroa, R., Arce, R. & Quiñones, E. Mechanism of formation of the MV+ radical during the UV excitation of methylviologen. *Journal of Photochemistry and Photobiology A: Chemistry* **142,** 19–24 (2001).

27. Wang, Z., Li, C. & Domen, K. Recent developments in heterogeneous photocatalysts for solar-driven overall water splitting. *Chemical Society Reviews* **48,** 2109–2125 (2019).

28. Reynal, A., Lakadamyali, F., Gross, M. A., Reisner, E. & Durrant, J. R. Parameters affecting electron transfer dynamics from semiconductors to molecular catalysts for the photochemical reduction of protons. *Energy & Environmental Science* **6,** 3291 (2013).

29. Rodenberg, A. *et al.* Mechanism of Photocatalytic Hydrogen Generation by a Polypyridyl-Based Cobalt Catalyst in Aqueous Solution. *Inorganic Chemistry* **54,** 646–657 (2015).

30. Pastor, E. *et al.* Spectroelectrochemical analysis of the mechanism of (photo)electrochemical hydrogen evolution at a catalytic interface. *Nature Communications* **8,** 14280 (2017).

31. Kroeze, J. E., Savenije, T. J., Vermeulen, M. J. W. & Warman, J. M. Contactless Determination of the Photoconductivity Action Spectrum, Exciton Diffusion Length, and Charge Separation Efficiency in Polythiophene-Sensitized TiO 2 Bilayers. *The Journal of Physical Chemistry B* **107,** 7696–7705 (2003).

32. Bruno, A., Reynolds, L. X., Dyer-Smith, C., Nelson, J. & Haque, S. A. Determining the exciton diffusion length in a polyfluorene from ultrafast fluorescence measurements of polymer/fullerene blend films. *Journal of Physical Chemistry C* **117,** 19832–19838 (2013).

33. Shaw, P. E., Ruseckas, A. & Samuel, I. D. W. Exciton Diffusion Measurements in Poly(3-hexylthiophene). *Advanced Materials* **20,** 3516–3520 (2008).

34. Sprick, R. S. *et al.* Photocatalytic Hydrogen Evolution from Water Using Fluorene and Dibenzothiophene Sulfone-Conjugated Microporous and Linear Polymers. *Chemistry of Materials* **31,** 305–313 (2019).

35. Berendsen, H. J. C., van der Spoel, D. & van Drunen, R. GROMACS: A message-passing parallel molecular dynamics implementation. *Computer Physics Communications* **91,** 43–56 (1995).

36. Jorgensen, W. L., Maxwell, D. S. & Tirado-Rives, J. Development and Testing of the OPLS All-Atom Force Field on Conformational Energetics and Properties of Organic Liquids. *Journal of the American Chemical Society* **118,** 11225–11236 (1996).

37. Martínez, L., Andrade, R., Birgin, E. G. & Martínez, J. M. PACKMOL: A package for building initial configurations for molecular dynamics simulations. *Journal of Computational Chemistry* **30,** 2157–2164 (2009).

38. Becke, A. D. Density-functional thermochemistry. III. The role of exact exchange. *The Journal of Chemical Physics* **98,** 5648–5652 (1993).

39. Stephens, P. J., Devlin, F. J., Chabalowski, C. F. & Frisch, M. J. Ab Initio Calculation of Vibrational Absorption and Circular Dichroism Spectra Using Density Functional Force Fields. *The Journal of Physical Chemistry* **98,** 11623–11627 (1994).

40. Schäfer, A., Horn, H. & Ahlrichs, R. Fully optimized contracted Gaussian basis sets for atoms Li to Kr. *The Journal of Chemical Physics* **97,** 2571–2577 (1992).

41. Klamt, A. & Schüürmann, G. COSMO: a new approach to dielectric screening in solvents with explicit expressions for the screening energy and its gradient. *J. Chem. Soc., Perkin Trans. 2,* 799–805 (1993).

Chapter 5

Role of residual palladium in conjugated polymer photocatalysts

A central yet unresolved question for polymeric photocatalysts is where the catalytically active site in these all-organic materials lies. Residual metal impurities, which are an often unavoidable by-product of the metal-catalysed coupling reactions used for the synthesis of many polymers, have been suggested to act as active sites for photocatalytic hydrogen evolution. This chapter investigates the effect of such Pd impurities on the excited state kinetics of the solution-processable polymer F8BT, for which it is possible to lower the residual Pd content via a series of consecutive purification steps before processing it into polymer nanoparticles. The resulting series of F8BT nanoparticles with varying Pd content has shown a pronounced drop in hydrogen evolution performance at Pd contents below 100 ppm, suggesting that the presence of Pd is essential for the hydrogen evolution activity of these F8BT nanoparticles. This strong correlation between activity and Pd content makes this F8BT series an ideal model system to study how the excited state of the polymer is affected by the presence of residual Pd centres. Transient spectroscopic measurements reveal that Pd separates photogenerated electrons via oxidative quenching on the fs - ns timescale - in fact faster than the usual reductive quenching via the electron donor, in this case diethylamine, in solution. Using the spectroscopic signatures of the produced charges, it is found that this oxidative quenching process produces electrons localised on the Pd centres within the F8BT nanoparticles, whereas reductive quenching produces electrons localised on the polymer itself. Oxidative and reductive quenching pathways dominate at high and low Pd concentrations, respectively. A direct comparison to other conjugated polymers such as the dibenzo[*b,d*]thiophene sulfone homopolymer P10 (as investigated in Chapter 4)

under quasi-constant illumination conditions suggests that photogenerated electrons accumulate on Pd centres in unpurified F8BT but on the polymer itself in P10, despite very similar residual Pd contents. These results allow conclusions about different rate limiting steps in the process of hydrogen evolution for both materials, and show that the pronounced oxidative quenching in the presence of Pd in F8BT even goes beyond a merely catalytic function of this residual metal, suggesting relevance for fields such as organic light-emitting diodes or organic photovoltaics.

The results presented in this chapter are in part included in these publications:

Jan Kosco, Michael Sachs, Robert Godin, Mindaugas Kirkus, Laia Francàs, Matthew Bidwell, Muhammad Qureshi, Dalaver Anjum, James R. Durrant & Iain McCulloch. The Effect of Residual Palladium Catalyst Contamination on the Photocatalytic Hydrogen Evolution Activity of Conjugated Polymers. *Advanced Energy Materials* **8**, 1802181 (2018).

Michael Sachs, Hyojung Cha, Jan Kosco, Catherine M. Aitchison, Laia Francàs, Sacha Corby, Anna A. Wilson, Robert Godin, Alexander Fahey-Williams, Andrew I. Cooper, Reiner Sebastian Sprick, Iain McCulloch & James R. Durrant. The effect of residual palladium on charge separation and accumulation in conjugated polymer photocatalysts. *In preparation.*

The following results shown in this chapter have been contributed by collaborators:
The preparation of the investigated F8BT and P3HT nanoparticles, and their characterisation via TEM, DLS, ICP-OES and hydrogen evolution experiments were carried out by Jan Kosco. P10 was synthesised by Sebastian Sprick. The TCSPC experiments of F8BT nanoparticles with varying size were carried out by Hyojung Cha. Spectroelectrochemical measurements of Pd nanoparticles were carried out by Laia Francàs. The shown steady state absorbance spectrum and PL spectrum were recorded by Alex Fahey Williams.

5.1 Introduction

Despite the increasing popularity of organic photocatalysts, some of the most fundamental questions concerning these materials are still unanswered. One of these questions is where the active site in these materials lies, which strongly relates to the question whether such all-organic materials can catalyse multi-electron reactions without the addition of any co-catalyst. The ability to accumulate charges is key in other photocatalytic systems that drive multi-electron reactions

such as hydrogen or oxygen evolution, for which inorganic materials or metal organic molecules are typically employed as co-catalysts. These co-catalysts incorporate transition metal atoms, which are known for their ability to access a range of different oxidation states, and thus readily accumulate photogenerated charge carriers. In this way, co-catalysts can suppress recombination through the localisation of charges but also provide sites with for reaction intermediates favourable binding energies [1, 2]. Therefore, it is highly debated whether polymer photocatalysts as all-organic materials can perform such multi-electron reactions on their own with satisfactory efficiencies. For instance, carbon nitrides are prepared via metal-free routes and require the addition of co-catalysts to achieve appreciable photocatalytic efficiencies, whereas their activity is very low when no co-catalyst is added [3, 4].

For most polymer photocatalysts it is difficult to determine the importance of co-catalysts because they already contain residual metal from their metal-catalysed polymerisation reaction. As a result, the effect of any added co-catalyst may be masked by that of metal impurities if these impurities are also catalytically active. However, it is often not feasible to remove these metal impurities once polymerisation has occurred because most of the produced polymers are not soluble in organic solvents and are thus hard to purify. For instance, conjugated polymers that incorporate dibenzo[*b,d*]thiophene sulfone units have shown some of the highest quantum yields in this class of materials as discussed in Chapter 4, but the role of residual palladium has ultimately remained unclear due to their insolubility.

The solution processable polymer poly(9,9-dioctylfluorene-alt-benzothiadiazole) (F8BT), the structure of which is shown in Figure 5.1, is used herein as a photocatalyst for hydrogen evolution after being subjected to a sequence of purification steps. The resulting series of F8BT nanoparticles exhibits a gradual decease in Pd content, and hydrogen evolution experiments demonstrate a pronounced drop in performance below 100 ppm Pd. This chapter investigates the reasons for this strong Pd dependence using transient optical spectroscopy, particularly regarding the effect of Pd on the excited state of the polymer. Using constant illumination conditions, a comparison is made to the conjugated polymers P3HT, which is synthesised without any Pd precursors, and P10, which has a Pd content similar to F8BT but exhibits significantly higher hydrogen evolution performance. This comparison reveals that F8BT and P10 are affected differently by incorporated Pd, possibly because photogenerated charges encounter Pd centres on different time scales after photoexcitation.

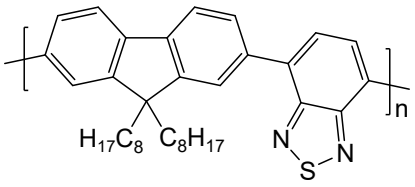

Figure 5.1: Molecular structure of poly(9,9-dioctylfluorene-alt-benzothiadiazole), commonly referred to as F8BT. F8BT is a donor-acceptor polymer where fluorene is the donor and benzothiadiazole is the acceptor unit.

5.2 Results

5.2.1 Purification and nanoparticle fabrication

The F8BT nanoparticles used herein were prepared by Jan Kosco in a two-stage fabrication process, where the synthesised polymer is (i) purified through a series of purification steps and then (ii) processed into nanoparticles. By processing F8BT obtained from different purification stages, a series of nanoparticles with continuously decreasing Pd content is obtained. Since purification and nanoparticle formation are separated, this two-step process yields the same nanoparticle morphology irrespective of the Pd content.

F8BT was synthesised using tris(dibenzylideneacetone)dipalladium(0) ($Pd_2(dba)_3$) catalysed Suzuki polymerisation following a procedure reported previously [5]. The synthesised polymer was initially purified using Soxhlet extraction. Purification via Soxhlet extraction is common for organic photocatalysts and will thus be the reference point for this study - the resulting F8BT batch is referred to as "unpurified", indicating that no further purification was undertaken. Inductively Coupled Plasma Optical Emission Spectrometry (ICP-OES) measurements were undertaken to determine Pd contents for all samples, in this case demonstrating that 1170 ppm Pd remain in the polymer following Soxhlet extraction. Parts of this polymer batch were then purified further using Gel Permeation Chromatography (GPC) and washing with sodium diethyldithiocarbamate (DTC). ICP-OES experiments confirmed that the Pd content decreased with each subsequent purification step: 195 ppm after GPC, 36 ppm after GPC plus one DTC wash, and <1ppm (below detection limit) after GPC plus two washes with DTC. The decrease in Pd content with consecutive purification steps can be seen in the TEM images shown in Figure 5.2. These images show that Pd is present in the form of nanoparticles with an average diameter of ∼4 nm, appearing as bright white dots in dark field TEM, and demonstrate a clear decrease in the number of Pd nanoparticles with increasing purification.

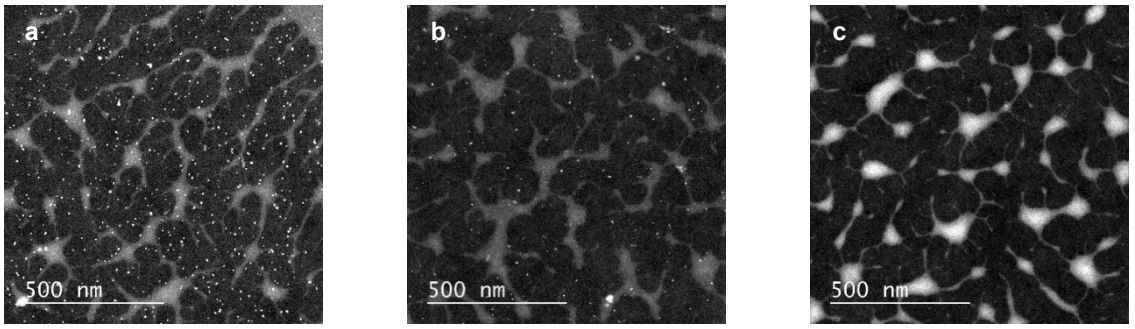

Figure 5.2: TEM images of F8BT in different purification levels prior to processing into nanoparticles, here deposited as films: (**a**) unpurified (1170 ppm) (**b**) GPC (195 ppm), (**c**) GPC + 2 DTC washes (<1 ppm). The number of palladium particles, which appear as white dots in these dark field TEM images, decreases visibly with increasing purification.

F8BT at different purification stages was blended with poly(styrene-*co*-maleic anhydride) (PSMA) and the resulting blend was then processed into nanoparticles by nanoprecipitation, where PSMA acts as a stabilising agent to prevent aggregation of individual nanoparticles. To verify that observed activity trends are indeed due to the different Pd content and not due to other changes in the F8BT polymer during purification procedure, several control samples were fabricated by adding defined amounts of $Pd_2(dba)_3$ back into a part of the F8BT sample with the highest purification level (<1ppm Pd) prior to nanoparticle processing. Sizes of the obtained F8BT nanoparticles with varying Pd content lie in the 40 - 70 nm range as determined via Dynamic Light Scattering (DLS) by Jan Kosco (see Table 5.1), with no apparent correlation between size and Pd content.

Table 5.1: Average diameter and polydispersity index for the F8BT nanoparticles with different Pd content as determined by Dynamic Light Scattering.

Pd content (ppm)	Average diameter (nm)	Polydispersity index
1170	40.1	0.118
250	46.4	0.178
195	68.0	0.186
100	43.1	0.212
60	54.0	0.190
36	55.2	0.160
<1	49.6	0.101

5.2.2 Hydrogen evolution activity

As shown in Figure 5.3, the fabricated F8BT nanoparticles with varying Pd content were then tested for photocatalytic H_2 evolution in the presence of diethylamine (DEA) as a sacrificial

electron donor using a 3:7 DEA/H_2O mixture. These experiments were carried out by Jan Kosco as described in reference [6]. Nanoparticles fabricated from unpurified F8BT (1170 ppm Pd) showed the highest activity (producing 8.47 µmol H_2 over 24 h), which was comparable to the performance of samples with Pd contents down to 100 ppm. However, a sharp drop in H_2 evolution activity was observed below 100 ppm, and the amount of evolved H_2 for the most purified sample (<1 ppm) was below the detection limit of the gas chromatograph used for its quantification. Importantly, the activity of this <1 ppm Pd F8BT was restored when adding defined amounts of Pd precursor before nanoparticle formation (open circles), which shows that the observed trends are indeed due to differences in Pd concentration.

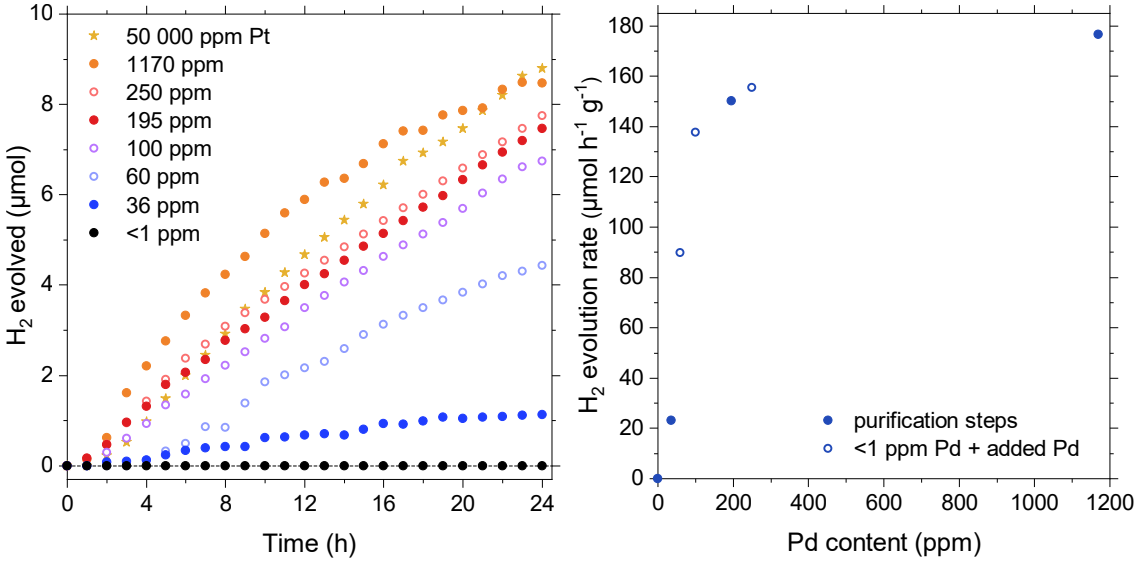

Figure 5.3: Hydrogen evolution activity of F8BT nanoparticles with varying palladium content. (**a**) Hydrogen evolution runs over a period of 24 h, where one run with 50 000 ppm added platinum is shown for comparison. (**b**) Average hydrogen evolution rate over the same period as a function of their palladium content. All experiments were conducted using 2 mg photocatalyst in 15 mL of a 3:7 DEA/H_2O mixture, irradiated by the output of a 300 W xenon lamp (385 - 700 nm).

These results demonstrate that two different regimes can be distinguished: A region of low Pd concentration (here <100 ppm) where the hydrogen evolution activity of the nanoparticle depends strongly on its Pd content, and a saturation regime above this threshold concentration where additional Pd only leads to a comparably small increase in performance. In fact, even the addition of 50 000 ppm platinum, known for its superior proton reduction performance, via photodeposition does not lead to a significant increase in the amount of produced H_2 (Figure 5.3a). The EQE was estimated for unpurified F8BT at 340 nm, yielding a value of 0.02%. While this value is rather low, it should be noted that the purpose of this set of samples is to investigate the effect of residual Pd on their performance rather than to maximise their activity. A comparable

level of control over the amount of residual metal cannot be achieved using many of the higher performing polymer photocatalysts due to their insolubility.

5.2.3 Exciton quenching pathways

The shapes of absorbance and photoluminescence emission spectra were essentially identical across the series of F8BT nanoparticles with varying Pd concentration, and are exemplarily shown for nanoparticles made from unpurified F8BT in Figure 5.4 as recorded by Alex Fahey Williams. These nanoparticles exhibit two absorption peaks centred around 322 nm and 459 nm, and have a photoluminescence maximum around 533 nm. These features are in good agreement with spectra measured for F8BT films [7, 8], suggesting that the packing behaviour in these nanoparticles is comparable to that in films.

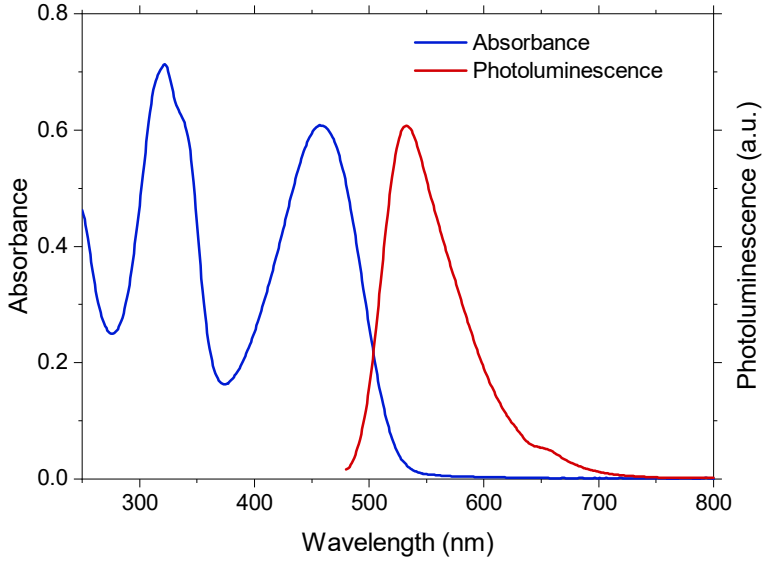

Figure 5.4: Absorbance and photoluminescence emission spectra of the used F8BT nanoparticle suspensions, here for unpurified F8BT dispersed in H_2O. An excitation wavelength of 455 nm was used for the photoluminescence measurement.

Time-resolved spectroscopic techniques were used to monitor the evolution of the excited state in these nanoparticles to determine at which point in the photocatalytic reaction sequence Pd effects come into play. First, Time-Correlated Single Photon Counting (TCSPC) experiments were carried out to investigate how the presence of different Pd concentrations affects the population of photogenerated excitons. For these measurements, photoluminescence decays were probed at 545 nm following 465 nm excitation, which is close to the photoluminescence and visible absorption maxima shown in Figure 5.4. Suspensions of F8BT nanoparticles with different Pd content were prepared with the same absorbance at the excitation wavelength to ensure that

the same number of photons is absorbed for all samples. Emitted photons are then counted for a time period of 10 s in all cases, thus allowing for a quantitative comparison of absolute signal amplitudes in addition to the decay profile.

Photoluminescence decay kinetics obtained from aqueous dispersions of F8BT nanoparticles with varying Pd concentration are shown in Figure 5.5a, demonstrating a gradual decrease in lifetime with increasing Pd concentration. This decrease in lifetime suggests that excitons are quenched by the Pd centres within the F8BT nanoparticles, and is here assigned to non-radiative recombination of excitons at Pd centres. Such metal-mediated recombination has been observed in Pt-decorated CdSe nanosheets, where the vast majority of photogenerated excitons undergoes energy transfer to Pt [9, 10]. In contrast, Pt-decorated CdS nanowires display sub-ps hole trapping, which enables charge separation by electron transfer to Pt with subsequent removal of the trapped hole via an electron donor [11, 12]. Since there is no evidence for such ultrafast hole trapping in the F8BT nanoparticles investigated herein (e.g. pronounced defect emission [11]), the observed exciton quenching in the presence of Pd is assigned to energy transfer and thus recombination.

By integrating the kinetic traces over the entire recorded time range of 100 ns, it can be estimated that at least 54% of the generated excitons recombine at Pd centres in nanoparticles made from unpurified F8BT, compared to those made from F8BT with <1 ppm Pd. This recombination yield decreases with decreasing Pd content, however, even at 36 ppm Pd 28% of the photogenerated excitons are quenched by Pd (Table 5.2). The extent of this recombination via Pd sites is perhaps surprising, suggesting that at least 54% of excitons are generated less than one exciton diffusion length away from a Pd centre in the case of unpurified F8BT, with exciton diffusion lengths for amorphous F8BT being reported on the order of 8 - 12 nm [13]. The differences in initial amplitudes in Figure 5.5a suggests that some of this recombination already occurs before the time-resolution of the instrument (∼200 ps for this TCSPC configuration). For instance, a comparison of initial signal amplitudes suggests that 23% excitons recombine via Pd at such fast times for unpurified F8BT.

While exciton quenching via Pd leads to recombination and thus a loss of photogenerated charges, exciton quenching via a sacrificial electron donor in solution produces long-lived electrons. Since the photocatalyst becomes reduced during the electron transfer reaction from the electron donor, this process is referred to as reductive quenching. Reductive quenching via an electron donor is how charge separation in such conjugated polymer photocatalysts is usually thought to occur, for

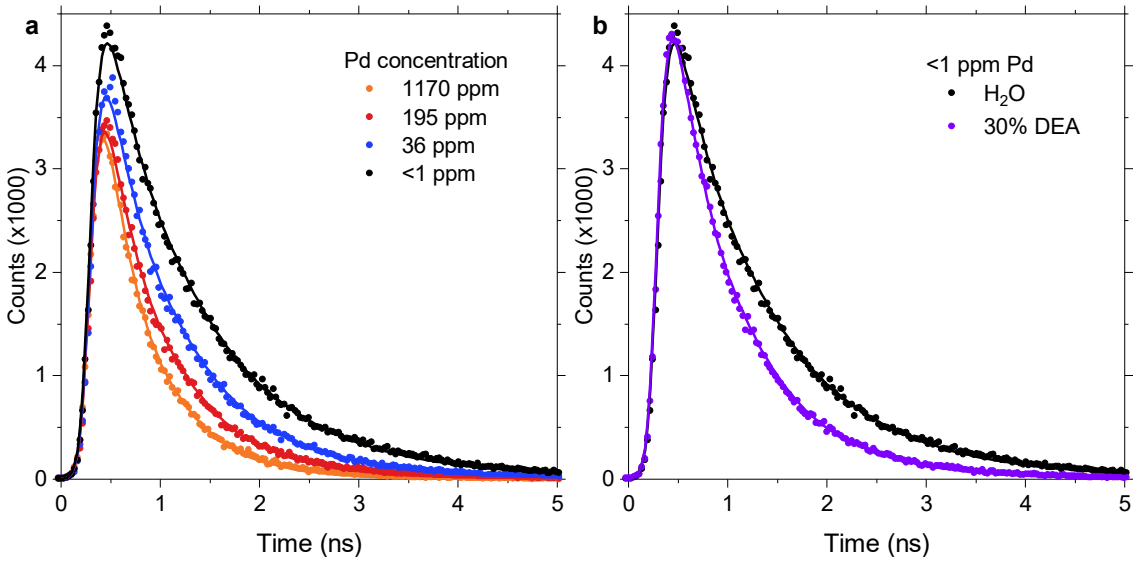

Figure 5.5: Photoluminescence decay kinetics of F8BT nanoparticle suspensions probed at 545 nm upon 467 nm excitation. (**a**) Nanoparticles with varying Pd content dispersed in H_2O, and (**b**) nanoparticles with <1 ppm Pd dispersed in H_2O and a 3:7 DEA/H_2O mixture. All samples were prepared with an absorbance of 0.10 at the excitation wavelength and emitted photons were counted over a time period of 10 s, which enables a quantitative comparison of signal amplitudes. The full lines represent fits to the data obtained using iterative reconvolution of the measured instrument response and a stretched exponential function $y \propto exp(-kt^b)$ with a constant stretching exponent $b = 0.87$. Fit parameters are summarised in Table 5.2.

example in the case of the polymer photocatalysts discussed in Chapter 4. Figure 5.5b compares the photoluminescence decays of F8BT with <1 ppm Pd in pure H_2O to those obtained in a 3:7 DEA/H_2O mixture. This comparison shows that the presence of DEA does accelerate the decay due to reductive quenching, but overall only quenches 24% of photogenerated excitons this way. In addition, the initial signal amplitude is not noticeably affected by the presence of DEA. This suggests that reductive quenching by DEA does not take place faster than ~200 ps, in contrast to recombination via Pd where a proportion of excitons is quenched already before this time. As the Pd concentration increases, kinetic differences between nanoparticles in H_2O and in DEA/H_2O become less and less pronounced (Figure B.1). In the case of unpurified F8BT, for instance, little additional exciton quenching is observed when DEA is present in the solution phase, which is consistent with recombination via Pd becoming more dominant as the number of Pd centres increases.

The photoluminescence decays can be fitted well using a stretched exponential function $y \propto exp(-kt^b)$ as represented by the full lines in Figure 5.5. Stretched exponential decay functions are common for disordered materials where disorder gives rise to a distribution of lifetimes [14, 15], rather than a single lifetime as in the case of a single exponential. Since the value of b

affects the unit of the rate constant k, the same b was used for all decays to ensure that k is comparable between samples. Herein, the stretching exponent was fixed to $b = 0.87$ for all traces, which is its average fitted value between samples. It should be noted that the resulting stretched exponential decay is not far from a single exponential decay where b would be equal to 1, suggesting that the degree of disorder in these nanoparticles is not excessive. Fits were performed using iterative reconvolution with the instrument response, meaning that the stretched exponential model function was convoluted with the measured instrument response for each iteration of the fit procedure. The obtained rate constants are summarised in Table 5.2, showing that the photoluminescence decay for unpurified F8BT ($k = 2.3\,\mathrm{ns}^{-0.87}$) is about twice as fast as for F8BT with <1 ppm Pd ($k = 1.2\,\mathrm{ns}^{-0.87}$). The presence of 30 vol.% DEA gives rise to a rate constant in between that of 36 ppm and 195 ppm in the absence of DEA.

Table 5.2: Comparison of exciton quenching in F8BT nanoparticles with varying Pd concentration in H_2O and with <1 ppm Pd in a 3:7 DEA/H_2O mixture. The exciton decay rate constant k is obtained from fits to a stretched exponential function $y \propto exp(-kt^b)$, where the stretching exponent $b = 0.87$ was fixed for all decays to enable comparison of k between samples. The overall quenching efficiency I_Q/I_0 is calculated by integrating the kinetic traces until 100 ns and comparing the integrated signal intensities in the presence of a quencher I_Q (with Pd or DEA as quenchers) to that of F8BT with <1 ppm Pd in H_2O, here referred to as I_0, assuming that no quenching takes place at this Pd concentration in pure H_2O.

Pd content (ppm)	Solvent	k ($ns^{-0.87}$)	I_Q/I_0
1170	H_2O	2.3	0.54
195	H_2O	1.8	0.44
36	H_2O	1.5	0.28
<1	H_2O	1.2	0
<1	3:7 DEA/H_2O	1.7	0.24

Overall, a change in the dominant exciton quenching pathway can be observed with an increase in Pd content: In the absence of Pd, reductive quenching via hole transfer to DEA in the solution phase takes place. In contrast, when the Pd content increases, exciton recombination via Pd centres embedded into the F8BT nanoparticles rapidly starts to dominate. Based on a consideration of overall quenching efficiencies, it can be concluded that this recombination via Pd in fact already dominates at 36 ppm Pd.

5.2.4 Charge localisation

Next, the influence of increasing Pd content on the reaction intermediates observed on the timescale relevant for hydrogen evolution, typically reported to occur on the millisecond to early second timescale after photoexcitation [16–18], is considered. Transient absorption spectra of F8BT nanoparticles with varying Pd content, dispersed in a 3:7 DEA/H_2O mixture and probed at 100 µs to 100 ms times, are shown in Figure 5.6. A pronounced change in spectral shape is observed as the Pd content of the polymer is lowered: While the transient spectrum of unpurified F8BT is dominated by an absorption feature that steadily increases from longer to shorter probe wavelengths, a gradual transformation to a peak centred around 700 – 750 nm takes place when the Pd content is reduced (Figure 5.6a towards Figure 5.6c). This change in spectral shape suggests that different photogenerated species are present in the extreme cases of high and no Pd content, and that a mixture of these two species is observed at intermediate Pd concentrations.

Similar to the arguments made in Subsection 4.2.2 in the previous chapter, the peak-like spectral shape is consistent with signatures of charged polymers [19–21], and is in reasonable agreement a report of the electron polaron absorption peak in F8BT films at 674 nm [22]. In contrast, the increasing absorption towards shorter probe wavelengths which dominates for unpurified F8BT (Figure 5.6a) is not commonly observed for organic polymers, suggesting that it might originate from charges on the metallic Pd. To test this hypothesis, Pd nanoparticles were deposited on a FTO-coated glass substrate by Anna A. Wilson and their optical response upon reduction was tested via spectroelectrochemical measurements (SEC) by Laia Francàs. As shown in Figure 5.7, increasingly negative potentials applied to this Pd nanoparticle film give rise to a spectral feature which looks very similar to the transient absorption observed for nanoparticles made from unpurified F8BT. Due to this close similarity, the spectral feature observed for unpurified F8BT is assigned to electrons localised on the Pd centres within these F8BT nanoparticles. This Pd electron feature becomes less and less pronounced when Pd is removed from the polymer, in good agreement with this assignment, while the F8BT electron polaron peak becomes more and more dominant.

The transient data shown above was recorded using F8BT nanoparticles with varying Pd concentration but with small differences in size (60 - 80 nm diameter) in order to reduce effects that might arise from differences in surface area when investigating the effect of Pd. In the following, a series of F8BT nanoparticles with much larger differences in size (42 - 189 nm) but

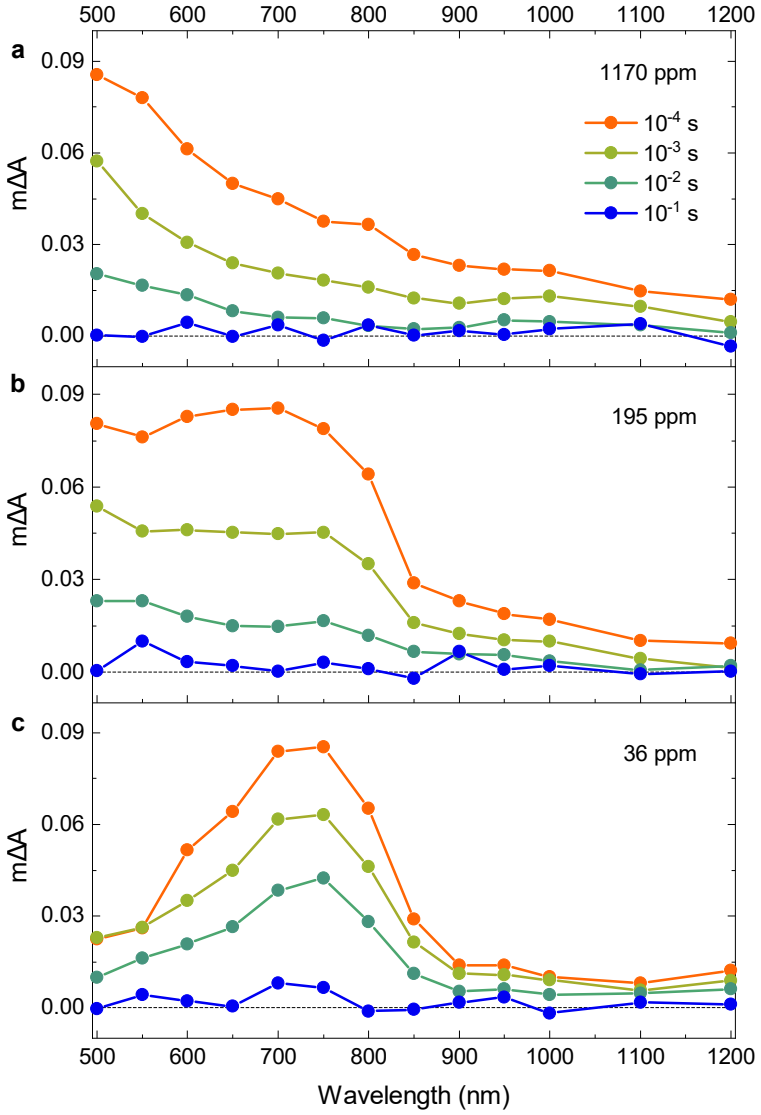

Figure 5.6: Transient absorption spectra recorded at 100 µs, 1 ms, 10 ms, and 100 ms for F8BT nanoparticles suspended in a 3:7 DEA/H_2O mixture with Pd contents of (**a**) 1170 ppm, (**b**) 195 ppm, and (**c**) 36 ppm. All spectra were obtained using an excitation wavelength of 460 nm and a fluence of 0.54 mJ cm^{-2}. The used nanoparticles suspensions were prepared with the same absorbance of 0.41 at the excitation wavelength.

the same Pd content (all unpurified) is studied. As shown in Figure 5.8a using data recorded by Jan Kosco, a pronounced increase in H_2 evolution rate is observed at particle sizes below ~100 nm, whereas activity differences for particles larger than this size are comparably small. TCSPC experiments on these nanoparticles with different sizes were carried out by Hyojung Cha and show a shorter photoluminescence lifetime for smaller particles (Figure B.2). This shorter lifetime suggests that the rate of recombination via Pd centres increases when particles become smaller, indicating a shorter average distance between photogenerated excitons and Pd centres, which might be due to a preferential localisation of Pd centres in the surface-near region of the

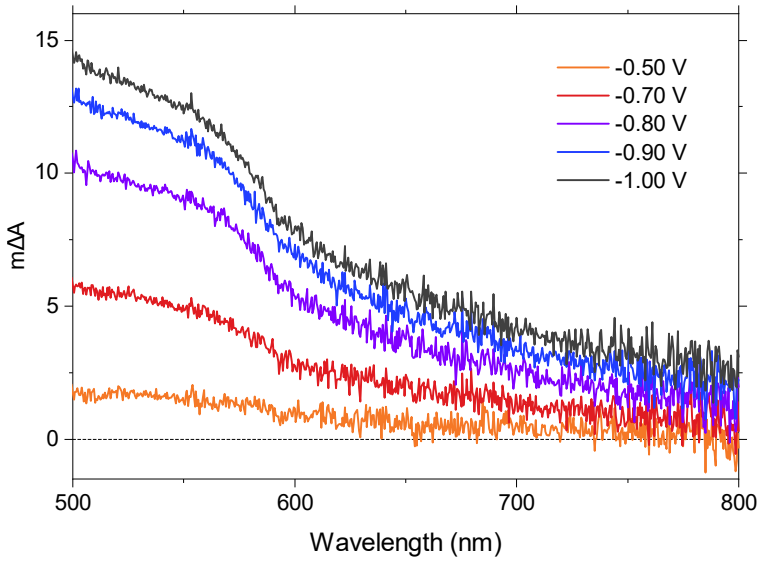

Figure 5.7: Absorption difference spectra between open circuit (−0.10 V vs. Ag/AgCl) and a series of applied potentials between −0.50 V and −1.00 V vs. Ag/AgCl for Pd nanoparticles deposited on an FTO-coated glass substrate.

polymer nanoparticles. As shown in Figure 5.8b, the signal amplitude observed in µs - s TAS measurements increases with decreasing particle size. As suggested above, the signal amplitude observed in TAS experiments on nanoparticles made from unpurified F8BT on this timescale is a direct measure of the electron population on Pd centres since the spectral contribution from polymer polarons is negligible. The larger population of Pd-centred electrons for smaller particles is in line with their higher hydrogen evolution performance. In addition, this larger yield of electrons on Pd centres is observed despite the pronounced Pd-induced exciton recombination described earlier, and indicates that Pd might be able to lower the recombination of separated electrons once the hole has been eliminated via reductive quenching.

5.2.5 Charge accumulation

Finally, these insights into the F8BT system are compared to the conjugated polymers poly(3-hexylthiophene-2,5-diyl) (P3HT) and the dibenzo[*b,d*]thiophene sulfone homopolymer P10. P3HT (95% regioregular) nanoparticles with 40 nm diameter exhibit an about 20-fold lower activity than unpurified F8BT in the presence of 5 wt.% photodeposited Pt (Figure B.3). These P3HT nanoparticles contain residual Ni but no residual Pd as they were synthesized via Grignard metathesis polymerization, and are investigated in the absence of photodeposited Pt in the charge accumulation experiment herein. P10 is synthesized via Suzuki coupling just like F8BT and thus contains residual Pd (0.40 wt.% for P10 as detailed in Subsection 4.2.1, corresponding

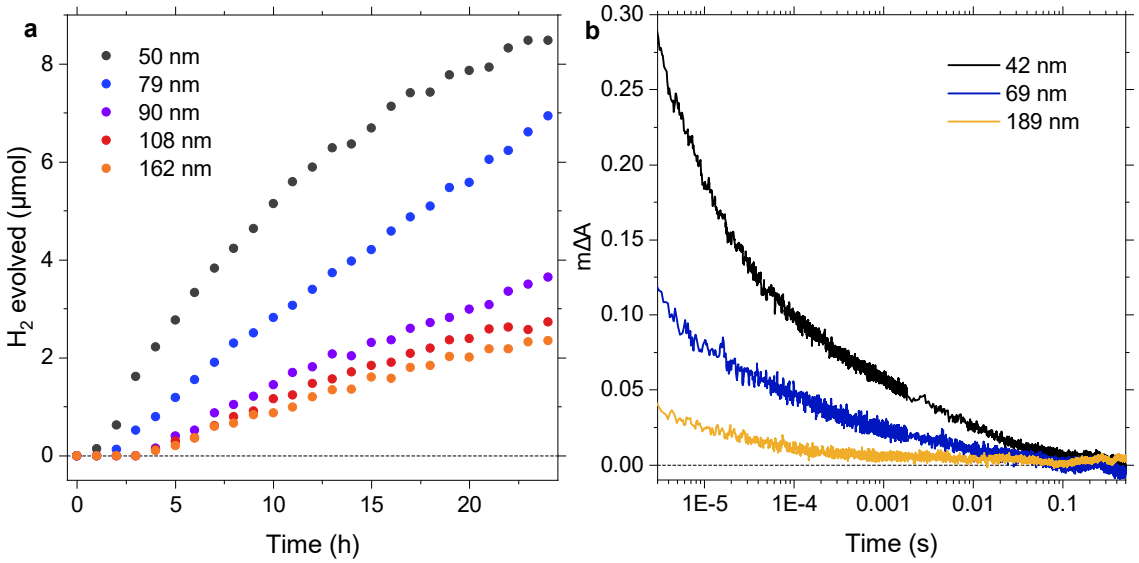

Figure 5.8: Effects of varying particle size for F8BT nanoparticles with diameters from 42 - 189 nm, all made from unpurified F8BT. (**a**) Photocatalytic hydrogen evolution over a period of 24 h in a 3:7 DEA/H_2O mixture, and (**b**) transient absorption decay kinetics following 460 nm excitation in the same solvent mixture, probed at 750 nm in order to avoid the photoluminescence artefacts present at µs times for shorter probe wavelengths. A fluence of 0.54 mJ cm^{-2} was used and all suspensions were prepared with an absorbance of 0.41 at the excitation wavelength.

to 4000 ppm, vs. 1170 ppm for unpurified F8BT). This comparison is carried out using Photoinduced Absorption Spectroscopy (PIAS), where light pulses of several seconds duration lead to an accumulation of photogenerated charge carriers in a quasi-steady state, thus simulating the constant illumination conditions of actual hydrogen evolution experiments. This accumulation occurs before the rate limiting step, i.e. the slowest step of the photocatalytic reaction.

Figure 5.9 shows the PIAS spectra obtained upon illumination of unpurified F8BT, P3HT, and P10 in the presence of an electron donor, corresponding to the absorption of photogenerated charges that accumulate before the rate determining step. The PIAS spectrum of unpurified F8BT (Figure 5.9a) closely resembles its transient spectrum (Figure 5.6a), suggesting that the photogenerated electrons which are observed on Pd centres transiently also accumulate on these Pd centres under constant illumination. In contrast, the PIAS spectrum of P3HT is characterised by a narrow peak around 650 nm and a second absorption feature which rises towards the NIR (Figure 5.9b), consistent with general absorption features of polymer polarons as detailed above. This accumulation of charges on the polymer, generated by reductive quenching via the electron donor in the solution phase, is in line with the absence of residual Pd in these P3HT nanoparticles. The PIAS spectrum for P10 exhibits a clear and intense peak around ~630 nm (Figure 5.9c) and is virtually identical to its transient spectrum shown in Chapter 4 where it has

been assigned to electron polarons on µs - s timescales after excitation. This result demonstrates that photogenerated electrons accumulate on Pd centres in F8BT but on the polymer in P10 particles, although the residual Pd content of P10 is even higher than that of unpurified F8BT.

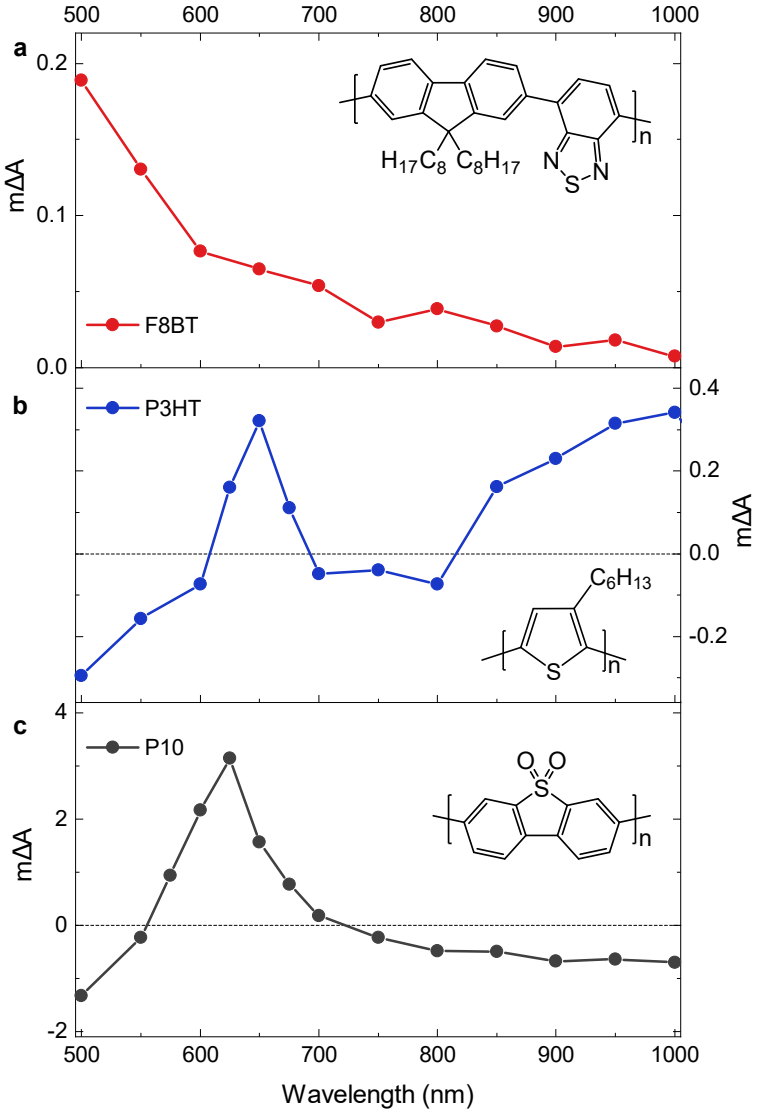

Figure 5.9: Photoinduced absorption spectra of nanoparticle suspensions recorded upon illumination with light pulses of several seconds duration for (**a**) unpurified F8BT (1170 ppm Pd, corresponding to 0.117 wt. %) in a 3:7 DEA/H_2O mixture, (**b**) P3HT (no Pd) in a 1:1:1 H_2O/MeOH/TEA mixture, and (**c**) P10 (0.40 wt. % Pd) in a 1:1:1 H_2O/MeOH/TEA mixture. Further experimental conditions: F8BT: 465 nm excitation, 25.6 mW cm^{-2} fluence, 10 mm path length cuvette; P3HT: 365 nm excitation, 7.1 mW cm^{-2} fluence, 10 mm path length cuvette; P10: 365 nm excitation, 5.5 mW cm^{-2} fluence, 2 mm path length cuvette.

5.3 Discussion

Residual metal impurities, which are incorporated in essentially all polymer photocatalysts that are synthesised via metal-catalysed polymerisation reactions, have been suggested to act as catalytically active sites. However, the insolubility of most reported polymer photocatalysts in common solvents has so far prevented the complete removal of such impurities from these materials in order to determine their how relevant they are for catalysis. By subjecting the solution processable polymer F8BT to a series of purification steps before processing it into nanoparticles, it has been shown that the hydrogen evolution activity of this polymer strongly depends on its residual Pd content for Pd concentrations below ∼100 ppm [6]. Above this threshold concentration, the hydrogen evolution approaches an activity plateau, in qualitative agreement with a study on bipyridyl-based polymers [23]. This threshold palladium content of 100 ppm (corresponding to 0.01 wt. %) is considerably lower than the residual Pd content of most polymer photocatalysts synthesised via Pd-based catalysed routes, which typically fall into the 0.05 - 1 wt. % range [23–29]. Although this threshold concentration might vary between polymers, the fact that an activity plateau is reached at very low Pd concentrations seems to explain why many studies report performances that are relatively independent of Pd content, for instance when even more metal is added. Due to this pronounced Pd effect, these F8BT nanoparticles present an ideal model system to investigate how Pd affects the excited state of a conjugated polymer photocatalyst.

Photoluminescence lifetime measurements demonstrate that Pd promotes non-radiative exciton recombination. All observed photoluminescence decay kinetics are described well by stretched exponential functions, which is common for disordered semiconductors and implies that the diffusion of photogenerated excitons to Pd centres is affected by defects in the material. In unpurified F8BT, at least 54% of the photogenerated excitons are quenched by Pd, which can be considered a lower limit as it is determined relative to the <1 ppm sample and assumes that no exciton quenching takes place at this Pd concentration. The exciton decay in unpurified F8BT is about twice as fast as in F8BT nanoparticles with <1 ppm Pd based on a comparison of the rate constants obtained from the stretched exponential fits. This pronounced exciton recombination via residual Pd centres has further implications for other fields that rely on conjugated polymers: For instance, in organic light-emitting diodes (OLEDs), the combination of injected charges to excitons which then recombine radiatively might be affected by the presence

of the non-radiative recombination pathway induced by such Pd centres. In organic photovoltaics (OPVs), the interface between a donor and an acceptor material is used to separate photogenerated excitons, effectively similar to the interface between an electron donor such as DEA and a polymer photocatalyst. Although domain sizes in OPVs are typically smaller than the nanoparticles investigated herein, residual Pd might lead to a loss of photogenerated excitons in neat polymer domains.

The exciton decay in the presence of 30% DEA in the solution phase is found to be roughly comparable to the presence of only 36 ppm Pd within the F8BT nanoparticle, both in terms of overall quenching an in terms of the rate constant of its decay. This might be related to the fact that exciton quenching via Pd can occur in the bulk of an F8BT particle, whereas reductive quenching via DEA only occurs at its surface. In this way, the distance a photogenerated exciton has to cover to reach a Pd centre is on average shorter than the distance it has to travel to encounter a DEA molecule, which explains why exciton quenching via Pd rapidly starts to dominate when the Pd content increases.

TAS experiments on the µs - s timescale show that the spectral signature of long-lived photogenerated electrons gradually changes when Pd is removed from the F8BT polymer, which is assigned to a shift in their predominant location from Pd centres within the polymer nanoparticles at high Pd content to the polymer itself at very low Pd content. This assignment is in line with the presence of different numbers of Pd centres in F8BT samples of different purification levels, which can be accessed by long-lived electrons. To compare the electron populations produced at high and low Pd content, knowledge of the relative attenuation coefficients of electrons on F8BT and on Pd would be desirable. The attenuation coefficient of electrons on F8BT at their peak absorption in the visible range is $(30\,000 \pm 3000)\,\mathrm{M^{-1}\,cm^{-1}}$ [22], but that of Pd-centred electrons has not yet been reported. However, the attenuation coefficient of electrons on an inorganic material such as Pd can be expected to be lower than for the organic F8BT, which, given the similar signal amplitudes in Figure 5.6, would imply a higher electron yield for F8BT nanoparticles with higher Pd content. This higher charge yield would then occur despite the loss of photogenerated excitons via Pd at early times, and would thus suggest that the localisation of long-lived electrons on Pd might reduce their tendency to recombine.

When comparing nanoparticles with different sizes made from unpurified F8BT in the absence of an electron donor, a gradual decrease in photoluminescence lifetime is observed when particles become smaller. This decreasing lifetime suggests that more excitons are able to find Pd

centres in smaller particles, and might indicate that Pd centres are preferentially located in the surface-near region of these F8BT nanoparticles which would make the faster exciton quenching compared to DEA even more striking.

Finally, the charge accumulation in nanoparticles made from unpurified F8BT (1170 ppm Pd) under constant illumination in PIAS is compared to P3HT (no Pd) and the much more active P10 (4000 ppm Pd) introduced in Chapter 4. For F8BT, electrons accumulate on the Pd centres within the nanoparticles, which appears reasonable given that they reside on these Pd centres even transiently when probed by TAS on the µs - s TAS measurements timescale. Photogenerated electrons in P3HT, generated via reductive quenching using the electron donor triethylamine (TEA), reside on the polymer in line with the absence of Pd centres in this polymer. These P3HT nanoparticles are inactive without photodeposited Pt (which was not present in the studied sample), suggesting that the observed accumulated electrons are not able to reduce protons in the absence of a co-catalyst. In P10, which is insoluble in common solvents and thus contains hard to remove Pd, the PIAS spectrum is essentially identical to the transient spectrum obtained from these suspensions and thus demonstrates that electrons accumulate on the polymer despite the high Pd content of this material. Given the dominant character of charge localisation on Pd centres in F8BT at such high Pd content, this behaviour seems rather surprising but has implications for the rate limiting step in the hydrogen evolution reaction for both materials: For unpurified F8BT, electrons already reside on Pd centres before the timescale of hydrogen evolution, typically thought to occur on millisecond to early second timescales [16–18], which means that the overall reaction is likely limited by the fact that the hydrogen evolution reaction is kinetically slow. Since no accumulation on Pd is observed for P10, the diffusion of photogenerated electrons to Pd centres appears to be the rate limiting step.

This difference between F8BT and P10 might be related to the electron mobility of the respective polymer, as studies using films of small molecule semiconductors [30, 31] and conjugated polymers [32] have demonstrated that the use of monomers with large dipole moments can lead to a significant reduction in charge carrier mobility. Due to the large 5.7 D dipole moment of the dibenzo[*b,d*]thiophene sulfone unit (Subsection 4.2.5), a rather low electron mobility might therefore be expected for P10, especially once it is surrounded by polar H_2O molecules. Although an accurate comparison of the mobility of polyfluorenes is challenging due to large mobility variations between different preparation conditions [33], the likely low mobility of P10 could prolong the time it takes for photogenerated electrons to find a Pd centre. The fast generation of electron polarons (or at least their precursor) with a half-rise time of only 1.6 ps, as discussed in

Subsection 4.2.2, would then be key for efficient charge separation. Different Pd distributions within the respective polymer are also a possibility given the different Pd catalysts used for the polymerisation reaction ($Pd_2(dba)_3$ for F8BT, $Pd(PPh_3)_4$ for P10) and the different reaction conditions (1 d at 110 °C for F8BT, 2 d at 150 °C for P10).

5.4 Conclusions

The hydrogen evolution activity of F8BT nanoparticles strongly depends on their residual Pd content below ∼100 ppm Pd, whereas an activity plateau is approached above this threshold concentration. In concentrations that are typical for polymers prepared via Pd-catalysed coupling reactions (>1000 ppm or >0.1 wt.%), photogenerated excitons in F8BT predominantly recombine via Pd centres. Depending on the Pd content, such exciton quenching via Pd is found to occur up to two times faster than reductive quenching via the electron donor DEA in the solution phase. Therefore, reductive quenching via DEA only dominates at very low Pd content, but at such low Pd content there is only a limited number of catalytic Pd sites which ultimately limits activity. As a result, the long-lived electrons produced by reductive quenching are located on the F8BT polymer at very low Pd content, but quickly become located on Pd centres within the polymer nanoparticles as the Pd content increases. Under constant illumination, long-lived electrons accumulate on Pd centres in unpurified F8BT, suggesting that the kinetically slow hydrogen evolution is the rate limiting step for this material. In contrast, photogenerated electrons in the more efficient P10 accumulate on the polymer itself and do so in higher yields, which suggests that Pd-mediated exciton recombination is less pronounced than in F8BT and indicates that hydrogen evolution in P10 is instead limited by electron diffusion to Pd centres. These results demonstrate that residual Pd acts as a co-catalyst for hydrogen evolution but also affects the number of excitons available for reductive quenching by promoting fast exciton recombination. To avoid these Pd-induced recombination losses, the Pd content of the polymer needs to be low and/or reductive quenching via a suitable electron donor needs to be fast. The pronounced exciton quenching at common Pd concentrations likely has further implications for fields unrelated to catalysis such as organic light-emitting diodes and organic photovoltaics.

5.5 Materials and methods

Preparation of F8BT nanoparticles

F8BT (Mn = 39.6 kD, Mw = 84.4 kD, PDI = 2.13) was synthesized, purified, and processed into nanoparticles as described previously [6]. Nanoparticles were formed using the reprecipitation process, and gradually reducing the volume of water used for reprecipitation from 40 mL to 1 mL increased the Z average nanoparticle diameter from (40 ± 10) nm to (120 ± 10) nm. In brief, F8BT was synthesised using tris(dibenzylideneacetone) dipalladium(0) ($Pd_2(dba)_3$) catalysed Suzuki polymerisation [5] and then subjected to Soxhlet extraction with methanol, acetone, and hexane for 24 h each. The resulting polymer is referred to as unpurified F8BT herein. The obtained polymer was then purified further using Gel Permeation Chromatography (GPC) and washing with sodium diethyldithiocarbamate (DTC) to produce batches with different Pd content and processed into nanoparticles as detailed in Subsection 5.2.1.

Preparation of P3HT nanoparticles

P3HT (Mn = 98 kD, Mw = 136 kD, PDI = 1.39) was synthesized via Grignard metathesis (GRIM) polymerization following a previously reported procedure [34]. Nanoparticles of P3HT were formed using the reprecipitation process, like in the case of F8BT. In a typical preparation, a solution of P3HT (0.50 mg mL^{-1}) and polystyrene-co-maleic anhydride (0.10 mg mL^{-1}) in tetrahydrofuran (5 mL) was filtered (0.2 µm PTFE syringe filter), then rapidly injected into MilliQ water (40 mL) under sonication in an ultrasonic bath. The mixture was sonicated for a further 2 min, and then heated in an oil bath at 80 °C under constant nitrogen bubbling to remove the THF and concentrate the solution to 10 mL. Finally, the concentrated solution was filtered (0.45 µm glass fibre syringe filter) to remove large agglomerates.

P10 synthesis

P10 was synthesised via tetrakis(triphenylphosphine)palladium(0) ($Pd(PPh_3)_4$) catalysed Suzuki-Miyaura polycondensation as detailed in reference [35].

Sample preparation for spectroscopy

F8BT and P3HT nanoparticles were obtained and stored as aqueous dispersions. These dispersions were found to be stable for several months without any settling, which is likely due to the small and uniform sizes of the suspended nanoparticles and the fact they incorporate poly(styrene-*co*-maleic anhydride) (PSMA) as a stabiliser. For the spectroscopic measurements,

these stock suspensions were diluted with water or a scavenger/water mixture to obtain nanoparticle suspensions with the indicated absorbances. Cuvettes with 10 mm x 10 mm were used for F8BT and P3HT samples, partially in order to produce transient absorption and PIAS signals with meaningful amplitudes using the given nanoparticle suspensions.

P10 suspensions were prepared as described in Section 4.5. P10 suspensions were considerably less stable than those of F8BT and P3HT and started to settle after a few hours likely due to the larger particle size, but were stable on the seconds timescale of the PIAS experiments. The much higher PIAS amplitudes compared to the other two polymers allowed the use of smaller cuvettes with 2 mm path length, which also seemed to enhance the stability of the dispersion.

5.6 References

1. Yang, J., Wang, D., Han, H. & Li, C. Roles of Cocatalysts in Photocatalysis and Photoelectrocatalysis. *Accounts of Chemical Research* **46,** 1900–1909 (2013).
2. Savateev, A. & Antonietti, M. Heterogeneous Organocatalysis for Photoredox Chemistry. *ACS Catalysis* **8,** 9790–9808 (2018).
3. Ye, S., Wang, R., Wu, M.-Z. & Yuan, Y.-P. A review on g-C3N4 for photocatalytic water splitting and CO2 reduction. *Applied Surface Science* **358,** 15–27 (2015).
4. Pati, P. B. *et al.* An experimental and theoretical study of an efficient polymer nanophotocatalyst for hydrogen evolution. *Energy Environ. Sci.* **10,** 1372–1376 (2017).
5. Zhang, W. *et al.* Systematic Improvement in Charge Carrier Mobility of Air Stable Triarylamine Copolymers. *Journal of the American Chemical Society* **131,** 10814–10815 (2009).
6. Kosco, J. *et al.* The Effect of Residual Palladium Catalyst Contamination on the Photocatalytic Hydrogen Evolution Activity of Conjugated Polymers. *Advanced Energy Materials* **8,** 1802181 (2018).
7. Donley, C. L. *et al.* Effects of Packing Structure on the Optoelectronic and Charge Transport Properties in Poly(9,9-di- n -octylfluorene- alt -benzothiadiazole). *Journal of the American Chemical Society* **127,** 12890–12899 (2005).
8. Ohkita, H. Charge generation dynamics in polymer/polymer solar cells studied by transient absorption spectroscopy. *Journal of Photonics for Energy* **1,** 011118 (2011).

9. Wu, K., Li, Q., Du, Y., Chen, Z. & Lian, T. Ultrafast exciton quenching by energy and electron transfer in colloidal CdSe nanosheet–Pt heterostructures. *Chemical Science* **6,** 1049–1054 (2015).

10. Li, Q. & Lian, T. Exciton dissociation dynamics and light-driven H2 generation in colloidal 2D cadmium chalcogenide nanoplatelet heterostructures. *Nano Research* **11,** 3031–3049 (2018).

11. Wu, K., Zhu, H., Liu, Z., Rodríguez-Córdoba, W. & Lian, T. Ultrafast Charge Separation and Long-Lived Charge Separated State in Photocatalytic CdS–Pt Nanorod Heterostructures. *Journal of the American Chemical Society* **134,** 10337–10340 (2012).

12. Wu, K., Zhu, H. & Lian, T. Ultrafast Exciton Dynamics and Light-Driven H 2 Evolution in Colloidal Semiconductor Nanorods and Pt-Tipped Nanorods. *Accounts of Chemical Research* **48,** 851–859 (2015).

13. Mikhnenko, O. V., Blom, P. W. M. & Nguyen, T.-Q. Exciton diffusion in organic semiconductors. *Energy & Environmental Science* **8,** 1867–1888 (2015).

14. Regan, K. P., Koenigsmann, C., Sheehan, S. W., Konezny, S. J. & Schmuttenmaer, C. A. Size-Dependent Ultrafast Charge Carrier Dynamics of WO 3 for Photoelectrochemical Cells. *The Journal of Physical Chemistry C* **120,** 14926–14933 (2016).

15. Soloviev, V. N., Eichhöfer, A., Fenske, D. & Banin, U. Size-Dependent Optical Spectroscopy of a Homologous Series of CdSe Cluster Molecules. *Journal of the American Chemical Society* **123,** 2354–2364 (2001).

16. Reynal, A., Lakadamyali, F., Gross, M. A., Reisner, E. & Durrant, J. R. Parameters affecting electron transfer dynamics from semiconductors to molecular catalysts for the photochemical reduction of protons. *Energy & Environmental Science* **6,** 3291 (2013).

17. Rodenberg, A. *et al.* Mechanism of Photocatalytic Hydrogen Generation by a Polypyridyl-Based Cobalt Catalyst in Aqueous Solution. *Inorganic Chemistry* **54,** 646–657 (2015).

18. Pastor, E. *et al.* Spectroelectrochemical analysis of the mechanism of (photo)electrochemical hydrogen evolution at a catalytic interface. *Nature Communications* **8,** 14280 (2017).

19. Österbacka, R., An, C. P., Jiang, X. M. & Vardeny, Z. V. Two-Dimensional Electronic Excitations in Self-Assembled Conjugated Polymer Nanocrystals. *Science* **287,** 839–842 (2000).

20. Baniya, S., Vardeny, S. R., Lafalce, E., Peygambarian, N. & Vardeny, Z. V. Amplitude-Mode Spectroscopy of Charge Excitations in PTB7 π-Conjugated Donor-Acceptor Copolymer for Photovoltaic Applications. *Physical Review Applied* **7,** 064031 (2017).

21. Fesser, K., Bishop, A. R. & Campbell, D. K. Optical absorption from polarons in a model of polyacetylene. *Physical Review B* **27,** 4804–4825 (1983).

22. Bird, M. J., Bakalis, J., Asaoka, S., Sirringhaus, H. & Miller, J. R. Fast Holes, Slow Electrons, and Medium Control of Polaron Size and Mobility in the DA Polymer F8BT. *The Journal of Physical Chemistry C* **121,** 15597–15609 (2017).

23. Li, L. *et al.* Rational Design of Porous Conjugated Polymers and Roles of Residual Palladium for Photocatalytic Hydrogen Production. *Journal of the American Chemical Society* **138,** 7681–7686 (2016).

24. Kochergin, Y. S. *et al.* Exploring the "Goldilocks Zone" of Semiconducting Polymer Photocatalysts by Donor-Acceptor Interactions. *Angewandte Chemie International Edition* **57,** 14188–14192 (2018).

25. Lan, Z.-A., Ren, W., Chen, X., Zhang, Y. & Wang, X. Conjugated donor-acceptor polymer photocatalysts with electron-output "tentacles" for efficient hydrogen evolution. *Applied Catalysis B: Environmental* **245,** 596–603 (2019).

26. Aitchison, C. M., Sprick, R. S. & Cooper, A. I. Emulsion polymerization derived organic photocatalysts for improved light-driven hydrogen evolution. *Journal of Materials Chemistry A,* 37–39 (2019).

27. Sprick, R. S. *et al.* Tunable Organic Photocatalysts for Visible-Light-Driven Hydrogen Evolution. *Journal of the American Chemical Society* **137,** 3265–3270 (2015).

28. Wang, Z. *et al.* Dibenzothiophene Dioxide Based Conjugated Microporous Polymers for Visible-Light-Driven Hydrogen Production. *ACS Catalysis* **8,** 8590–8596 (2018).

29. Dai, C. *et al.* Dibenzothiophene- S , S -Dioxide-Based Conjugated Polymers: Highly Efficient Photocatalyts for Hydrogen Production from Water under Visible Light. *Small* **14,** 1801839 (2018).

30. Friederich, P. *et al.* Molecular Origin of the Charge Carrier Mobility in Small Molecule Organic Semiconductors. *Advanced Functional Materials* **26,** 5757–5763 (2016).

31. Friederich, P. *et al.* Rational In Silico Design of an Organic Semiconductor with Improved Electron Mobility. *Advanced Materials* **29,** 1703505 (2017).

32. Borsenberger, P. M. & Bässler, H. Concerning the role of dipolar disorder on charge transport in molecularly doped polymers. *The Journal of Chemical Physics* **95,** 5327–5331 (1991).

33. Kreouzis, T., Bradley, D. D. C. & Campbell, A. J. *Hole and electron transport in poly(9,9-dioctylfluorene) and poly (9,9-dioctylfluorene- co -benzothiadiazole)* in *Organic Light-Emitting Materials and Devices VII* (eds Kafafi, Z. H. & Lane, P. A.) **5214** (2004), 141.

34. Loewe, R. S., Ewbank, P. C., Liu, J., Zhai, L. & McCullough, R. D. Regioregular, head-to-tail coupled poly(3-alkylthiophenes) made easy by the GRIM method: Investigation of the reaction and the origin of regioselectivity. *Macromolecules* **34,** 4324–4333 (2001).

35. Sachs, M. *et al.* Understanding structure-activity relationships in linear polymer photocatalysts for hydrogen evolution. *Nature Communications* **9,** 4968 (2018).

Chapter 6

Effect of oxygen deficiency on the excited state kinetics of WO_3

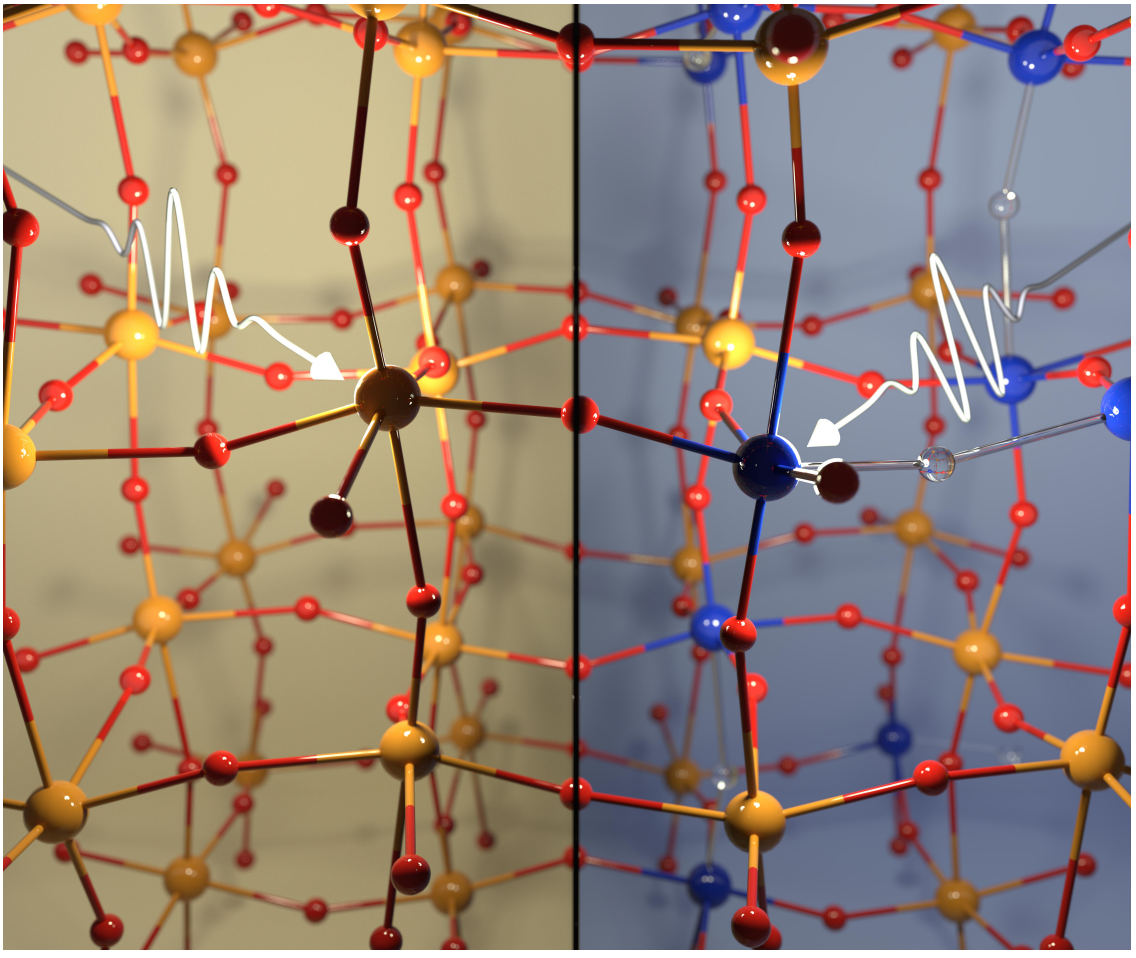

Figure 6.1: Graphical abstract for Chapter 6.

Oxygen vacancies are the primary defects in many metal oxides, and the deliberate use of oxygen sub-stoichiometry has become a popular tool to enhance the often poor visible light absorption of semiconducting metal oxides. Although oxygen vacancies are common point defects in metal oxides even when not introduced deliberately, their impact on the behaviour of photogenerated charges, and ultimately on catalysis, has so far remained unexplored. In this chapter, WO_3 is used as a model material to investigate how the excited state dynamics of metal oxides are affected by large differences in oxygen vacancy concentration. For WO_3 films characterised by a high oxygen vacancy density, an over 2 eV broad distribution of defect states is observed within the bandgap which gives rise to pronounced visible light absorption and a strong blue colouration in this otherwise pale yellow material. First principles defect calculations support this observation and suggest that oxygen vacancies aggregate to defect clusters at such high degrees of oxygen deficiency. Transient absorption experiments show that photogenerated holes trap within 200 fs into the high density of defect states situated in the bandgap, which leads to an increase in their lifetime but lowers their oxidative driving force. This loss in driving force lowers the efficiency of kinetically challenging reactions such as water oxidation for metal oxides with significant degrees of oxygen deficiency, while the concomitant increase in lifetime might enhance the efficiency of oxidations that require lower driving force such as pollutant degradation. These results emphasize that the defect state distribution of a photocatalyst needs to be tuned for a desired target reaction in order to optimise its performance.

The results presented in this chapter are in part included in this publication:

Michael Sachs, Ji-Sang Park, Ernest Pastor, Andreas Kafizas, Anna A. Wilson, Laia Francàs, Sheraz Gul, Min Ling, Chris Blackman, Junko Yano, Aron Walsh & James R. Durrant. Effect of oxygen deficiency on the excited state kinetics of WO_3 and implications for photocatalysis. *Chemical Science* **10**, 5667 (2019).

The following results shown in this chapter have been contributed by collaborators:
Ji-Sang Park carried out the DFT calculations, Ernest Pastor carried out the XANES and EXAFS experiments, Andreas Kafizas performed the XRD and Hall effect measurements, and Anna A. Wilson carried out the IPCE measurements. The SEM images were acquired together with Andreas Kafizas.

6.1 Introduction

Although metal oxides are the most commonly used photocatalyst materials for solar-driven water splitting, their often poor visible light absorption fundamentally limits their activity. Many metal oxides have large bandgaps and are thus only able to absorb high-energy UV light which accounts for less than 5% of the overall solar irradiance [1]. Yet, achieving efficient absorption over the visible part of the solar spectrum is the primary challenge in the search for inorganic systems with economically attractive efficiencies [2]. In contrast to their stoichiometric analogues, sub-stoichiometric metal oxides often exhibit strong visible light absorption, and strategies such as the deliberate creation of oxygen vacancies are thus explored in attempts to overcome this limitation [3]. Numerous studies have explored this possibility and showed improved light absorption as well as enhanced photocatalytic activities for metal oxides with moderate oxygen deficiency such as TiO_2 [4–11], WO_3 [12–14], ZnO [1, 15, 16], and SnO_2 [17]. At higher oxygen deficiency, however, the photocatalytic activity of materials modified in this way is typically found to decrease despite their concomitantly increasing ability to absorb more visible light. Therefore, a closer investigation of the behaviour of photogenerated charges in the presence of different degrees of oxygen deficiency in such materials is required to evaluate the practicability of creating oxygen vacancies in attempts to improve the photocatalytic activity of a metal oxide - particularly as only few studies discuss the impact of oxygen vacancies on observed charge carrier dynamics. To address these questions, the photoinduced processes upon irradiation of UV, visible, and NIR light are compared for near-stoichiometric and highly oxygen-deficient WO_3 films in this chapter.

WO_3 is a widely used n-type metal oxide in the field of photocatalysis and in solar water splitting devices [18, 19]. It is one of few metal oxides which are stable in acidic media [20], exhibits good charge carrier transport [20–22], and has been reported to feature particularly fast water oxidation kinetics [23]. WO_3 can adopt a variety of different polymorphs, all of which consist of a network of corner-sharing WO_6 octahedra [24, 25]. In its most regular form, this arrangement results in a cubic crystal structure, which has computationally been found to be the most unstable configuration among all WO_3 polymorphs [25]. Stabilisation can be achieved via Jahn-Teller distortion of these WO_6 octahedra, which gives rise to a set of polymorphs with triclinic, monoclinic, orthorhombic, and tetragonal crystal structures. The degree of distortion is temperature dependent and phase transitions can thus be induced through heating [25, 26].

WO_3 was chosen as a model system for this study because it tends to adopt substoichiometric compositions more readily than other metal oxides. Sub-stoichiometry is achieved through the release of oxygen from the crystal lattice, causing the oxide to become reduced [27, 28]. When oxygen vacancy sites are created, the bonding environment is altered with respect to that of the periodic crystal lattice. The new bonding situation results in a modified splitting between bonding and antibonding orbitals and therefore gives rise to states at different energy levels, e.g. within the band gap of the metal oxide [29] as described in Subsection 2.1.1. For each removed oxygen atom, two electrons are donated into the lattice and localise at the created vacancy sites, reducing two W^{VI} centres to W^{V} [30, 31]. These W^{V} centres may be situated in the vicinity of the oxygen vacancy (herein referred to as W^{V}_{ov}) or further away in the stoichiometric crystal that gives rise to conduction band states (herein referred to as W^{V}_{cb}). Due to the formation of these W^{V} centres, the creation of oxygen vacancies not only increases the doping level of the material but also modifies the optical properties of the semiconductor. The transition from a sub-bandgap state to a conduction band state (i.e. from W^{V}_{ov} to W^{VI}_{cb}) gives rise to visible light absorption, which causes a distinct blue colouration in the case of WO_3 [32]. The number of W^{V} centres and thus the colouration intensity can be modified in a number of different ways such as electrochemical, photochemical, and thermal stimuli [32, 33], which makes WO_3 one of the leading materials for electrochromic applications.

As a result of this popularity in the field of electrochromism, the mechanism of the blue colouration in WO_3 has been subject to a number of studies. In the most widely accepted colouration model, an electron on a tungsten centre perturbs its surrounding crystal lattice due to a sufficiently strong electron-phonon interaction and therefore becomes localised on that tungsten centre. The resulting cluster is referred to as a W^{V} polaron, which can be described as an electron at the bottom of a parabolic potential well centred on a given tungsten site [27, 34]. Given a certain overlap between adjacent potential wells, this electron can then be excited into the potential well on a neighbouring tungsten site through visible light irradiation, which causes the two involved tungsten centres to swap oxidation states in a process that is often referred to as an intervalence charge transfer. In this way, the W^{V} polaron hopping between neighbouring tungsten sites leads to visible light absorption and, depending on the number of polarons, blue colouration may be observed. The activation energy for this polaron hopping has been estimated to be at least 0.1 - 0.2 eV [35, 36], corresponding to the occupied W^{V}_{ov} states closest to the conduction band.

With this colouration mechanism in mind, the excited state dynamics of WO_3 are investigated

as a function of oxygen deficiency in this chapter. To this end, the temporal evolution of photogenerated carriers is monitored via transient absorption spectroscopy (TAS) in two types of films: (i) regular monoclinic WO_3 (m-WO_3), and (ii) highly oxygen-deficient, blue WO_3 (b-WO_3). WO_3 is particularly suitable for this study, also due to existing knowledge about the interplay between reduced tungsten centres in the process of visible light absorption as described above. This knowledge about the process of visible light absorption in this material facilitates assignments of TAS signals to explicit chemical species, which are typically challenging for metal oxides. Of particular interest is a comparison of the carrier dynamics observed upon bandgap excitation using UV light to those resulting from sub-bandgap excitation using visible/NIR light. It will be shown that the overall charge lifetime is significantly longer in the highly oxygen-deficient b-WO_3 than it is in m-WO_3, owing to rapid trapping of photogenerated holes into sub-bandgap oxygen vacancy states. However, because this trapping process corresponds to an energetic relaxation, it also compromises the efficiency of reactions that require high oxidative driving force.

6.2 Results

6.2.1 Light absorption and charge reactivity

Both types of WO_3 thin films investigated herein exhibit a nano-needle structure as evidenced by the scanning electron microscopy (SEM) images shown in Figure 6.2. These nano-needles are relatively sharp in the case of b-WO_3 and form a film with ∼200 nm thickness. When the highly oxygen-deficient b-WO_3 is converted to near-stoichiometric m-WO_3 via annealing, these needles broaden and partially fuse together, also leading to a reduced film thickness of ∼150 nm. X-ray diffraction experiments (Figure C.1) suggest monoclinic structures for both types of films, which is common for WO_3 at room temperature [12, 21, 37]. For b-WO_3, two distinct peaks are found, which have previously been attributed to the (010) and (020) reflections of the monoclinic $W_{17}O_{47}$ ($WO_{2.77}$) structure with a [010] growth direction [38].

m-WO_3 and b-WO_3 films exhibit a striking difference in colour, which is evident from their distinct optical properties shown in Figure 6.3. This difference is mainly the result of a broad absorption feature, which extends throughout the visible and NIR range. This feature is due to the absorption of W^V polarons formed alongside oxygen vacancies, and is strongly suppressed in m-WO_3 in line with the lower W^V polaron concentration in this material. The higher energy

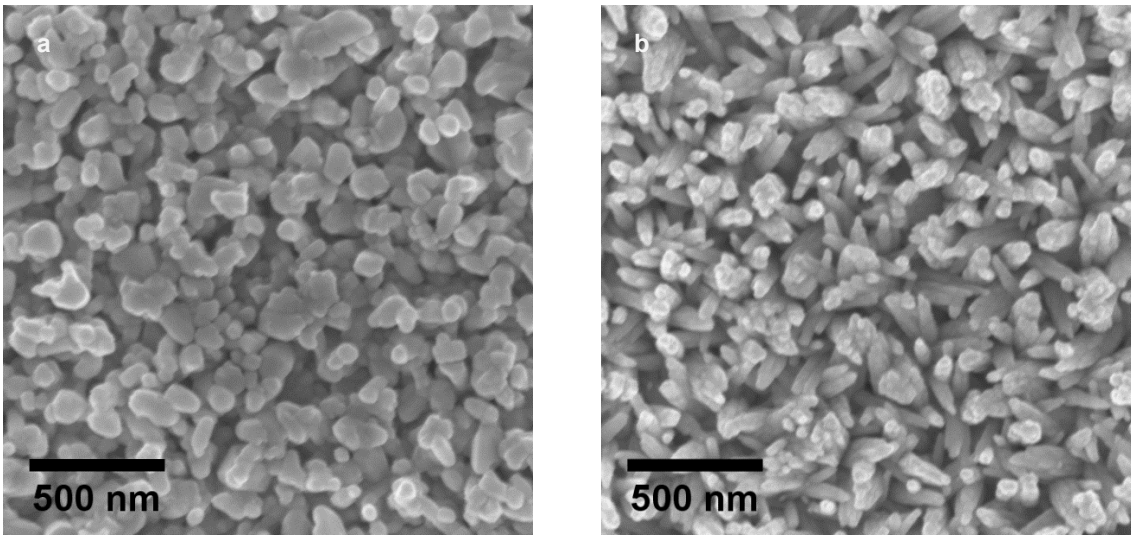

Figure 6.2: Scanning electron microscopy images of (**a**) m-WO_3 and (**b**) b-WO_3 thin films on quartz glass substrates.

bandgap transition appears visually similar for both types of films, but indirect bandgap Tauc plots [39] suggest that b-WO_3 exhibits a slightly larger optical bandgap (2.90 ± 0.02) eV than m-WO_3 (2.80 ± 0.05) eV (Figure C.2). A sharp photoluminescence peak around 440 nm (2.82 eV) is observed for m-WO_3, which is assigned to the recombination of shallowly trapped charges as it lies very close to the bandgap transition. In contrast, the only photoluminescence signal observed for b-WO_3 is essentially that of the quartz glass substrate, and this absence of photoluminescence for b-WO_3 suggests that non-radiative recombination becomes more dominant with increasing oxygen vacancies concentration.

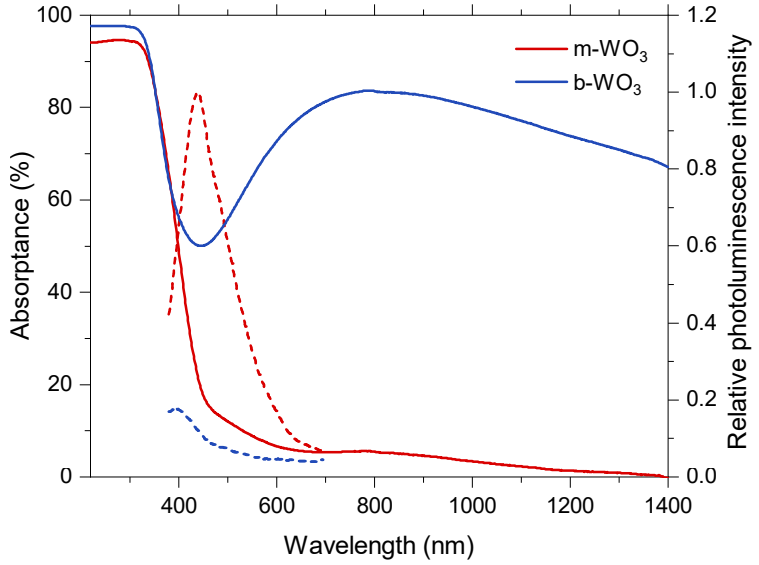

Figure 6.3: UV-NIR absorptance spectra (full lines) and photoluminescence spectra upon 355 nm excitation (dashed lines) of m-WO_3 and b-WO_3 films. The divergence in absorptance between the two types of films below 350 nm is likely related to difficulties in obtaining accurate reflectance data at energies above the absorption onset.

As recorded by Anna Wilson and shown in Figure 6.4, m-WO_3 reaches incident photon-to-current conversion efficiencies (IPCEs) of up to 23% for water oxidation at 1.23 V vs. RHE, which is similar to the performance of previously reported analogously prepared WO_3 films [40]. In contrast, b-WO_3 films only yield IPCEs of less than 1%, which demonstrates that the extended visible light absorption of b-WO_3 does not translate into visible light activity, but in addition the high degree of oxygen deficiency also compromises the activity of b-WO_3 in the UV region compared to m-WO_3.

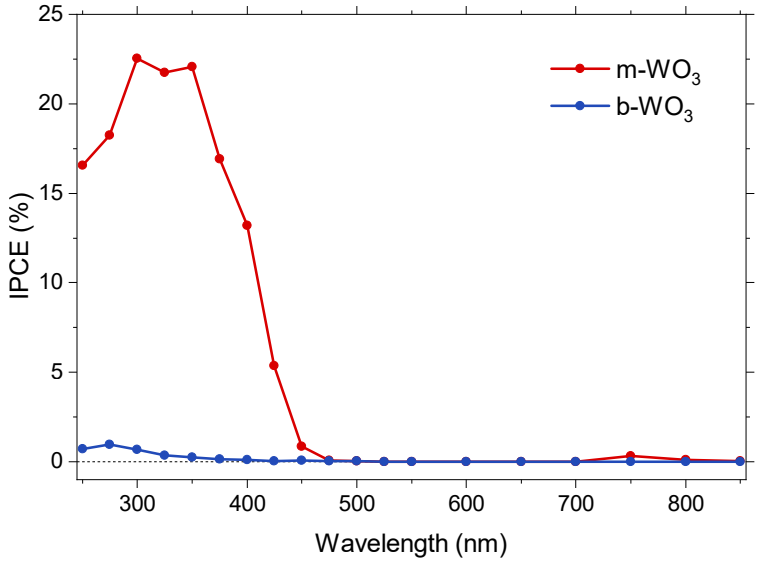

Figure 6.4: Incident photon-to-current conversion efficiency (IPCE) spectra for water oxidation at 1.23 V vs. RHE for m-WO_3 and b-WO_3 films.

6.2.2 Polaron formation and energetics

The reduction of tungsten centres following electron localisation was further confirmed by of x-ray absorption near-edge structure (XANES) spectroscopy experiments which show a shift of the W L_{III}-edge to lower energies at higher oxygen vacancies concentrations (Figure C.3), hence suggesting that more reduced tungsten centres are present. In addition, the extended x-ray absorption fine structure (EXAFS) reveals that samples with higher degrees of oxygen deficiency exhibit more heterogeneous bond distances (Figure C.4, Table C.1, Table C.2). This is consistent with a considerable change in the local coordination environment upon W^V polaron formation observed in DFT calculations, where bond distances d(W^{VI}-O) = 1.89 - 1.95 Å and d(W^V-O) = 1.75 – 1.92 Å are observed.

The formation of W^V polarons at the film surface, which is particularly important for interfacial reactions, was next investigated using x-ray photoelectron spectroscopy (XPS). Figure 6.5a shows XPS spectra obtained from m-WO_3 and b-WO_3 films when probed at low binding energies. These XPS spectra reflect the density of occupied states in the bandgap region, where the broad peak at binding energies above 2 eV is attributed to valence band states and the less intense, narrower peak at binding energies near 0 eV is assigned to W^V_{ov} states. A comparison of the number of W^V_{ov} states between m-WO_3 and b-WO_3 based on the relative signal amplitudes in these samples shows a considerably higher photoelectron emission signal for b-WO_3. This higher photoelectron emission signal is due to a larger number of W^V_{ov} states, which supports the larger numbers of W^V polarons observed in the form of the intense absorption in Figure 6.3a. Deconvolution of the W 4f photoelectron emission signal (Figure C.5) reveals that 8% of all surface tungsten centres are W^V in m-WO_3, as opposed to 18% W^V for b-WO_3. Interestingly, the difference in optical absorption is disproportionately larger than this ca. twofold difference in the number of W^V polarons at the surface, which suggest that a large number of W^V polarons are present in the bulk of b-WO_3 were they can be observed in a transmission measurement but not in a surface-sensitive XPS experiment. The presence of additional bulk W^V polarons in b-WO_3 is supported by its larger intrinsic n-type carrier density, determined from Hall effect measurements with $\sim 4 \times 10^{21}\,cm^{-3}$ as compared to $\sim 5 \times 10^{16}\,cm^{-3}$ for m-WO_3. This larger number of mobile carriers in b-WO_3 is a result of more thermally accessible sub-bandgap states close to the conduction band edge, but the overall doping efficiency (ratio of such W^V_{ov} states within thermal energy from conduction band edge over the overall number of W^V_{ov} states) is low as evidenced by the broad distribution of W^V_{ov} states which reaches far into the bandgap in Figure 6.5a.

The broad distribution of W^V_{ov} states observed experimentally is rationalised using first-principles calculations of sub-bandgap states introduced for isolated oxygen vacancies, and also for defect complexes that involve multiple vacancies since the formation of such complexes becomes increasingly likely at higher oxygen vacancy concentrations. Herein, a neutral oxygen vacancy is represented by $[W^V\text{-}V_O^{2+}\text{-}W^V]^0$, which is converted to $[W^{VI}\text{-}V_O^{2+}\text{-}W^V]^+$ when singly ionised and $[W^{VI}\text{-}V_O^{2+}\text{-}W^{VI}]^{2+}$ when doubly ionised. The removal of an oxygen atom along the x, y, or z direction in monoclinic WO_3 results in the formation of a $V_O(x)$, $V_O(y)$, $V_O(z)$ defects, respectively. As shown in Figure 6.6a, the predicted energetic positions associated with an isolated $V_O(y)$ vacancy are located 0.48 eV and 0.62 eV below the conduction band. In addition, the defect complexes $V_O(zy)$, composed of a $V_O(z)$ and a $V_O(y)$ defect, and $V_O(zz)$, composed

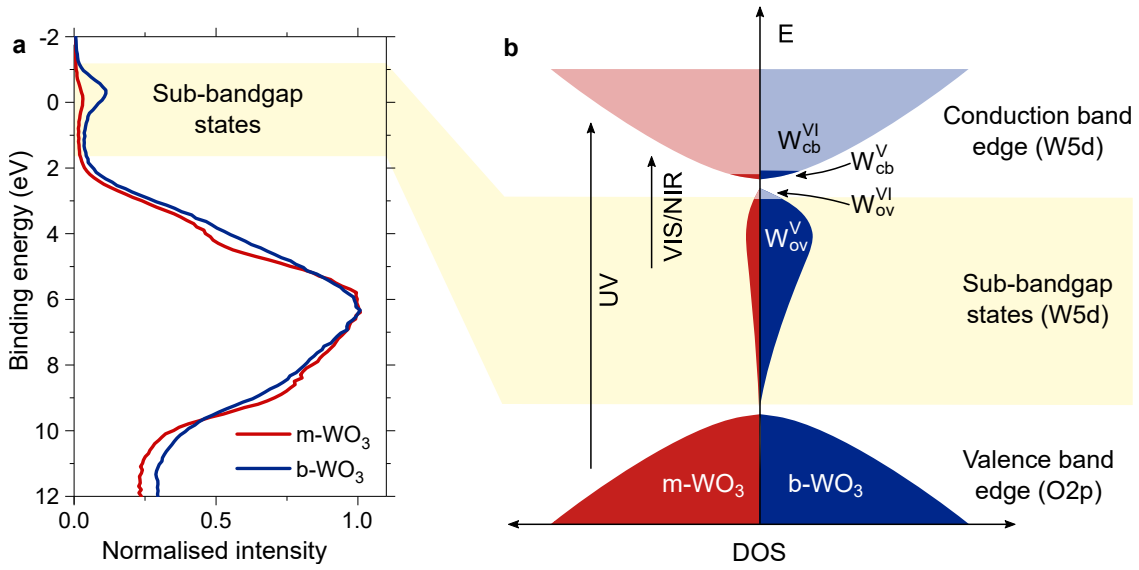

Figure 6.5: Density of states in the bandgap region. (**a**) X-ray photoelectron spectroscopy (XPS) spectra of m-WO_3 and b-WO_3 at low binding energies. (**b**) Schematic illustration of the broad distribution of sub-bandgap states. The small number of occupied states in the conduction band (W^{V}_{cb}) results from thermal excitation of sub-bandgap (W^{V}_{ov}) and leads to n-type conductivity. Transitions induced upon irradiation of UV and visible/NIR light are indicated exemplarily.

of two V_O(z) defects, are considered. While the formation of V_O(zz) is endothermic with an energy penalty of 1.8 eV per defect, the formation of V_O(zy) in n-type WO_3 is predicted to be exothermic (up to 0.4 eV) (Figure C.6). Figure 6.6b shows that a wider range of charge states becomes accessible upon V_O(zy) complex formation, which gives rise to states between 0.23 eV and 0.87 eV below the condition band. This broader defect state distribution upon formation of vacancy complexes supports the experimental results presented above and demonstrates that defect-defect interactions can explain such broad distributions of oxygen vacancy defect states.

6.2.3 Charge carrier dynamics

Transient absorption experiments were carried out to investigate how the different degrees of oxygen deficiency and the different numbers of defect states within the bandgap impact on the charge carrier dynamics in m-WO_3 and b-WO_3. To compare the behaviour of charges generated upon bandgap excitation and upon direct excitation of W^{V}_{ov} states, a range of different excitation wavelengths was used and absorption changes were probed in the visible and NIR range. In both samples, excitation with UV light promotes electrons from the valence band to the conduction band, thus converting W^{VI}_{cb} states to W^{V}_{cb}. In contrast, excitation with visible/NIR light promotes an electron from a vacancy state (W^{V}_{ov}) to the bulk conduction band (thus also forming W^{V}_{cb}). As

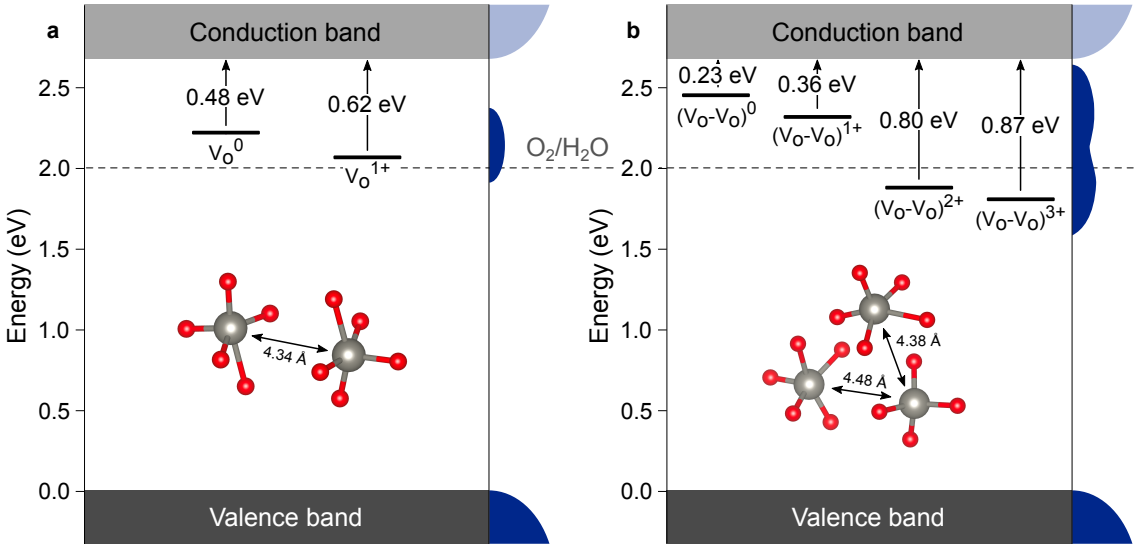

Figure 6.6: Defect ionisation levels of oxygen vacancies in different charge states calculated from hybrid density functional theory (DFT) for (**a**) an isolated oxygen vacancy $V_O(y)$ and (**b**) a defect complex $V_O(zy)$ composed of two oxygen vacancies. Energies are given relative to the valence band edge and resulting densities of states are shown schematically at the right side of each panel. The insets show local atomic structures with the distance between tungsten atoms being indicated.

previously discussed in general terms in Section 3.3, a positive ΔA signal indicates the absorption of a state that is newly generated upon photoexcitation. For WO_3, positive transient signals between 400 - 500 nm have previously been attributed primarily to holes, whereas positive signals above 750 nm were found to be mainly due to electrons (e.g. W_{cb}^V herein) [41]. In contrast, a negative ΔA signal results from the photoinduced depopulation of an absorbing ground state, e.g. the depopulation of a W_{ov}^V state.

Figure 6.7 compares transient spectra obtained upon excitation at 800 nm and 355 nm, corresponding to visible/NIR and UV light. In general, all spectra show very broad features suggesting that the same photogenerated species are probed over most of the visible and NIR range. Following excitation of m-WO_3 at 800 nm (Figure 6.7a), a bleach is observed towards the NIR region at 1 ps but almost fully decays within 100 ps. Since this bleach is ascribed to a depopulation of W_{ov}^V states by the 800 nm light pulses, this fast decay indicates that most of the generated W_{cb}^V conduction band electrons re-trap within 100 ps. Since the depletion of W_{ov}^V states and the generation of W_{cb}^V states via the 800 nm excitation pulses are directly related, both states should be depleted/generated in equal numbers. However, only the negative signal associated with the loss of W_{ov}^V is observed, which suggests that this signal contributes more strongly to the overall spectrum than the positive W_{cb}^V signal. This difference in relative contributions can be ascribed to a higher attenuation coefficient of the respective W_{ov}^V transition, which will make it difficult

to monitor both W^{V}_{ov} and W^{V}_{cb} simultaneously at even higher degrees of oxygen deficiency.

When exciting m-WO_3 above its bandgap using 355 nm light (Figure 6.7b), a positive absorption throughout the probed spectral range is found at 1 ps which can be assigned predominantly to valence band holes below probe wavelengths of 500 nm and predominantly W^{V}_{cb} conduction band electrons above 700 nm. At 100 ps, some of this positive absorption is still observed in the visible range, but a negative signal is found in the NIR range. This negative NIR feature resembles the 1 ps signal at 800 nm excitation (Figure 6.7a), indicating that W^{V}_{ov} also become depopulated following 355 nm excitation, but at later times. This depopulation can be assigned to the trapping of valence band holes into W^{V}_{ov} states. The resulting bleach is not observed on the µs timescale onwards for m-WO_3 (Figure C.8), which suggests that W^{V}_{cb} conduction band electrons and W^{VI}_{ov} trapped holes complete their recombination on the nanosecond timescale. A small positive signal remains below 500 nm (Figure C.8), and is attributed to a small residual population of valence band holes.

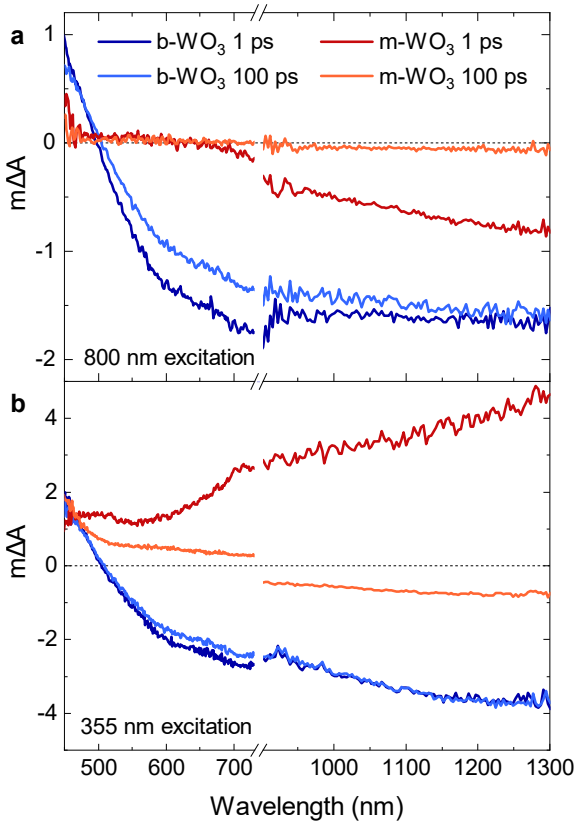

Figure 6.7: Transient absorption spectra for m-WO_3 and b-WO_3, probed at 1 ps and 100 ps following excitation at (**a**) 800 nm and (**b**) 355 nm using a fluence of 0.26 mJ cm^{-2}.

Using the same excitation conditions for the highly oxygen deficient b-WO_3, 800 nm excitation

gives rise to a positive signal below 500 nm and a bleach above 500 nm (Figure 6.7a). This is the case both at 1 ps and at 100 ps time delay, showing that little decay occurs between these times in stark contrast to m-WO_3. The bleach coincides with the W^V_{ov} polaron absorption (Figure 6.3), which further suggests that this bleach originates from the depopulation of W^V_{ov} states. Interestingly, the same spectral signature is observed using 355 nm light (Figure 6.7b), suggesting that the depopulation of W^V_{ov} does not only occur when they are excited directly using visible/NIR but also upon bandgap excitation.

To investigate the temporal evolution of the different photogenerated states the kinetics of photogenerated charges are monitored for a range of different excitation wavelengths spanning the UV to NIR region. The transient kinetics shown in Figure 6.8 are probed at 1200 nm following bandgap excitation (Figure 6.8a, c) and sub-bandgap excitation (Figure 6.8b, d). Upon bandgap excitation of m-WO_3, a positive excited state absorption (half-time of 1.4 ps for 355 nm excitation) evolves into a bleach over time which reaches its maximum amplitude around 400 ps (Figure 6.8a). As indicated in the spectral comparison, this excited state absorption is due to W^V_{cb} and becomes increasingly dominated by the depopulation of W^V_{ov} through trapping of valence band holes. In contrast, sub-bandgap excitation directly excites W^V_{ov} states and thus depopulates them, hence giving rise to an immediate bleach (Figure 6.8b). This bleach undergoes a stretched exponential decay ($\Delta A \propto exp(-kt^b)$ with b varying 0.19-0.34 between excitation wavelengths), which suggests that photogenerated charges exhibit a distribution of different lifetimes [42, 43] as can be expected in the presence of a distribution of trap states at various energies within the bandgap.

For the more oxygen deficient b-WO_3, substantially more long-lived signals are observed. Bandgap excitation gives rise to an immediate bleach which hardly decays over the 6 ns time window of the experiment (Figure 6.8c), in stark contrast to m-WO_3 where bleaching only occurs from 20 ps onwards. The immediate appearance of this bleach suggests that trapping of valence band holes into W^V_{ov} states takes place within the time resolution of the instrument (<200 fs). This fast trapping process is likely the reason why no photoluminescence is observed from b-WO_3 (Figure 6.3), as holes do not reside in the valence band for a sufficient amount of time to recombine radiatively. The acceleration of hole trapping also appears consistent with the much higher number of W^V_{ov} states within the bandgap.

Sub-bandgap excitation of b-WO_3 gives rise to a similarly long-lived bleach but also produces an additional decay component at times below 0.8 ps (Figure 6.8d), which is assigned to carrier

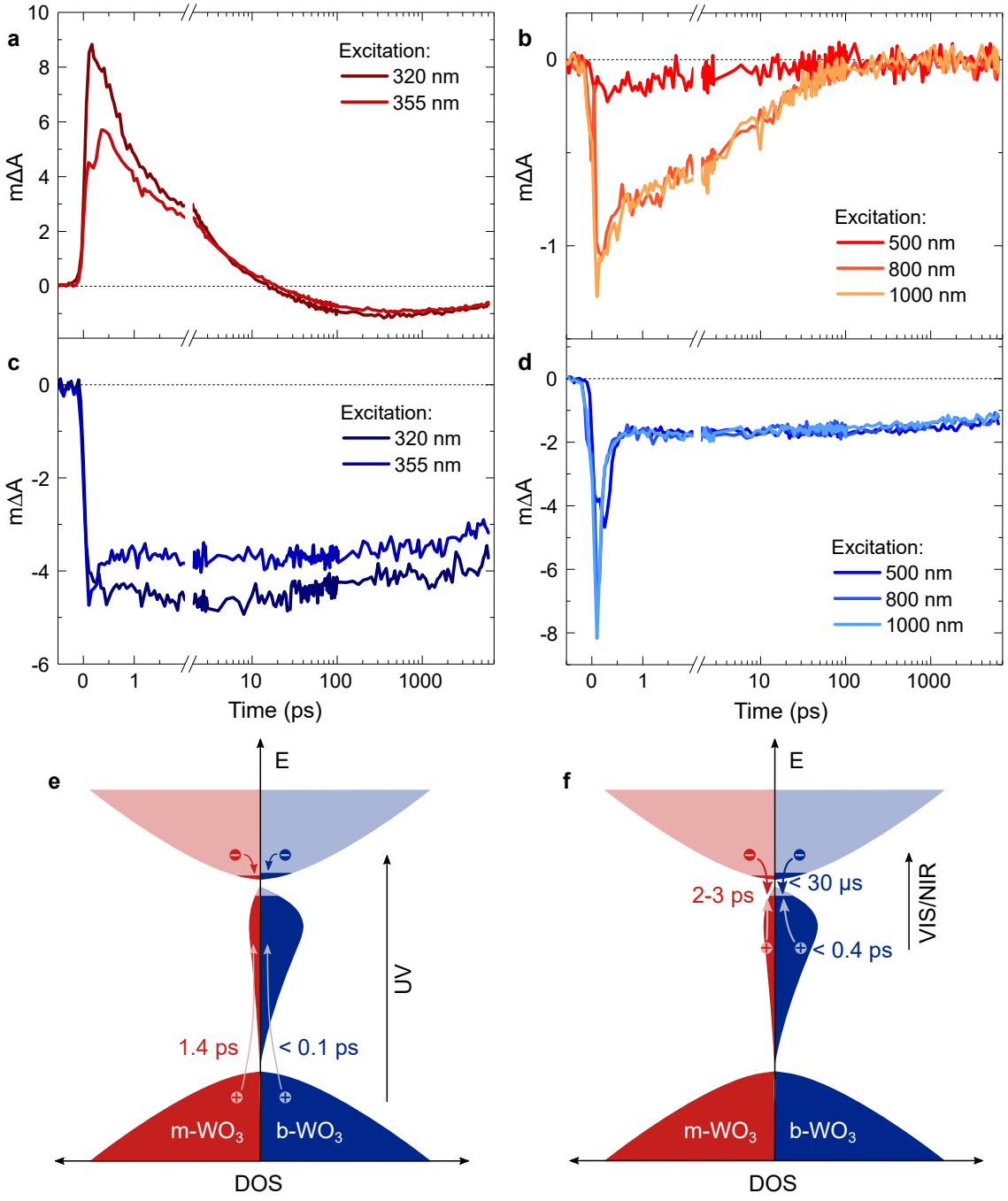

Figure 6.8: Transient absorption kinetics probed at 1200 nm for a range of different excitation wavelengths corresponding to (**a**) bandgap excitation of m-WO_3, (**b**) sub-bandgap excitation of m-WO_3, (**c**) bandgap excitation of b-WO_3, and (**d**) sub-bandgap excitation of b-WO_3. All experiments were carried out using a fluence of 0.26 mJ cm^{-2}. The photoinduced processes are illustrated schematically for (**e**) bandgap excitation (**f**) and sub-bandgap excitation for m-WO_3 (left of energy axis) and b-WO_3 (right of energy axis). The indicated times are decay half-times for the respective processes. For simplicity, W^{V}_{cb} states (electrons on tungsten centres away from a vacancy) are shown only in the conduction band, however, it should be noted that polaron formation through self-trapping of such electrons could also lead to localisation at energies within the bandgap.

relaxation through a high density of states as discussed below. The long-lived bleach signals obtained for both bandgap and sub-bandgap excitation of b-WO_3 are observed up to µs - ms timescales where they follow an identical power law decay $\Delta A \propto t^{-a}$ with $a = 0.51$ (Figure 6.9), which suggests highly dispersive recombination in the presence of trap states [44]. The identical decay behaviour on this longer timescale provides further evidence that both bandgap and sub-bandgap excitation eventually lead to the depopulation of W_{ov}^{V} states, effectively producing trapped holes in the form of W_{ov}^{VI}. By monitoring the decay kinetics of these sub-bandgap state holes in b-WO_3 films when immersed in H_2SO_4 and comparing them to kinetics in solutions of different oxidisable substrates, these trapped holes were found to be unreactive towards high concentrations of the commonly used hole scavengers methanol, Na_2SO_3, and triethanolamine (Figure 6.10). This lack of reactivity suggests that these holes are either thermodynamically unable to oxidise these substrates or spatially situated too far from the surface to interact with them.

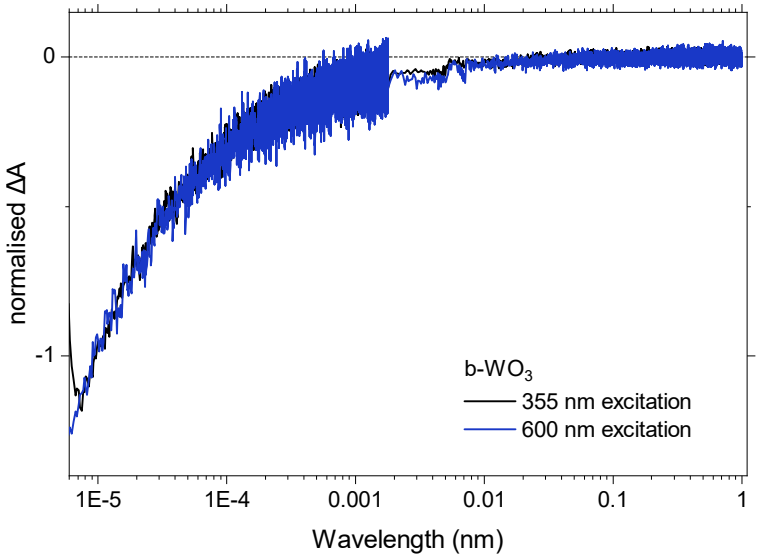

Figure 6.9: Transient absorption decay kinetics for b-WO_3 upon 355 nm (600 nm probe) and 600 nm (650 nm probe) excitation. Fluences of 3.0 mJ cm^{-2} and 1.5 mJ cm^{-2} were used at 355 nm and 600 nm, respectively. The visible excitation wavelength of 600 nm (instead of 800 nm like in the faster timescale experiments) was chosen due to limitations in the transmission characteristics of the light guide between laser and sample. Samples were excited through the quartz substrate to allow for the use of higher fluences.

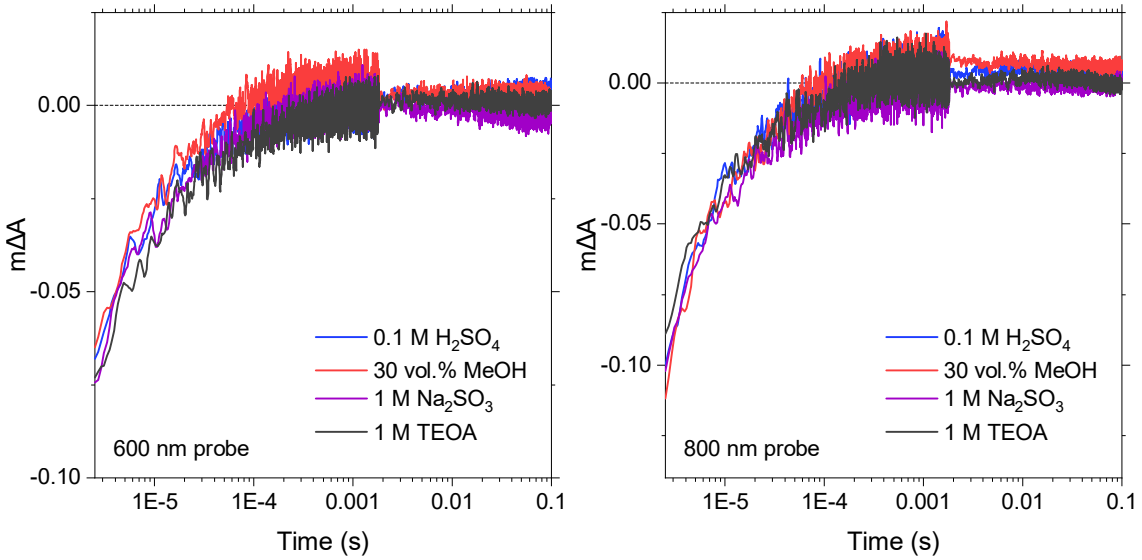

Figure 6.10: Transient absorption decay kinetics for for b-WO_3 upon 355 nm, probed at (**a**) 600 nm and (**b**) 800 nm. Kinetics were recorded at an excitation intensity of 1.5 mJ cm^{-2} in 0.1 M H_2SO_4 electrolyte and after addition of 30 vol% methanol, or in the presence of 1 M Na_2SO_3 or 1M triethanolamine.

6.3 Discussion

This chapter compares the charge carrier dynamics in near-stoichiometric m-WO_3 and strongly oxygen-deficient b-WO_3 thin films, which are summarised in Figure 6.8e and Figure 6.8f for bandgap excitation and sub-bandgap excitation, respectively. For bandgap excitation, the presented transient data suggests that photogenerated valence band holes rapidly trap into occupied oxygen vacancy states within the bandgap (referred to as W^V_{ov} herein). For m-WO_3 this hole trapping process is highly dispersive and extends out to 200 ps, whereas it occurs within the experimental time resolution (<100 fs) for b-WO_3. This faster hole trapping in b-WO_3 is consistent with its higher density of W^V_{ov} states as observed in UV-vis experiments and supported by XPS and XANES measurements. In contrast, sub-bandgap excitation directly generates holes in sub-bandgap W^V_{ov} states which recombine with a decay half-time of 2-3 ps in m-WO_3, but persist up to milliseconds in b-WO_3. Hall effect measurements demonstrate that the concentration of dark carriers in b-WO_3 is ∼5 orders of magnitude higher than in m-WO_3, which is due to a higher number of thermally excited W^V_{ov} states at room temperature. However, the broad distribution of sub-bandgap W^V_{ov} states as determined by XPS and first principles defect calculations suggests that the number of W^V_{ov} which are sufficiently close to the conduction band edge for thermal excitation is very small compared to the number of W^V_{ov} states situated deeper within the bandgap. These deeper W^V_{ov} states thus remain occupied which suggests an overall low doping efficiency as only few state contribute to the conductivity of the material.

Since occupied sub-bandgap oxygen vacancy states (W_{ov}^{V}) trap holes and unoccupied ones (W_{ov}^{VI}) trap electrons, the much larger number of W_{ov}^{V} states makes trapping of photogenerated holes the dominant process. Since the density of W_{ov}^{V} states in b-WO_3 spans most of the bandgap and extends towards the conduction band edge, this hole trapping process results in a large energy loss as illustrated by the energy difference between valence band and calculated oxygen vacancy energies in Figure 6.6. For example, a relaxation via trapping of the valence band holes into high-lying W_{ov}^{V} states as determined by XPS/DFT would correspond to an energy loss of $\sim$2 eV or more. The fast decay component observed upon sub-bandgap excitation of b-WO_3 on the fs timescale (Figure 6.8d) can be attributed to fast hole relaxation as it is characteristic of fast carrier relaxation through a high density of states. Such behaviour is usually observed for metals and degenerate semiconductors [45–47], but has recently also been described for substoichiometric WO_3 [48]. The virtually constant signal amplitude following this fast decay can thus be assigned to holes trapped in sub-bandgap states close to the conduction band, and the long lifetime of these holes correlates with their deeply trapped character. In addition, recombination might be slowed down by carriers being trapped at different sites within the material, since DFT calculations suggest that a range of different coordination environments give rise to the observed broad W_{ov}^{V} distribution. For m-WO_3, sub-bandgap excitation produces a stretched exponential decay (Figure 6.8b), which suggests that holes recombine from various energy levels within the bandgap and thus implies that the energetic relaxation of trapped holes is less pronounced than in b-WO_3. In contrast to the trapping of photogenerated holes, trapping of photogenerated electrons into the rather low density of W_{ov}^{VI} states produces shallowly trapped charges and thus incurs a relatively small energy loss (shallow trapping). These interpretations are consistent with reports of pronounced hole trapping into occupied oxygen vacancy states in α-Fe_2O_3 photoelectrodes in the absence of a space charge layer [44]. When a space charge layer is formed under strong anodic potentials, the highest lying oxygen vacancy states are emptied. Electron trapping into these now unoccupied oxygen vacancy states results in the accumulation of α-Fe_2O_3 holes with a sufficient lifetime for water oxidation at the photoelectrode surface [44, 49].

The highest performances are typically obtained using moderately oxygen-deficient films without excessive numbers of sub-bandgap states and thus without intense colouration. In agreement the IPCE spectrum of b-WO_3 (Figure 6.4), little to no activity has been observed in different metal oxides when exciting absorption features that arise from sub-bandgap oxygen vacancy states [4, 6–8, 12, 16, 50]. Instead of the use of a higher number of photons via enhanced

absorption, the higher performance of moderately oxygen-deficient oxides is attributed to a more efficient conversion of high energy photons [51]. This improved conversion efficiency can be attributed to increased conductivity due to the increased doping density that results from oxygen vacancy formation [52], as well as enhanced band bending close to the semiconductor liquid interface [37] where most high energy photons are absorbed. More detailed investigations show that such improved conductivity can be related to suppressed recombination of surface holes with bulk electrons on slow timescales [49, 53]. An activity maximum at moderate oxygen deficiency suggests that it is necessary to achieve a balance between a sufficiently high doping density and a sufficiently low number of W_{ov}^{V} states to achieve good performance. The presented transient data helps to rationalise this balance as a trade-off between a favourable enhancement in conductivity at higher doping densities and an unfavourable decrease in the driving force of trapped holes, which results from a concomitantly growing number of hole trap states. At high numbers of W_{ov}^{V} states, such losses in driving force severely compromise the efficiency of oxidation reactions that require high oxidative power. Similar issues have been observed in carbon nitride photocatalysts, where charge carrier trapping slows down recombination times at the expense of a loss in driving force [54]. As a result, metal oxides with excessive oxygen vacancy densities are rather unlikely to achieve higher activities for demanding oxidation reactions such as water oxidation than their more stoichiometric analogues. However, the prolonged hole lifetimes could be advantageous for less demanding reactions with less positive oxidation potentials such as the degradation of pollutants. In the absence of deep electron traps, electron trapping likely results in a less substantial loss in reductive driving, which suggests potential for applications such as CO_2 reduction [55]. Overall, developing strategies to engineer oxygen vacancies would be desirable to fine-tune the energetic positions of their associated sub-bandgap states, which would allow to control losses in driving force.

6.4 Conclusions

This chapter compares charge carrier dynamics in WO_3 films with low and high oxygen vacancy concentrations, referred to as m-WO_3 and b-WO_3, respectively. Oxygen vacancy formation creates sub-bandgap states, most of which are occupied and are herein referred to as W_{ov}^{V} states. In the highly oxygen deficient b-WO_3, these W_{ov}^{V} states give rise to a pronounced absorption throughout the visible and NIR region due to their broad distribution, which is supported by first-principles defect calculations suggesting the formation of defect clusters. Since the broad

distribution of these W_{ov}^{V} states reaches far into the bandgap, the vast majority of them remains occupied at room temperature and thus acts as trapping sites for photogenerated valence band holes. Upon bandgap excitation of the near-stoichiometric m-WO_3, trapping of valence band holes into these W_{ov}^{V} states occurs over a time period of up to 200 ps after light absorption. In the highly oxygen-deficient b-WO_3, in contrast, this trapping process occurs within 200 fs due to the higher density of W_{ov}^{V} states, leading to virtually complete photoluminescence quenching.

This fast hole trapping in b-WO_3 prolongs the lifetime of charges generated upon visible/NIR excitation by several orders of magnitude, but also results in a significant loss in oxidative driving force of up to ∼2 eV. This loss in driving force consequently compromises the activity of highly oxygen-deficient metal oxides for demanding oxidation reactions such as water oxidation. These results also help to rationalise why the best photoelectrochemical water oxidation performance is typically observed for metal oxide films with moderate oxygen deficiency, where driving force losses do not dominate yet but where the higher intrinsic carrier density improves electrode conductivity and supports the formation of a well-defined space charge layer. However, the enhanced lifetime of photogenerated charges in highly oxygen-deficient films could be beneficial for reactions with less positive oxidation potentials such as pollutant degradation or for suitable reduction reactions. These results demonstrate why the energetic distribution of sub-bandgap states, rather than just that of valence and conduction band states, needs to be tuned with respect to the redox potential of a targeted photocatalytic or photoelectrocatalytic reaction.

6.5 Materials and Methods

Experimental details have been described in reference [56] and are largely reproduced here for convenience.

Film preparation

b-WO_3 thin films were deposited via aerosol assisted chemical vapor deposition based on a previously reported procedure [38]. Following this procedure, 0.060 g $W(CO)_6$ precursor was dissolved in a 2:1 mixture consisting of acetone (99%, Emplura) and methanol (99.5%, Emplura) with a total volume of 15 mL. Aerosols were generated from the resulting solution using an ultrasonic humidifier (Liquifog, Johnson Matthey) operating at 2 MHz and were carried to the reactor using nitrogen gas (99.99%, BOC) at a flow rate of 400 sccm. The gas flow was regulated using a mass flow controller (MFC, Brooks). Aerosols were deposited onto a quartz glass substrate

for 10 min at 350 °C, after which heater and humidifier were switched off and the reactor was allowed to cool to room temperature while maintaining the nitrogen atmosphere.

m-WO_3 thin films with near-stoichiometric composition were obtained by annealing b-WO_3 thin films prepared as reported above at 600 °C using a ramp rate of 4.8 °C min^{-1}. Subsequently, the annealed films were allowed to cool to room temperature inside the furnace.

Sample storage

m-WO_3 and b-WO_3 were stored in air between measurements. While b-WO_3 films were stable over time, m-WO_3 films tend to become more oxygen deficient on the timescale of several months. m-WO_3 can be converted back to its original state through re-annealing.

Transient absorption experiments

TAS experiments were carried out in the standard configuration described in Section 3.3. Films were excited from the front side unless stated otherwise.

X-ray diffraction (XRD)

X-ray diffraction (XRD) patterns were measured with a modified Bruker-Axs D8 diffractometer with parallel beam optics equipped with a PSD LinxEye silicon strip detector. The instrument uses a Cu source for X-ray generation (V = 40 kV, I = 30 mA) with Cu $K_{\alpha 1}$ (λ= 1.540 56 Å) and Cu $K_{\alpha 2}$ radiation (λ= 1.544 39 Å) emitted with an intensity ratio of 2:1. The incident beam was kept at 1° and the angular range of the patterns collected between $10 \leq 2\Theta° \leq 66$ with a step size of 0.05°. Patterns were fit to a Le Bail refined model using GSAS-EXPGUI software [57].

X-ray photoelectron spectroscopy (XPS)

X-ray photoelectron spectroscopy (XPS) was carried out using a Thermo Scientific K-Alpha instrument with monochromatic Al K_{α} source to identify the oxidation state and chemical constituents. Survey scans were collected over the 0 - 1400 eV binding energy range with 1 eV resolution and a pass energy of 200 eV. Higher resolution scans were collected in the binding energy regions of W4f, O1s, C1s, Si2p and the valence band region from -5 - 30 eV with 0.1 eV resolution and a pass energy of 40 eV. An argon ion gun was used to etch the surface layers of

samples to record a depth profile. Peaks were modelled using Casa XPS software with binding energies adjusted to adventitious carbon (284.5 eV).

Hall Effect

Room temperature Hall effect measurements were carried out on an Ecopia HMS-3000 in the van der Pauw configuration [58]. Measurements were acquired at 0.58 T and a variable current of 0.1 mA to 1 nA on square-cut samples ($\sim$ 1 cm x 1 cm). Silver paint (Agar Scientific) was used to form Ohmic contacts, the integrity of which were tested prior to measurement.

X-ray Absorption Spectroscopy (XAS)

X-ray absorption data at W L_{III}-edge was collected on beamline 7-3 at Stanford Synchrotron Radiation Lightsource (SSRL) under standard ring conditions of 3.0 GeV and 500 mA current. A Si (220) double crystal monochromator was used for energy selection which was detuned to 50% of flux maximum at W L_{III}-edge. The intensities of incident and transmitted X-ray beam were monitored using N_2-filled ion chambers before the sample (I_0) and after the sample (I_1), respectively. The monochromator energy was calibrated with the first inflection point energy of a W foil spectrum (10.3 keV). The data was collected as fluorescence excitation spectra using a 30-element Ge solid-state detector (Canberra) and energy calibration for each spectrum was done using a monochromator crystal glitch in the I_0 intensity relative to the absorption edge of W foil as no transmission data could be collected due to thick substrates. Data reduction of XAS spectra was performed using SamView (SixPack software, available at http://www.sams-xrays.com/sixpack). Athena program of Demeter software package (Demeter version 0.9.25, B. Ravel) [59] was used to subtract the pre-edge and post-edge backgrounds from absorption spectra after which the spectra were normalized to the edge jump. EXAFS Fitting was performed in r-space with Artemis software (Demeter version 0.9.25, B. Ravel) as previously described [60], using a passive electron reduction factor (S02) of 0.85 (obtained from a fit of a W foil spectrum) and maintaining a total coordination number of N_{tot}=6 whilst varying the coordination number of each shell (N).

Density functional theory calculation

Hybrid density functional theory (DFT) calculations were performed using the screened-hybrid ex-change-correlation functional proposed by Heyd, Scuseria, and Ernzerhof (HSE06) [61] and the Projector-Augmented Wave (PAW) [62] pseudo-potentials as implemented in the Vienna ab initio Simulation Package (VASP). The plane-wave basis set [62] was expanded up to 400 eV, and the atomic structures were optimized until the residual forces were less than 0.05 eV $Å^{-1}$. A 2x2x2 supercell containing 256 host atoms was employed and the Γ point was used for Brillouin zone integration. The SXDEFECTALIGN code was used to account for electrostatic potential alignment and finite-size effects in the formation energy of defects using the calculated low-frequency dielectric constants [63]. The calculations were spin-polarized allowing for a correct description of paramagnetic W^V d^1 centres.

6.6 References

1. Xia, T. *et al.* Hydrogenated black ZnO nanoparticles with enhanced photocatalytic performance. *RSC Adv.* **4,** 41654–41658 (2014).
2. Chen, S., Takata, T. & Domen, K. Particulate photocatalysts for overall water splitting. *Nature Reviews Materials* **2,** 17050 (2017).
3. Chen, X., Liu, L. & Huang, F. Black titanium dioxide (TiO 2) nanomaterials. *Chem. Soc. Rev.* **44,** 1861–1885 (2015).
4. Chen, X., Liu, L., Yu, P. Y. & Mao, S. S. Increasing Solar Absorption for Photocatalysis with Black Hydrogenated Titanium Dioxide Nanocrystals. *Science* **331,** 746–750 (2011).
5. Wang, Z. *et al.* H-Doped Black Titania with Very High Solar Absorption and Excellent Photocatalysis Enhanced by Localized Surface Plasmon Resonance. *Advanced Functional Materials* **23,** 5444–5450 (2013).
6. Wang, G. *et al.* Hydrogen-Treated TiO 2 Nanowire Arrays for Photoelectrochemical Water Splitting. *Nano Letters* **11,** 3026–3033 (2011).
7. Xu, C. *et al.* Electrochemically hydrogenated TiO2 nanotubes with improved photoelectrochemical water splitting performance. *Nanoscale Research Letters* **8,** 391 (2013).
8. Zhang, Z., Hedhili, M. N., Zhu, H. & Wang, P. Electrochemical reduction induced self-doping of Ti3+ for efficient water splitting performance on TiO2 based photoelectrodes. *Physical Chemistry Chemical Physics* **15,** 15637 (2013).

9. Lu, H. *et al.* Safe and facile hydrogenation of commercial Degussa P25 at room temperature with enhanced photocatalytic activity. *RSC Adv.* **4,** 1128–1132 (2014).

10. Naldoni, A. *et al.* Effect of Nature and Location of Defects on Bandgap Narrowing in Black TiO2 Nanoparticles. *Journal of the American Chemical Society* **134,** 7600–7603 (2012).

11. Liu, N. *et al.* Black TiO2 Nanotubes: Cocatalyst-Free Open-Circuit Hydrogen Generation. *Nano Letters* **14,** 3309–3313 (2014).

12. Wang, G. *et al.* Hydrogen-treated WO3 nanoflakes show enhanced photostability. *Energy & Environmental Science* **5,** 6180–6187 (2012).

13. Li, J. *et al.* A full-sunlight-driven photocatalyst with super long-persistent energy storage ability. *Scientific Reports* **3,** 2409 (2013).

14. Ling, M. *et al.* Correlation of Optical Properties, Electronic Structure, and Photocatalytic Activity in Nanostructured Tungsten Oxide. *Advanced Materials Interfaces* **4,** 1700064 (2017).

15. Guo, H.-L. *et al.* Oxygen deficient ZnO 1-x nanosheets with high visible light photocatalytic activity. *Nanoscale* **7,** 7216–7223 (2015).

16. Lu, X. *et al.* Efficient photocatalytic hydrogen evolution over hydrogenated ZnO nanorod arrays. *Chemical Communications* **48,** 7717 (2012).

17. Fan, C.-M. *et al.* Synproportionation Reaction for the Fabrication of Sn 2+ Self-Doped SnO 2-x Nanocrystals with Tunable Band Structure and Highly Efficient Visible Light Photocatalytic Activity. *The Journal of Physical Chemistry C* **117,** 24157–24166 (2013).

18. Kafizas, A., Godin, R. & Durrant, J. R. in *Semiconductors for Photocatalysis* (eds Zetian Mi, L. W., Semiconductors, C. J. B. T. .-.-. & Semimetals) 3–46 (Elsevier, 2017).

19. Liu, X., Wang, F. & Wang, Q. Nanostructure-based WO3 photoanodes for photoelectrochemical water splitting. *Physical Chemistry Chemical Physics* **14,** 7894 (2012).

20. Zhang, T. *et al.* Iron-doping-enhanced photoelectrochemical water splitting performance of nanostructured WO 3 : a combined experimental and theoretical study. *Nanoscale* **7,** 2933–2940 (2015).

21. Mi, Q., Zhanaidarova, A., Brunschwig, B. S., Gray, H. B. & Lewis, N. S. A quantitative assessment of the competition between water and anion oxidation at WO3 photoanodes in acidic aqueous electrolytes. *Energy & Environmental Science* **5,** 5694 (2012).

22. Yourey, J. E. & Bartlett, B. M. Electrochemical deposition and photoelectrochemistry of CuWO4, a promising photoanode for water oxidation. *Journal of Materials Chemistry* **21,** 7651 (2011).

23. Corby, S. *et al.* Water Oxidation and Electron Extraction Kinetics in Nanostructured Tungsten Trioxide Photoanodes. *Journal of the American Chemical Society* **140,** 16168–16177 (2018).

24. Saenger, M. F. *et al.* Polaron and phonon properties in proton intercalated amorphous tungsten oxide thin films. *Physical Review B* **78,** 245205 (2008).

25. Wang, F., Di Valentin, C. & Pacchioni, G. Electronic and Structural Properties of WO 3 : A Systematic Hybrid DFT Study. *The Journal of Physical Chemistry C* **115,** 8345–8353 (2011).

26. Corà, F., Stachiotti, M. G., Catlow, C. R. A. & Rodriguez, C. O. Transition Metal Oxide Chemistry: Electronic Structure Study of WO 3 , ReO 3 , and NaWO 3. *The Journal of Physical Chemistry B* **101,** 3945–3952 (1997).

27. Johansson, M. B., Zietz, B., Niklasson, G. A. & Österlund, L. Optical properties of nanocrystalline WO3 and WO3-x thin films prepared by DC magnetron sputtering. *Journal of Applied Physics* **115,** 213510 (2014).

28. Wang, W., Janotti, A. & Van de Walle, C. G. Role of oxygen vacancies in crystalline WO 3. *J. Mater. Chem. C* **4,** 6641–6648 (2016).

29. Heller, A. Conversion of sunlight into electrical power and photoassisted electrolysis of water in photoelectrochemical cells. *Accounts of Chemical Research* **14,** 154–162 (1981).

30. Di Valentin, C. & Pacchioni, G. Spectroscopic Properties of Doped and Defective Semiconducting Oxides from Hybrid Density Functional Calculations. *Accounts of Chemical Research* **47,** 3233–3241 (2014).

31. Dixon, R. *et al.* Electronic states at oxygen deficient WO3(001) surfaces: a study by resonant photoemission. *Surface Science* **399,** 199–211 (1998).

32. Deb, S. K. Opportunities and challenges in science and technology of WO3 for electrochromic and related applications. *Solar Energy Materials and Solar Cells* **92,** 245–258 (2008).

33. Chen, H. *et al.* Electrochromic properties of WO3 nanowire films and mechanism responsible for the near infrared absorption. *Journal of Applied Physics* **101,** 114303 (2007).

34. Kuzmin, A. & Purans, J. X-ray absorption spectroscopy study of local structural changes in a-WO 3 under colouration. *Journal of Physics: Condensed Matter* **5,** 2333–2340 (1993).

35. Bondarenko, N., Eriksson, O. & Skorodumova, N. V. Polaron mobility in oxygen-deficient and lithium-doped tungsten trioxide. *Physical Review B* **92,** 165119 (2015).

36. Larsson, A. Optical absorption of Li-intercalated polycrystalline tungsten oxide films: comparison to large polaron theory. *Solid State Ionics* **165,** 35–41 (2003).

37. Wang, G. *et al.* An electrochemical method to enhance the performance of metal oxides for photoelectrochemical water oxidation. *Journal of Materials Chemistry A* **4,** 2849–2855 (2016).

38. Ling, M. & Blackman, C. Growth mechanism of planar or nanorod structured tungsten oxide thin films deposited via aerosol assisted chemical vapour deposition (AACVD). *physica status solidi (c)* **12,** 869–877 (2015).

39. Tauc, J. Optical properties and electronic structure of amorphous Ge and Si. *Materials Research Bulletin* **3,** 37–46 (1968).

40. Kafizas, A. *et al.* Optimizing the Activity of Nanoneedle Structured WO 3 Photoanodes for Solar Water Splitting: Direct Synthesis via Chemical Vapor Deposition. *The Journal of Physical Chemistry C* **121,** 5983–5993 (2017).

41. Pesci, F. M., Cowan, A. J., Alexander, B. D., Durrant, J. R. & Klug, D. R. Charge Carrier Dynamics on Mesoporous WO3 during Water Splitting. *The Journal of Physical Chemistry Letters* **2,** 1900–1903 (2011).

42. Regan, K. P., Koenigsmann, C., Sheehan, S. W., Konezny, S. J. & Schmuttenmaer, C. A. Size-Dependent Ultrafast Charge Carrier Dynamics of WO 3 for Photoelectrochemical Cells. *The Journal of Physical Chemistry C* **120,** 14926–14933 (2016).

43. Soloviev, V. N., Eichhöfer, A., Fenske, D. & Banin, U. Size-Dependent Optical Spectroscopy of a Homologous Series of CdSe Cluster Molecules. *Journal of the American Chemical Society* **123,** 2354–2364 (2001).

44. Barroso, M., Pendlebury, S. R., Cowan, A. J. & Durrant, J. R. Charge carrier trapping, recombination and transfer in hematite (α-Fe2O3) water splitting photoanodes. *Chemical Science* **4,** 2724 (2013).

45. Staleva, H. *et al.* Coupling to light, and transport and dissipation of energy in silver nanowires. *Physical Chemistry Chemical Physics* **11,** 5889 (2009).

46. Daraszewicz, S. L. *et al.* Determination of the electron–phonon coupling constant in tungsten. *Applied Physics Letters* **105,** 023112 (2014).

47. Brorson, S. D. *et al.* Femtosecond room-temperature measurement of the electron-phonon coupling constant γ in metallic superconductors. *Physical Review Letters* **64,** 2172–2175 (1990).

48. Johns, R. W. *et al.* Charge carrier concentration dependence of ultrafast plasmonic relaxation in conducting metal oxide nanocrystals. *Journal of Materials Chemistry C* **5,** 5757–5763 (2017).

49. Forster, M. *et al.* Oxygen deficient α-Fe 2 O 3 photoelectrodes: a balance between enhanced electrical properties and trap-mediated losses. *Chem. Sci.* **6,** 4009–4016 (2015).

50. Zheng, Z. *et al.* Hydrogenated titania: synergy of surface modification and morphology improvement for enhanced photocatalytic activity. *Chemical Communications* **48,** 5733 (2012).

51. Hu, Y. H. A Highly Efficient Photocatalyst-Hydrogenated Black TiO2 for the Photocatalytic Splitting of Water. *Angewandte Chemie International Edition* **51,** 12410–12412 (2012).

52. Wang, H., Zhang, C. & Rana, F. Ultrafast Dynamics of Defect-Assisted Electron–Hole Recombination in Monolayer MoS 2. *Nano Letters* **15,** 339–345. arXiv: 1409.4518 (2015).

53. Pesci, F. M., Wang, G., Klug, D. R., Li, Y. & Cowan, A. J. Efficient Suppression of Electron–Hole Recombination in Oxygen-Deficient Hydrogen-Treated TiO2 Nanowires for Photoelectrochemical Water Splitting. *The Journal of Physical Chemistry C* **117,** 25837–25844 (2013).

54. Godin, R., Wang, Y., Zwijnenburg, M. A., Tang, J. & Durrant, J. R. Time-Resolved Spectroscopic Investigation of Charge Trapping in Carbon Nitrides Photocatalysts for Hydrogen Generation. *Journal of the American Chemical Society* **139,** 5216–5224 (2017).

55. Liang, L. *et al.* Infrared Light-Driven CO 2 Overall Splitting at Room Temperature. *Joule* **2,** 1004–1016 (2018).

56. Sachs, M. *et al.* Effect of oxygen deficiency on the excited state kinetics of WO3 and implications for photocatalysis. *Chemical Science* **10,** 5667–5677 (2019).

57. Toby, B. H. EXPGUI , a graphical user interface for GSAS. *Journal of Applied Crystallography* **34,** 210–213 (2001).

58. Van der Pauw, L. J. A method of measuring specific resistivity and Hall effect of discs of arbitrary shapes. *Philips Research Reports* **13,** 1–9 (1958).

59. Ravel, B. & Newville, M. ATHENA , ARTEMIS , HEPHAESTUS : data analysis for X-ray absorption spectroscopy using IFEFFIT. *Journal of Synchrotron Radiation* **12,** 537–541 (2005).

60. Lassalle-Kaiser, B. *et al.* Evidence from in Situ X-ray Absorption Spectroscopy for the Involvement of Terminal Disulfide in the Reduction of Protons by an Amorphous Molybdenum Sulfide Electrocatalyst. *Journal of the American Chemical Society* **137,** 314–321 (2015).

61. Heyd, J., Scuseria, G. E. & Ernzerhof, M. Hybrid functionals based on a screened Coulomb potential. *The Journal of Chemical Physics* **118,** 8207–8215 (2003).

62. Blöchl, P. E. Projector augmented-wave method. *Physical Review B* **50,** 17953–17979 (1994).

63. Freysoldt, C., Neugebauer, J. & Van de Walle, C. G. Fully Ab Initio Finite-Size Corrections for Charged-Defect Supercell Calculations. *Physical Review Letters* **102,** 016402 (2009).

Chapter 7

Localisation of photogenerated charges in metal oxides

Despite the widespread use of metal oxides in the field of photocatalysis, what fundamentally causes certain oxides to have higher photocatalytic activities than others is still not well-understood. While metal cations with d^0 and d^{10} electronic configurations empirically appear to yield more efficient materials than open d-shell oxides, it is not clear why this is might be case. In this chapter, a series of 11 different metal oxides with varying electronic configuration is studied by means of ultrafast transient absorption spectroscopy in order to establish similarities and differences between these classes of oxides from a photophysical perspective. A rapid initial decay of delocalised electrons with a time constant of ∼400 fs is observed for the open d-shell oxides Cr_2O_3, Fe_2O_3, Co_3O_4, and NiO, which is assigned to the rapid formation of electron small polarons in these materials upon photoexcitation. In contrast, oxides with empty d-shells exhibit more long-lived delocalised electrons, with up to three orders of magnitude longer lifetimes for some materials such as anatase TiO_2 or CdO. These results point to a general problem of charge localisation in oxides with open d-shell configurations. In this way, oxides with d^0 and d^{10} configurations can be expected to be more active for rapid charge transfer and charge separation reactions on the picosecond timescale, as well as to exhibit overall more favourable charge transport properties.

The results presented in this chapter are in part included in these publications:

Sachs, M., Pastor, E., Park, J.-S., Walsh, A. & Durrant, J. R. Effect of excitation energy on charge localisation in Cr_2O_3. *In preparation.*

Sachs, M., Pastor, E., Park, J.-S., Kafizas, A., Selim, S., Corby, S., Walsh, A. & Durrant, J. R. Localisation of photogenerated charges in metal oxides. *In preparation.*

The following materials used in this chapter have been contributed by collaborators:
The TiO_2 and WO_3 thin films were synthesised by Andreas Kafizas, and the $BiVO_4$ thin films were prepared by Shababa Selim. All other oxide films were prepared by myself.

7.1 Introduction

As described in Chapter 2, the development of efficient photocatalyst materials is key for the implementation of solar-driven fuel synthesis as a technology at large scale. However, despite a large body of research on inorganic photocatalysts, there are still surprisingly few design guidelines to aid the development of more efficient materials. Comparisons of larger numbers of different photocatalyst materials have been carried out via computational [1] and experimental [2] screening, but a direct comparison of a wide range of metal oxides based on their photophysics has so far not been attempted. In this chapter, a series of metal oxides with different electronic configurations is investigated using time-resolved spectroscopy, ranging from oxides with an empty *d*-shell (d^0 configuration) to oxides with an open *d*-shell (d^1-d^9 configuration) to materials with a closed d-shell (d^{10} configuration). This comparison is carried out primarily based on the ultrafast dynamics of the investigated materials, thus covering the timescale on which the main losses in photocatalytic processes occur.

Figure 7.1 illustrates how the electronic structure of binary metal oxides changes when progressing through the transition metal series. Class 1 are empty *d*-shell oxides such as TiO_2 or WO_3, where the valence band consists primarily of *O2p* orbitals while the conduction band has mainly *d*-orbital character [3, 4]. The *O2p* band is typically located at around 3 V vs. NHE (at pH = 0) [5], which induces a large bandgap for these materials due to their high ionic character [6] and causes them to absorb only little visible light. d^0 oxides tend to form oxygen vacancies, and class 1a are thus oxygen-deficient open *d*-shell oxides in which defect states are created within the bandgap, as discussed in detail in Chapter 6. As shown for class 2, the *d*-bands of transition metal centres are systematically lowered in energy [7] when progressing towards higher nuclear charge (left to right in the periodic table) and thus start to become occupied, whereas the energetic position of the *O2p* bands remains largely unchanged. This *d*-band relaxation continues for open *d*-shell oxides in class 3, where a considerable amount of hybridisation between *O2p* bands

and *d*-bands starts to occurs in the valence band. The high *d*-occupancy in these materials gives rise to electron-electron correlation effects, and in many cases causes these materials to become Mott-Hubbard insulators. Such Mott-Hubbard insulators would in principle be expected to be metallic, but Coulomb repulsions and exchange interactions split their *d*-band [8, 9] and thus define the energy requirement for charge transfer from one metal centre to another. If the lowest energy transition in an electron-correlated oxide instead occurs between *O2p* band and the *d*-band, photoexcitation predominantly induces charge transfer between oxygen and metal centres, also referred to as ligand-to-metal charge transfer (LMCT), in which case the material is referred to as a charge-transfer insulator. Finally, class 4 depicts the case of an oxide with a closed *d*-shell. In such d^{10} oxides, the *d*-bands are stabilised even further and make up the valence band, whereas the conduction band has a different character such as metal *s* orbitals [10].

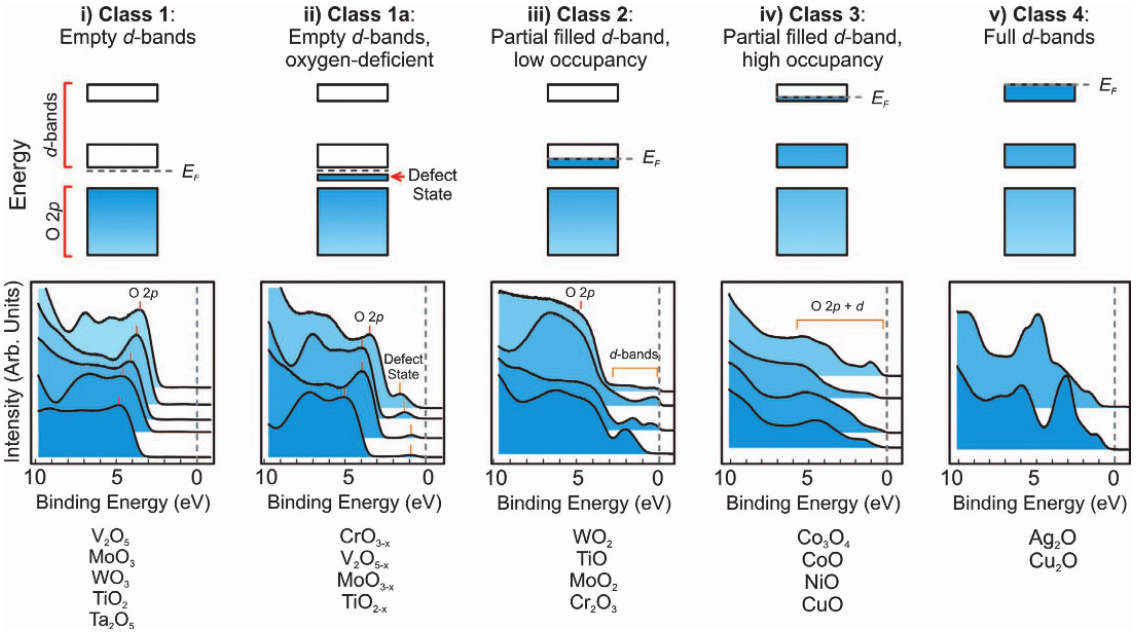

Figure 7.1: Schematic energy-band diagrams (top) and valence-band photoemission spectra (bottom) of different classes of transition metal oxides with varying d-orbital occupancy. Some of the shown examples are semiconductors while others are metals. Reproduced from reference [10], licensed under a Creative Commons (CC BY-NC-SA 3.0) License.

With these trends in mind, the results presented in this chapter will shed light onto the effect of the varying *d*-band contribution to valence and conduction band. Interestingly, metal oxides with d^0 and d^{10} configurations have often been targeted as photocatalyst materials [5, 11–15], but this focus has largely emerged on an empirical basis and a comprehensive photophysical

justification for the apparent higher activity of oxides with empty or closed d-shells has so far not been provided.

A particular focus in this chapter lies on a distinction between delocalised and localised charges. Delocalised charges can be considered to either occupy a band-like state, or a state in energetically close proximity to the band edge. A localised carrier, in the most commonly considered sense, is a charge is trapped at a defect site as has been discussed in Chapter 6 for charges trapped at oxygen vacancy sites in WO_3. As mentioned there, another possible pathway in which a charge can localise is through deformation of the lattice around it in order to minimise its free energy [16], thus effectively creating its own potential well. Such self-trapped charges are referred to as polarons, similarly to the W_{ov}^{V} polarons introduced in Chapter 6 except that such self-trapped polaronic charges do not require a physical defect site to become localised, although the presence of defect states may still affect polaron formation. The multivalent nature of transition metal cations, although often desired for charge accumulation in catalysis as outlined in Chapter 5, makes such charge localisation processes in metal oxides more likely than in conventional semiconductors [6]. In addition, the often narrow transport bands and large dielectric constants of metal oxides tend to favour a net energy gain of the lattice when localising a charge despite the strain penalty caused by the displacement of nearby ions [16]. In general, two types of polarons can be distinguished: Small polarons, which are strongly localised with a size on the order of the lattice constant, and large polarons, which are localised over several unit cells. The effective mass of a small polaron is related to quantum-mechanical tunnelling and small polaron transport is therefore thermally activated. In contrast, the mass of a large polaron is related to classical atomic motion and its mobility thus decreases with increasing temperature [17, 18].

For comparison of the photophysical properties of different metal oxides, a comprehensive interpretation of their transient spectra is required. The main contributions to a transient absorption signal, namely excited state absorption, ground state bleach, and stimulated emission, have been discussed in Section 3.3. For instance, the excited state absorption of delocalised electrons is classically described as Drude absorption [19, 20], which corresponds to an intra-band excitation of charges and thus mainly occurs at low, infrared-range energies. Nevertheless, the tails of such Drude-like absorption features may extend into the NIR range in the form of a broad excited state absorption. In contrast, localised charges typically induce relatively structured absorption features in the visible and/or NIR range.

In addition to the three mentioned primary signal contributions, transient signals which result

from more complex electronic effects also exist. One of these contributions are so-called Stark effects (also referred to as electroabsorption effects), where the ground state absorption features of a material are perturbed by electric fields between charge carriers, i.e. photogenerated charges in the case of optical excitation. Such perturbations can manifest as a change in the polarisability or in the dipole moment of the material upon photoexcitation, which gives rise to signals that resemble the first or second derivative of its ground state absorption, respectively [21]. In this way, the derivatives of the ground state absorbance can be compared to transient signals in order to identify polarisable excited states, broadly associated with relatively delocalised charges, or dipolar excited states, in which quasi-static dipole moments arise from the localisation of photogenerated charges [22–25]. Recently, Stark effects have been used to monitor the electron-hole separation process at the donor-acceptor interface in organic solar cells via the first-derivative-like transient absorption features [26–28].

In this chapter, 11 different metal oxides are investigated using ultrafast transient absorption spectroscopy in order to identify similarities and differences in their photophysical behaviour, especially with respect to their electronic *d*-configuration. By considering factors such as the fluence and excitation wavelength dependence of various transient signals, as well as ground state absorption derivatives, the degree of localisation of photogenerated charges is evaluated. While metal oxides with empty and closed *d*-shells feature delocalised charges with longer lifetimes, open *d*-shell oxides are found to exhibit rapid small polaron formation for photogenerated electrons.

7.2 Results

7.2.1 Co_3O_4

As will become clear throughout this chapter, transient absorption signals of fundamentally different origin are observed for a semiconducting metal oxide depending on whether the material absorbs strongly or weakly/not at all in the probed spectral region. In many cases, this distinction can be simplified to a consideration of probe energies above and below the bandgap transition. Co_3O_4 features both absorbing and non-absorbing spectral regions within the accessible probe energy range of the employed fs - ns TAS setup, and is thus discussed in detail here to illustrate these differences exemplarily.

Co_3O_4 is a multi-valence oxide which contains both Co^{II} and Co^{III} ions. It adopts a normal-spinel structure, where Co^{II} ions occupy tetrahedral sites Co^{III} and ions occupy octahedral sites [29, 30], meaning that Co_3O_4 incorporates both d^6 and d^7 metal centres. This mixed-valence character leads to a range of possible electronic transitions giving rise to the distinct absorption features shown in Figure 7.2, where distinguishable features can be observed at 400 nm, 740 nm, and 1200 - 1400 nm. The 400 nm absorption feature has been assigned to a ligand-to-metal charge transfer (LMCT) from oxygen to Co^{II}. The 740 nm feature can be attributed either to LMCT from oxygen to Co^{III} or to metal-to-metal charge transfer (MMCT) from Co^{III} to Co^{II}. The MMCT case is similar to the intervalence charge transfer discussed for WO_3 in Chapter 6, but in this case implies charge transfer from octahedral to tetrahedral sites rather than from an oxygen vacancy site to a bulk-like site in the crystal. Finally, the NIR absorption feature is identified as a Co^{II} to Co^{III} MMCT transition [29, 31, 32].

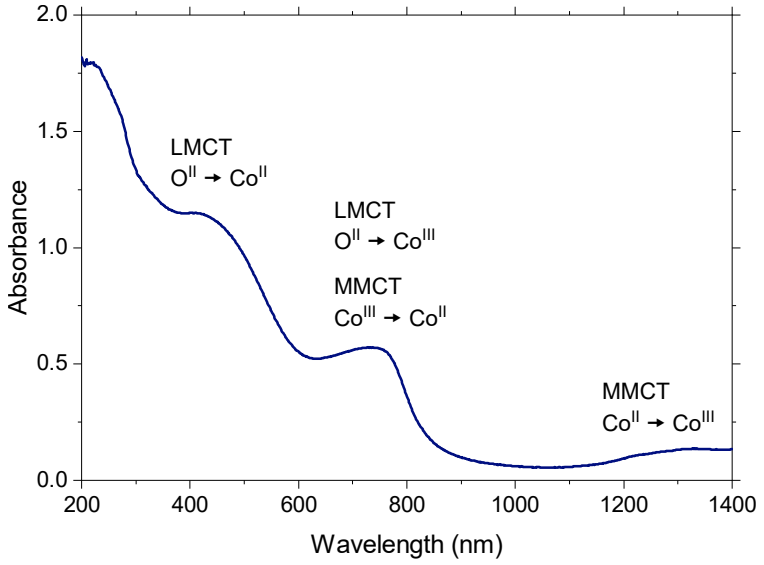

Figure 7.2: Absorbance spectrum of a Co_3O_4 thin film. Assignments of absorption features to ligand-to-metal charge transfer (LMCT) and metal-to-metal charge transfer (MMCT) transitions are indicated.

The transient absorption spectra Co_3O_4 following 740 nm excitation are shown in Figure 7.3 for a number of pump-probe delays between 0.5 ps - 6.0 ns. While excitation at 740 nm primarily induces the oxygen to Co^{III} LMCT/Co^{III} to Co^{II} MMCT transitions indicated above, other excitation wavelengths have been shown to produce essentially identical spectra [33], suggesting that the excited state probed here is general for Co_3O_4 irrespective of the selected transition. The transient spectra can broadly be divided into two regions: a structured region below 900 nm, which corresponds to the spectral region where the film absorbs more strongly, and a broad

region with little structure above 900 nm, corresponding to the spectral region where the material absorbs comparably weakly. The bleach components below 550 nm, around 750 nm, and above 1200 nm match the positions of the absorption features in Figure 7.2 well, suggesting that photoexcitation bleaches all of the described transitions as will be discussed further below in the context of Stark broadening. The most pronounced spectral evolution occurs within the first picosecond after excitation, where especially the broad NIR signal is characterised by a rapid decay. Interestingly, this fast decay appears to coincide with a growth of the peak around 600 nm, which is either due to the rapid rise of an excited state absorption or the rapid decay of the overlapping bleach signal at wavelengths below 600 nm. Both these possibilities will be explored in the next paragraph. Following this rapid initial decay, the probed transient spectra are largely dominated by the structured component which decays much more slowly.

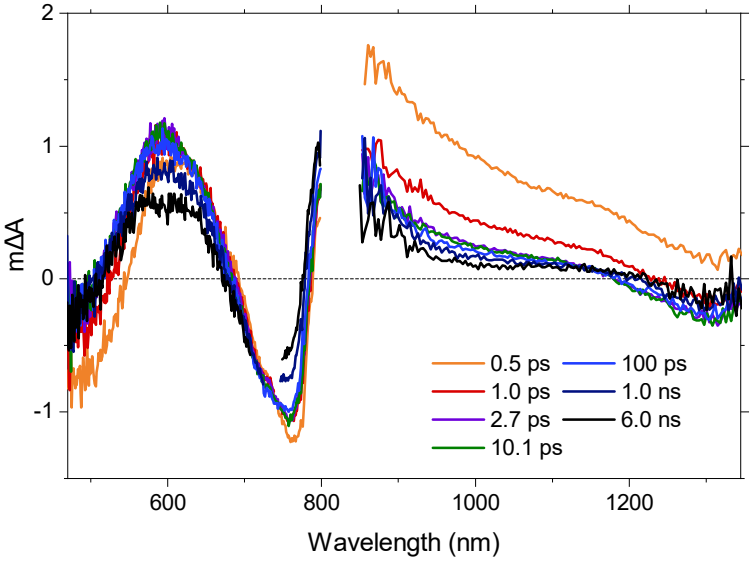

Figure 7.3: Transient absorption spectra of Co_3O_4 upon excitation at 740 nm using a fluence of 0.10 mJ cm^{-2}, corresponding to 2×10^{14} cm^{-2} photons absorbed.

The rapid initial evolution of the excited state is investigated further using global analysis, where the entire dataset is fitted to a kinetic model. Since the decays on the later ps and ns timescale are slow and non-exponential, only the initial signal over the first 4.5 ps is analysed in this way, focussing on the rapid initial decay dynamics. Two components are required to describe the dynamics over this temporal range, capturing both the rapidly decaying and long-lived parts of the signal. As indicated above, two plausible kinetic models are considered here where these two components are either connected or independent of each other: In the first case, the sequential model $A \rightarrow B$ is used, where component A is generated following excitation and then evolves into component B. In the second case, both A and B are generated directly upon excitation. A

then decays without generating B, and the population of the long-lived component B remains constant throughout this initial time window. The kinetics obtained from this global fit and the resulting component spectra are shown in Figure 7.4. Figure 7.4a,b correspond to the first case where the sequential model is used, whereas Figure 7.4c,d correspond to the second case where B is taken as a constant component. Both models produce a very good fit to the data (exemplarily shown in Figure D.1), which confirms that two components are sufficient to describe the observed dynamics and suggests that A indeed follows an exponential decay.

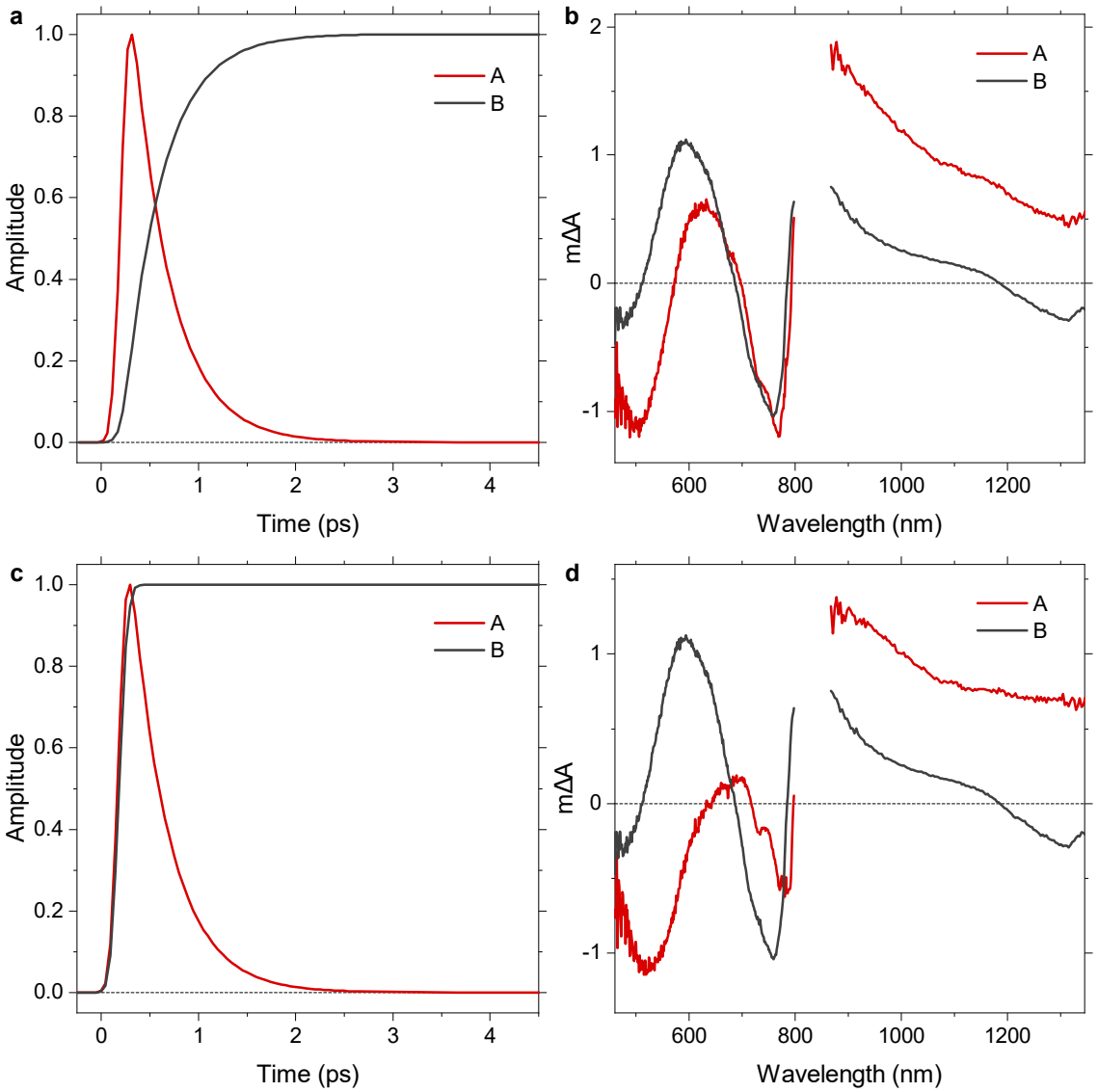

Figure 7.4: Global target analysis of the first 4.5 ps of a Co_3O_4 dataset acquired using an excitation wavelength of 740 nm and a fluence of 0.10 mJ cm^{-2}. Model 1: (**a**) Global fit kinetics and (**b**) species associated spectra using the evolutionary sequential model $A \rightarrow B$. Model 2: (**c**) Global fit kinetics and (**d**) species associated spectra using an exponentially decaying component A in the presence of a non-decaying constant component B.

In both cases, A decays with a rate constant of $2.6\,\mathrm{ps}^{-1}$ ($\tau = 0.4\,\mathrm{ps}$) as its decay is independent of whether or not B is produced in the course of its disappearance. The primary difference between the two models is the component spectrum of A, because it is affected by the presence or absence of the long-lived component B on the timescale of its decay. The main spectral features of the rapidly decaying component A, consistent between both models, are a bleach below 600 nm and a broad excited state absorption above 900 nm. In contrast, the component spectrum of B is essentially the same for both models and corresponds to that of the long-lived transient signal.

As outlined in Section 7.1, one possible origin of the structured transient spectra observed in spectral regions of relatively strong absorption is a perturbation of the ground state absorption by the electric fields between photogenerated charges, i.e. a Stark effect induced by the generated charge carriers. This perturbation can manifest as a change in the polarisability or in the dipole moment of the sample, which gives rise to signals that resemble the first or second derivative of its ground state absorption, respectively [21]. To investigate the possibility of derivative-like contributions to the transient signal, derivates of the ground state absorbance spectrum shown in Figure 7.2 were calculated from a high-quality Gaussian fit of the absorbance (Figure D.2). This fit procedure allows to eliminate random measurement noise which would otherwise dominate the calculated derivatives, especially in the case of the second derivative.

Figure 7.5a compares the transient spectrum of the rapidly decaying component A shown in Figure 7.4d to the first and second derivative of the ground state absorbance. The spectrum below 800 nm matches the first derivative rather well, which suggests that the rapid initial signal decay is due to the decay of a polarisable excited state [21, 24]. Such a polarisable excited state can broadly be associated with the presence of relatively mobile photogenerated charge carriers, which would suggest that the rapid decay of A can be associated with a rapid localisation of these mobile charges. The broad NIR excited state absorption above 800 nm in the transient signal matches neither of the derivatives, which is expected because there are no strong optical transitions in this spectral region that could be perturbed by the electric fields between photogenerated charges. Therefore, it is likely that this broad NIR transient absorption results from an absorption of the mobile charges themselves. This assignment places these mobile charges either in the conduction band or in shallow trap states very close to it. As introduced in Section 7.1, the absorption of free carriers is classically described using Drude absorption [19, 20], which mainly occurs in the infrared range and corresponds to an intra-band excitation of charges. It is thus possible that the broad absorption observed here corresponds to the high energy tail of such Drude-like carrier absorption features [34].

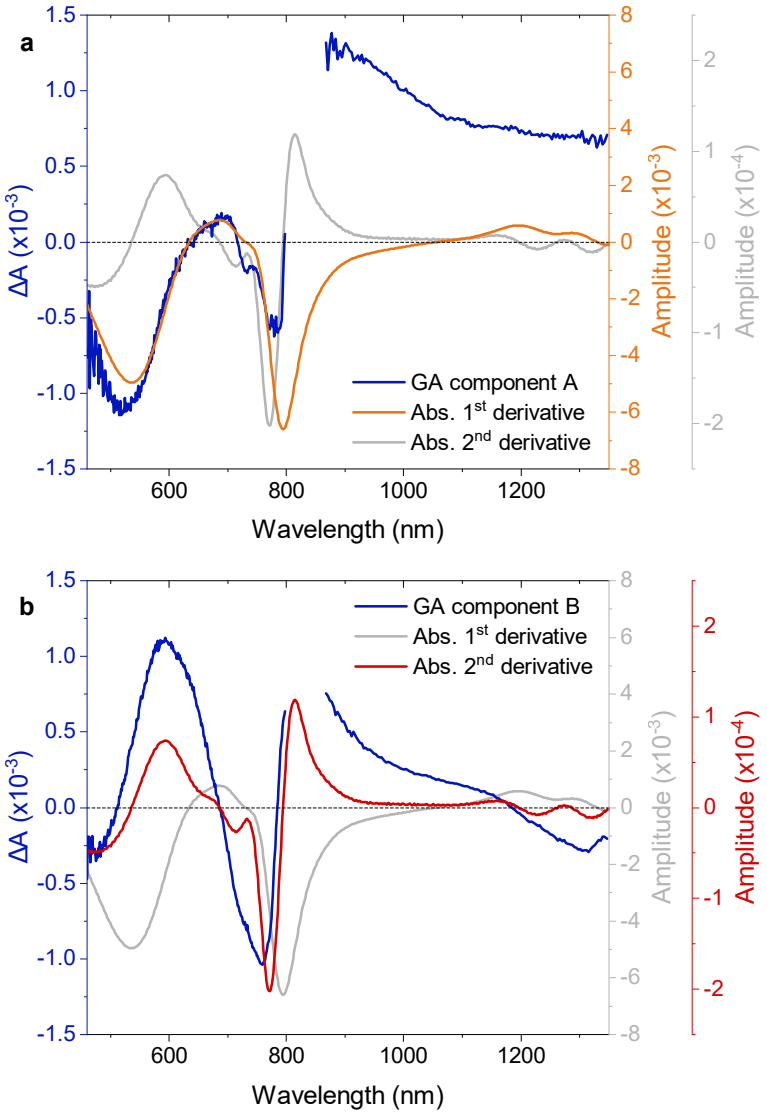

Figure 7.5: Co_3O_4 transient absorption spectra of (**a**) the rapidly decaying component *A* and (**b**) the long-lived component *B* as determined via global analysis using model 2 in Figure 7.4, together with the first and second derivative of the Co_3O_4 absorbance spectrum shown in Figure 7.2.

In contrast, the transient spectrum of the long-lived component *B* resembles the second derivative of the steady state absorbance as shown in Figure 7.5b. An underlying assumption of the derivatives calculated here is that all transitions are perturbed equally by the electric fields between photogenerated charges. Since there is little reason why this should be the case, the match in the relative amplitudes between transient signal and second derivative could be improved further by considering transition-specific degrees of perturbation. The positions of the zero crossing points are likely affected less by the degree of perturbation of a given transition, and their good agreement between transient signal and second derivative is thus particularly striking. The second derivative-like shape suggests that the transient signal of the long-lived

component B is due to an excited state with dipolar character [21, 24]. This behaviour can be associated with the presence of localised positive and negative charges in the material, which effectively behave like permanent dipoles on the timescale of their own lifetime. Since the distribution of these charges is random, the orientation of the electric fields between them is also random. These randomly oriented electric fields redshift the transitions of some unit cells and blueshift those of others, depending on the alignment of the respective unit cell with the dipolar electric field. For the simultaneous observation of many unit cells as is the case for the probe pulses employed here, these shifts thus result in the broadening of an absorption feature, which induces bleaching at the positions of the original transitions [22, 23] as indicated above. In materials with closely spaced optical transitions such as Co_3O_4 investigated here, this so-called Stark broadening of optical transitions leads to a second derivative-like shape [22, 25]. This description is in good agreement with studies on metal selenides [22–24] and halide perovskites [25], where similar observations of second derivative-like transient signals have been made.

To further elucidate the nature of the rapid initial decay, additional Co_3O_4 datasets were acquired at a range of different fluences around the $0.10\,\mathrm{mJ\,cm^{-2}}$ used for the dataset discussed above. Figure 7.6 shows transient kinetics for fluences ranging between 0.01 - $0.71\,\mathrm{mJ\,cm^{-2}}$, probed at 500 nm and 1150 nm where the fast decay component can be clearly observed. The kinetic traces were divided by the fluence at which they were recorded, and ΔA is therefore given in units of $1/(\mathrm{J\,cm^{-2}}) = \mathrm{J^{-1}\,cm^2}$. This division yields a ΔA-per-fluence signal for different intensities, which fall on top of each other if the underlying transient signal scales linearly with intensity. Any non-linear behaviour produces a continuous deviation of the decay profile over the used intensity range, which can be expected especially at high intensities where saturation effects are common.

The fluence-scaled kinetics shown in Figure 7.6 largely overlap, suggesting that the transient signal mostly scales linearly with intensity. Considering the wide range of used intensities, where the highest intensity is 71 times larger than the lowest one, only little variation in the decay profile of the fast component is observed. This is further confirmed by applying the above global analysis routine to the full range of used fluences, where the rate constant for the decay of the fast component lies between 2.3 - $2.6\,\mathrm{ps^{-1}}$ as shown in Table 7.1, with no apparent trend over the used intensity range. The fact that the rapid initial decay is largely insensitive to the number of absorbed photons precludes its assignment to a bimolecular recombination process, for which a strong intensity dependence of the decay would be expected. Instead, a localisation process appears more likely, in good agreement with the first derivative absorbance. Such a

localisation process can be expected to occur largely independently of excitation intensity if the localisation is due to self-trapping. If localisation occurs due to trapping into physical defect states, excitation intensity independence would imply that a sufficiently high number of localised states are available to accommodate the photogenerated charge carriers at all used fluences.

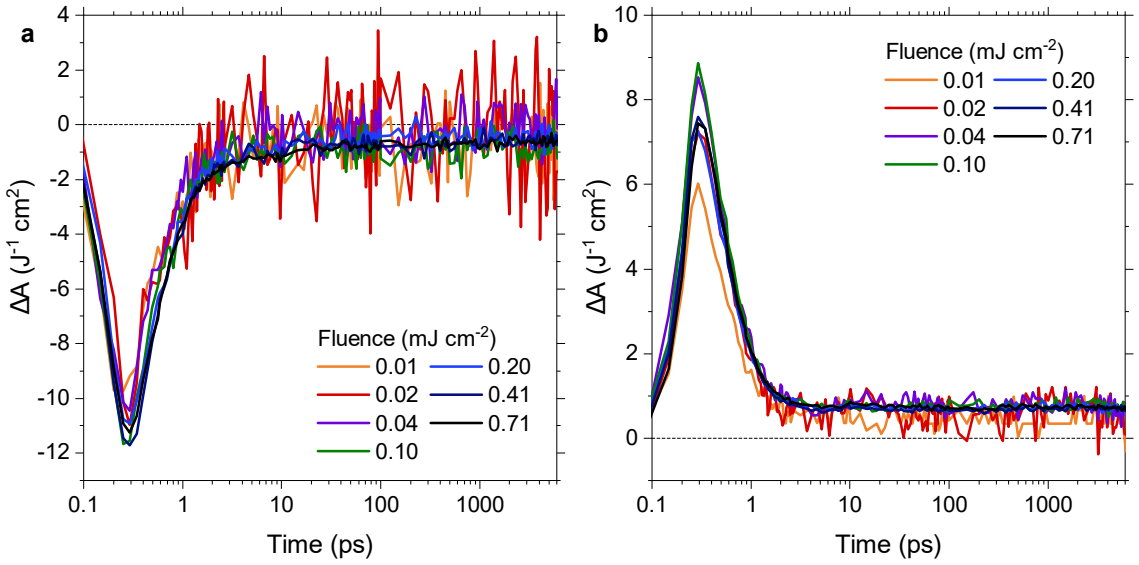

Figure 7.6: Fluence-scaled transient kinetics probed at (**a**) 500 nm and (**b**) 1150 nm upon excitation of Co_3O_4 at 740 nm. Each kinetic trace was divided by the fluence used to record it.

Quantification of the intensity dependence of the long-lived signal proves more difficult because its long lifetime only allows to partially resolve its decay in the 6 ns probe window of the used setup, as demonstrated in Figure 7.7 for kinetic traces probed at 600 nm. The signal starts to decay on the tens of picoseconds timescale with generally faster decays at higher fluences, before traces converge again at around 6 ns. The signal amplitude at 6 ns corresponds to about 60% of the maximum signal amplitude at this wavelength. Therefore, the half-lifetime for the intensity dependent part of the decay can be estimated by determining the time at which the overall signal reaches 80% of its initial amplitude ($t_{80\%}$). Since this analysis only considers the early intensity-dependent part of the decay, the estimated half life times can be seen as an upper limit that captures the maximum difference between fluences. As shown in Table 7.1, a 71 - fold increase in fluence results in a ∼6 - fold acceleration of the long-lived decay component. This intensity dependence can be considered rather moderate as differences with fluence are much lower than what would be expected for bimolecular recombination of free charges, where a 71 - fold acceleration would be expected under these conditions. Therefore, an assignment to localised charges with reduced mobility seems reasonable, for instance charges trapped at defect sites.

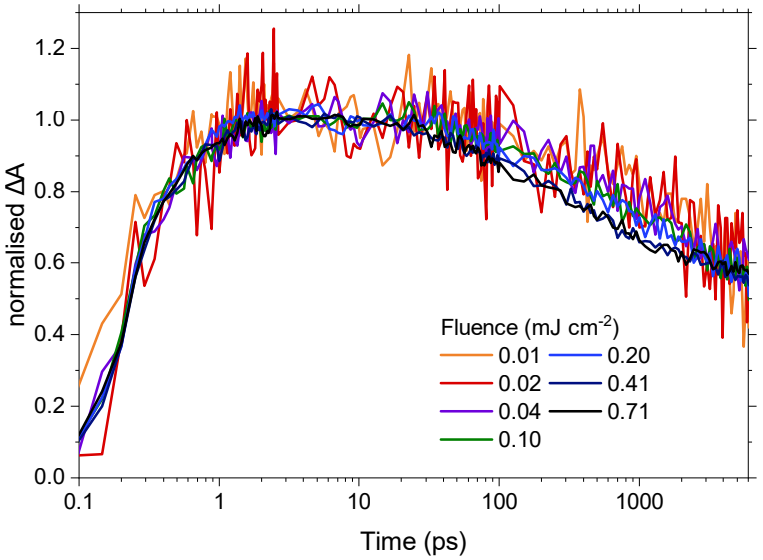

Figure 7.7: Normalised transient kinetics probed at 600 nm upon excitation of Co_3O_4 at 740 nm using a range of different fluences.

Table 7.1: Rate constants for the decays of the rapidly decaying initial component k_A and half-lifetimes for the long-lived component $t_{50\%}$(B) in Co_3O_4 recorded using an excitation wavelength of 740 nm. k_A was obtained from global analysis using the sequential model $A \rightarrow B$ as detailed above. An estimate for k_B was obtained by applying linear fits to the 0.2 - 2.0 ns region of the kinetics probed at 600 nm to determine the time at which the signal has reached 80% of its initial amplitude, which is where the largest variation of lifetime with fluence is observed as shown in Figure 7.7.

Fluence ($mJ\,cm^{-2}$)	k(A) (ps^{-1})	Estimated $t_{50\%}$(B) (ns)
0.01	2.3	1.1
0.02	2.4	1.1
0.04	2.6	0.8
0.10	2.6	0.5
0.20	2.4	0.4
0.41	2.5	0.3
0.71	2.5	0.2

The presented results demonstrate that the excited state decay of Co_3O_4 can be divided into two decay components: Firstly, a rapidly decaying component A, which decays with a rate constant of $\sim 2.5\,ps^{-1}$ and spectrally dominates in the NIR region where the used Co_3O_4 film absorbs only weakly. This component decays intensity independent and its decay is assigned to the localisation of mobile charges, in good agreement with the first derivative-like shape of its transient spectrum. Secondly, Co_3O_4 exhibits a long-lived component B which dominates in the spectral region where the material absorbs more strongly. The decay of this long-lived component accelerates only moderately when the used fluence is increased, and it is thus assigned to the presence of relatively localised charges, in line with the dipolar excited state suggested by

its second derivative-like transient spectrum.

7.2.2 Cr_2O_3

To explore how generalisable the behaviour observed for Co_3O_4 is for other metal oxides, the d^3 open shell oxide Cr_2O_3 is investigated next. As shown in the absorbance spectrum in Figure 7.8, Cr_2O_3 exhibits a range of transitions including an intense oxygen to Cr^{III} LMCT transition at 275 nm with a d-d shoulder at 365 nm, plus two isolated d-d transitions at 460 nm and 600 nm. Interestingly, this material thus allows for selective excitation of localised d-d transitions as will be discussed further below.

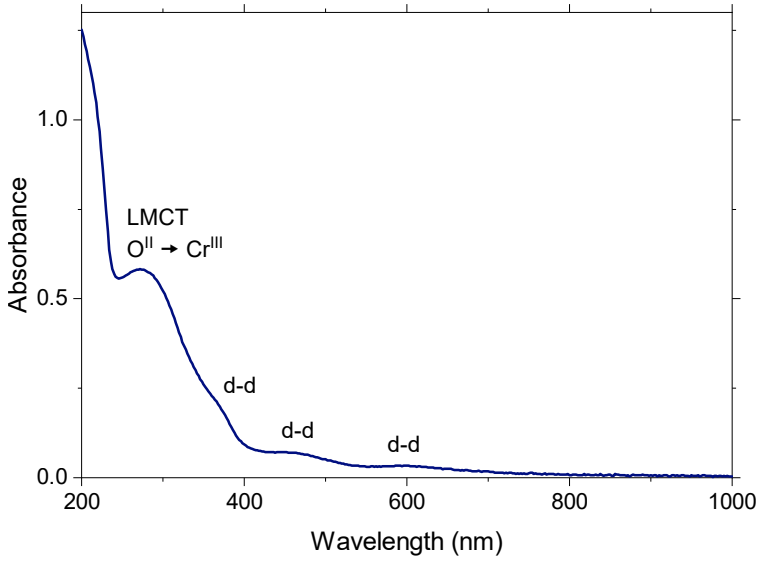

Figure 7.8: Absorbance spectrum of a Cr_2O_3 thin film. Assignments of absorption features to ligand-to-metal charge transfer (LMCT) and d-d transitions are indicated.

Figure 7.9 shows the transient spectrum recorded upon excitation at 365 nm, reflecting the simultaneous excitation of the oxygen to Cr^{III} LMCT transition and the d-d transition at this wavelength. Since the d-d transition is only a shoulder of the more intense LMCT transition, the primary signal contribution can the expected to result from LMCT excitation. Similar to Co_3O_4, a rapid initial decay is observed, in this case both in the visible and the NIR range. Since the d-d transitions absorb only weakly, the observation of this rapid decay in spectral regions without strong optical transitions is in good agreement with the Co_3O_4 data. Although these d-d transitions only absorb weakly, a long-lived structured signal is observed following the fast initial decay.

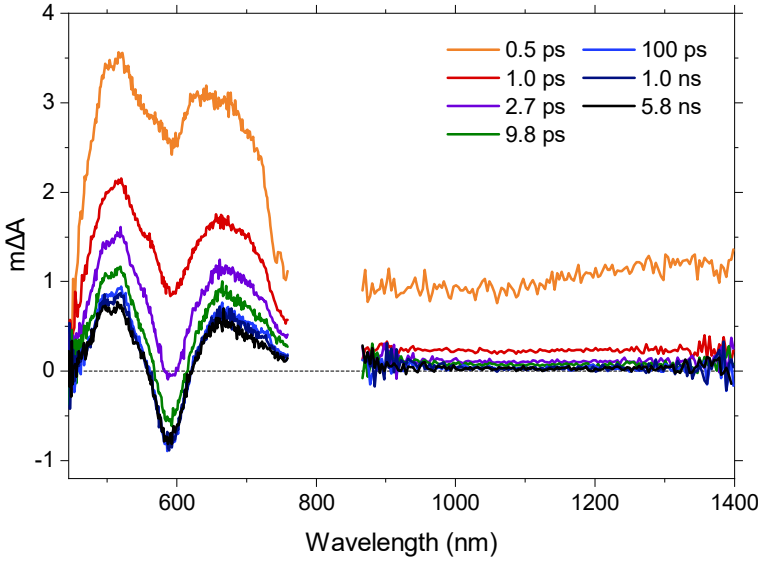

Figure 7.9: Transient absorption spectra of Cr_2O_3 upon excitation at 365 nm using a fluence of 0.57 mJ cm^{-2}, corresponding to 2×10^{14} cm^{-2} photons absorbed.

Fluence-scaled transient kinetics, probed both at the 510 nm peak and at 1150 nm in the broad NIR region, are shown in Figure 7.10. Like in Co_3O_4, the NIR region (Figure 7.10b) is dominated by a rapid initial decay, which again occurs with a rate that is largely independent of excitation intensity. However, an additional intensity-dependent component is present in the case of Cr_2O_3 and can be clearly observed once the rapid initial decay has taken place after ~1 ps. This intensity-dependent component is more pronounced when probed in the visible range (Figure 7.10a) where the different kinetics converge towards the ns timescale, which indicates that this intensity dependent component might be similar to that observed in Co_3O_4 between 10 ps and 6 ns, but already occurs much earlier in Cr_2O_3. At half-amplitude of the intensity dependent component (2.8 J^{-1} cm^2), the half-lifetime decreases by a factor of 6 when the fluence is increased 25-fold. This is a larger variation than for Co_3O_4 but still only corresponds to 24% of the bimolecular limit, suggesting that the underlying charges are also at least partially localised. The intensity dependent component already affects the transient signal soon after the signal rise and is difficult to account for as it decays non-exponentially. As a result, global analysis does not yield satisfactory fits for Cr_2O_3 and is thus not pursued for this material.

The long-lived component can be characterised further by simply considering the transient spectrum at the longest delay time (here 5.8 ns), where contributions from other components are negligible. The appearance of transient bleach signals at the positions of the d-d transitions in Figure 7.9 is reminiscent of the Stark broadening observed in Co_3O_4. As shown in Figure 7.11, the second derivative of the Cr_2O_3 absorbance spectrum indeed resembles the transient spectrum

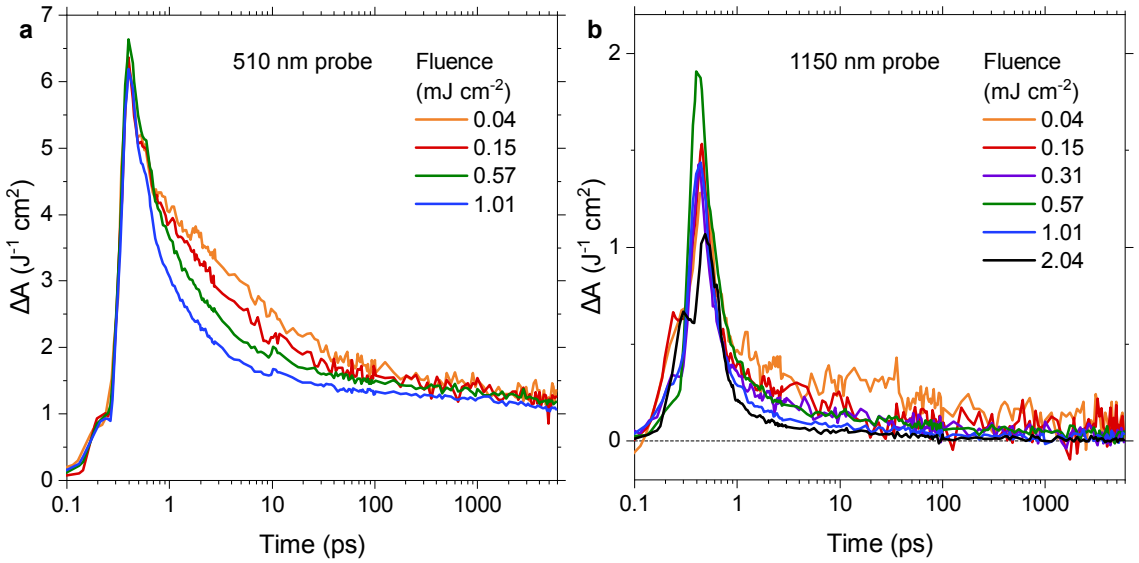

Figure 7.10: Fluence-scaled transient kinetics probed at (**a**) 510 nm and (**b**) 1150 nm upon excitation of Cr_2O_3 at 365 nm. Each kinetic trace was divided by the fluence used to record it.

at 5.8 ns, suggesting a dipolar excited state at this delay time due to the presence of localised charges like in Co_3O_4.

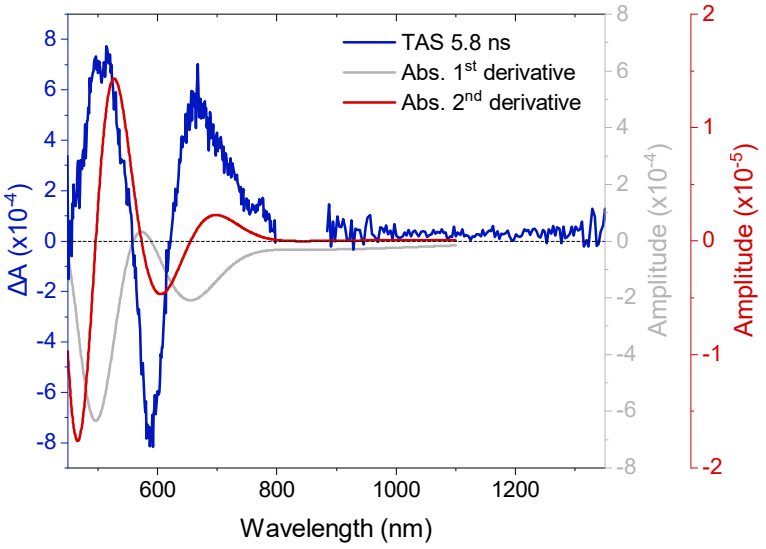

Figure 7.11: Cr_2O_3 transient absorption spectrum of the long-lived component probed at 6 ns upon 365 nm excitation using a fluence of 0.57 mJ cm^{-2}, together with the first and second derivative of the Cr_2O_3 absorbance spectrum shown in Figure 7.8.

While all excited states discussed so far were generated primarily via charge transfer transitions, Cr_2O_3 also offers the possibility to produce inherently localised excited states through its isolated d-d transitions in the visible range, where the excited carriers are physically confined to a single metal centre. Figure 7.12 compares transient spectra obtained by LMCT excitation at 330 nm

and by d-d excitation at 460 nm. Strikingly, the d-d excitation (Figure 7.12b) does not produce any rapidly decaying initial component, causing the NIR range to exhibit almost no signal, while the structured component that dominates at longer times is observed in both cases. The absence of the rapidly decaying component upon d-d excitation is in good agreement with its assignment to a localisation of relatively mobile charges, as such localisation cannot occur if the charges produced in the excitation event are already localised. The dipolar character of the excited state due to localised charges, as suggested by Stark broadening, is maintained upon d-d excitation in line with the localised character of the generated charges.

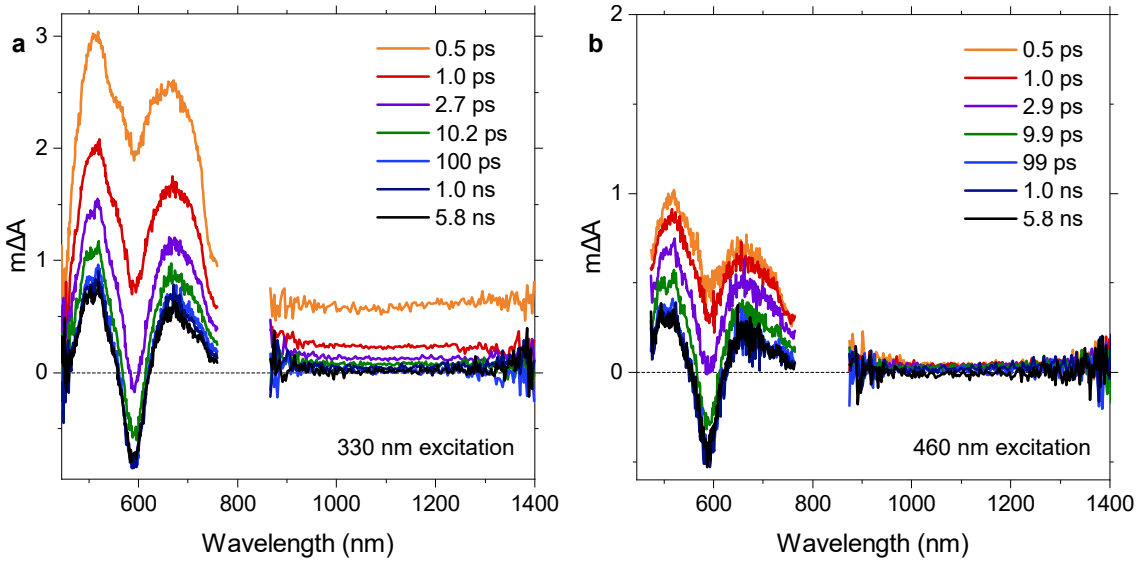

Figure 7.12: Transient absorption spectra upon excitation of Cr_2O_3 at (**a**) 330 nm and (**b**) 460 nm, obtained using 2×10^{14} cm^{-2} photons absorbed in both cases. The corresponding fluences were 0.39 mJ cm^{-2} and 1.43 mJ cm^{-2} for 330 nm and 460 nm excitation, respectively.

Figure 7.13 shows transient kinetics probed at 510 nm and 1150 nm for four different excitation wavelengths: 330 nm (LMCT transition), 365 nm (primarily LMCT transition), and 460 nm and 600 nm (d-d transitions). For all wavelengths, the fluence was chosen such that 2×10^{14} photons would be absorbed per cm^2 in order to minimise differences due to carrier density effects in the kinetic profiles. It can be seen that the probed kinetics generally group according to the dominating transition, i.e. LMCT or d-d. For the d-d excitations, oscillating features at early times are observed below ∼1 ps which are identified as instrument response-related artefacts resulting from the high fluences required to reach 2×10^{14} cm^{-2} photons absorbed for these weak transitions. This assignment is corroborated by measurements of a blank quartz slide under the same conditions (Figure D.4), demonstrating that the essentially same artefacts are observed in the absence of the Cr_2O_3 film. Disregarding these artefacts, only a negligible background signal

is observed upon d-d excitation in the NIR (Figure 7.13b), whereas LMCT excitation generates the rapidly decaying component at early times. The difference can be observed most clearly from ∼0.5 ps, by which time the artefacts have decayed. In contrast, the structured signal in the visible range is also produced through d-d excitation, albeit with a 60% - 70% lower amplitude. This difference in amplitude suggests that the excited state produced upon LMCT excitation plus subsequent localisation is not exactly the same as the localised excited state produced upon d-d excitation, and might be due to different distributions of photogenerated carriers which could lead to variations in electric field strength between the two types of transitions.

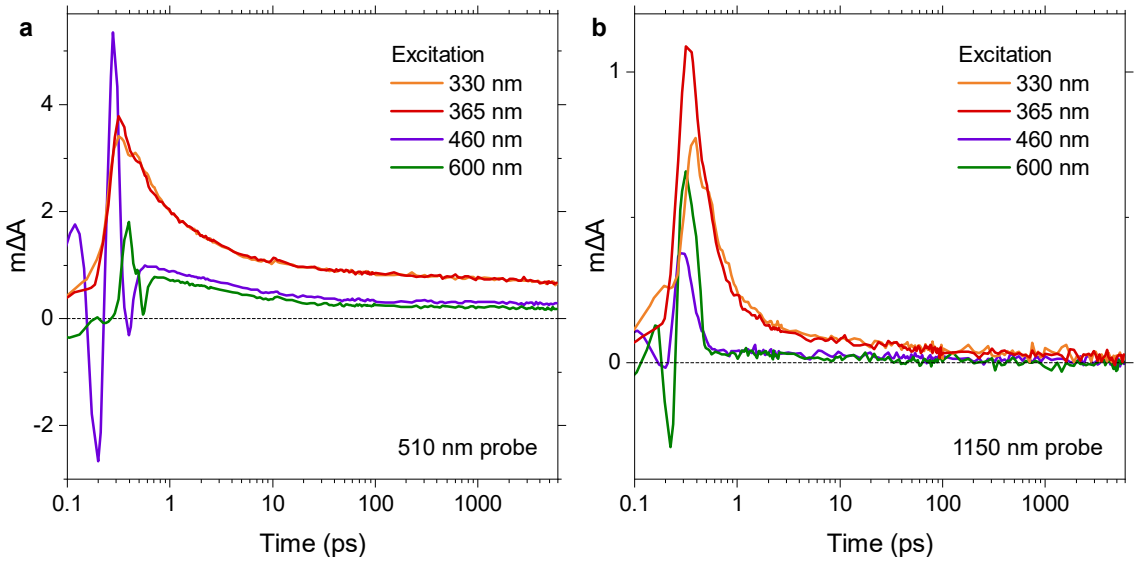

Figure 7.13: Transient absorption kinetics probed at (**a**) 510 nm and (**b**) 1150 nm upon excitation of Cr_2O_3 using excitation wavelengths between 330 - 600 nm, obtained with 2×10^{14} cm^{-2} photons absorbed in all cases. The longer excitation wavelengths show pronounced instrument response-related artefacts at early times, which can be attributed to the high fluences which were required to match the number of photons absorbed at these wavelengths. The used fluences were 0.39 mJ cm^{-2}, 0.57 mJ cm^{-2}, 1.43 mJ cm^{-2}, and 2.83 mJ cm^{-2} for 330 nm, 365 nm, 460 nm, and 600 nm excitation, respectively.

7.2.3 α-Fe_2O_3

α-Fe_2O_3, hereafter simply referred to as Fe_2O_3, is one of the most widely used materials in photoelectrochemical cells. Its widespread use have made it one of the most studied metal oxides, and it is here put in context to the two previously discussed materials to facilitate comparisons to the literature. Fe_2O_3 exhibits a d^5 configuration and is isostructural to Cr_2O_3, exhibiting the same corundum structure [35]. As shown in Figure 7.14, Fe_2O_3 exhibits an oxygen to Fe^{III} LMCT transition at 390 nm with a d-d shoulder at ∼530 nm. These absorption features

are very similar to those observed in Cr_2O_3 as might be expected, but are shifted towards lower energy, lending Fe_2O_3 its visible light absorption. Isolated d-d transitions are not resolved in the case of Fe_2O_3.

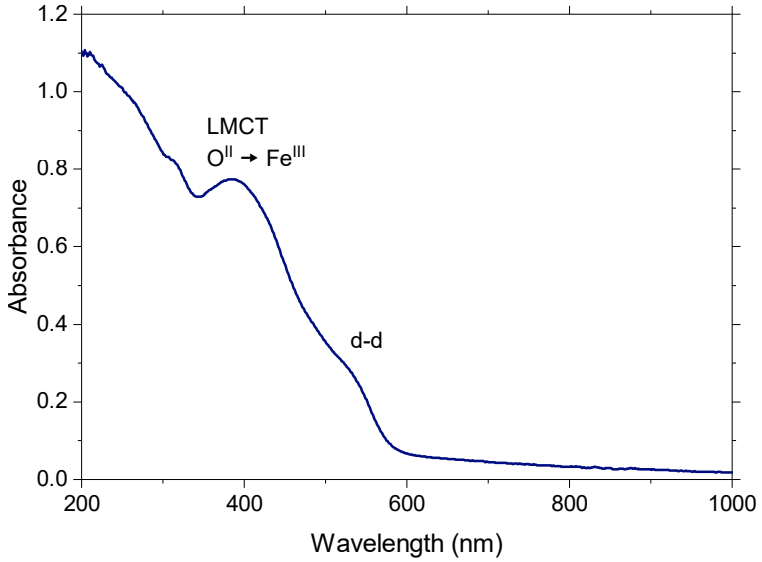

Figure 7.14: Absorbance spectrum of a Fe_2O_3 thin film. Assignments of absorption features to ligand-to-metal charge transfer (LMCT) and d-d transitions are indicated.

Like for Co_3O_4 and Cr_2O_3, the Fe_2O_3 transient spectra shown in Figure 7.15 exhibit a rapid initial decay in the spectral region of weak optical absorption above ∼650 nm, most clearly observed above ∼1200 nm. More long-lived, structured features are observed around the onset of strong optical absorption, with a dominant sharp peak around 580 nm. As shown in Figure 7.16, the second derivative of the absorbance spectrum matches well with this sharp transient peak, again suggesting an excited state of dipolar character due the presence of localised charges. Indeed, this 580 nm peak has previously been assigned to an optical transition from the valence band into localised states close to the conduction band edge [36–38], in good agreement with this assignment.

Fluence-scaled transient kinetics shown in Figure 7.17 demonstrate the presence of the fast initial decay component, which can be most clearly observed in the NIR (Figure 7.17b) at high fluences. At lower fluences, an intensity dependent component is present like in Cr_2O_3, but appears to be more pronounced in the case of Fe_2O_3. When probed at the 580 nm peak in the visible range, the initial amplitude of the fluence-scaled transient signals is reduced at higher fluences, but all kinetic traces converge around 6 ns. This reduction in initial amplitude might suggest that the intensity dependent component appears within the time resolution of the experiment, in contrast to Cr_2O_3, where its it can be distinguished from ∼1 ps, and Co_3O_4, where it is observed from

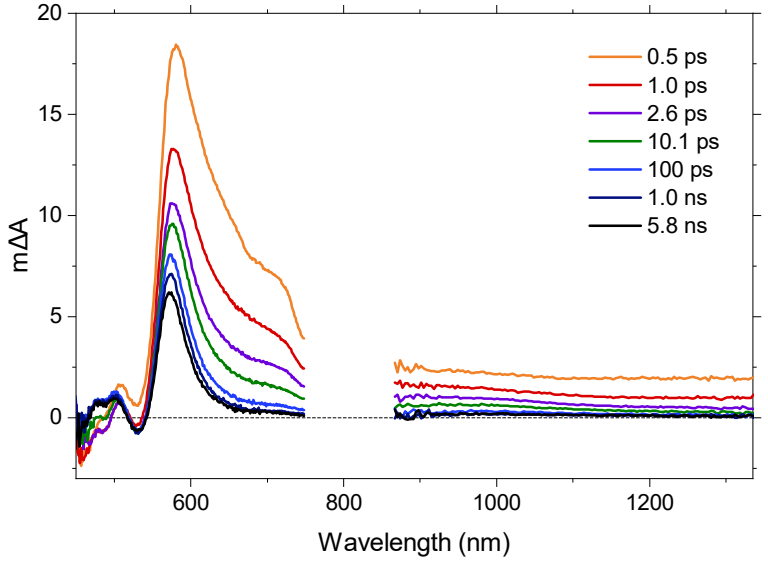

Figure 7.15: Transient absorption spectra of Fe_2O_3 upon excitation at 400 nm using a fluence of 0.357 mJ cm^{-2}, corresponding to 2×10^{14} cm^{-2} photons absorbed.

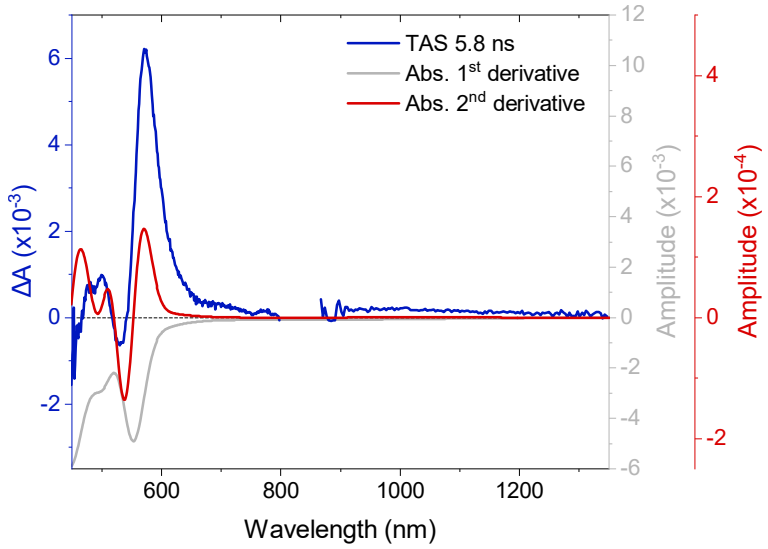

Figure 7.16: Transient absorption spectrum of the long-lived component in Fe_2O_3 probed at 6 ns upon 400 nm excitation using a fluence of 0.57 mJ cm^{-2}, together with the first and second derivative of the Fe_2O_3 absorbance spectrum shown in Figure 7.14.

~10 ps. The earlier appearance of the intensity dependent component in this material series appears to roughly correlate with how dominant it is with respect to the rest of the signal.

Overall, the same three components can be distinguished in all of the three materials discussed so far in this chapter: (i) an intensity independent rapid initial decay, assigned to reactively mobile charges in or near the conduction band, (ii) an intensity dependent component with varying onset time, and (iii) a long-lived structured component in spectral regions of strong optical absorption, assigned to localised charges.

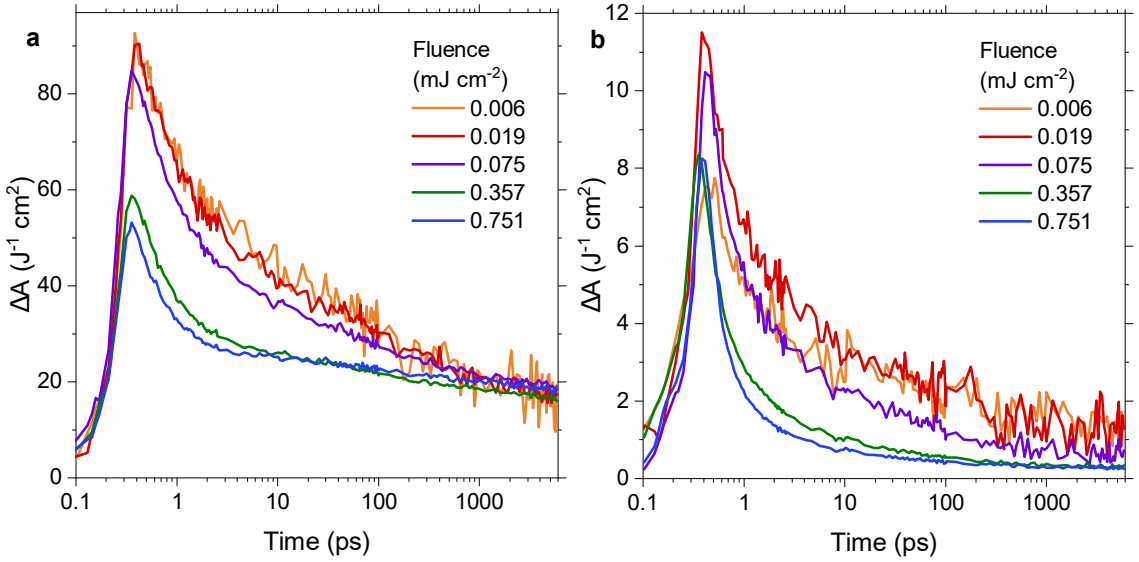

Figure 7.17: Fluence-scaled transient kinetics probed at (**a**) 580 nm and (**b**) 1150 nm upon excitation of Fe_2O_3 at 400 nm. Each kinetic trace was divided by the fluence used to record it.

7.2.4 Empty *d*-shells

After investigating the open *d*-shell systems Co_3O_4, Cr_2O_3, and Fe_2O_3, metal oxides with empty d-shells are now considered, i.e. materials with a d^0 electronic configuration. $BiVO_4$ is one of the highest performing photocatalyst materials as introduced in Section 2.4, and incorporates both d^0 (V^{5+}) and d^{10} (Bi^{3+}) metal centres. However, with its vanadium-dominated conduction band edge and its dominant oxygen 2p character at the valence band [39], it is similar to classic d^0 materials such as TiO_2 and WO_3 and is thus considered a d^0 oxide. As shown in Figure 7.18, the $BiVO_4$ thin film exhibits an absorption onset of around 500 nm, in good agreement with the reported ∼2.4 eV bandgap of monoclinic $BiVO_4$ [40–42].

The transient spectrum of $BiVO_4$ obtained upon excitation at 350 nm is shown in Figure 7.19, exhibiting a sharp peak at 480 nm and a broad absorption from ∼550 nm towards the NIR. The 480 nm peak dominates on the ns timescale and matches the second derivative of the absorbance spectrum as illustrated by Figure 7.19, again suggesting an assignment to localised charge carriers. The broad absorption feature dominates in the region of weak optical absorption like the broad features observed for the previously discussed open *d*-shell oxides, but appears to decay significantly more slowly.

This slower decay is further emphasized by the fluence-scaled transient kinetics of the broad absorption feature as shown in Figure 7.21b, which suggest that this broad feature is primarily composed of a decay component with a pronounced intensity dependence. In particular, there

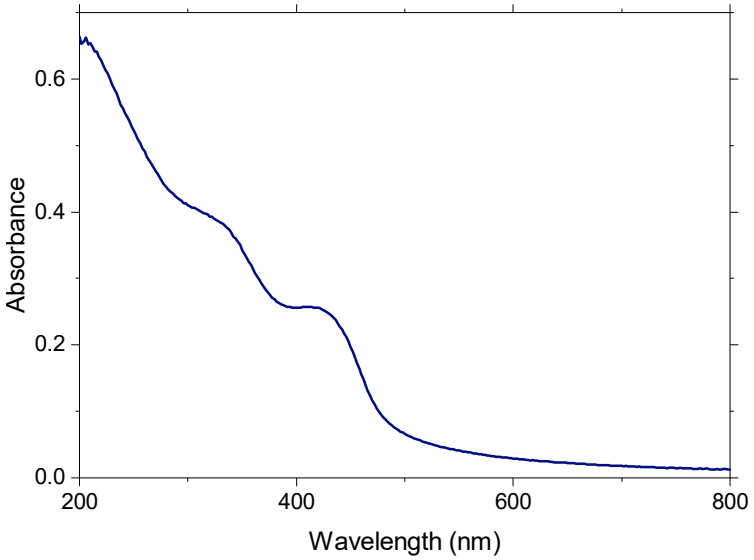

Figure 7.18: Absorbance spectrum of a $BiVO_4$ thin film.

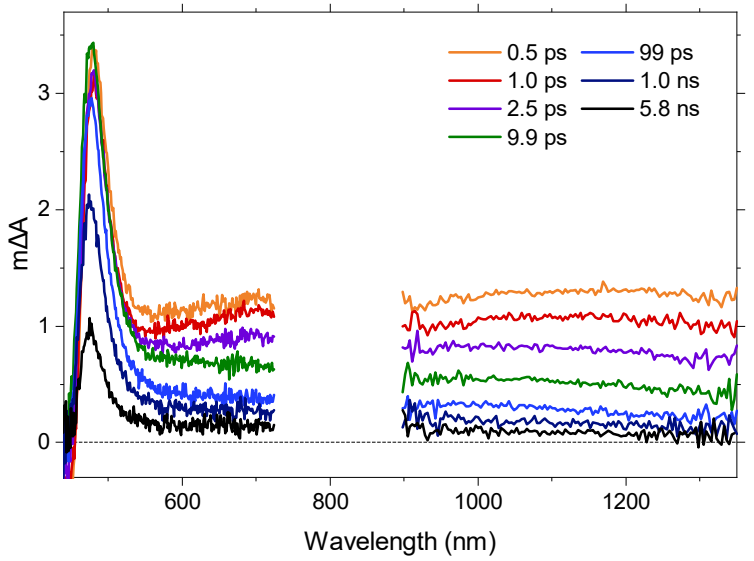

Figure 7.19: Transient absorption spectra of $BiVO_4$ upon excitation at 350 nm using a fluence of 0.22 mJ cm^{-2}, corresponding to 2×10^{14} cm^{-2} photons absorbed.

appears to be little evidence for an intensity-independent rapid decay on the early ps timescale like observed clearly in the case of Co_3O_4 and Cr_2O_3. The decay half time of the $BiVO_4$ NIR signal accelerates by a factor of ∼38 when the fluence is increased 66 - fold, which corresponds to 58% of the bimolecular limit and thus exhibits a much more bimolecular behaviour than in any of the discussed open *d*-shell oxides. The intensity dependence of the 480 nm peak is clearly more complex, with two peaks in the kinetic traces at 0.5 ps and 20 ps continuously diminishing as the fluence is increased. These features might be due to acoustic phonon modulations [43], but in any case appear to be very material-specific and are thus not considered in greater detail here. However, it can be noted that the overall lifetime of this 480 nm feature on the 100 ps -

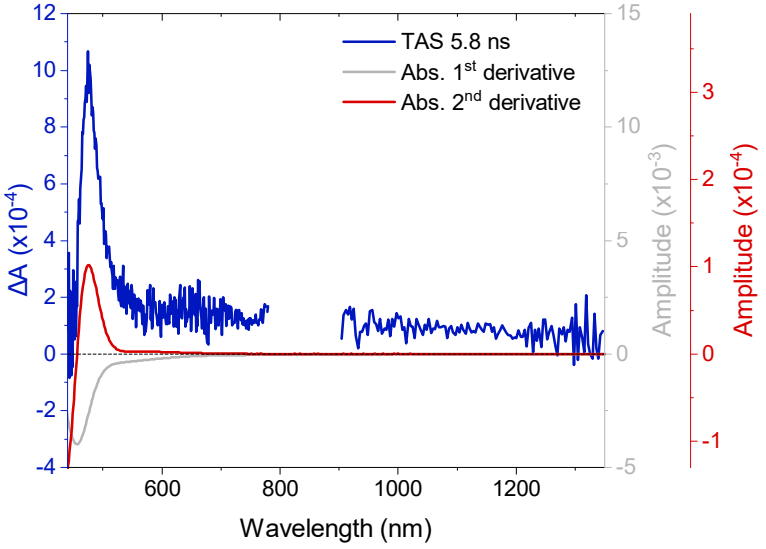

Figure 7.20: Transient absorption spectrum of the long-lived component in $BiVO_4$ probed at 6 ns upon 350 nm excitation using a fluence of 0.22 mJ cm^{-2}, together with the first and second derivative of the $BiVO_4$ absorbance spectrum shown in Figure 7.19.

6 ns timescale does not seem to be affected by the used fluence to a great extent.

The apparent absence of the rapid initial decay in $BiVO_4$ is suggests that a fast localisation like in the open *d*-shell oxides might not occur, which is in line with the more bimolecular behaviour of the intensity-dependent component, suggesting that the corresponding charges are overall less localised.

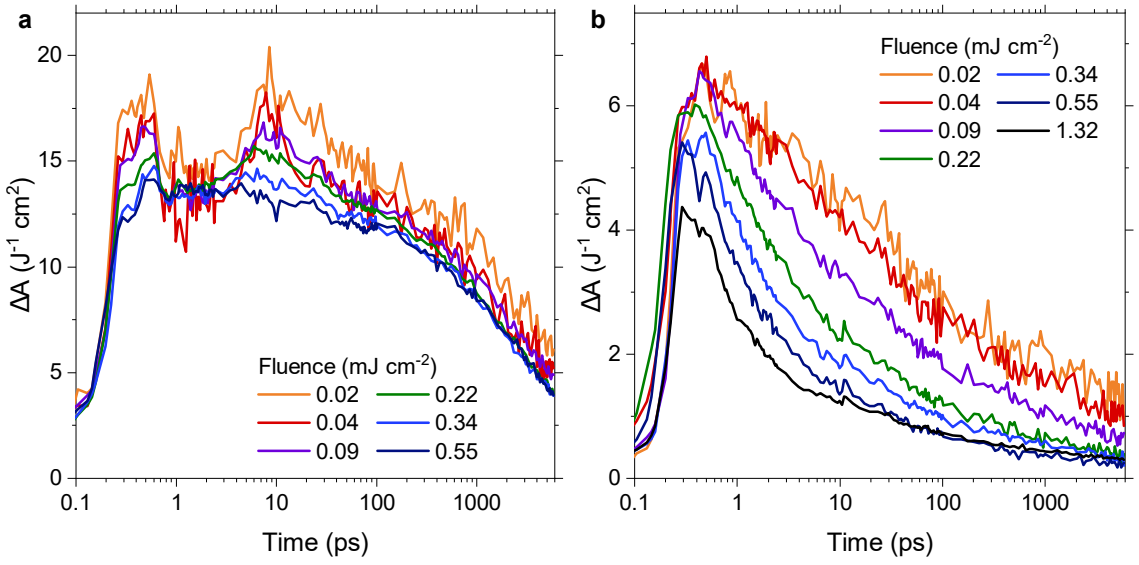

Figure 7.21: Fluence-scaled transient kinetics probed at (**a**) 480 nm and (**b**) 1150 nm upon excitation of $BiVO_4$ at 350 nm. Each kinetic trace was divided by the fluence used to record it.

Even more long-lived transient species with a similarly broad spectrum in the visible and NIR range have been reported previously for the prototypical d^0 metal oxide TiO_2 [44]. The normalised kinetics of a dense anatase TiO_2 film at 1100 nm are reproduced in here as shown in Figure 7.22. The estimated intensity dependence of the half lifetime corresponds to ~42% of the bimolecular limit, consistent with a less localised character of photogenerated charges in $BiVO_4$ compared to the discussed open *d*-shell oxides. In the case of rutile TiO_2, a shorter and less intensity dependent decay was found, assigned to the higher doping density in this polymorph [44] due to its higher defect density.

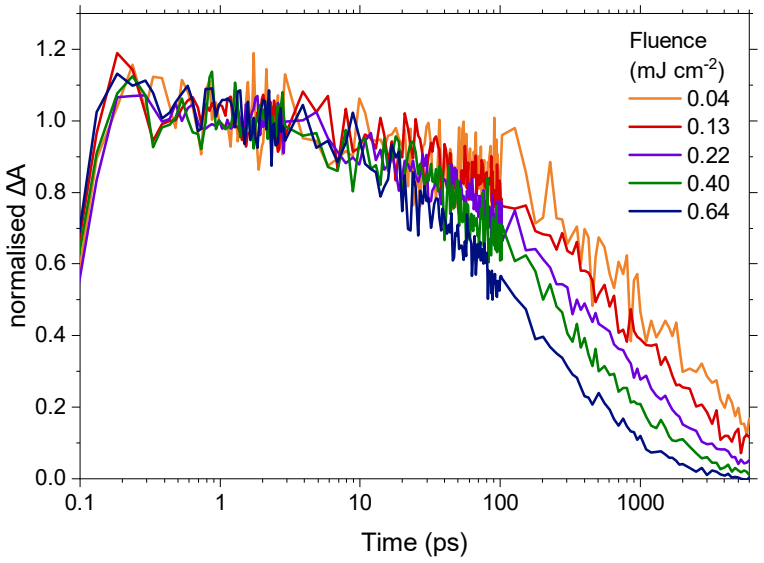

Figure 7.22: Normalised transient kinetics probed at 1100 nm upon excitation of anatase TiO_2 at 355 nm.

The d^0 metal oxide WO_3 has already been discussed in detail in Chapter 6. For better comparison to the oxide films used in the present chapter, flat WO_3 films were prepared in contrast to the nanostructured WO_3 films used in Chapter 6. Despite the different morphologies, the transient spectra shown in Figure 7.23a are remarkably similar to those of m-WO_3 shown in Figure 6.7. The fluence-scaled transient kinetics in Figure 7.23b represent the decay of the Drude-like NIR absorption feature and show an acceleration of the decay at higher fluences. While there appears to be a bimolecular component involved, the fact that the long-lived bleach signal becomes more pronounced at higher fluences complicates a more detailed analysis. Overall, WO_3 exhibits the fastest NIR decay among the empty d-shell oxides investigated herein, but in the low fluence regime its signal still about an order of magnitude more long-lived than that of the open d-shell materials discussed above.

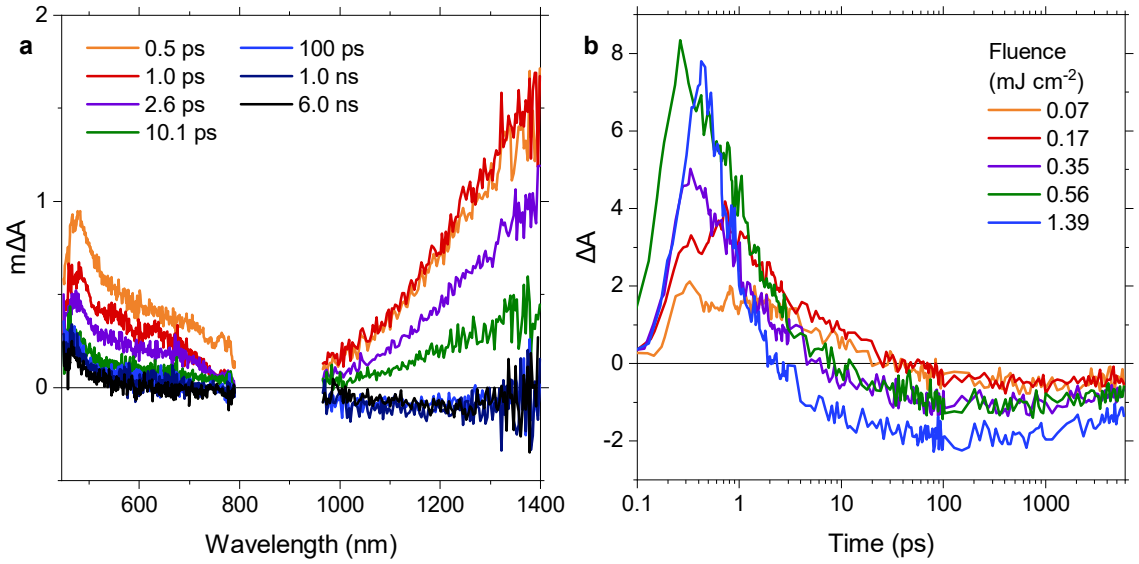

Figure 7.23: Transient absorption spectra and kinetics for WO_3 upon 350 nm excitation. (**a**) Transient absorption spectra obtained using a fluence of 0.17 mJ cm^{-2}, corresponding to 2×10^{14} cm^{-2} photons absorbed. (**b**) Fluence-scaled transient kinetics probed at 1150 nm, where each kinetic trace was divided by the fluence used to record it.

7.2.5 Effect of the bandgap size

One of the primary differences between empty/closed d-shell oxides and open d-shell oxides is their typical bandgap size. d^0 and d^{10} oxides usually have large bandgaps and thus absorb no or little light in the visible range, whereas oxides with open d-shells tend to have much smaller bandgaps due the gradual stabilisation of their d-bands. Given that fundamentally different transient features are observed in spectral regions of strong and weak optical absorption, the fixed 450 - 1400 nm (2.76 - 0.89 eV) probe window of the used transient absorption setup determines which features are observed for a given oxide depending on its bandgap. To rule out that the observed effects are simply due to variation in the bandgap size between different oxides, this subsection investigates the effect of the bandgap size on the lifetimes of mobile carriers. CdO and NiO are two materials which suggest that these two parameters are not directly related, as will be discussed in the following.

CdO belongs to the class of closed d-shell oxides with a d^{10} electronic configuration (this class will be further discussed in Subsection 7.2.6 below), but exhibits a considerably smaller bandgap than most other d^0 and d^{10} oxides. The bandgap of CdO is commonly reported around 2.2 - 2.4 eV [45–47], which is similar to the open d-shell oxide Fe_2O_3. The absorbance spectrum shown in Figure 7.24a demonstrates an absorption onset in good agreement with these literature reports. As shown in Figure 7.24b, the transient absorption spectrum of CdO is dominated by a sharp

bleach close to 500 nm, which exhibits a comparably long lifetime. This bleach also extends towards the NIR, but exhibits much smaller amplitudes at longer wavelengths. The absolute amplitude of this sharp bleach signal at $2 \times 10^{14}\,\mathrm{cm}^{-2}$ photons absorbed is much higher than observed for any of the other oxides discussed so far, which suggests an origin different from the previously discussed signals. Since this bleach occurs close to the band edge of the material, it is herein assigned to stimulated near-band edge emission of charges close to the conduction band, in good agreement with reports of a similarly sharp peak in this spectral region in the photoluminescence spectrum of CdO thin films [48, 49]. In addition, a comparably small but relatively quickly decaying excited state absorption is observed in the NIR region, which will be discussed further below.

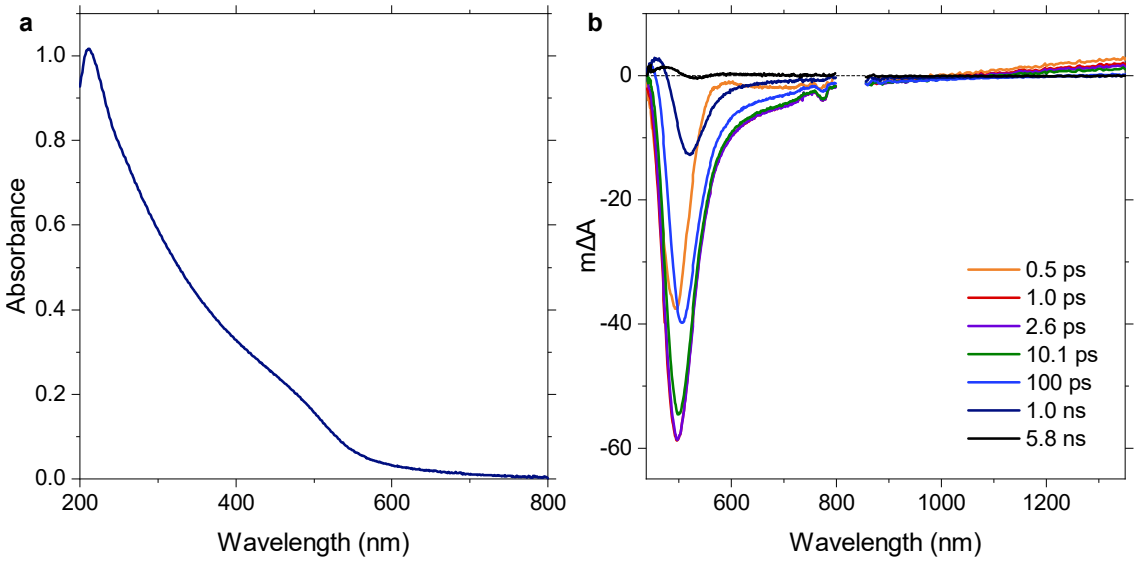

Figure 7.24: (**a**) Absorbance spectrum of a CdO thin film. (**b**) Transient absorption spectra of CdO upon excitation at 350 nm using a fluence of $0.26\,\mathrm{mJ\,cm}^{-2}$, corresponding to $2 \times 10^{14}\,\mathrm{cm}^{-2}$ photons absorbed.

As demonstrated by the 1.0 ps transient spectra shown in Figure 7.25, the position of the bleach maximum progressively blueshifts with increasing fluence. This shift occurs from 2.37 eV (525 nm) at $0.001\,\mathrm{mJ\,cm}^{-2}$ to 2.53 eV (490 nm) at $1.273\,\mathrm{mJ\,cm}^{-2}$, corresponding to a 0.16 eV blueshift for a 1273-fold increase in fluence. This blueshift is in line with a trap filling effect where increasing numbers of photogenerated charges occupy progressively higher-lying trap states and thus force radiative recombination from higher energy levels, in good agreement with the assignment of this bleach feature to stimulated emission from charges close to the conduction band.

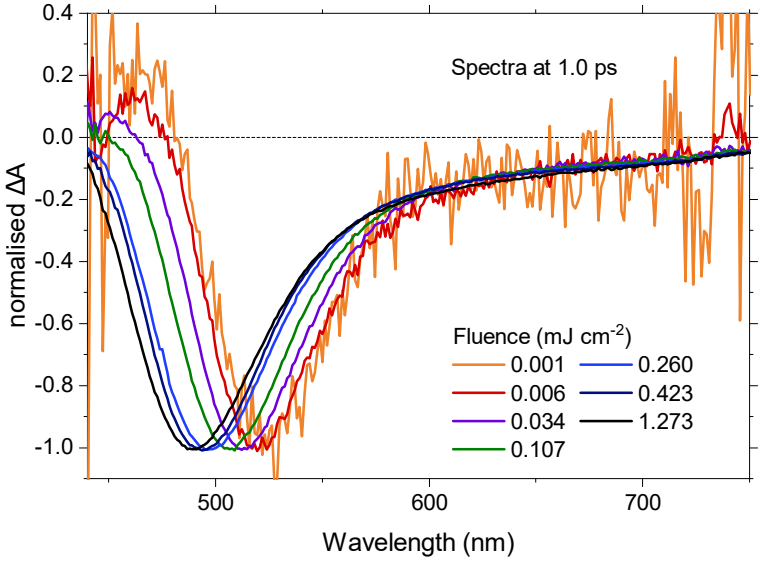

Figure 7.25: Normalised transient spectra probed at 1.0 ps upon excitation of CdO at 350 nm using a range of fluences between 0.001 - 1.273 mJ cm^{-2}.

Since the stimulated emission signal thus is a direct measure of the population of delocalised charges near the conduction band, their recombination kinetics can be probed by following the decay of the associated bleach. Transient kinetics shown in the following are probed at the position of the bleach maximum for each fluence in an attempt to account for the discussed blueshift. The fluence-scaled transient kinetics shown in Figure 7.26a demonstrate that the bleach signal scales linearly for the two lowest fluences, and then saturates rapidly when the excitation intensity is increased. The transient kinetics for these two lowest fluences are very similar and correspond to a mono-exponential decay, yielding time constants τ of 3.7 ns and 3.1 ns for excitation at 0.001 mJ cm^{-2} and 0.006 mJ cm^{-2}, respectively. In good agreement with the deviation from linearity at higher fluences, Figure 7.26b shows that the decays accelerate and become increasingly non-mono-exponential when the fluence is increased further, indicating that the number of photogenerated carriers starts to be comparable to the number of dark carriers, thus accelerating recombination.

The already mentioned excited state absorption in the NIR is found to become more dominant at high fluences as shown by the transient spectra in Figure 7.27a, which represent the highest used fluence of 1.273 mJ cm^{-2}. Like in the previously discussed materials, this feature is assigned to relatively mobile charges close to the band edge. The appearance of this feature at higher fluences in CdO is in excellent agreement with the demonstrated trap filling effect, and further corroborates its assignment to delocalised charges as the filling of trap states progressively increases the population of mobile charges close to the band edge. The fluence-scaled kinetics in

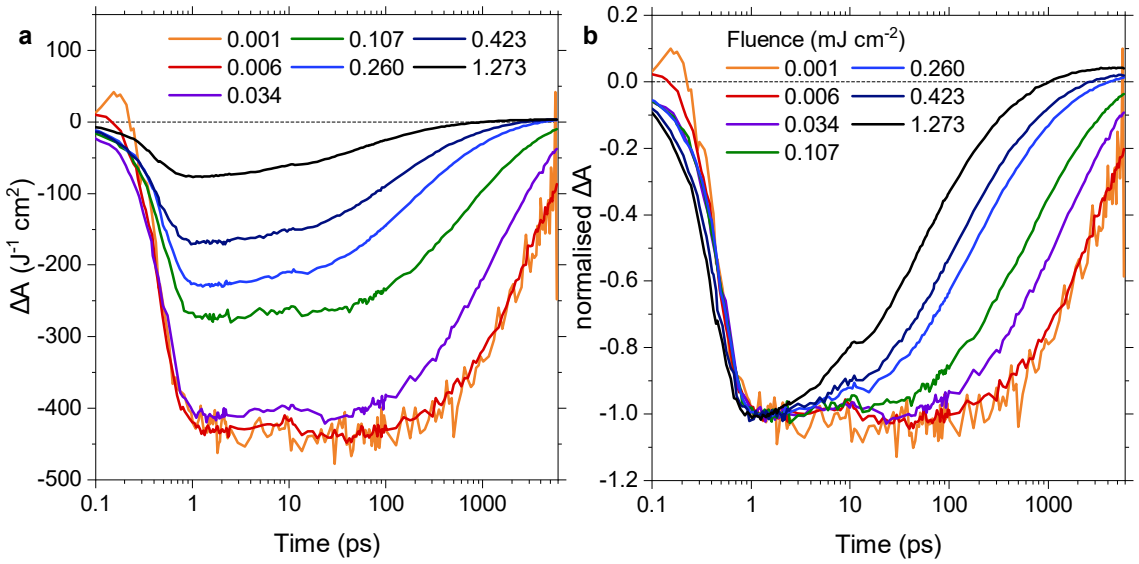

Figure 7.26: Transient kinetics probed at the bleach maximum upon excitation of CdO at 350 nm using a range of fluences between 0.001 - 1.273 mJ cm^{-2}. (**a**) Fluence-scaled transient kinetics, where each kinetic trace was divided by the fluence used to record it, and (**b**) normalised transient kinetics.

Figure 7.27b show that this NIR absorption dominates the underlying broad bleach more and more at higher fluences. The decay occurs relatively fast but still appears to be slower than the rapid initial decay in Co_3O_4 and Cr_2O_3, and is likely dominated by energetic relaxation of the probed charges as lower-energetic trap states become available.

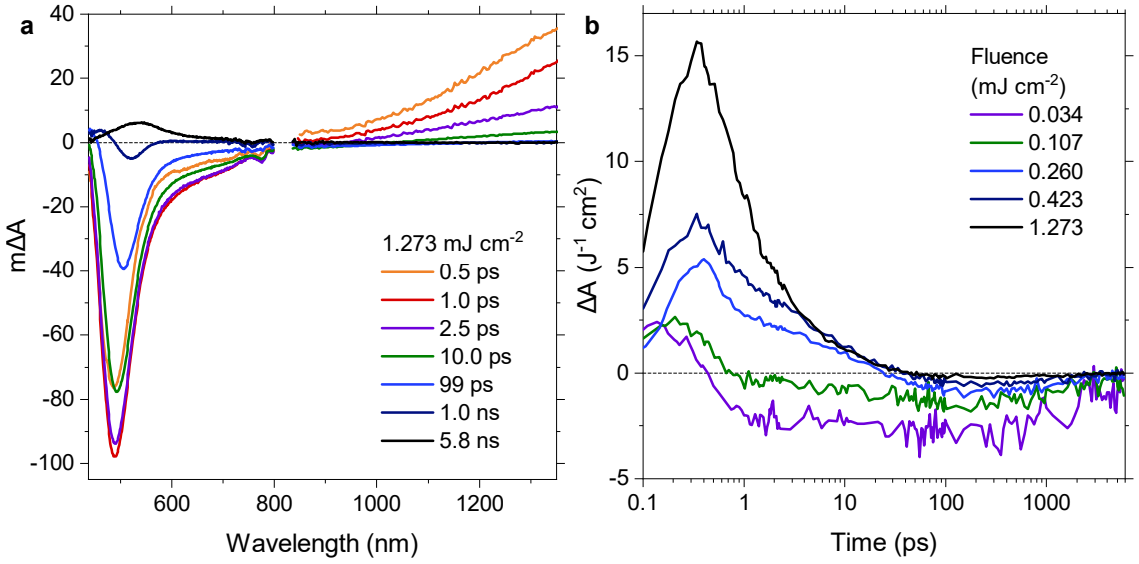

Figure 7.27: (**a**) Transient spectra recorded upon excitation of CdO using a fluence of 1.273 mJ cm^{-2}. (**b**) Fluence-scaled transient kinetics probed at 1150 nm upon excitation of CdO using a range of fluences between 0.034 - 1.273 mJ cm^{-2}. The excitation wavelength was 350 nm in all cases.

Overall, the large amplitude of the stimulated emission signal allows for a very sensitive detection

of mobile charges. The observed long lifetimes of mobile charges are comparable to TiO_2 and nowhere near the fast decay of small-bandgap open *d*-shell oxides such as Co_3O_4 and Cr_2O_3. It can thus be concluded that the bandgap size is not a primary determinant of the lifetime of mobile charges.

This conclusion is further corroborated by the p-type transparent oxide NiO. NiO has a d^8 electronic configuration but exhibits a large bandgap for an open *d*-shell oxide, mostly reported in the 3.3 - 3.9 eV range [50–55]. The lower end of this energy range is in good agreement with the absorbance spectrum of NiO shown in Figure 7.28a. The transient spectra recorded upon 300 nm excitation of NiO shown in Figure 7.28b are broad over the entire visible - NIR probe range, as can be expected due to the absence of strong optical absorption of NiO in this spectral range. It is evident that a rapid initial decay, as clearly observed for Co_3O_4 and Cr_2O_3, is also present over the entire probe range in NiO.

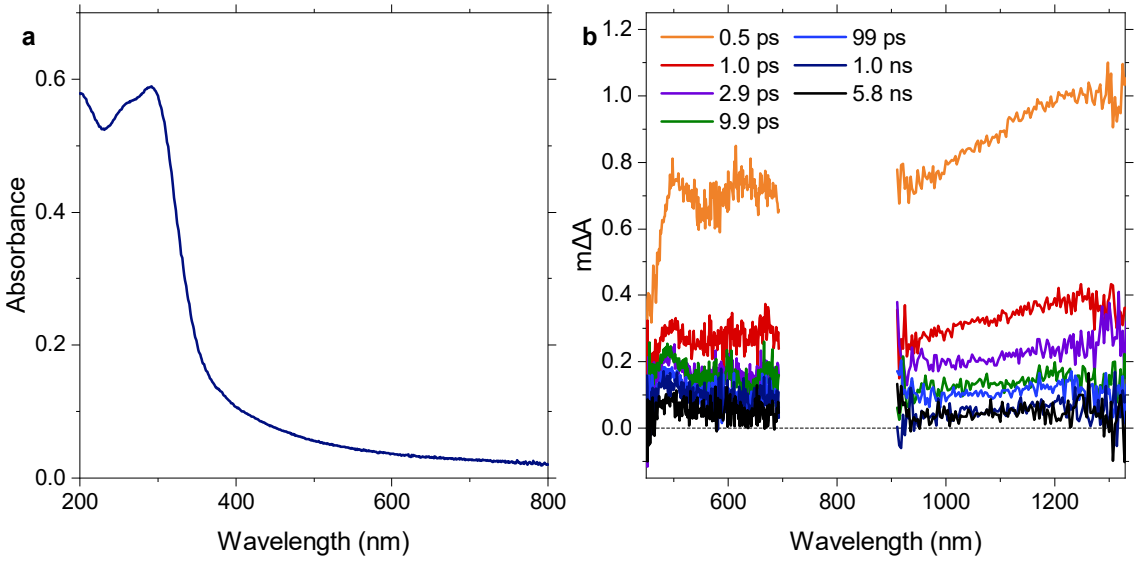

Figure 7.28: (**a**) Absorbance spectrum of NiO deposited as a thin film. (**b**) Transient absorption spectra of NiO upon excitation at 300 nm using a fluence of 0.37 mJ cm^{-2}, corresponding to 2×10^{14} cm^{-2} photons absorbed.

Due to these broad transient spectra, fluence-scaled transient kinetics probed in the visible and NIR are very similar as shown in Figure 7.29. A kinetically intensity-independent rapid initial decay and a smaller intensity-dependent background signal can be distinguished, comparable to the NIR signal observed for Cr_2O_3 (Figure 7.10b).

This NiO example demonstrates that the rapid initial decay component, assigned to rapid charge localisation, is not limited to small-bandgap oxides. Conversely, mobile charges with long lifetimes are observed in the relatively small-bandgap oxide CdO. The bandgap thus primarily

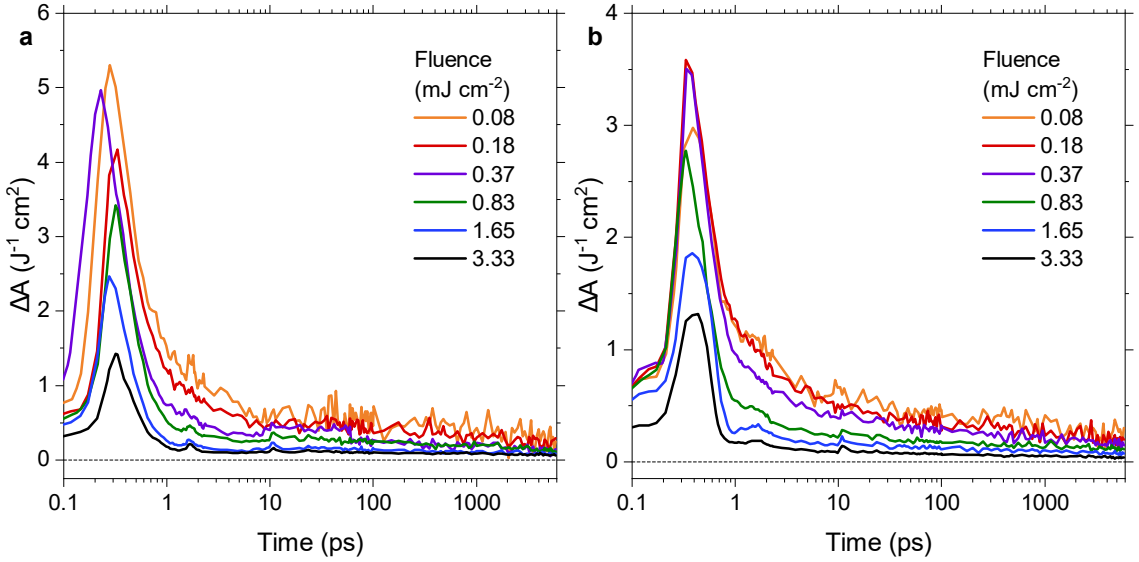

Figure 7.29: Fluence-scaled transient kinetics probed at (**a**) 600 nm and (**b**) 1150 nm upon excitation of NiO at 300 nm. Each kinetic trace was divided by the fluence used to record it.

determines which transient features can be observed in the spectral probe window of the used setup, but does not seem to inherently limit the lifetime of mobile charges.

7.2.6 Closed *d*-shells

After introducing CdO as a first closed *d*-shell oxide, this section extends the discussed observations to a group of other d^{10} oxides, starting with ZnO as one of the most widely studied representatives of this class. ZnO is an n - type semiconductor [56] with a ∼3.3 eV bandgap and an unusually large exciton binding energy of ∼60 meV [57], which enables the persistence of stable excitons at room temperature. The absorbance spectrum shown in Figure 7.30a is in good agreement with these characteristics and indeed shows a pronounced excitonic absorption peak at 367 nm (3.4 eV) close to the band edge, which has been subject to several studies in the literature [58, 59].

The transient absorption spectra obtained upon 300 nm excitation of ZnO, shown in Figure 7.30b, exhibit a broad bleach throughout the visible and NIR range with a peak around 510 nm, plus an excited state absorption in the NIR at early times. These features are qualitatively similar to those observed for CdO, except that the sharp near-band edge emission peak is not observed in the case of ZnO. The absence of this feature is, however, not surprising, since ZnO has a much larger bandgap than CdO and the near-band edge range of ZnO is therefore not accessible by the probe continuum of the used setup. The observed bleach is relatively far from the band edge,

and it coincides with the well-known "green emission" of ZnO. This green emission has been attributed to recombination of shallowly trapped electrons with deeply trapped holes in a range of studies [60–62]. While this deep hole trap state seems to lie ∼2 eV below the conduction band edge, its origin has not been fully clarified: it was assigned to oxygen vacancies in early studies [63, 64], but further evidence emerging over time seems to rather support an assignment to zinc vacancies [65, 66] or external impurities such as copper centres [67]. Irrespective of the physical origin of this state, its deeply trapped holes explains the large energy offset of the observed emission with respect to the band edge. Long lifetimes up to the µs range have been observed for this green emission [60], further supporting its association with trap states.

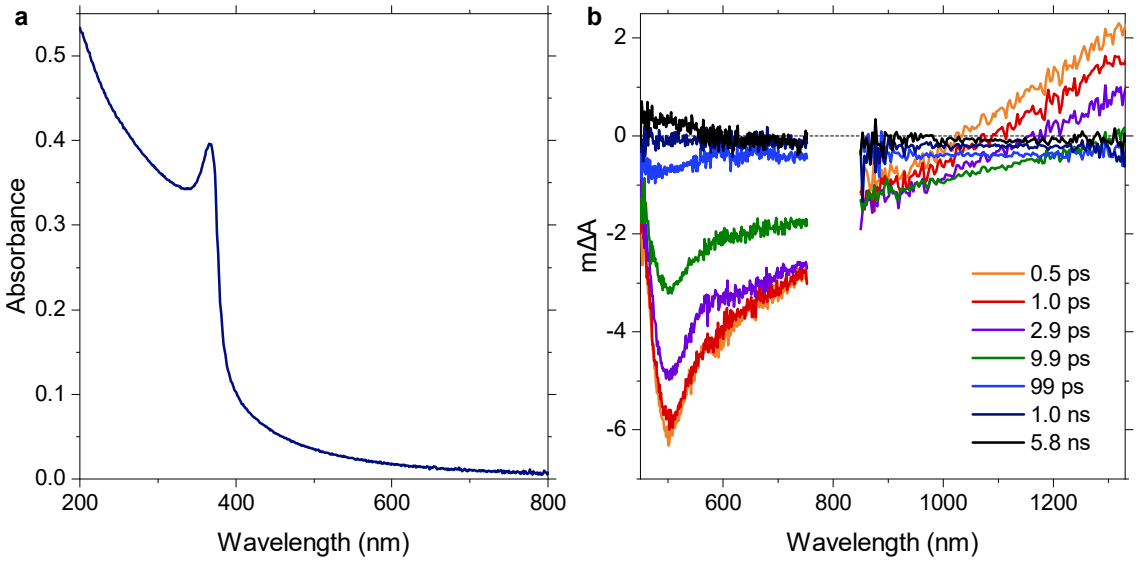

Figure 7.30: (**a**) Absorbance spectrum of ZnO as a thin film. (**b**) Transient absorption spectra of ZnO upon excitation at 300 nm using a fluence of 0.37 mJ cm^{-2}, corresponding to 2×10^{14} cm^{-2} photons absorbed.

As shown in Figure 7.31, the spectral position of the 510 nm bleach does not shift with fluence like the near-band edge emission peak in CdO. This insensitivity to the used fluence further corroborates the involvement of trapped charges, since the trap state distribution is not expected to change with fluence. Like in CdO, the excited state absorption in the NIR becomes more and more pronounced with increasing fluence, suggesting the increasing occupation of near-band edge energy states which implies that trap filling also occurs in ZnO. The presence of delocalised charges is in line with the stimulation of green emission, which involves shallowly trapped electrons as discussed above. Indeed, a very similar spectral feature has been observed in spectroelectrochemical experiments of ZnO thin films at potentials cathodic of open circuit [68], which further corroborates its assignment to electrons in or near the conduction band.

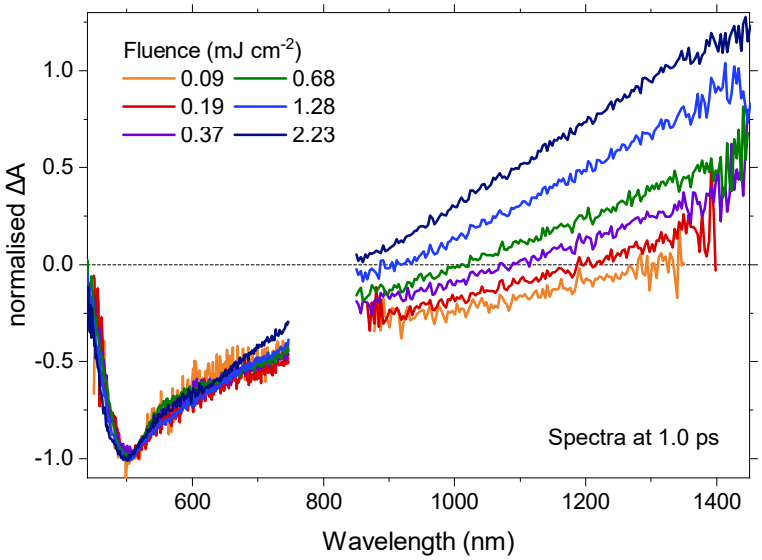

Figure 7.31: Normalised transient spectra probed at 1.0 ps upon excitation of ZnO at 300 nm using a range of fluences between 0.09 - 2.23 mJ cm^{-2}.

Perhaps surprisingly, the normalised kinetics probed at 510 nm upon 300 nm excitation shown in Figure 7.32a still exhibit a relatively strong fluence dependence, despite the involvement of deeply trapped holes. When probed in the NIR upon 300 nm excitation, the excited state absorption of electrons close to the conduction band becomes more and more pronounced with increasing fluence (Figure 7.32b) as already suggested by the spectra shown in Figure 7.31. Once it dominates the underlying bleach at high fluences, this NIR absorption appears to exhibit a half-life time of ∼1.4 ps and seems to scale linearly with fluence. When the excitation wavelength is changed to 373 nm, i.e. exciting the exciton absorption peak (Figure 7.30a) at its lower energy end, this excited state electron absorption virtually disappears as shown in Figure 7.32c. Direct excitation of this exciton peak primarily generates excitons with little excess energy to help their separation into free charges, and exciton recombination is thus the dominant recombination pathway. The absence of the NIR excited state absorption under these excitation conditions provides further evidence for its attribution to separated electrons, and rules out an assignment to coulombically bound electron-hole pairs.

In_2O_3 is another wide bandgap semiconductor with a d^{10} electronic configuration, exhibiting a ∼3.6 - 3.8 eV bandgap [69] in good agreement with the absorption spectrum of the thin film used herein as shown in Figure 7.33a. Again, the transient spectrum upon 300 nm excitation as shown in Figure 7.33b is qualitatively similar to ZnO, with a bleach in the visible range and an excited states absorption in the NIR at early times. Like in ZnO, the bleach is therefore assigned to the recombination of deeply trapped holes and shallowly trapped electrons, and the

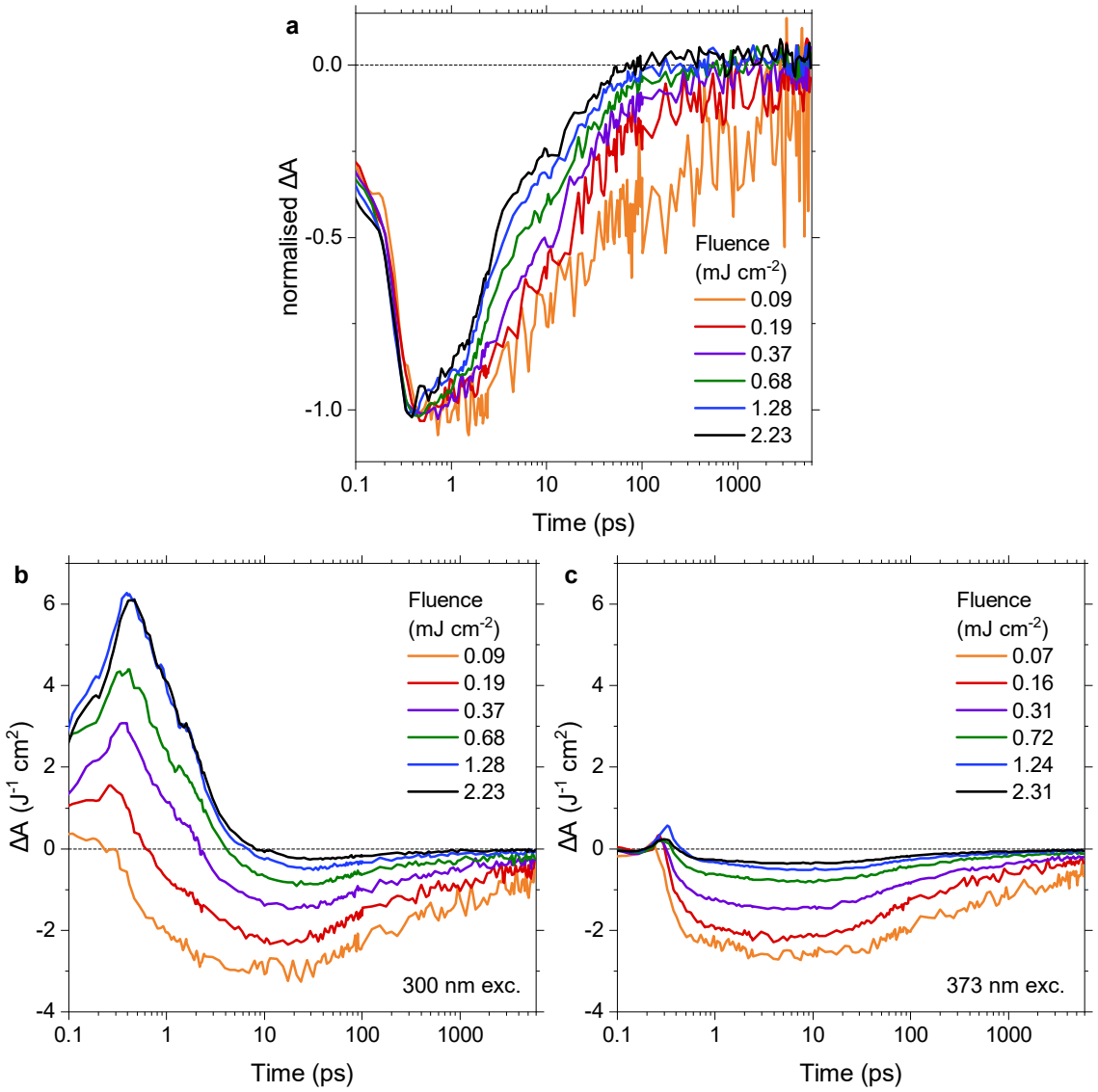

Figure 7.32: (**a**) Normalised transient kinetics probed at 510 nm upon 300 nm excitation of ZnO, and fluence-scaled transient kinetics probed at 1150 nm upon excitation at (**b**) 300 nm and (**c**) 373 nm where each kinetic trace was divided by the fluence used to record it.

NIR absorption is assigned to electrons in or near the conduction band. Interestingly, the bleach does not seem to extend into the NIR in the case of In_2O_3, which allows to exclusively probe the dynamics of electrons near the conduction band in this spectral range. Very similar spectral features have been observed in an earlier transient study on In_2O_3 nanowires [70].

As shown in Figure 7.34a, the bleach kinetics are relatively fluence independent, apart from an early-time artefact which is assigned to the instrument response like discussed for Cr_2O_3 above (compare Figure 7.13). The NIR electron signal in Figure 7.34b also decays largely independently of the used fluence and exhibits a half-life time of ∼1.4 ps, very similar to ZnO. Like in ZnO,

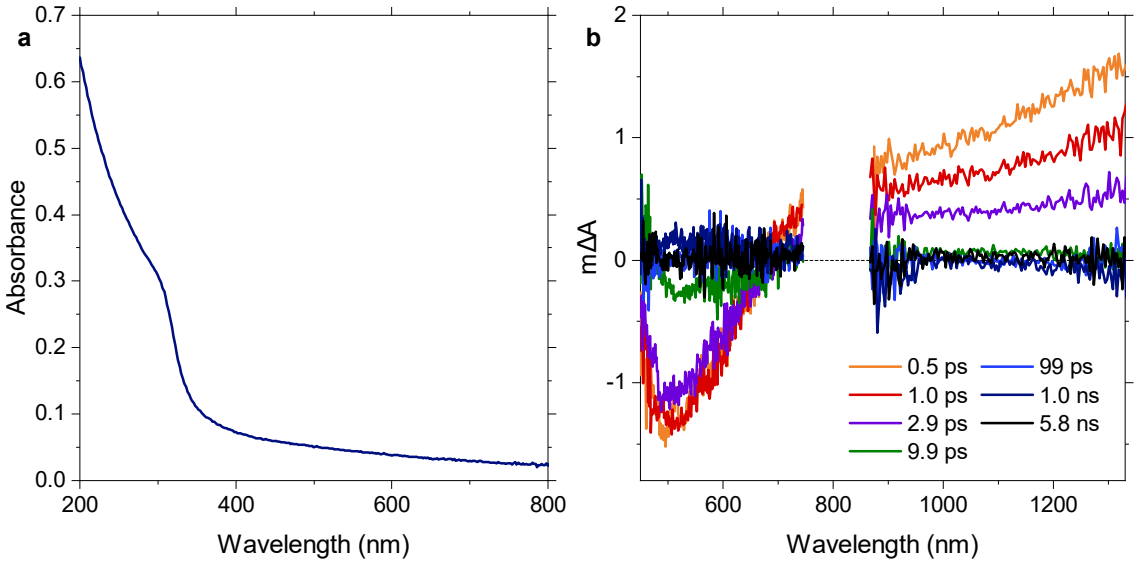

Figure 7.33: (**a**) Absorbance spectrum of In_2O_3 as a thin film. (**b**) Transient absorption spectra of In_2O_3 upon excitation at 300 nm using a fluence of 0.43 mJ cm^{-2}, corresponding to 2×10^{14} cm^{-2} photons absorbed.

the fluence-scaled kinetics suggest that the amplitude of this NIR signal increases approximately linearly with fluence.

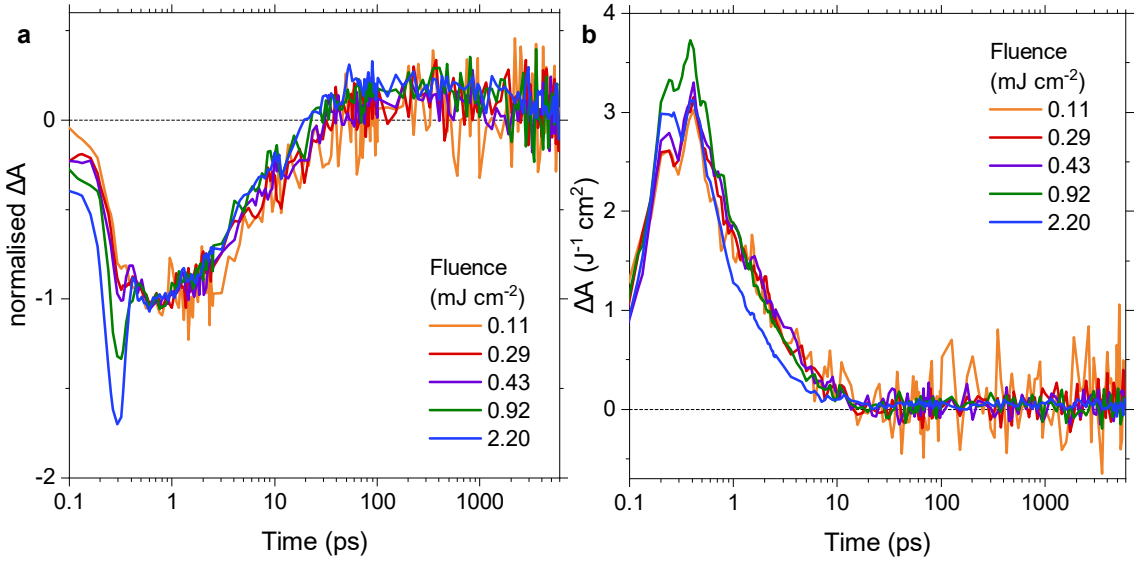

Figure 7.34: (**a**) Normalised transient kinetics probed at 510 nm upon 300 nm excitation of In_2O_3, and (**b**) fluence-scaled transient kinetics probed at 1150 nm upon excitation at 300 nm where each kinetic trace was divided by the fluence used to record it.

In the case of SnO_2, a n-type d^{10} oxide with a ~3.6 eV bandgap [71], a broad transient bleach is observed throughout the visible and NIR range as shown in Figure 7.35b. This bleach partially coincides with a small visible-NIR absorption feature as is evident in the absorbance spectrum in Figure 7.35a. This absorption feature is likely due to trap states and the transient bleach might

then be again due to stimulated emission from this trap state distribution. However, in an earlier time-resolved study of SnO_2 an excited state absorption in the NIR has been observed [72] in a similar way to ZnO, suggesting that this feature might be covered by a somewhat unusual trap state distribution in the herein investigated film.

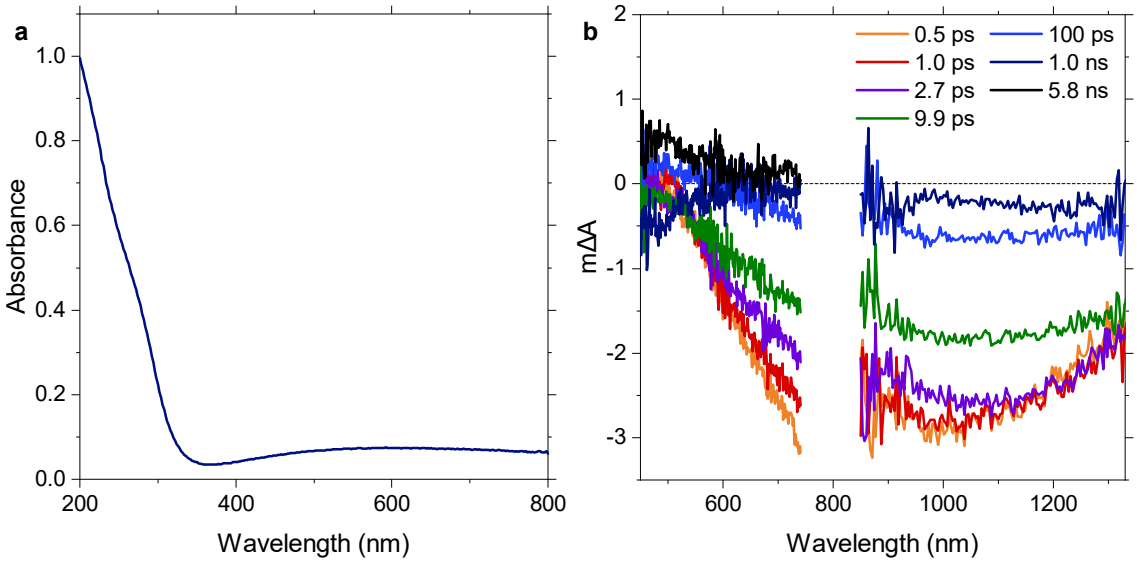

Figure 7.35: (**a**) Absorbance spectrum of SnO_2 as a thin film. (**b**) Transient absorption spectra of SnO_2 upon excitation at 300 nm using a fluence of 0.60 mJ cm^{-2}, corresponding to 2×10^{14} cm^{-2} photons absorbed.

Finally, the d^{10} oxide Bi_2O_3 is a wide bandgap material with a reported ~2.9 eV bandgap [73] as evidenced by the absorbance spectrum shown in Figure 7.36a. Its transient absorption spectrum shown in Figure 7.36b exhibits a peak around 630 nm and is overall unusually structured considering that this peak is located far from the band edge. This structure suggests an assignment to trapped charges, especially considering that the transient signal tails off towards and in the NIR region. Similar to SnO_2, this signal from trapped charges appears to conceal any signal from delocalised charges.

7.2.7 Lifetime of delocalised charges

Based on all the data discussed so far, Figure 7.37 shows a summary of the observed lifetimes of delocalised charges, here plotted against the *d*-electron configuration of the respective metal centre. These values correspond to the signals which have been assigned to delocalised charges above: the excited state absorption in the NIR in the case of empty *d*-shell oxides, the rapid initial decay observed for open *d*-shell oxides, and the NIR excited state absorption observed upon trap filling in the case of closed *d*-shell oxides, except for CdO in which case the near-band

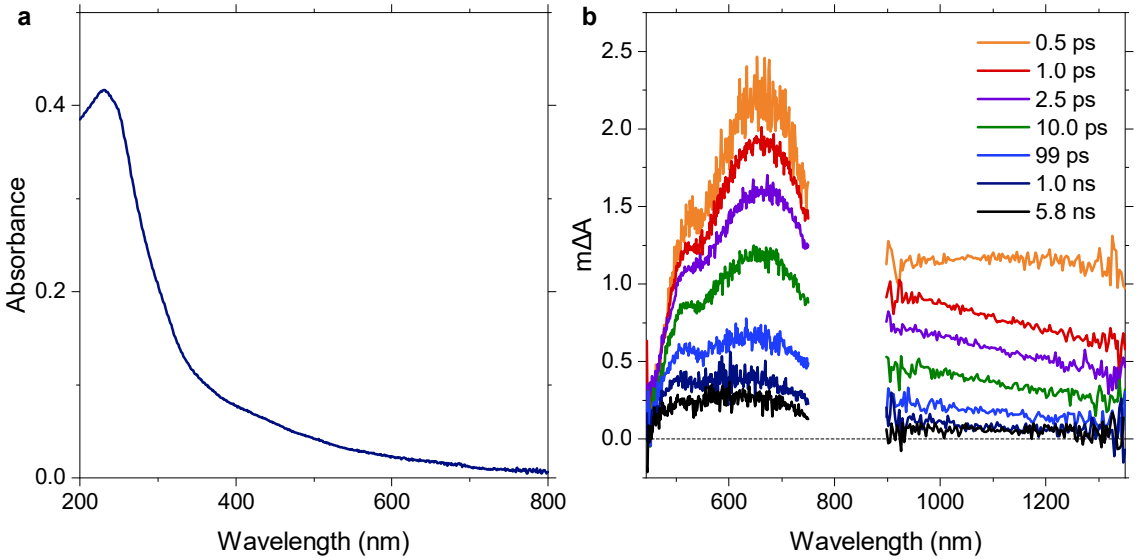

Figure 7.36: (**a**) Absorbance spectrum of a Bi_2O_3 thin film. (**b**) Transient absorption spectra of Bi_2O_3 upon excitation at 300 nm using a fluence of 0.64 mJ cm^{-2}, corresponding to 2×10^{14} cm^{-2} photons absorbed.

edge stimulated emission was used. In the case of fluence-dependent lifetimes, the value for the lowest measured intensity is shown.

Figure 7.37 demonstrates that delocalised charges in all investigated open *d*-shell oxides (Cr_2O_3, Fe_2O_3, Co_3O_4, and NiO), all exhibiting a $t_{50\%}$ of ∼0.6 ps, decay considerably faster than in oxides with empty or closed *d*-shells. This suggests a common relaxation pathway in these open *d*-shell materials which limits the lifetime of charges close to the band edge, as will be further discussed below. It should be noted that higher $t_{50\%}$ might be observed for ZnO and In_2O_3 if it were possible to probe near-band edge emission for these materials like in the case of CdO.

7.2.8 Photoluminescence

Further evidence for the fast decay of delocalised charges in the investigated open *d*-shell oxides can be found in the photoluminescence intensities of these materials. Figure 7.38 compares the photoluminescence intensities of oxides with open *d*-shells (Figure 7.38a) to that of oxides with empty/closed *d*-shells (Figure 7.38b), demonstrating that open *d*-shell oxides exhibit negligible photoluminescence. Based on the presented transient data, this lack of photoluminescence is assigned to a rapid localisation of delocalised charges in these materials, producing localised non-emissive states.

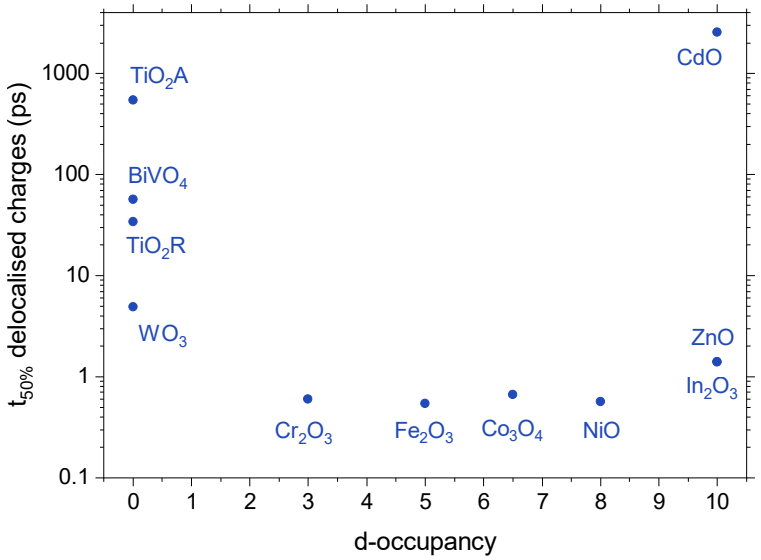

Figure 7.37: Half-lifetime of delocalised charges in different metal oxides as a function of their d-orbital occupancy. In the case of fluence dependent kinetics, the indicated half-lifetime corresponds to the lowest measured fluence.

It should be noted that this photoluminescence data was obtained using a first-generation set of films with much wider distributions in film thickness and morphology than the films investigated above. While these differences make the agreement with the presented transient data even more striking, they also mean that this photoluminescence data should merely be considered a qualitative estimate, especially due to the varying absorbance of these films at the 355 nm excitation wavelength. Photoluminescence quantum yield measurements on the new set of films will provide a more quantitative description of the emissive properties of the films investigated above.

7.3 Discussion

This chapter investigates a wide range of different metal oxides and aims to establish trends in their photophysical behaviour in order to ultimately correlate differences in their photophysics to their photocatalytic performance. The observed spectral features can broadly be divided into signal contributions from delocalised and localised charges, as will be discussed in the following.

7.3.1 Delocalised charges

Delocalised charges can primarily be observed in the form of a broad excited state absorption in spectral regions where the investigated oxide absorbs weakly or not at all. For most of the

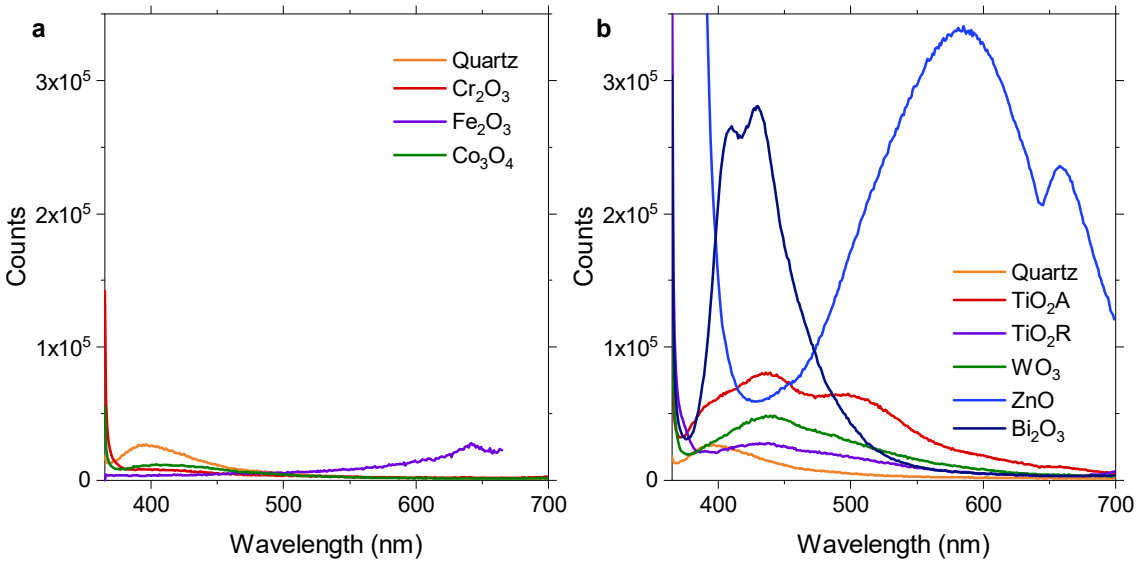

Figure 7.38: Photoluminescence measurements on (**a**) open *d*-shell oxides and (**b**) empty/closed *d*-shell oxides, all obtained upon 355 nm excitation. Note that this data was obtained on a first-generation set of films, i.e. not the same ones that have been investigated in the rest of this chapter.

materials investigated herein, this condition is met in the NIR range, which coincides with the onset intra-band absorption of free charges. This free charge absorption is typically referred to as Drude absorption [19]. Since Drude absorption mainly occurs in the infrared range, it can be expected to manifest as an absorption feature which continuously increases towards lower probe energies when progressing further into NIR range probed here. For instance, such rising absorption is observed for CdO, ZnO, In_2O_3, and NiO, and has been observed in other oxides such as TiO_2 [34] or $SrTiO_3$ [74]. However, since only the very onset of the infrared range lies within the probe window of the setup used herein, this Drude absorption onset might appear rather flat in this spectral range, as seems to be the case for e.g. Cr_2O_3 and Fe_2O_3.

The primary difference between the oxides investigated herein seems to lie in how fast the population of photogenerated delocalised charges decays as summarised by Figure 7.37. This decay can in principle occur via localisation, thus producing localised charges which occupy energetic states further away from the band edge, or via recombination, which restores the ground state. The fastest decay of these delocalised charges is observed for the four investigated open *d*-shell oxides: Cr_2O_3, Fe_2O_3, Co_3O_4, and NiO. This fast decay process occurs with a half-decay time of ~0.6 ps and is thus faster than typical recombination processes [75]. Instead, this rapid initial decay is herein assigned to the localisation of photogenerated charges via small polaron formation. As previously described in Chapter 6, polarons are charges which become self-trapped because they distort the crystal lattice around them [6, 16, 18]. This self-trapping

process leads to an energetic relaxation and causes charges to occupy energy levels within the bandgap of the semiconductor, which can be thought of as a carrier creating its own trap state by displacing surrounding lattice atoms from their equilibrium positions. The term 'small polaron' indicates that this self-trapping process confines the charge carrier to a spatial size on the order of the lattice constant [17], and polaron transport thus occurs via temperature-activated hopping [18]. Such polarons can then further localise at defect sites such as the W_{ov}^{V} polarons described in Chapter 6, but at least for the self-trapping process a physical defect is not necessarily required.

The widely investigated oxide Fe_2O_3 is known for its tendency to localise electrons as small polarons [6]. The formation of small polarons has been observed upon injection from excited dyes [76], and in recent years more and more evidence of polaron formation upon direct excitation of the Fe_2O_3 semiconductor has emerged. For instance, the relaxation associated with polaron formation has been found to result in an effective electronic bandgap of 1.75 eV for Fe_2O_3, rather than the nominal 2.2 eV [77]. This 0.45 eV relaxation is in good agreement with first-principles calculations, which suggest an energy gain of 0.48 eV upon lattice distortion and localisation and also yield an activation barrier of ∼0.2 eV for small polaron hopping [78]. The time constant of this polaron formation process is not fully consistent across different time-resolved experiments, but lies on the sub-ps timescale in all studies reported so far: Time-resolved x-ray absorption spectroscopy experiments have reported time constants of (240 ± 30) fs [79] and (90 ± 5) fs [80], a extreme UV transient absorption study has found a time constant of 660 fs [75], and a study in which polaronic charges were re-excited to the conduction band after their formation has suggested that polarons form within ∼600 fs [78].

The similarities in the decay of delocalised charges in Cr_2O_3, Fe_2O_3, Co_3O_4, and NiO indicates that rapid small polaron formation might be a general problem of open *d*-shell oxides. While the rapid decay of delocalised charges could only be fitted reliably for Co_3O_4 owing to the absence of an additional intensity dependent component at early times in this material, the obtained time-constant of 400 fs generally agrees with the timescale of the above literature values. Note that the fluences used here are much lower than e.g. for the described x-ray absorption experiments, suggesting that the conditions probed here are closer to photocatalytic operation conditions. Given the very similar half-lifetimes of the broad delocalised charge signal in these open *d*-shell oxides, the time constant of small polaron formation for the Cr_2O_3, Fe_2O_3, and NiO data presented herein can be expected to be very similar. This similarity is in good agreement with the report of highly localised excited states on the order of a single metal-oxygen bond in Fe_2O_3, Co_3O_4, and NiO, determined using an extreme UV probe [75].

While Fe_2O_3 is an n-type oxide, Cr_2O_3 [81–83], Co_3O_4 [84], and NiO [52, 55] are usually reported to be p-type semiconductors, suggesting that small polaron formation does not depend on the type of intrinsic doping. It is, however, interesting to consider whether it is electrons or holes that form small polarons in these materials. In the case of Fe_2O_3, the broad NIR absorption has been assigned to Fe^{2+} centres [85], which corresponds to electrons in this material and is in line the reported formation of small electron polarons [6]. For NiO, a transient absorption study employing an extreme UV probe has also reported the formation of small electron polarons upon photoexcitation [86]. It thus appears that the broad NIR signal might be related to electrons irrespective of whether they are minority or majority carriers in the oxide under study.

In contrast to this rapid initial decay of delocalised electrons in open *d*-shell oxides, Figure 7.38 demonstrates that delocalised electrons in oxides with open or closed d-shells exhibit up to three orders of magnitude longer lifetimes. These longer lifetimes suggest that the formation of electron small polarons is not as pronounced in these d^0 and d^{10} materials. Instead of small polaron formation, the decay of delocalised electrons in these materials can rather be assigned to trapping at physical trap states or to recombination. For instance, delocalised electrons in anatase TiO_2 and $BiVO_4$ exhibit a strongly fluence-dependent decay, suggesting a recombination process with at least partially bimolecular character. For rutile TiO_2, a more intensity independent decay is observed, which has been assigned to the higher carrier density of this polymorph [44] related to its more defect-rich character.

For CdO, ZnO, and In_2O_3, pronounced trap filling effects are observed, and the rather fast decay of the delocalised NIR electron signal ($t_{50\%} = \sim 1.4\,ps$) is thus likely due to the localisation of these electrons at trap sites, in line with the mostly fluence-independent decay kinetics of this NIR electron feature (when accounting for the effect of overlapping bleach signals). This assignment is supported by CdO in particular, where a fast decay of the NIR electron signal occurs although the presence of largely delocalised charges can still be inferred from their intense near-band edge stimulated emission. It is possible that similarly long-lived charges could be observed in ZnO and In_2O_3 if their band edge region could be probed in a similar way. In contrast, such near-band edge emission was not observed for open *d*-shell oxides at least in the cases of Cr_2O_3, Fe_2O_3, and Co_3O_4 in transient absorption and/or photoluminescence experiments, which supports the formation of non-radiative polaron states.

7.3.2 Localised charges

In contrast to the broad absorption of delocalised charges, spectral features produced by localised charges are usually more structured. Structured absorption features with long lifetimes are observed for almost all of the materials studied in this chapter, pointing towards the persistence of localised charges. In the materials discussed herein, spectral features arising from localised charges can be divided into two groups which appear to have different origins:

(i) *Stark effects.* When electric fields between photogenerated charges perturb the ground state absorption of the material, derivative-like differential absorption features may be observed. While a first-derivative-like spectral shape indicates the generation of a polarisable excited state, second-derivative-like spectra are suggestive of a dipolar excited state. For all oxides which exhibit sufficiently strong optical absorption within the accessible probe range, the long-lived component in the transient signal agrees reasonably well with the second derivative of the ground state absorption, especially at the band edge. This agreement suggests an assignment of these long-lived transient features to localised charges, which act like permanent dipoles on the timescale of their own lifetime. This would imply that these long-lived transient features are a result of localised charges, e.g. charges trapped at oxygen vacancies, but are not features that arise from these localised charges directly via their absorption or emission of photons.

(ii) *Defect state absorption/photoluminescence.* In the second case, in contrast, defect states are directly involved in the absorption or emission of photons. This is particularly clear in the case of wide bandgap oxides which exhibit relatively structured transient features in the visible/NIR range. For instance, the Bi_2O_3 transient spectrum is characterised by the excited-state absorption of trapped carriers, and that of ZnO, In_2O_3, and SnO_2 is dominated by stimulated emission related to deeply trapped holes.

Localised charge signals of type (ii) mostly reflect defect state distributions which can often be expected to be specific to a certain material or even the way in which it was prepared, and are thus not considered in detail herein. However, it is interesting to consider whether derivative-like localised charge signals of type (i) appear over time or whether they are already present within the time resolution of the experiment, especially in the case of the open *d*-shell oxides where the rapid formation of small polarons occurs. This question relates back to the two global analysis models used for Co_3O_4 in Subsection 7.2.1, where the fast component either evolves into the long-lived one or decays independently of it. The better match of first derivative

and the transient signal of polarisable delocalised charges supports the appearance of the long-lived signal within the time resolution of the experiment, but cannot be considered sufficiently conclusive evidence. For Cr_2O_3 and Fe_2O_3, an analysis of the early time signal is complicated by the presence of an additional intensity dependent decay component. These two materials also exhibit some spectral evolution over the course of the measurement as is most clearly observed for the growth in relative amplitude of the bleach signal in Cr_2O_3, however, this evolution continues even after the formation of electron small polarons. Given that a second-derivative-like signal is also observed for $BiVO_4$ at early times although the rapid formation of electron small polarons does not seem to occur in this material, an assignment of the underlying Stark effect to carriers which are trapped at physical defect sites such as oxygen vacancies seems at present most likely.

7.4 Conclusions

In this chapter, the photophysics of 11 different metal oxides have been discussed in order to identify shared patterns and ultimately relate their photophysical behaviour to photocatalytic activity. A common rapid relaxation of delocalised electrons with a time constant of ∼400 fs, assigned to the formation of electron small polarons, has been identified for all presented open *d*-shell oxides (Cr_2O_3, Fe_2O_3, Co_3O_4, NiO). This rapid small polaron formation was found to quench near-band edge photoluminescence and thus seems to result in non-radiative recombination. In contrast, delocalised electrons in all investigated oxides with open or closed *d*-shells exhibited longer lifetimes, in some cases up to three orders of magnitude longer. Such striking differences in lifetime of delocalised electrons, which reside either in the conduction band or very close to it and thus exhibit high reductive driving force as well as high mobilities, are likely to have a pronounced effect on the photocatalytic properties of these materials. For instance, charge transfer on the ps timescale has been observed in numerous cases, whereas charge transfer on the fs timescale prior to small polaron formation is likely to prove difficult. As a result, metal oxides with open or closed d-shells are preferable as candidates for photocatalytic applications, which helps to rationalise the empirical observation that metal centres with d^0 or d^{10} configuration have often been the materials of choice for the development of active photocatalysts.

7.5 Materials and Methods

All metal oxide films were prepared as dense thin films with ∼100 nm thickness on quartz glass substrates.

For all film prepared via spin coating, substrates were cleaned by subsequently sonicating in detergent (20 min, decon 90, Decon Laboratories Ltd.), 2x H_2O (5 min each), 2x acetone (5 min each), 2x isopropanol (5 min each).

TiO_2

Dense TiO_2 anatase and rutile thin films were grown via atmospheric pressure chemical vapor deposition (APCVD) using $TiCl_4$ as a precursor as reported previously [44].

WO_3

WO_3 thin films were prepared similarly to the ones used in Chapter 6, but conditions were adjusted to yield dense rather than nanostructured thin films. WO_3 films were grown on quartz glass substrates using aerosol-assisted chemical vapour deposition (AACVD) in a cold wall reactor. Substrates were heated from underneath using a graphite heating block. The inlet to the reactor was equipped with a cooling water jacket to prevent decomposition of the precursor before reaching the reactor. The precursor solution contained $W(CO)_6$ (0.12 g, 0.34 mmol) in an acetone:methanol mixture (2:1; 30 ml). The solution was sonicated for 10 min to dissolve the precursors (VWR ultrasonic cleaner, 30 W, 45 kHz). The solution was then aerosolized using an ultrasonic humidifier (2 MHz, Liquifog, Johnson Matthey) and carried over the heated quartz glass substrate (325 °C) using an inert N_2 carrier gas (99.99%, BOC) at a flow rate of 1000 L min^{-1} (MFC, Brooks) over a period of ∼20 min, until the solution had been fully transferred. The film was subsequently annealed at 500 °C in air for 12 h.

$BiVO_4$

$BiVO_4$ thin films were prepared via sol-gel synthesis as reported previously [87].

Cr_2O_3

$Cr(NO_3)_3x9H_2O$ (0.25 g, 0.06 mmol) and propyleneoxide 469 µL were dissolved in ethanol (2.5 mL). The solution was stirred at 60 °C for 4 h and then taken off the hotplate. Rapid gelation started to occur after 30 min of resting. The gelating solution was spin coated onto quartz glass substrates (4000 rpm, 1 min), yielding a series of films with different thicknesses which were then annealed in air (15 min to 80 °C, 30 min at 80 °C, 1 h to 500 °C, 3 h at 500 °C). The film with the most appropriate thickness was then selected after the preparation.

Fe_2O_3

Fe_2O_3 thin films were prepared via sol-gel synthesis based on a previously reported procedure [88]. $FeCl_2x4H_2O$ (0.42 g, 0.33 mmol) , citric acid (0.64 g, 0.33 mmol), and ascorbic acid (0.059 g, 0.33 mmol) were dissolved in N_2-saturated ethanol (10 mL), where citric acid acts as chelating agent and ascorbic acid is an antioxidant. Note that inert conditions were not strictly required for the preparation of Fe_2O_3 since iron centres were oxidised during the annealing procedure, but were maintained here for comparability to other iron oxide polymorphs (not shown herein). The resulting solution was stirred in a closed round bottom flask at 60 °C for 5-6 h. After this time, DMF 20 µL was added as a drying control reagent and the solution was stirred for additional 30 min. The solution was then spin coated onto quartz glass substrates (5000 rpm, 1 min) and the deposited films were annealed in air (20 min to 300 °C, 30 min at 300 °C). A second layer was then spin coated on top of the first one (5000 rpm, 1 min) and the films were annealed again (20 min to 300 °C, 30 min at 300 °C). Finally, the films were annealed at 450 °C for 3 h to complete the conversion to α-Fe_2O_3.

Co_3O_4

Co_3O_4 thin films were prepared via sol-gel synthesis based on a previously reported procedure [89]. $Co(NO_3)_2x6H_2O$ (0.50 g, 1.72 mmol) was dissolved in ethanol (2.5 ml). A second solution was prepared by dissolving ethylcellulose (0.125 g) and α-terpineol (2.35 g, 15.3 mmol), and eventually decanted since ethylcellulose did not fully dissolve. Both solutions were then mixed inside a round bottom flask and stirred for 30 min at room temperature. The solution was then spin coated onto quartz glass substrates (2000 rpm, 1 min) and the deposited films were annealed in air (15 min to 100 °C, 15 min at 100 °C, 30 min to 500 °C, 1 h at 500 °C).

NiO

Nickel acetate tetrahydrate (498 mg, 2 mmol) and ethanolamine (240 µL) were dissolved in 2-methoxyethanol (3 ml). The solution turned deep blue in colour immediately upon addition of ethanolamine and was then and stirred at 100 °C for 30 min. The solution was then spin coated onto quartz glass substrates (4000 rpm, 40 s) and the deposited films were annealed in at 350 °C for 3 h in air.

CdO

Cadmium acetate (461 mg, 2 mmol) and ethanolamine (120 µL) were dissolved in 2-methoxyethanol (2 ml) and stirred at room temperature overnight (∼15 h). The solution was then spin coated onto quartz glass substrates (5000 rpm, 1 min) and the deposited films were annealed in air (40 min to 130 °C, 20 min at 130 °C, 1.5 h to 500 °C, 4 h at 500 °C).

ZnO

Zinc acetate dihydrate (440 mg) and ethanolamine (120 µL) were dissolved in 2-methoxyethanol (2 ml) and stirred at room temperature overnight (∼15 h). The solution was then spin coated onto quartz glass substrates (5000 rpm, 1 min) and the deposited films were annealed in air (10 min to 130 °C, 15 min at 130 °C, 40 min to 550 °C, 3 h at 550 °C).

In_2O_3

In_2O_3 thin films were prepared via sol-gel synthesis based on a previously reported procedure [90]. $In(NO_3)_3 x x H_2O$ (0.20 g) was dissolved in acetylacetone 6 mL. The solution was stirred at 95 °C for 2.25 h, which caused it to turn light brown. After this period, the temperature was reduced to 70 °C and the solution was stirred at this temperature for additional 5 h, during which the light brown colour intensified. The solution was then spin coated onto quartz glass substrates (3000 rpm, 40 s) and a total of 5 layers were deposited. Films were annealed after the deposition of each sublayer (15 min to 135 °C, 10 min at 135 °C, 35 min to 350 °C, 20 min at 350 °C) and after the deposition of the final layer (15 min to 135 °C, 30 min at 135 °C, 1 h to 450 °C, 4 h at 450 °C).

7.6 References

1. Pan, J. & Yan, Q. Data-driven material discovery for photocatalysis: a short review. *Journal of Semiconductors* **39,** 071001 (2018).
2. Seyler, M., Stoewe, K. & Maier, W. F. New hydrogen-producing photocatalysts—A combinatorial search. *Applied Catalysis B: Environmental* **76,** 146–157 (2007).
3. Scanlon, D. O. *et al.* Band alignment of rutile and anatase TiO2. *Nature Materials* **12,** 798–801 (2013).
4. Chen, B. *et al.* The band structure of WO 3 and non-rigid-band behaviour in Na 0.67 WO 3 derived from soft x-ray spectroscopy and density functional theory. *Journal of Physics: Condensed Matter* **25,** 165501 (2013).
5. Chen, S., Takata, T. & Domen, K. Particulate photocatalysts for overall water splitting. *Nature Reviews Materials* **2,** 17050 (2017).
6. Lany, S. Semiconducting transition metal oxides. *Journal of Physics: Condensed Matter* **27,** 283203 (2015).
7. Mattheiss, L. F. Electronic Structure of the 3d Transition-Metal Monoxides. I. Energy-Band Results. *Physical Review B* **5,** 306–315 (1972).
8. Hubbard, J. Electron correlations in narrow energy bands. *Proceedings of the Royal Society of London. Series A. Mathematical and Physical Sciences* **276,** 238–257 (1963).
9. Mott, N. F. The transition to the metallic state. *Philosophical Magazine* **6,** 287–309 (1961).
10. Greiner, M. T. & Lu, Z.-H. Thin-film metal oxides in organic semiconductor devices: their electronic structures, work functions and interfaces. *NPG Asia Materials* **5,** e55 (2013).
11. Maeda, K. & Domen, K. New non-oxide photocatalysts designed for overall water splitting under visible light. *Journal of Physical Chemistry C* **111,** 7851–7861 (2007).
12. Sato, J., Saito, N., Nishiyama, H. & Inoue, Y. New photocatalyst group for water decomposition of RuO2-loaded p-block metal (In, Sn, and Sb) oxides with d10 configuration. *Journal of Physical Chemistry B* **105,** 6061–6063 (2001).
13. Sato, J., Kobayashi, H., Saito, N., Nishiyama, H. & Inoue, Y. Photocatalytic activities for water decomposition of RuO2-loaded AInO2 (A = Li, Na) with d10 configuration. *Journal of Photochemistry and Photobiology A: Chemistry* **158,** 139–144 (2003).
14. Inoue, Y. Photocatalytic water splitting by RuO2-loaded metal oxides and nitrides with d0- and d10 -related electronic configurations. *Energy & Environmental Science* **2,** 364 (2009).

15. Osterloh, F. E. Inorganic Materials as Catalysts for Photochemical Splitting of Water. *Chemistry of Materials* **20,** 35–54 (2008).

16. Rettie, A. J. E., Chemelewski, W. D., Emin, D. & Mullins, C. B. Unravelling Small-Polaron Transport in Metal Oxide Photoelectrodes. *The Journal of Physical Chemistry Letters* **7,** 471–479 (2016).

17. Mott, N. F. & Stoneham, A. M. The lifetime of electrons, holes and excitons before self-trapping. *Journal of Physics C: Solid State Physics* **10,** 3391–3398 (1977).

18. Emin, D. Optical properties of large and small polarons and bipolarons. *Physical Review B* **48,** 13691–13702 (1993).

19. Bass, M. *et al. Handbook of Optics, Third Edition Volume I: Geometrical and Physical Optics, Polarized Light, Components and Instruments* 3rd ed. (McGraw-Hill, Inc., New York, NY, USA, 2010).

20. Koch, S. W., Kira, M., Khitrova, G. & Gibbs, H. M. Semiconductor excitons in new light. *Nature Materials* **5,** 523–531 (2006).

21. Vance, F. W., Williams, R. D. & Hupp, J. T. Electroabsorption spectroscopy of molecular inorganic compounds. *International Reviews in Physical Chemistry* **17,** 307–329 (1998).

22. Klimov, V. I. Optical Nonlinearities and Ultrafast Carrier Dynamics in Semiconductor Nanocrystals. *The Journal of Physical Chemistry B* **104,** 6112–6123 (2000).

23. Norris, D. J., Sacra, A., Murray, C. B. & Bawendi, M. G. Measurement of the size dependent hole spectrum in CdSe quantum dots. *Physical Review Letters* **72,** 2612–2615 (1994).

24. Colvin, V. L. & Alivisatos, A. P. CdSe nanocrystals with a dipole moment in the first excited state. *The Journal of Chemical Physics* **97,** 730–733 (1992).

25. Scholz, M., Flender, O., Oum, K. & Lenzer, T. Pronounced Exciton Dynamics in the Vacancy-Ordered Bismuth Halide Perovskite (CH 3 NH 3) 3 Bi 2 I 9 Observed by Ultrafast UV–vis–NIR Transient Absorption Spectroscopy. *The Journal of Physical Chemistry C* **121,** 12110–12116 (2017).

26. Jakowetz, A. C. *et al.* Visualizing excitations at buried heterojunctions in organic semiconductor blends. *Nature Materials* (2017).

27. Gelinas, S. *et al.* Ultrafast Long-Range Charge Separation in Organic Semiconductor Photovoltaic Diodes. *Science* **343,** 512–516 (2014).

28. Menke, S. M. *et al.* Order enables efficient electron-hole separation at an organic heterojunction with a small energy loss. *Nature Communications* **9,** 277 (2018).

29. Kim, K. J. & Park, Y. R. Optical investigation of charge-transfer transitions in spinel Co3O4. *Solid State Communications* **127,** 25–28 (2003).

30. Spencer, C. D. & Schroeer, D. Mössbauer study of several cobalt spinels using Co57 and Fe57. *Physical Review B* **9,** 3658–3665 (1974).

31. Miedzinska, K., Hollebone, B. & Cook, J. An assigment of the optical absorption spectrum of mixed valence Co3O4 spinel films. *Journal of Physics and Chemistry of Solids* **48,** 649–656 (1987).

32. Ngamou, P. H. T. & Bahlawane, N. Influence of the Arrangement of the Octahedrally Coordinated Trivalent Cobalt Cations on the Electrical Charge Transport and Surface Reactivity. *Chemistry of Materials* **22,** 4158–4165 (2010).

33. Waegele, M. M., Doan, H. Q. & Cuk, T. Long-Lived Photoexcited Carrier Dynamics of d – d Excitations in Spinel Ordered Co 3 O 4. *The Journal of Physical Chemistry C* **118,** 3426–3432 (2014).

34. Yoshihara, T. *et al.* Identification of Reactive Species in Photoexcited Nanocrystalline TiO 2 Films by Wide-Wavelength-Range (400-2500 nm) Transient Absorption Spectroscopy. *The Journal of Physical Chemistry B* **108,** 3817–3823 (2004).

35. Grygar, T., Ka, P. B. Č., Ek, J., Petrovský, E. & Schneeweiss, O. Fe2O3-Cr2O3 system revised. *Ceramics - Silikaty* **47,** 32–39 (2003).

36. Pendlebury, S. R. *et al.* Ultrafast Charge Carrier Recombination and Trapping in Hematite Photoanodes under Applied Bias. *Journal of the American Chemical Society* **136,** 9854–9857 (2014).

37. Barroso, M., Pendlebury, S. R., Cowan, A. J. & Durrant, J. R. Charge carrier trapping, recombination and transfer in hematite (α-Fe2O3) water splitting photoanodes. *Chemical Science* **4,** 2724 (2013).

38. Forster, M. *et al.* Oxygen deficient α-Fe 2 O 3 photoelectrodes: a balance between enhanced electrical properties and trap-mediated losses. *Chem. Sci.* **6,** 4009–4016 (2015).

39. Walsh, A., Yan, Y., Huda, M. N., Al-Jassim, M. M. & Wei, S.-H. Band Edge Electronic Structure of BiVO 4 : Elucidating the Role of the Bi s and V d Orbitals. *Chemistry of Materials* **21,** 547–551 (2009).

40. Kim, T. W. & Choi, K.-S. Nanoporous BiVO4 Photoanodes with Dual-Layer Oxygen Evolution Catalysts for Solar Water Splitting. *Science* **343,** 990–994 (2014).

41. Zhong, D. K., Choi, S. & Gamelin, D. R. Near-Complete Suppression of Surface Recombination in Solar Photoelectrolysis by "Co-Pi" Catalyst-Modified W:BiVO 4. *Journal of the American Chemical Society* **133,** 18370–18377 (2011).

42. Kudo, A., Omori, K. & Kato, H. A Novel Aqueous Process for Preparation of Crystal Form-Controlled and Highly Crystalline BiVO 4 Powder from Layered Vanadates at Room Temperature and Its Photocatalytic and Photophysical Properties. *Journal of the American Chemical Society* **121,** 11459–11467 (1999).

43. Corby, S. *et al.* Charge Separation, Band-Bending, and Recombination in WO3 Photoanodes. *The Journal of Physical Chemistry Letters* **10,** 5395–5401 (2019).

44. Sachs, M., Pastor, E., Kafizas, A. & Durrant, J. R. Evaluation of Surface State Mediated Charge Recombination in Anatase and Rutile TiO2. *The Journal of Physical Chemistry Letters* **7,** 3742–3746 (2016).

45. Jefferson, P. H. *et al.* Bandgap and effective mass of epitaxial cadmium oxide. *Applied Physics Letters* **92,** 022101 (2008).

46. Vasheghani Farahani, S. K., Muñoz-Sanjosé, V., Zúñiga-Pérez, J., McConville, C. F. & Veal, T. D. Temperature dependence of the direct bandgap and transport properties of CdO. *Applied Physics Letters* **102,** 022102 (2013).

47. Koffyberg, F. P. Thermoreflectance spectra of CdO: Band gaps and band-population effects. *Physical Review B* **13,** 4470–4476 (1976).

48. Anitha, M. *et al.* Influence of Carrier Gas Pressure on the Physical Properties of CdO Thin Films. *Zeitschrift für Physikalische Chemie* **233,** 913–932 (2019).

49. Saravanakumar, K., Muthuraj, V. & Jeyaraj, M. The design of novel visible light driven Ag/CdO as smart nanocomposite for photodegradation of different dye contaminants. *Spectrochimica Acta Part A: Molecular and Biomolecular Spectroscopy* **188,** 291–300 (2018).

50. Srivastava, A. K., Thota, S. & Kumar, J. Preparation, Microstructure and Optical Absorption Behaviour of NiO Thin Films. *Journal of Nanoscience and Nanotechnology* **8,** 4111–4115 (2008).

51. Irwin, M. D., Buchholz, D. B., Hains, A. W., Chang, R. P. H. & Marks, T. J. p-Type semiconducting nickel oxide as an efficiency-enhancing anode interfacial layer in polymer bulk-heterojunction solar cells. *Proceedings of the National Academy of Sciences* **105,** 2783–2787 (2008).

52. Zhang, K. H. L. *et al.* Electronic Structure and Band Alignment at the NiO and SrTiO 3 p–n Heterojunctions. *ACS Applied Materials & Interfaces* **9,** 26549–26555 (2017).

53. Ahmed, A. A., Hashim, M. & Rashid, M. Control of the structural, electrical and optical properties of spin coated NiO films by varying precursor molarity. *Thin Solid Films* **690,** 137554 (2019).

54. Mohanty, P., Sheppard, C. J., Doyle, B. P., Carleschi, E. & Prinsloo, A. R. Evolution of NiO phase at the expense of metallic nickel: Structure, magnetic and electronic properties. *Physica B: Condensed Matter* **570,** 285–290 (2019).

55. Boschloo, G. & Hagfeldt, A. Spectroelectrochemistry of Nanostructured NiO. *The Journal of Physical Chemistry B* **105,** 3039–3044 (2001).

56. Janotti, A. & Van de Walle, C. G. Fundamentals of zinc oxide as a semiconductor. *Reports on Progress in Physics* **72,** 126501 (2009).

57. Özgür, Ü. *et al.* A comprehensive review of ZnO materials and devices. *Journal of Applied Physics* **98,** 041301 (2005).

58. Muth, J. F., Kolbas, R. M., Sharma, A. K., Oktyabrsky, S. & Narayan, J. Excitonic structure and absorption coefficient measurements of ZnO single crystal epitaxial films deposited by pulsed laser deposition. *Journal of Applied Physics* **85,** 7884–7887 (1999).

59. Thomas, D. The exciton spectrum of zinc oxide. *Journal of Physics and Chemistry of Solids* **15,** 86–96 (1960).

60. Van Dijken, A., Meulenkamp, E. A., Vanmaekelbergh, D. & Meijerink, A. The Kinetics of the Radiative and Nonradiative Processes in Nanocrystalline ZnO Particles upon Photoexcitation. *The Journal of Physical Chemistry B* **104,** 1715–1723 (2000).

61. Van Dijken, A., Meulenkamp, E. A., Vanmaekelbergh, D. & Meijerink, A. Influence of Adsorbed Oxygen on the Emission Properties of Nanocrystalline ZnO Particles. *The Journal of Physical Chemistry B* **104,** 4355–4360 (2000).

62. Cohn, A. W., Janßen, N., Mayer, J. M. & Gamelin, D. R. Photocharging ZnO Nanocrystals: Picosecond Hole Capture, Electron Accumulation, and Auger Recombination. *The Journal of Physical Chemistry C* **116,** 20633–20642 (2012).

63. Wu, X. L., Siu, G. G., Fu, C. L. & Ong, H. C. Photoluminescence and cathodoluminescence studies of stoichiometric and oxygen-deficient ZnO films. *Applied Physics Letters* **78,** 2285–2287 (2001).

64. Vanheusden, K. *et al.* Mechanisms behind green photoluminescence in ZnO phosphor powders. *Journal of Applied Physics* **79,** 7983–7990 (1996).

65. Leung, Y. *et al.* Green emission in ZnO nanostructures—Examination of the roles of oxygen and zinc vacancies. *Applied Surface Science* **271,** 202–209 (2013).

66. Heo, Y. W., Norton, D. P. & Pearton, S. J. Origin of green luminescence in ZnO thin film grown by molecular-beam epitaxy. *Journal of Applied Physics* **98,** 073502 (2005).

67. Reshchikov, M. *et al.* Luminescence properties of defects in ZnO. *Physica B: Condensed Matter* **401-402,** 358–361 (2007).

68. Bauer, C., Boschloo, G., Mukhtar, E. & Hagfeldt, A. Ultrafast relaxation dynamics of charge carriers relaxation in ZnO nanocrystalline thin films. *Chemical Physics Letters* **387,** 176–181 (2004).

69. Hamberg, I., Granqvist, C. G., Berggren, K. .-.-F., Sernelius, B. E. & Engström, L. Band-gap widening in heavily Sn-doped In2O3. *Physical Review B* **30,** 3240–3249 (1984).

70. Tsokkou, D., Othonos, A. & Zervos, M. Ultrafast time-resolved spectroscopy of In2O3 nanowires. *Journal of Applied Physics* **106,** 084307 (2009).

71. Ganose, A. M. & Scanlon, D. O. Band gap and work function tailoring of SnO 2 for improved transparent conducting ability in photovoltaics. *Journal of Materials Chemistry C* **4,** 1467–1475 (2016).

72. Othonos, A., Zervos, M. & Tsokkou, D. Tin Oxide Nanowires: The Influence of Trap States on Ultrafast Carrier Relaxation. *Nanoscale Research Letters* **4,** 828–833 (2009).

73. Ho, C.-H., Chan, C.-H., Huang, Y.-S., Tien, L.-C. & Chao, L.-C. The study of optical band edge property of bismuth oxide nanowires α-Bi_2O_3. *Optics Express* **21,** 11965 (2013).

74. Yamada, Y., Yasuda, H., Tayagaki, T. & Kanemitsu, Y. Photocarrier recombination dynamics in highly excited SrTiO3 studied by transient absorption and photoluminescence spectroscopy. *Applied Physics Letters* **95,** 121112 (2009).

75. Biswas, S., Husek, J., Londo, S. & Baker, L. R. Highly Localized Charge Transfer Excitons in Metal Oxide Semiconductors. *Nano Letters* **18,** 1228–1233 (2018).

76. Katz, J. E. *et al.* Electron Small Polarons and Their Mobility in Iron (Oxyhydr)oxide Nanoparticles. *Science* **337,** 1200–1203 (2012).

77. Lohaus, C., Klein, A. & Jaegermann, W. Limitation of Fermi level shifts by polaron defect states in hematite photoelectrodes. *Nature Communications* **9,** 4309 (2018).

78. Pastor, E. *et al.* In situ observation of picosecond polaron self-localisation in α-Fe2O3 photoelectrochemical cells. *Nature Communications* **10,** 3962 (2019).

79. Vura-Weis, J. *et al.* Femtosecond M 2,3 -Edge Spectroscopy of Transition-Metal Oxides: Photoinduced Oxidation State Change in α-Fe 2 O 3. *The Journal of Physical Chemistry Letters* **4,** 3667–3671 (2013).

80. Carneiro, L. M. *et al.* Excitation-wavelength-dependent small polaron trapping of photoexcited carriers in α-Fe2O3. *Nature Materials* **16,** 819–825 (2017).

81. Cao, H., Qiu, X., Liang, Y., Zhao, M. & Zhu, Q. Sol-gel synthesis and photoluminescence of p-type semiconductor Cr2O3 nanowires. *Applied Physics Letters* **88,** 241112 (2006).

82. Lebreau, F., Islam, M. M., Diawara, B. & Marcus, P. Structural, Magnetic, Electronic, Defect, and Diffusion Properties of Cr 2 O 3 : A DFT+ U Study. *The Journal of Physical Chemistry C* **118,** 18133–18145 (2014).

83. Santulli, A. C., Feygenson, M., Camino, F. E., Aronson, M. C. & Wong, S. S. Synthesis and Characterization of One-Dimensional Cr2O3 Nanostructures. *Chemistry of Materials* **23,** 1000–1008 (2011).

84. Cheng, C.-S., Serizawa, M., Sakata, H. & Hirayama, T. Electrical conductivity of Co3O4 films prepared by chemical vapour deposition. *Materials Chemistry and Physics* **53,** 225–230 (1998).

85. Hayes, D. *et al.* Electronic and nuclear contributions to time-resolved optical and X-ray absorption spectra of hematite and insights into photoelectrochemical performance. *Energy Environ. Sci.* **9,** 3754–3769 (2016).

86. Biswas, S., Husek, J., Londo, S. & Baker, L. R. Ultrafast Electron Trapping and Defect-Mediated Recombination in NiO Probed by Femtosecond Extreme Ultraviolet Reflection–Absorption Spectroscopy. *The Journal of Physical Chemistry Letters* **9,** 5047–5054 (2018).

87. Selim, S. *et al.* WO 3 /BiVO 4 : impact of charge separation at the timescale of water oxidation. *Chemical Science* **10,** 2643–2652 (2019).

88. Tang, N. *et al.* Nanostructured magnetite (Fe3O4) thin films prepared by sol–gel method. *Journal of Magnetism and Magnetic Materials* **282,** 92–95 (2004).

89. Jeon, H. S. *et al.* Simple Chemical Solution Deposition of Co 3 O 4 Thin Film Electrocatalyst for Oxygen Evolution Reaction. *ACS Applied Materials & Interfaces* **7,** 24550–24555 (2015).

90. Chen, Z. *et al.* Fabrication of Highly Transparent and Conductive Indium–Tin Oxide Thin Films with a High Figure of Merit via Solution Processing. *Langmuir* **29,** 13836–13842 (2013).

Chapter 8

Conclusions and future work

The aim of this thesis was to contribute to a better understanding of what dictates the activity of photocatalyst materials for solar-driven fuel generation using insights obtained via time-resolved spectroscopy. Given the application in the field of photocatalysis, the range of investigated materials could not have been much more diverse: The first two results chapters dealt with organic polymers, whereas the latter two were concerned with a wide range of inorganic metal oxides with various electronic configurations. The presented results address various aspects of the photocatalytic activity of these materials and demonstrate the versatility of the employed transient spectroscopic techniques in extracting activity-related information from such disordered semiconductors.

8.1 Polymer photocatalysts

Photocatalytic activities in the relatively new class of organic photocatalysts tend to result from a complex interplay of many factors such as excited state lifetimes, thermodynamic driving forces, and interfacial interactions. None of these factors seem to be well understood at present owing to the novelty of organic materials for application as photocatalysts, and their relative importance is therefore unclear. The sulfone polymers P7 and P10 investigated in Chapter 4 provided the opportunity to explore what determines the hydrogen evolution activity of some of the best performing conjugated polymers reported for this application to date. It was found that the generation of the active species (or at least its precursor) occurs on the early picosecond timescale, which is surprisingly fast even for the initial step of a photocatalytic reaction. The

resulting yield of long-lived electrons was found to increase with the sulfone-content of the respective polymer, in good agreement with the measured H_2 evolution activity. The vital role of the sulfone groups in the polymer backbone was further supported by DFT calculations and molecular dynamics simulations, demonstrating that their dipolar character attracts water to the polymer, and that the resulting higher polarity of the solvent environment favourably affects driving forces for the TEA oxidation reaction.

In Chapter 5, the importance of co-catalysts, present in the form of residual palladium impurities in many of these all-organic photocatalyst materials, was investigated. F8BT nanoparticles had previously shown a strong dependence of hydrogen evolution activity on their residual Pd content, and were thus used to elucidate at which point in the photocatalytic reaction sequence Pd comes into play. It was found that exciton quenching via energy transfer to Pd, a recombination process, directly competes with reductive quenching by hole transfer to the electron donor diethylamine (DEA) in solution. Energy transfer to Pd is found to occur about two times faster than reductive quenching via DEA, and already starts to dominate the overall exciton quenching at trace amounts of Pd. Depending on the Pd content, the produced long-lived electrons reside either on the Pd centres within the F8BT nanoparticles or on the F8BT polymer itself. Similarly, under quasi-constant illumination, charge accumulation in these F8BT nanoparticles occurs on Pd centres at higher Pd content. Interestingly, charges in P10 accumulate on the polymer itself even in the presence of high Pd concentrations, which points to electron transfer to Pd being the rate limiting step in this material. In contrast, the limitation in F8BT at similarly high Pd content appears to be the kinetically slow hydrogen evolution reaction, since electrons already reside on Pd centres before the typical timescale of hydrogen evolution.

Although these results provide a significant addition to the polymer photocatalyst literature, not all open questions have been fully resolved in the studies reported herein. Firstly, it has remained unclear whether the species generated on the early picosecond timescale in P10 is an already separated charge or rather a precursory state such as a bound polaron pair. It would be of interest to further clarify how this rapid charge generation process occurs in order to enable targeted implementation in other materials. For instance, polarisation dependent transient absorption measurements could be useful in this regard. Secondly, the exact mechanism of proton reduction on these polymer photocatalysts has so far remained elusive. The first step towards obtaining detailed mechanistic information has been made herein by employing quasi-steady state photoinduced absorption measurements. Conducting these experiments for a

number of different light intensities could provide insight into quantities such as the order of the rate limiting reaction step as previously demonstrated for metal oxides [1, 2].

8.2 Metal oxide photocatalysts

Although metal oxides are are far more established in the field of photocatalysis than their polymeric counterparts, design guidelines on a fundamental photophysical level are still not readily available. As elaborated further in Chapter 7, metal oxides with empty d-shell configurations are promising photocatalyst materials. However, due to the high ionic character of these materials, they typically exhibit large bandgaps and thus absorb little visible light. In Chapter 6, the deliberate introduction of oxygen vacancies as a strategy to overcome this lack of visible light absorption was explored. To this end, WO_3 was used as a model material due to its strong tendency towards oxygen vacancy formation. It was found that highly oxygen-deficient WO_3 exhibits a large density of oxygen vacancy states within the bandgap. These sub-bandgap states induce a strong blue colouration in the material, but also give rise to rapid trapping of photogenerated valence band holes. While this rapid trapping process prolongs the lifetime of photogenerated charges by several orders of magnitude, it also causes a pronounced loss in oxidative driving force. As a result, the efficiency of kinetically demanding oxidation reactions such as water oxidation is severely compromised, yet the prolonged carrier lifetimes suggest potential benefits for reactions that require less oxidative driving force or for reduction reactions. These results demonstrate that the distribution of sub-bandgap states, and not just the energetic positions of valence and conduction band, need to be tuned with respect to a targeted photocatalytic reaction.

Chapter 7 presented a broad survey of the photophysical properties of 11 different metal oxides in order to identify common features that could either benefit or limit their photocatalytic activity. A particular focus was the lifetime of band-like delocalised charges, which can be expected to significantly impact on the extent of spatial charge separation immediately after photoexcitation as well as on the overall charge transport properties of the material. It was found that all investigated open d-shell oxides exhibited a rapid initial relaxation of photogenerated electrons with a time constant of $\sim$400 fs following photoexcitation, which was assigned to the rapid formation of small polarons. In contrast, all studied oxides with empty (d^0) or closed d-shells (d^{10}) exhibited longer lifetimes of delocalised electrons, reaching up to three orders of magnitude higher values in some cases. Several d^{10} oxides exhibited rapid hole trapping similar to the

oxygen-deficient WO_3 reported in Chapter 6, and the long lifetime of photogenerated electrons might therefore be related to a rapid immobilisation of photogenerated holes in at least some of these materials. WO_3 itself shows the fastest delocalised electron decay among all investigated d^0 oxides, which might be due to a large number of electron traps within its overall high trap density. Nevertheless, even this fast decay is still about one order of magnitude slower than the decay of delocalised electrons in open d-shell oxides, which further supports the assignment of the latter to a different mechanism such as small polaron formation. On longer timescales, transient signals which resembled the second derivative of the ground state absorbance were found for all materials with sufficiently strong absorption features in the probed spectral range. These derivative-like features point towards the presence of highly localised charges at these longer times, possibly following localisation at defect sites.

Despite the already large amount of data presented in this chapter, some additional insights would still be desired. Firstly, although the steady-state and transient optical signatures of the samples investigated herein are in good agreement with literature reports, additional structural characterisations such as XRD and Raman experiments need to be carried out. Secondly, the complexity of the presented transient signals due to overlapping components significantly complicates quantitative comparisons between materials, especially for the open d-shell oxides where a fluence-dependent component often overlaps the rapid initial delocalised electron decay. The non-exponential decay of many of the signal components has so far prevented the consistent use of global analysis techniques, but adaptations to common routines could in principle be made to account for such behaviour. Thirdly, while the rate of small polaron formation appears to be very similar for all investigated open d-shell oxides, the amount of energy lost through this relaxation pathway is at present unclear for most materials. DFT calculations, as carried out previously for Fe_2O_3 [3], should be able to shed light on this aspect and could even include open d-shell materials not investigated experimentally herein. Lastly, the accessible spectral probe range of the experimental setup used in this work currently has a lower limit of $\sim$450 nm, which precludes the proper investigation of long-lived transients in the larger bandgap materials investigated herein. Upgrading the existing setup with a UV continuum would allow to study these derivative-like signals in greater depth.

8.3 References

1. Le Formal, F. *et al.* Rate Law Analysis of Water Oxidation on a Hematite Surface. *Journal of the American Chemical Society* **137,** 6629–6637 (2015).

2. Mesa, C. A. *et al.* Kinetics of Photoelectrochemical Oxidation of Methanol on Hematite Photoanodes. *Journal of the American Chemical Society* **139,** 11537–11543 (2017).

3. Pastor, E. *et al.* In situ observation of picosecond polaron self-localisation in α-Fe2O3 photoelectrochemical cells. *Nature Communications* **10,** 3962 (2019).

Appendix A

Hydrogen evolution activity of amphiphilic conjugated polymers

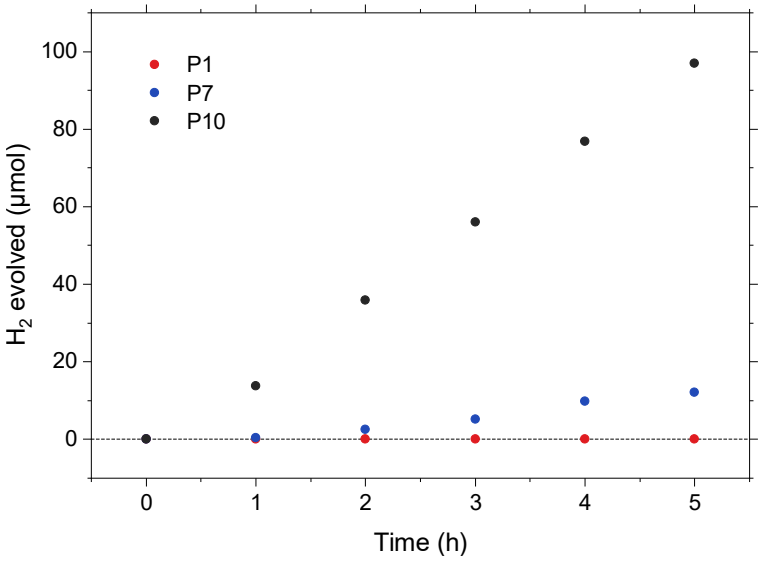

Figure A.1: Photocatalytic hydrogen evolution under visible light (>420 nm) illumination using P1, P7, and P10 in an aqueous solution of 0.35 M Na_2S and 0.25 M Na_2SO_3 as inorganic sacrificial electron donors.

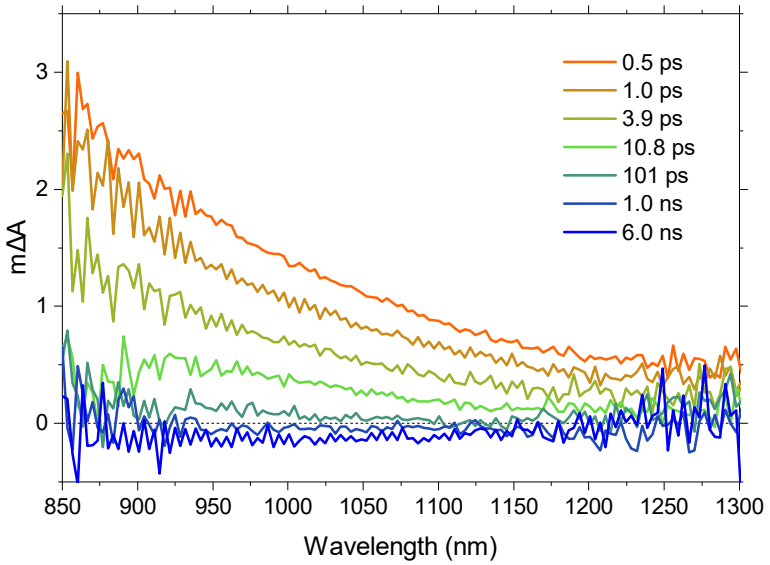

Figure A.2: Transient absorption spectrum of an aqueous P10 suspension probed in the NIR, acquired using an excitation wavelength of 355 nm and a fluence of 0.08 mJ cm^{-2}.

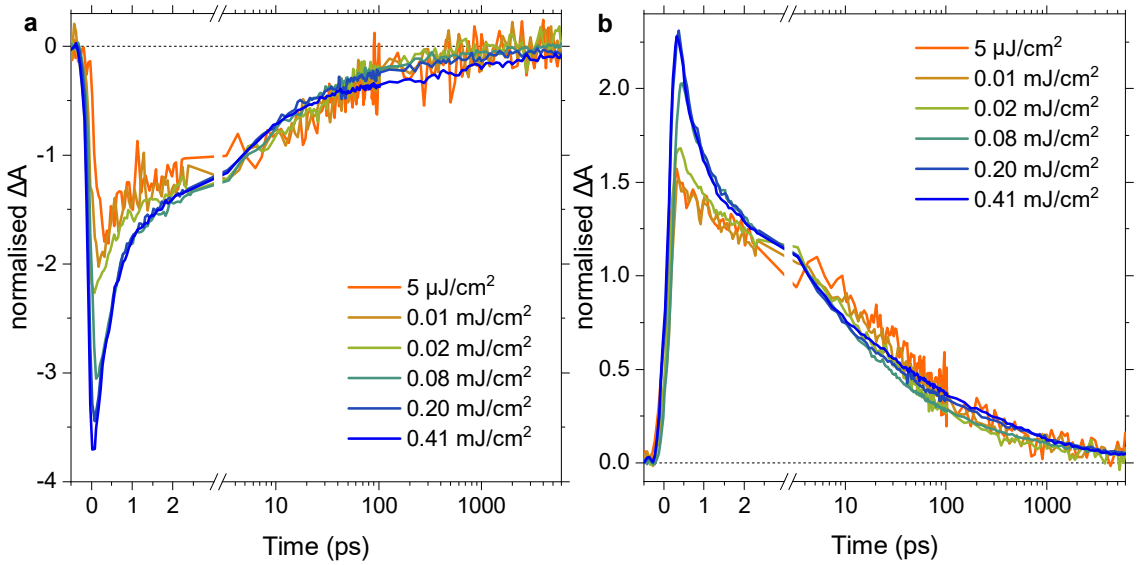

Figure A.3: Transient absorption kinetics of P7 in aqueous suspension probed at (**a**) 500 nm and (**b**) 760 nm, which correspond to the broad simulated emission bleach and the exciton excited state absorption, respectively. Different fluences between 5 μJ cm^{-2} and 0.41 mJ cm^{-2} were used to investigate the excitation intensity dependence of the probed kinetics. All kinetics were normalised at 3 ps for better comparability of the decay profile.

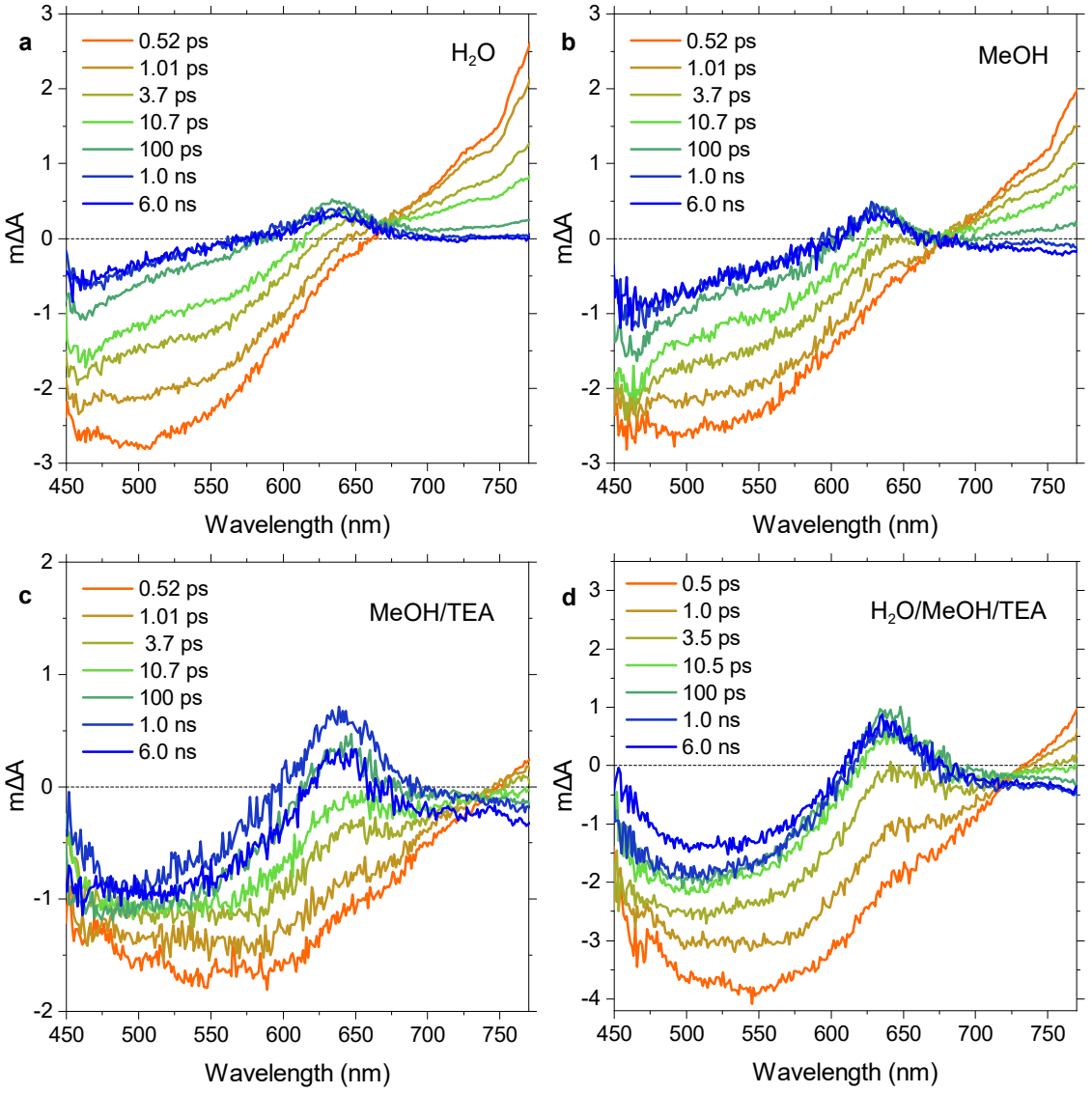

Figure A.4: Transient absorption spectra of P10 suspended in (**a**) H_2O only, (**b**) MeOH only, (**c**) a 1:1 MeOH/TEA mixture, and (**d**) a 1:1:1 H_2O/MeOH/TEA mixture. Note that (**a**) and (**d**) are identical to the data shown in Figure 4.5 and are reproduced here for convenience. All transient spectra were obtained using an excitation wavelength of 355 nm and a fluence of 0.08 mJ cm^{-2}.

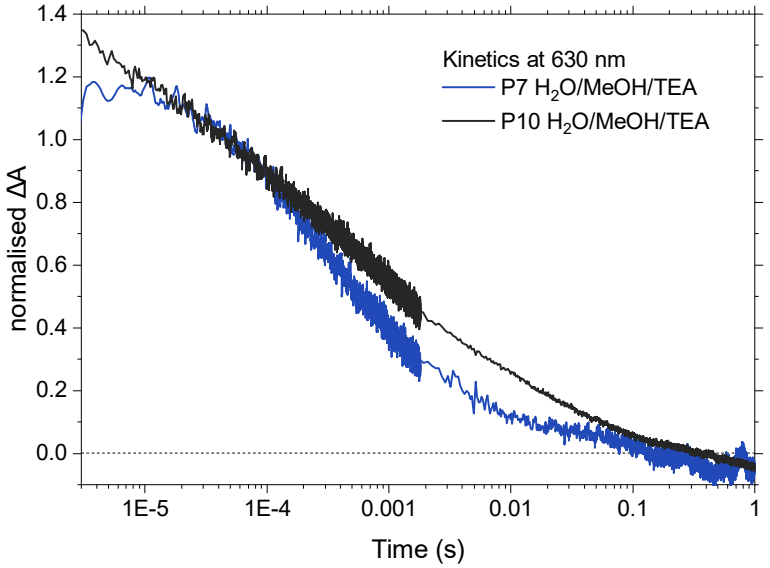

Figure A.5: Normalised transient kinetics for P7 and P10 in H_2O/MeOH/TEA, probed at 630 nm following 355 nm excitation using a fluence of 0.32 mJ cm^{-2}. The shown kinetics are the same ones as in Figure 4.8.

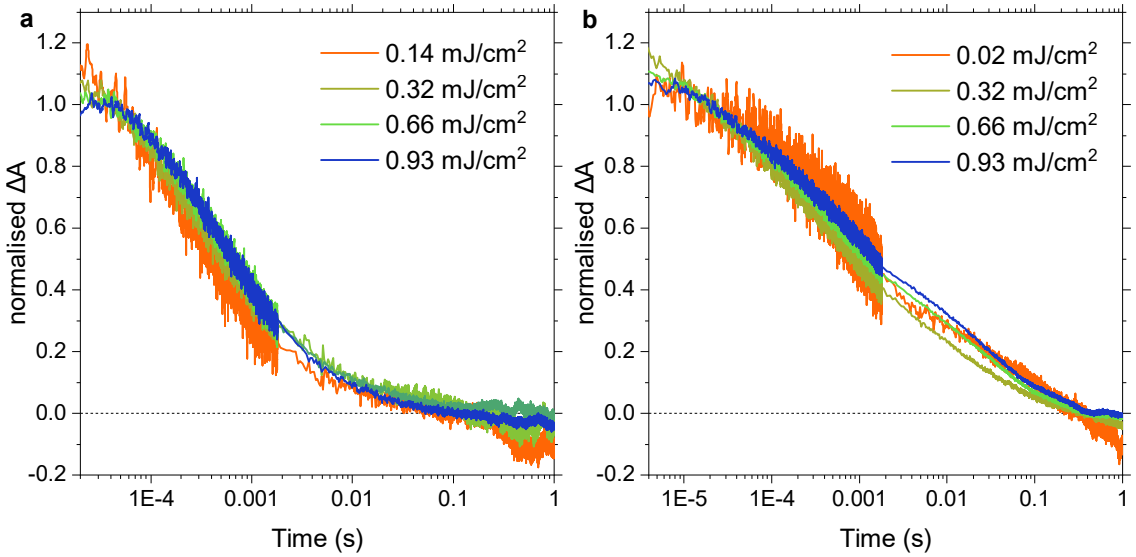

Figure A.6: Normalised transient kinetics for (**a**) P7 and (**b**) P10 in H_2O/MeOH/TEA, probed at 630 nm following 355 nm excitation using a range of different fluences between 0.02 - 0.93 mJ cm^{-2}.

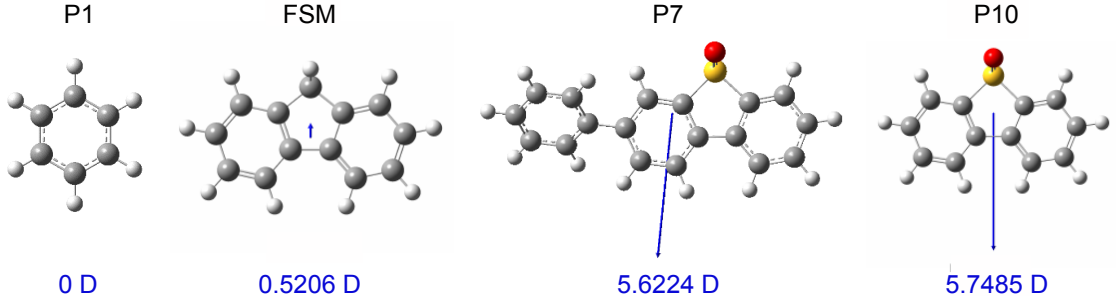

Figure A.7: Dipole moments for monomers of P1, FSM, P7, and P10, calculated using DFT, B3LYP/6-311G(d,p) with Gaussian 16.

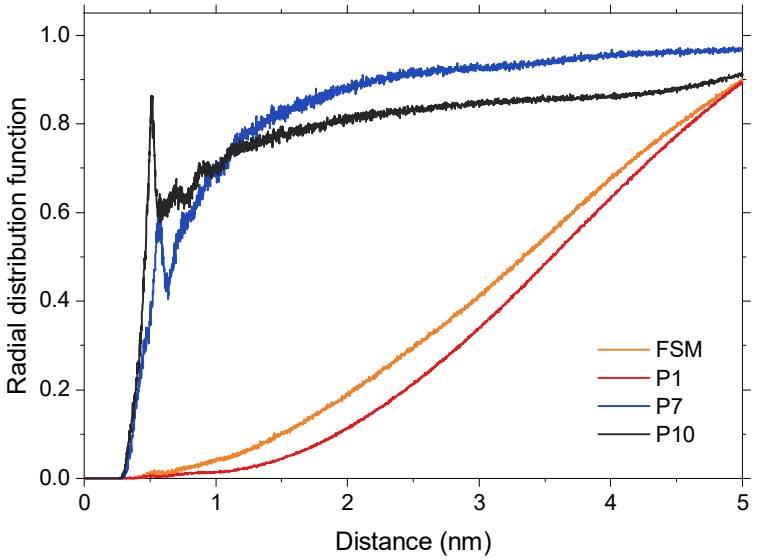

Figure A.8: Radial distribution function between water and the sulfone group in the dibenzo[*b,d*]thiophene sulfone unit in P7 and P10, the bridging fluorene carbon atom in FSM, or one of the aromatic carbon atoms in P1.

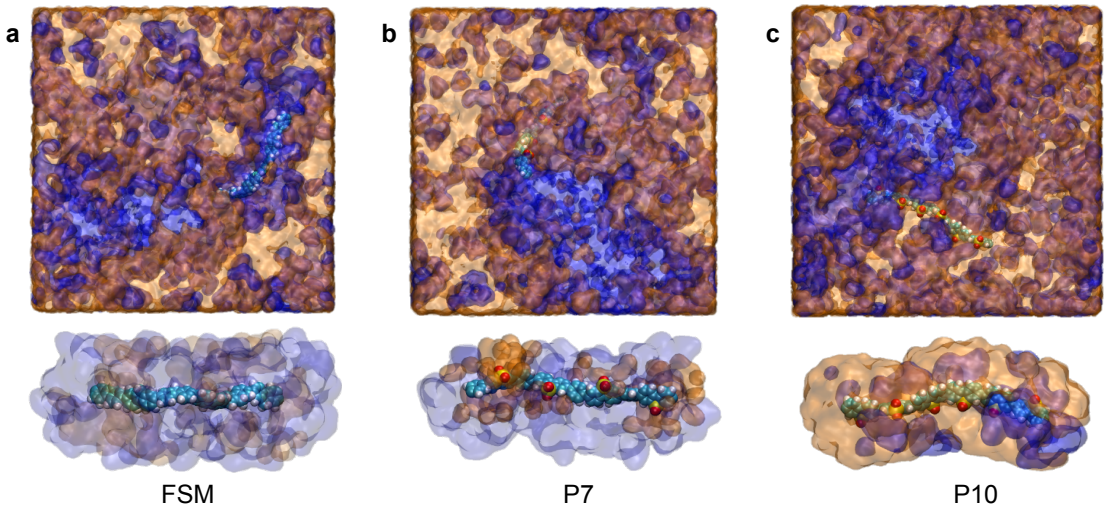

Figure A.9: Snapshots of atomistic molecular dynamics simulations showing (**a**) the fluorene polymer as a model for P1, (b) P7, and (c) P10 in a mixed environment of H_2O, MeOH (both orange) and TEA (blue). Like in the H_2O/TEA simulation in Figure 4.11, the P7 and P10 polymers establish a water shell around their sulfone groups whereas the fluorene polymer surrounds itself with TEA.

Appendix B

Role of residual palladium in conjugated polymer photocatalysts

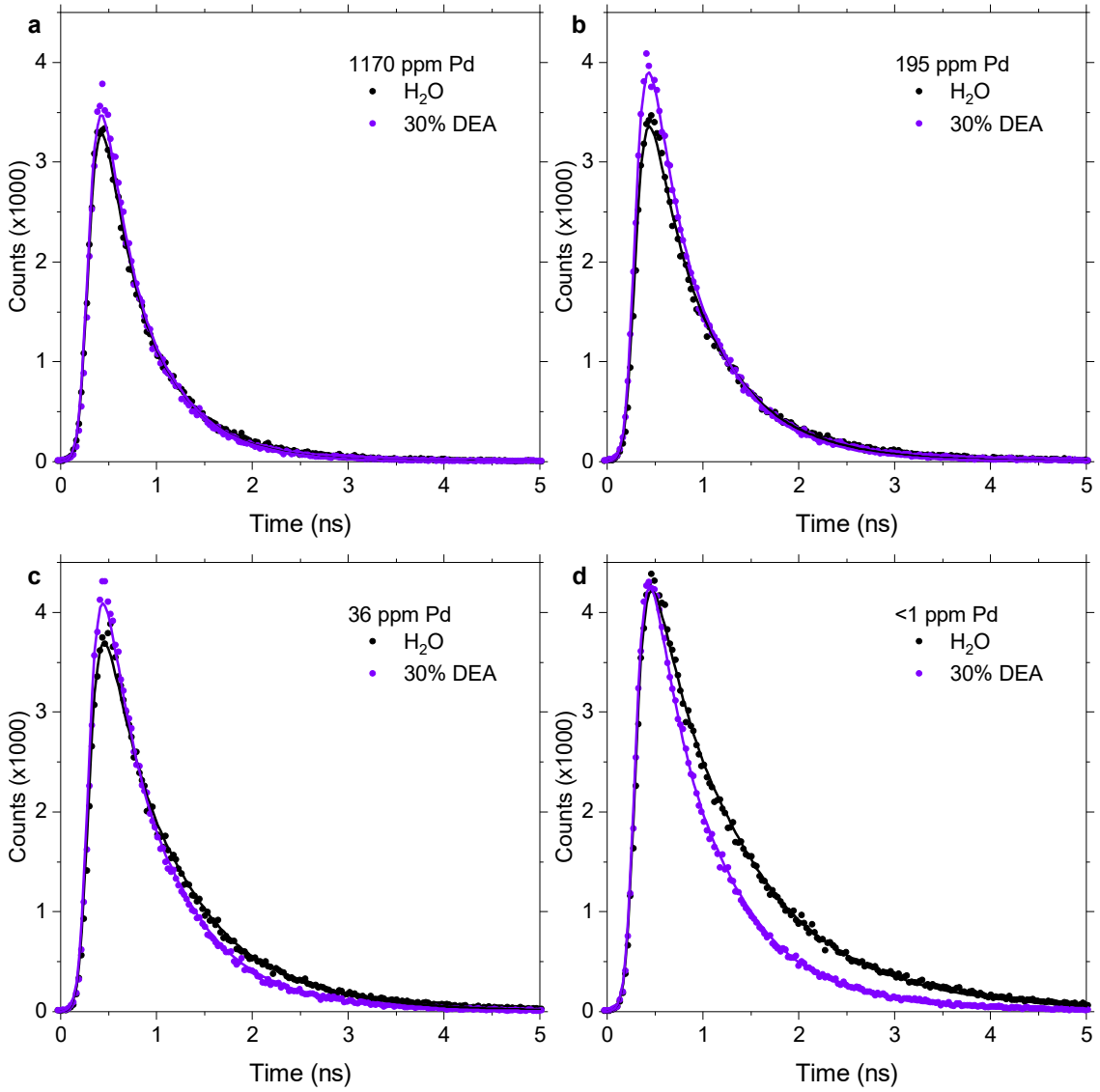

Figure B.1: Photoluminescence decay kinetics of F8BT nanoparticle suspensions in H_2O and a 3:7 DEA/H_2O mixture, probed at 545 nm upon 467 nm excitation for F8BT nanoparticles with (**a**) 1170 ppm Pd, (**b**) 195 ppm Pd, (**c**) 36 ppm Pd, and (**d**) <1 ppm Pd. The higher signal amplitude in DEA/H_2O compared to pure H_2O observed for **a** - **c** is assigned to the evaporation of some of the relatively volatile DEA during the argon purge prior to the measurement. All samples were prepared with an absorbance of 0.10 at the excitation wavelength and emitted photons were counted over a time period of 10 s, which enables a quantitative comparison of signal amplitudes. The full lines represent fits to the data obtained using iterative reconvolution of the measured instrument response and a stretched exponential function $y \propto exp(-kt^b)$ with a constant stretching exponent $b = 0.87$.

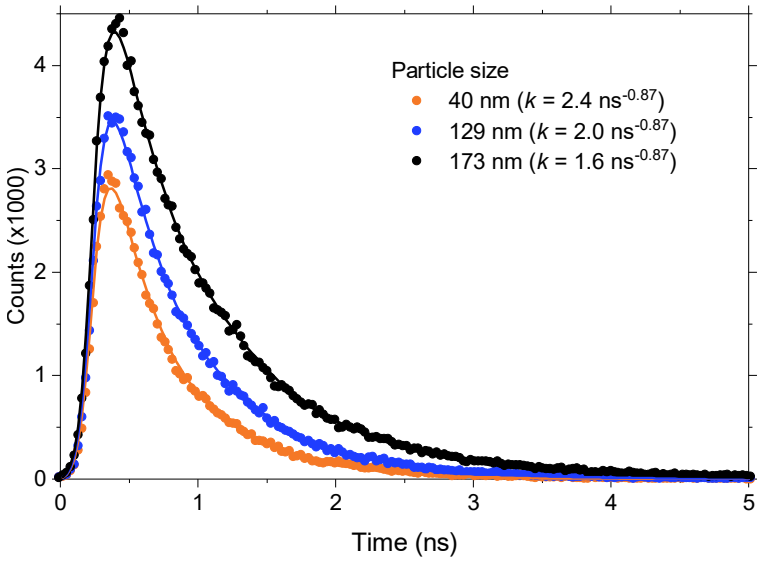

Figure B.2: Photoluminescence decay kinetics of nanoparticles made from unpurified F8BT with sizes ranging from 40 - 173 nm, suspended in H_2O and probed at 545 nm upon 467 nm excitation. All samples were prepared with an absorbance of 0.10 at the excitation wavelength and emitted photons were counted over a time period of 10 s, which enables a quantitative comparison of signal amplitudes. The full lines represent fits to the data obtained using iterative reconvolution of the measured instrument response and a stretched exponential function $y \propto exp(-kt^b)$ with a constant stretching exponent $b = 0.87$, and the resulting rate constants k are stated in the legend.

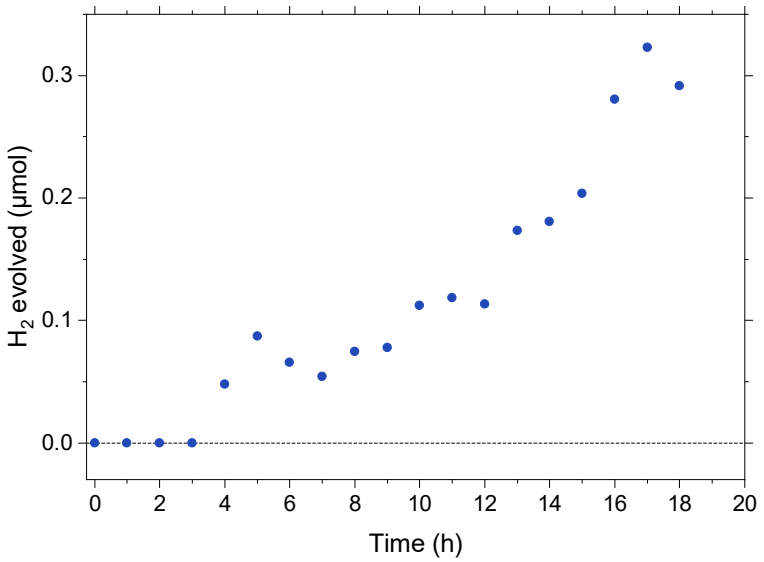

Figure B.3: Hydrogen evolution runs of P3HT nanoparticles with 40 nm diameter and 5 wt.% photodeposited Pt in a 1:1:1 H_2O/methanol/triethylamine mixture, irradiated by the output of a 300 W xenon lamp (385 - 700 nm).

Appendix C

Effect of oxygen deficiency on the excited state kinetics of WO_3

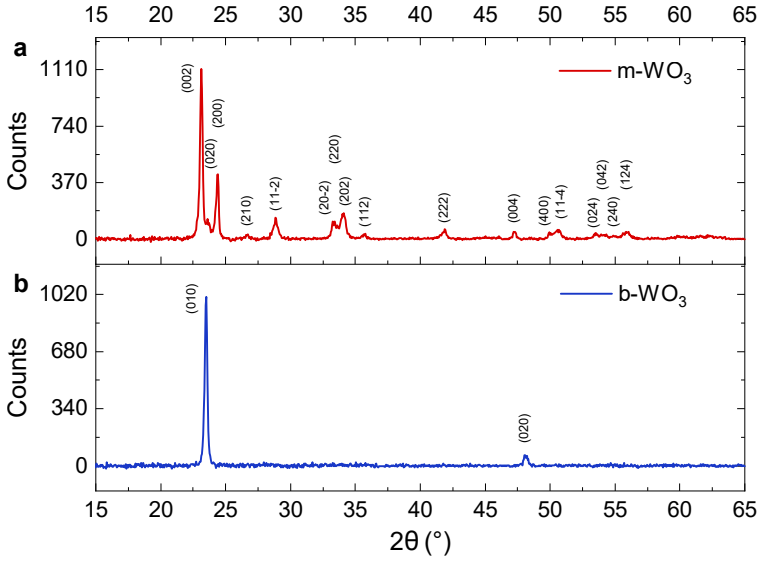

Figure C.1: X-ray diffraction patterns recorded for (a) m-WO_3 and (b) b-WO_3. Labels correspond to the structures ICSD 01-083-0950 and ICSD 01-079-0171 for m-WO_3 and b-WO_3, respectively.

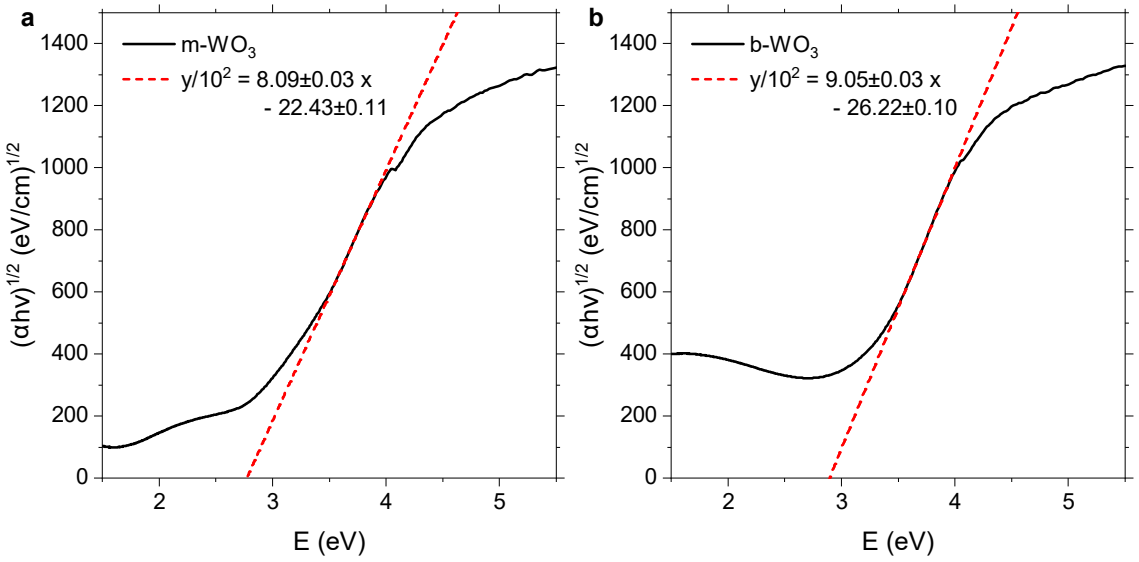

Figure C.2: Tauc plots for (**a**) m-WO3 and (**b**) b-WO_3, assuming an indirect bandgap in both cases. Error estimates given in the main paper reflect variations of the bandgap value over different seemingly suitable linear fits.

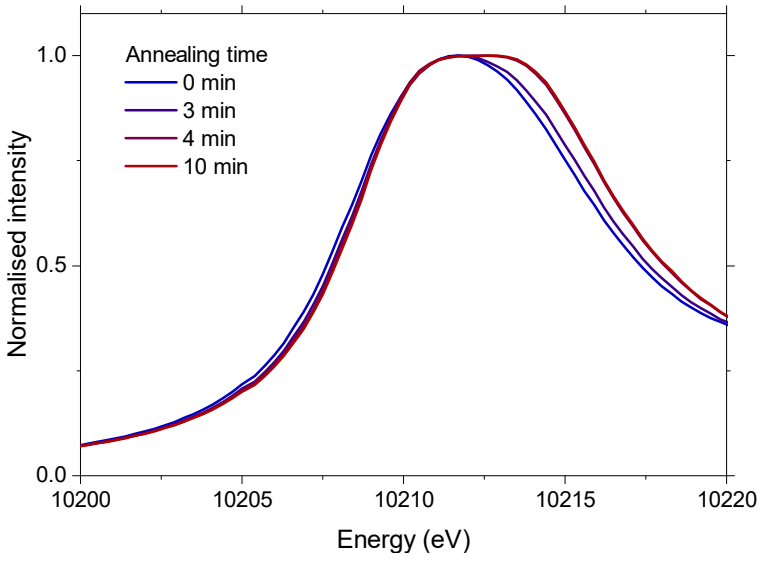

Figure C.3: Tungsten L_{III}-edge x-ray absorption near edge structure (XANES) spectra obtained from a set of WO_3 films prepared using a deposition temperature of 300 °C with variable subsequent annealing times between 0 min (unannealed) to 10 min. These annealing times are shorter than those used for the main samples in this study since the lower deposition temperature compared to the 350 °C used for the samples denoted m-WO3 and b-WO3 results in a flatter morphology, where filling of oxygen vacancies requires shorter subsequent annealing times.

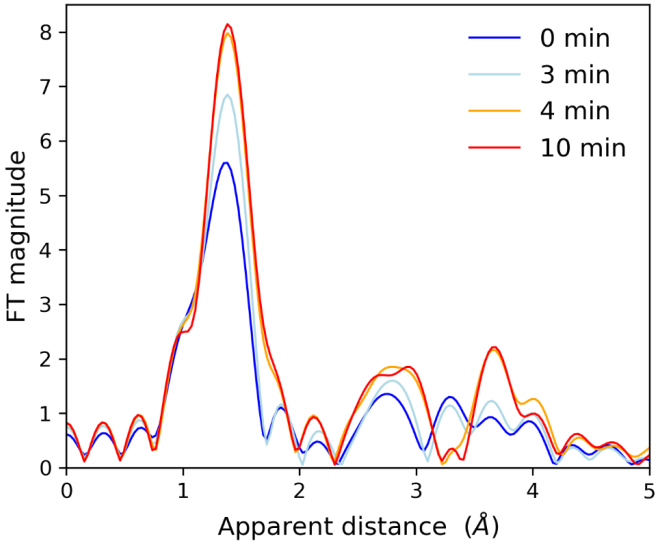

Figure C.4: W L_{III}-edge Fourier Transformed EXAFS (k^3-weighted) of a set of WO_3 samples prepared at different annealing times. The extreme cases are: 0 min, corresponding to highly oxygen deficient WO_3 (b-WO_3) and 10 min, corresponding to near-stoichiometric WO_3 (m-WO_3).

Figure C.4 shows the Fourier Transform K^3-weighed EXAFS spectra of b-WO_3 (0 min annealing) and m-WO_3 (10 min annealing) as well as intermediate states. Comparison of the FT data for the extreme samples reveals a different bonding environment as previously observed for similar samples [1]. In line with reference [2], the different scattering peaks observed are assigned to: (i) 1 - 2 Å, first shell of oxygen atoms; (ii) 2.3 - 3.1 Å, multiple scattering within the first shell; this peak is divided in two parts suggesting the existence of two distinctive W - O distances and (iii) 3.1 - 4 Å W - W distances. As expected, fits of the first shell require two W - O distances. As shown in Table C.1, for the near-stoichiometric sample the fits improve upon increasing the W-O distance and a reasonable fit is obtained with a coordination of 4:2, expected for a distorted octahedral. In contrast, for the oxygen deficient b-WO_3 sample better fits are obtained with shorter W-O distanced and reasonable results are obtained for different coordination number (2:4, 3:3, and 4:2) as shown in Table C.2. These fit results indicate that m-WO_3 cannot be described as purely octahedral but that a larger heterogeneity of distances exists. Together with the lower amplitude observed for this sample this is indicative of a larger disorder. These results suggest that the generation of oxygen vacancies results in geometric deformations around the tungsten centre.

Table C.1: EXAFS fit parameters for m-WO_3.

Bond	N	R (Å)	σ^2 ($Å^2$)	R (%)
W-O1	2	1.768±0.017	0.000±0.001	4.3
W-O2	4	2.01±0.04	0.023±0.009	
W-O1	3	1.771±0.012	0.002±0.001	1.62
W-O2	3	2.045±0.019	0.012±0.003	
W-O1	4	1.767±0.013	0.005±0.001	1.2
W-O2	2	2.056±0.014	0.005±0.002	
W-O1	5	1.73±0.05	0.009±0.003	18.9
W-O2	1	2.54±0.11	0.002±0.012	
W-O1	6	1.71±0.06	0.012±0.003	27

Table C.2: EXAFS fit parameters for b-WO_3.

Bond	N	R (Å)	σ^2 (Å^2)	R (%)
W-O1	2	1.770±0.008	0.004±0.001	0.53
W-O2	4	1.75±0.06	0.021±0.005	
W-O1	3	1.783±0.010	0.006±0.001	0.56
W-O2	3	1.95±0.04	0.024±0.006	
W-O1	4	1.787±0.010	0.008±0.001	0.51
W-O2	2	2.01±0.03	0.020±0.006	
W-O1	5	1.793±0.015	0.009±0.001	0.78
W-O2	1	2.06±0.03	0.009±0.006	
W-O1	6	1.771±0.021	0.013±0.001	3.6

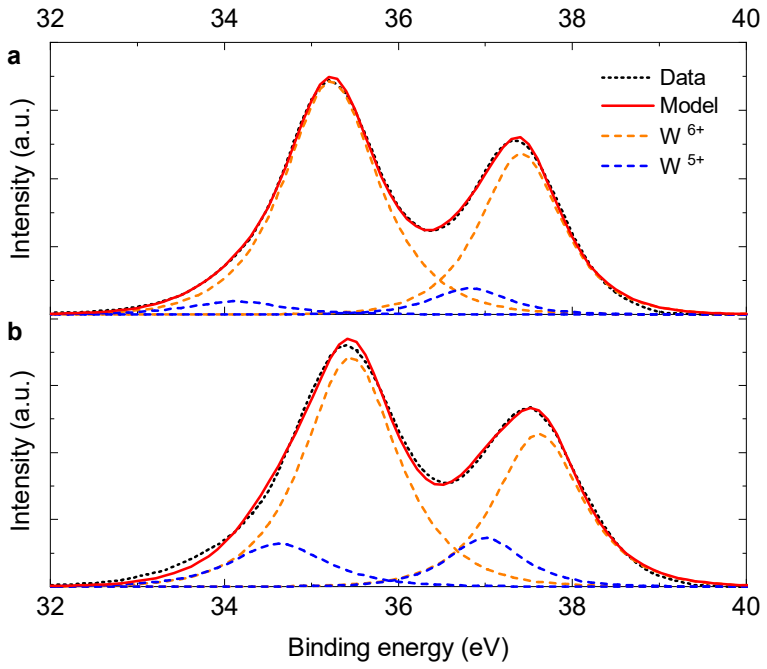

Figure C.5: XPS spectra of (**a**) m-WO_3 and (**b**) b-WO_3 in the W binding energy region, reflecting the W^{5+} to W^{6+} ratio at the film surface.

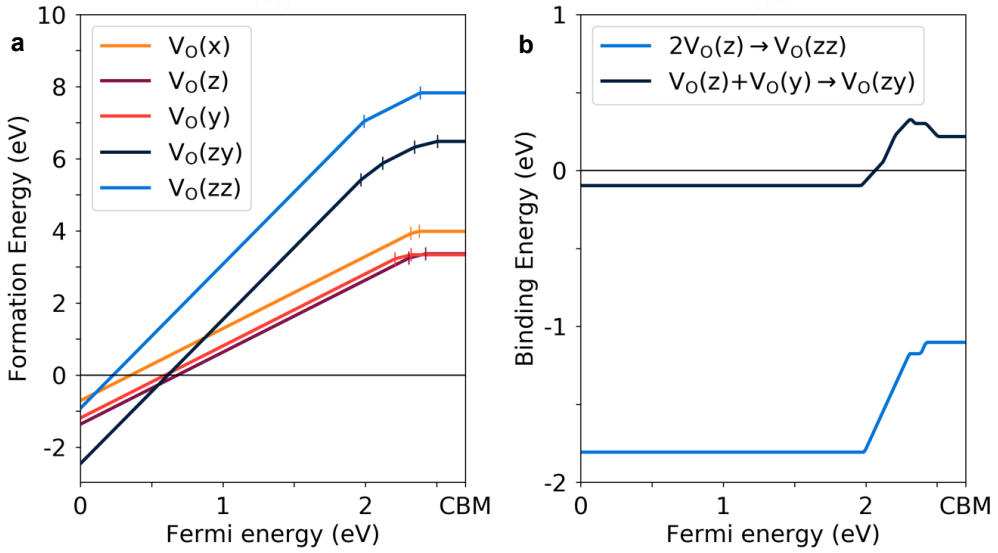

Figure C.6: The calculated (**a**) formation energy of oxygen vacancy defects and (**b**) binding energy of defect complexes. In (**a**), each solid line represents the formation energy of a given defect. Only the formation energy of the most stable charge state is plotted for a given Fermi energy. The slope represents the charge state (q); the formation energies contain a term qEF in this grand-canonical formalism. Short vertical lines indicate the thermal transition levels at which the charge state changes. Data in (**b**) shows how much energy is donated to the ambient system when two oxygen vacancies form a defect complex. This quantity is referred to as binding energy. The binding energy is in general represented as $Eb(A+B;E_F) = E_f(A;E_F) + E_f(B;E_F) - E_f(A+B;E_F)$. In this case, $E_f(A;E_F)$ represent the formation energy of defect A at a given E_F, which can be found in panel (**a**). Positive binding energies indicate that the defect complex is formed spontaneously.

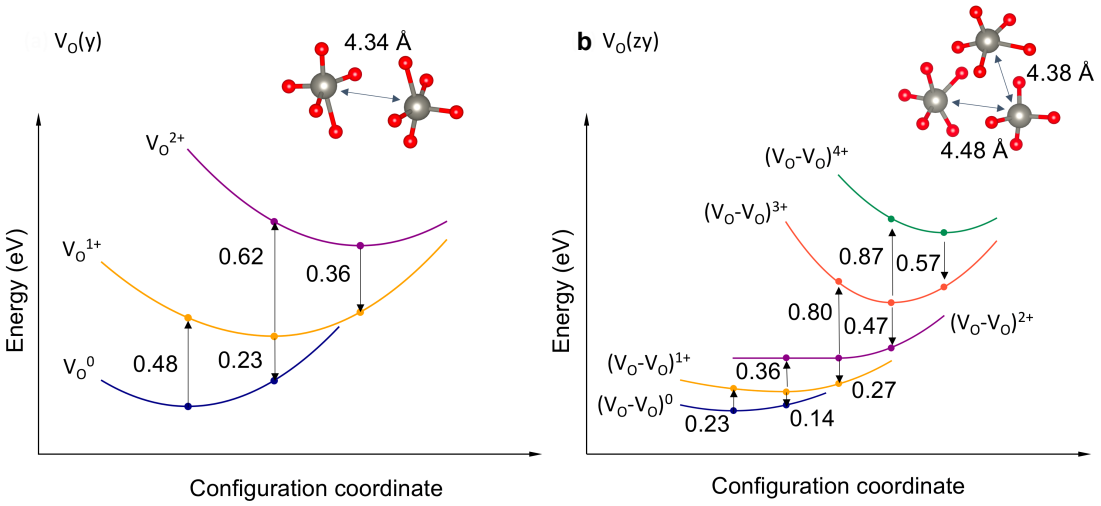

Figure C.7: Configuration coordinate diagrams showing the potential energy surface associated with defect ionization calculated from density functional theory for (**a**) a single oxygen vacancy and (**b**) a defect complex composed of two oxygen vacancies. Local atomic structures and the distance between the W atoms are shown schematically as insets. The V_O^0 to V_O^{1+} and V_O^{1+} to V_O^{2+} transitions are 0.5 eV and 0.2 eV for the isolated vacancy, respectively. Upon complex formation, a wider range of charge states are accessible (four excess electrons), with excitation energies ranging from 0.2 eV to 0.9 eV. These calculations assume n-type conditions with the Fermi level at the WO_3 conduction band minimum.

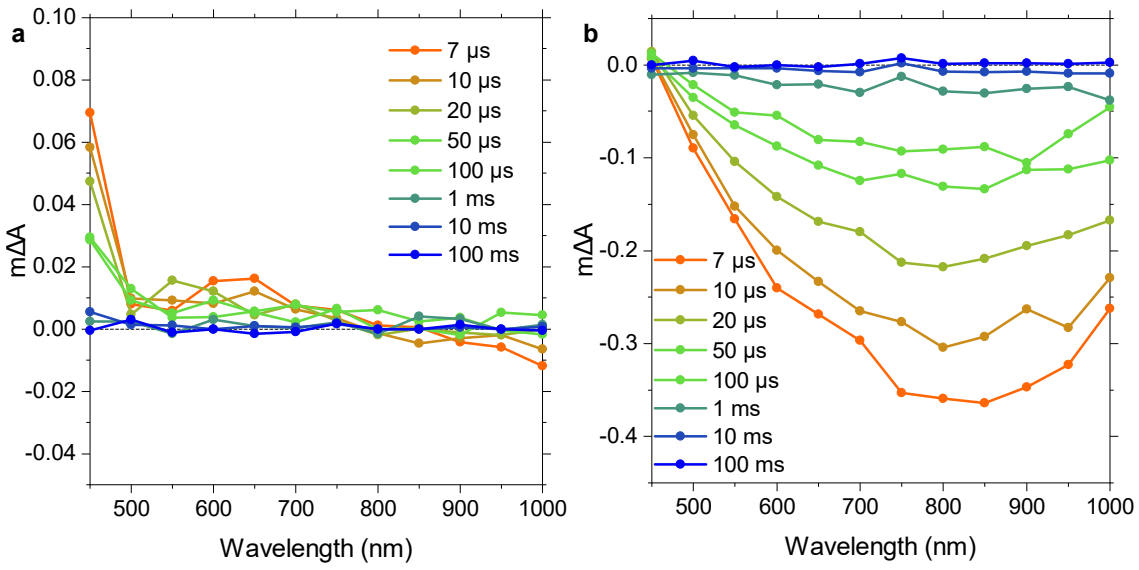

Figure C.8: Transient absorption spectra of (**a**) m-WO_3 and (**b**) b-WO_3 upon excitation at SI355nm using a fluence of 3.0 mJ cm^{-2}.

C.1 References

1. Kuzmin, A. & Purans, J. X-ray absorption spectroscopy study of local structural changes in a-WO 3 under colouration. *Journal of Physics: Condensed Matter* **5,** 2333–2340 (1993).

2. Pauporté, T., Soldo-Olivier, Y. & Faure, R. XAS Study of Amorphous WO 3 Formation from a Peroxo-Tungstate Solution. *The Journal of Physical Chemistry B* **107,** 8861–8867 (2003).

Appendix D

Localisation of photogenerated charges in metal oxides

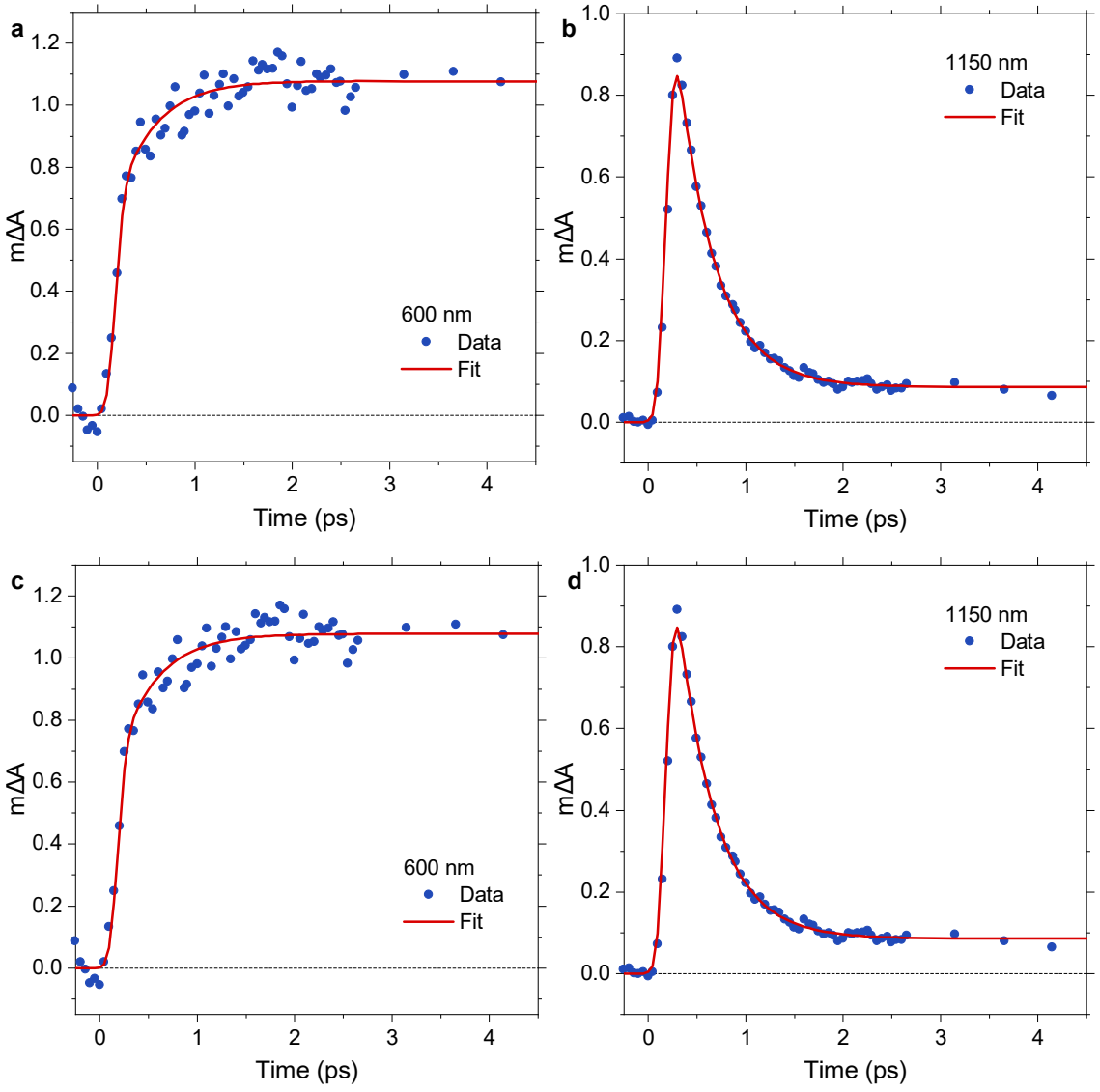

Figure D.1: Fits produced via global target analysis of the first 4.5 ps of a Co_3O_4 dataset acquired using an excitation wavelength of 740 nm and a fluence of 0.10 mJ cm^{-2}, here illustrated exemplary for kinetics probed at (**a**, **c**) 600 nm and (**b**, **d**) 1150 nm. An (**a**, **b**) evolutionary sequential model $A \rightarrow B$ or (**c**, **d**) exponentially decaying component A in the presence of a non-decaying constant component B were used. These are exemplary kinetics for the global fits shown in Figure 7.4.

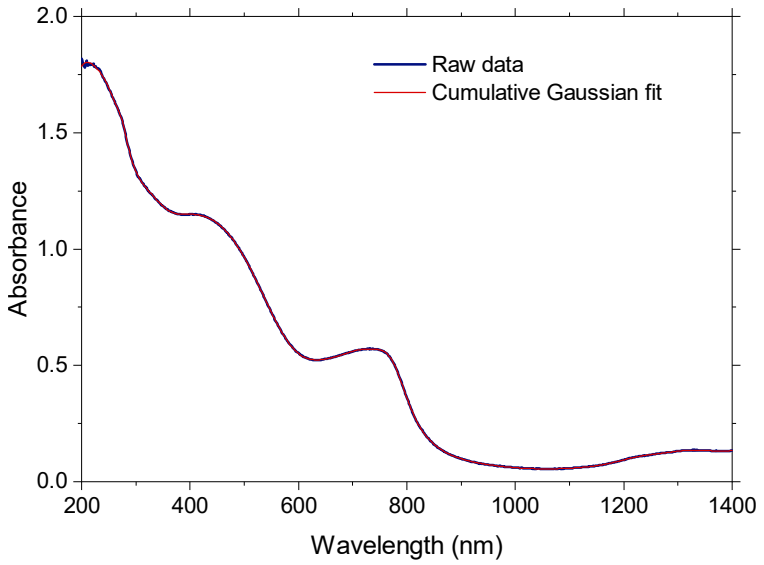

Figure D.2: Fit of the absorbance spectrum of Co_3O_4 shown in Figure 7.2 using a sum of 13 Gaussians. The purpose of this fit is not to extract physically meaningful information, but rather to generate a noise-free version of the absorbance spectrum from which high-quality derivative signals can be calculated.

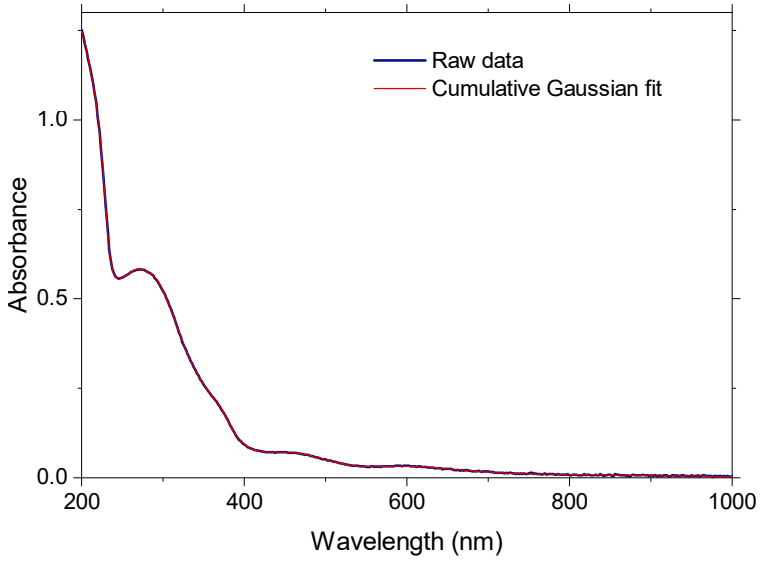

Figure D.3: Fit of the absorbance spectrum of Cr_2O_3 shown in Figure 7.2 using a sum of 15 Gaussians. The purpose of this fit is not to extract physically meaningful information, but rather to generate a noise-free version of the absorbance spectrum from which high-quality derivative signals can be calculated.

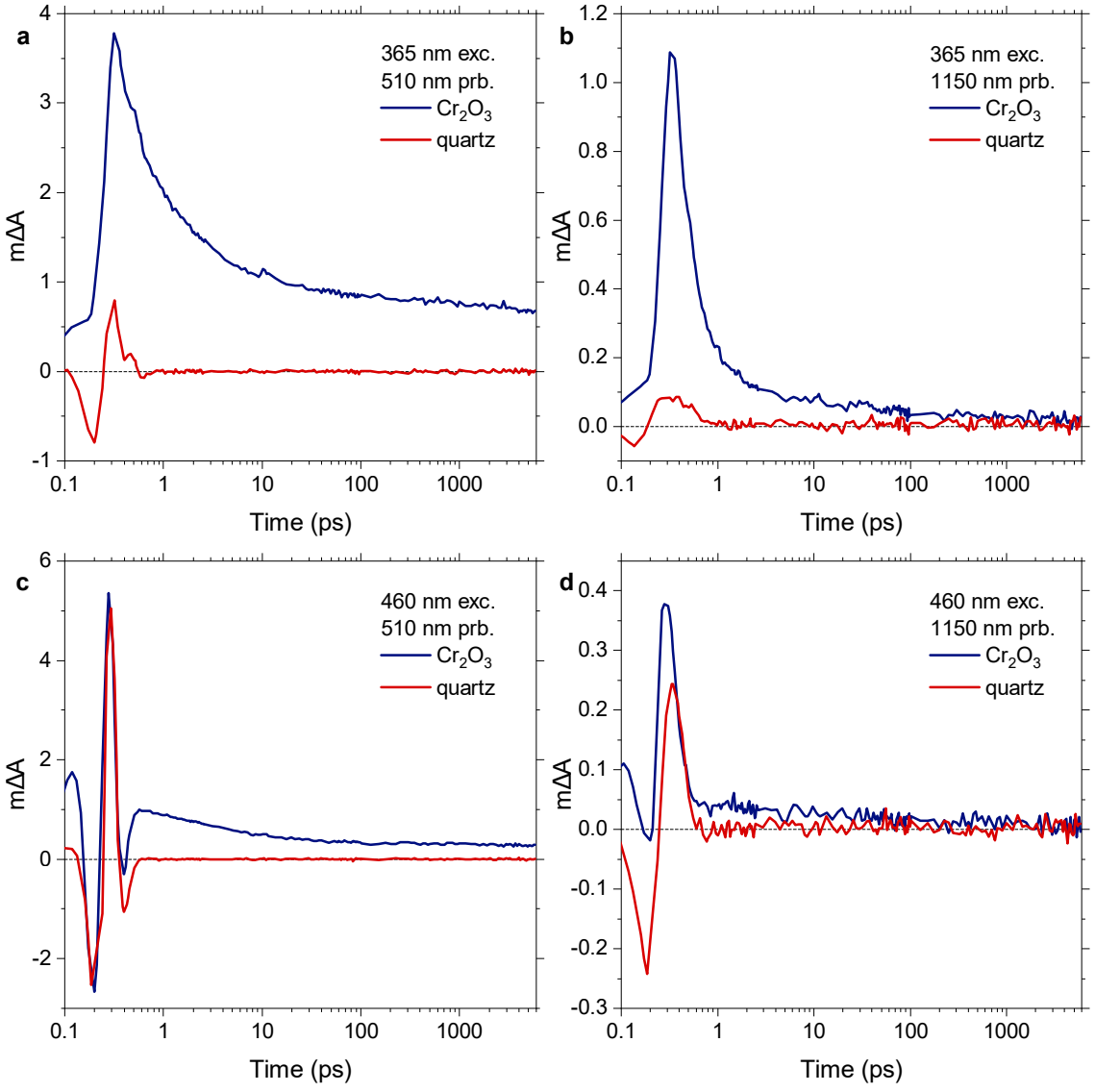

Figure D.4: Exemplary comparison of some of the transient absorption kinetics obtained from a Cr_2O_3 film and a blank quartz glass substrate, excited at (**a**, **b**) 365 nm and (**c**, **d**) 460 nm, and probed at (**a**, **c**) 510 nm and (**b**, **d**) 1150 nm. The used fluences were 0.57 mJ cm^{-2} and 1.43 mJ cm^{-2} for 365 nm and 460 nm excitation, respectively. This comparison demonstrates that the early-time signal observed upon 460 nm excitation is a instrument response-related artefact, whereas the rapid decay found upon 365 nm excitation in the NIR is a real signal.

Appendix E

Copyright agreements

Elements:

- Copyright agreement for Figure 2.4

RightsLink Printable License

SPRINGER NATURE LICENSE
TERMS AND CONDITIONS

Jan 26, 2020

This Agreement between Imperial College London ("You") and Springer Nature ("Springer Nature") consists of your license details and the terms and conditions provided by Springer Nature and Copyright Clearance Center.

License Number	4676090311705
License date	Sep 25, 2019
Licensed Content Publisher	Springer Nature
Licensed Content Publication	Nature Reviews Materials
Licensed Content Title	Semiconducting materials for photoelectrochemical energy conversion
Licensed Content Author	Kevin Sivula, Roel van de Krol
Licensed Content Date	Jan 20, 2016
Licensed Content Volume	1
Licensed Content Issue	2
Type of Use	Thesis/Dissertation
Requestor type	academic/university or research institute
Format	print and electronic
Portion	figures/tables/illustrations
Number of figures/tables /illustrations	1

RightsLink Printable License

High-res required	no
Will you be translating?	no
Circulation/distribution	50000 or greater
Author of this Springer Nature content	no
Title	PhD student
Institution name	Imperial College London
Expected presentation date	Sep 2019
Portions	Figure 2a
Requestor Location	Imperial College London Molecular Sciences Research Hub White City Campus 80 Wood Lane London, W12 0BZ United Kingdom Attn: Imperial College London
Total	0.00 GBP

Terms and Conditions

Springer Nature Customer Service Centre GmbH
Terms and Conditions

This agreement sets out the terms and conditions of the licence (the **Licence**) between you and **Springer Nature Customer Service Centre GmbH** (the **Licensor**). By clicking 'accept' and completing the transaction for the material (**Licensed Material**), you also confirm your acceptance of these terms and conditions.

1. Grant of License

1. 1. The Licensor grants you a personal, non-exclusive, non-transferable, world-wide licence to reproduce the Licensed Material for the purpose specified in your order only. Licences are granted for the specific use requested in the order and for no other use, subject to the conditions below.

1. 2. The Licensor warrants that it has, to the best of its knowledge, the rights to license reuse of the Licensed Material. However, you should ensure that the material you are requesting is original to the Licensor and does not carry the copyright of

another entity (as credited in the published version).

1. 3. If the credit line on any part of the material you have requested indicates that it was reprinted or adapted with permission from another source, then you should also seek permission from that source to reuse the material.

2. Scope of Licence

2. 1. You may only use the Licensed Content in the manner and to the extent permitted by these Ts&Cs and any applicable laws.

2. 2. A separate licence may be required for any additional use of the Licensed Material, e.g. where a licence has been purchased for print only use, separate permission must be obtained for electronic re-use. Similarly, a licence is only valid in the language selected and does not apply for editions in other languages unless additional translation rights have been granted separately in the licence. Any content owned by third parties are expressly excluded from the licence.

2. 3. Similarly, rights for additional components such as custom editions and derivatives require additional permission and may be subject to an additional fee. Please apply to Journalpermissions@springernature.com/bookpermissions@springernature.com for these rights.

2. 4. Where permission has been granted **free of charge** for material in print, permission may also be granted for any electronic version of that work, provided that the material is incidental to your work as a whole and that the electronic version is essentially equivalent to, or substitutes for, the print version.

2. 5. An alternative scope of licence may apply to signatories of the STM Permissions Guidelines, as amended from time to time.

3. Duration of Licence

3. 1. A licence for is valid from the date of purchase ('Licence Date') at the end of the relevant period in the below table:

Scope of Licence	Duration of Licence
Post on a website	12 months
Presentations	12 months
Books and journals	Lifetime of the edition in the language purchased

4. Acknowledgement

4. 1. The Licensor's permission must be acknowledged next to the Licenced Material in print. In electronic form, this acknowledgement must be visible at the same time as the figures/tables/illustrations or abstract, and must be hyperlinked to the journal/book's homepage. Our required acknowledgement format is in the Appendix below.

5. Restrictions on use

5. 1. Use of the Licensed Material may be permitted for incidental promotional use and

RightsLink Printable License

Appendix 1 — Acknowledgements:

For Journal Content:
Reprinted by permission from [**the Licensor**]: [**Journal Publisher** (e.g. Nature/Springer/Palgrave)] [**JOURNAL NAME**] [**REFERENCE CITATION** (Article name, Author(s) Name), [**COPYRIGHT**] (year of publication)

For **Advance Online Publication papers:**
Reprinted by permission from [**the Licensor**]: [**Journal Publisher** (e.g. Nature/Springer/Palgrave)] [**JOURNAL NAME**] [**REFERENCE CITATION** (Article name, Author(s) Name), [**COPYRIGHT**] (year of publication), advance online publication, day month year (doi: 10.1038/sj.[JOURNAL ACRONYM].)

For Adaptations/Translations:
Adapted/Translated by permission from [**the Licensor**]: [**Journal Publisher** (e.g. Nature/Springer/Palgrave)] [**JOURNAL NAME**] [**REFERENCE CITATION** (Article name, Author(s) Name), [**COPYRIGHT**] (year of publication)

Note: For any republication from the British Journal of Cancer, the following credit line style applies:

Reprinted/adapted/translated by permission from [**the Licensor**]: on behalf of Cancer Research UK: : [**Journal Publisher** (e.g. Nature/Springer/Palgrave)] [**JOURNAL NAME**] [**REFERENCE CITATION** (Article name, Author(s) Name), [**COPYRIGHT]** (year of publication)

For **Advance Online Publication** papers:
Reprinted by permission from The [**the Licensor**]: on behalf of Cancer Research UK: [**Journal Publisher** (e.g. Nature/Springer/Palgrave)] [**JOURNAL NAME**] [**REFERENCE CITATION** (Article name, Author(s) Name), [**COPYRIGHT**] (year of publication), advance online publication, day month year (doi: 10.1038/sj.[JOURNAL ACRONYM])

For Book content:
Reprinted/adapted by permission from [**the Licensor**]: [**Book Publisher** (e.g. Palgrave Macmillan, Springer etc) [**Book Title**] by [**Book author**(s)] [**COPYRIGHT**] (year of publication)

Other Conditions:

Version 1.2

Questions? customercare@copyright.com or +1-855-239-3415 (toll free in the US) or +1-978-646-2777.

5 of 5